Development of Comprehensive Dynamic Damage Assessment Methodology for High-Bypass Air Breathing Propulsion Subject to Foreign Object Ingestion

Yangkun Song

Dissertation submitted to the faculty of the Virginia Polytechnic Institute and State University in partial fulfillment of the requirements for the degree of

Doctor of Philosophy
in
Mechanical Engineering

Javid Bayandor
Francine Battaglia
Walter F. O'Brien
Alfred L. Wicks
Joseph P. Veres

Sept. 20th, 2016
Blacksburg, VA

Keywords: Foreign Object Ingestion, Fluid-Structure Interaction, Finite Element, Bird, Ice, Advanced Propulsion, Composite Structures, Particle Methods

Development of Comprehensive Dynamic Damage Assessment Methodology for High-Bypass Air Breathing Propulsion Subject to Foreign Object Ingestion

Yangkun Song

Academic Abstract

The purpose of this study is to develop a unique methodology to assess the response and dynamic damage progression of an advanced, high-bypass propulsion system in the event of an FOI during operation. Using a finite element framework, a unique modeling methodology has been proposed in order to characterize the response of a system subjected to a foreign object ingestion (FOI). To demonstrate versatility of the computational analysis, the impact characteristics of two most common foreign object materials, bird and ice, were investigated. These materials were then defined in finite element domain, verified computationally, and then validated against the existing physical experiments. In addition to the mechanics of the two FOI materials, other material definitions, used to characterize the structures of the high-bypass propulsion system, were also explored. Both composite materials and rate dependent definitions for metal alloys were investigated to represent the damage mechanics in the event of an FOI.

Subsequently, damage sequence of high-bypass propulsion systems subject to FOI was developed and assessed, using a uniquely devised Fluid-Structure Interaction (FSI) technique. Using advanced finite element formulation, this approach enabled the accurate simulation of the comprehensive damage progression of the propulsion systems by including aerodynamic interaction. Through this strategy, fluid mechanics was combined with structural mechanics in order to simulate the mutual interaction between the two continua, allowing the interpretation of both the additional damage caused by the fluid flow and disrupted aerodynamics induced by the deforming fan blades. Subsequently, this multidisciplinary-multiphysics computational approach, in the framework of the comprehensive analysis methodology introduced, uniquely enabled the effective determination of complete overall progressive impact damage, not traditionally available to propulsion designers.

Development of Comprehensive Dynamic Damage Assessment Methodology for High-Bypass Air Breathing Propulsion Subject to Foreign Object Ingestion

Yangkun Song

Generic Audience Abstract

Foreign object ingestion (FOI) into jet engines is a recurring scenario during the operation life of aircraft. Objects can range from as small as a pebble on the tarmac to the size of a large bird. Among the potential ingestion scenarios, damage caused by smaller objects may be considered to be negligible. On the other hand, larger objects can initiate progressive damage, potentially leading to catastrophic failure, compromising the integrity of the structure, and endangering the safety of passengers. Considering the dramatic increase in air traffic, FOI represents a crucial safety hazard, and must be better understood to minimize possible damage and structural failure. However, full-scale FOI experiments using real engines are prohibitively expensive.

Hence, in this doctoral study, we have developed a full-scale virtual engine model to computationally simulate the damage evolution caused by FOI. The model uniquely incorporates the contributions of aerodynamic distortion to the growth of the structural damage. The flow distortion is a result of the initial FOI damage sustained by engine components. The ability to simulate full-scale FOI through close coupling of the fluid field with engine structures can help improve the design procedures and reduce cost by supporting experimental testing through representative and complementary simulations. In addition to improving the design cycle, our developed methodology is aimed to be a stepping stone in realizing future jet engine certifications by analysis.

Table of Contents

List of Tables

List of Figures

1 Introduction

The demand for aircraft transportation has been increasing dramatically for decades. In 2012, 732 million people worldwide used domestic and international flight. This is approximately twice the entire population of the U.S. in 2012 [1]. Current aviation industries heavily rely on air-breathing propulsion systems, which can be vulnerable to foreign object ingestion. The propulsion system generates a very high thrust during the take-off, with the majority of the thrust produced by the front fan section of the engine because of the massive airflow through the wide inlet. A high speed fan rotation is required to generate the airflow to produce the required thrust, so extremely high stresses can occur along the blade by centrifugal force when operated at maximum design conditions. To maximize the efficiency of the system, the gap between the tip of blade and casing is often a fraction of a centimeter to prevent pressure losses due to leakage. As a result of these narrow design margins and operating conditions, numerous dangerous situations are possible when a foreign object impacts occurs. Due to the sudden impact, the compressor can possibly experience a stall. Another critical situation is the vibration and deformation of the fan blade; this is vitally important, because it causes the system to become progressively unbalanced. The rotational axis of the damaged system will become more unstable by continuous rotation, which leads to excessive vibration and will eventually cause critical damage to the propulsion system.

Because the fan is located at the throat of a large inlet area, in order to maximize the mass airflow through the system, FOI into a high-bypass propulsion system is a common occurrence. Additionally, the fan creates a large negative pressure gradient that in turn increases the chance of FOI. According to an investigation, the engine has the highest chance of being subjected to FOI among the potential impact areas over the entire aircraft [2]. According to Dolbeer et al., 142,603 wildlife strikes were reported between 1990 and 2013, which resulted in approximately $660 million dollars of economic loss. Since 1988, 255 people have been killed and 243 airplanes were damaged by bird ingestion [3].

Ingestion may cause significant damage to the system depending on the size and mechanical properties of the ingested object. In 1977, Southern Airways flight 242 was struck by a severe thunderstorm when flying between 14,000 feet and 17,000 feet. As a result of the severe condition, the system failed and the pilot executed an emergency landing in New Hope, Georgia. Of the 84 casualties, 62 were fatalities and 22 were serious injuries. The National Transportation Safety Board (NTSB) investigated and concluded that the incident occurred due to the sudden thrust loss by ingesting a massive amount of water and hail. During the incident, the cockpit windows were

destroyed and the propulsion system was damaged by hail and suffered from compressor stall due to both the damaged compressor and large amount of water ingestion [4].

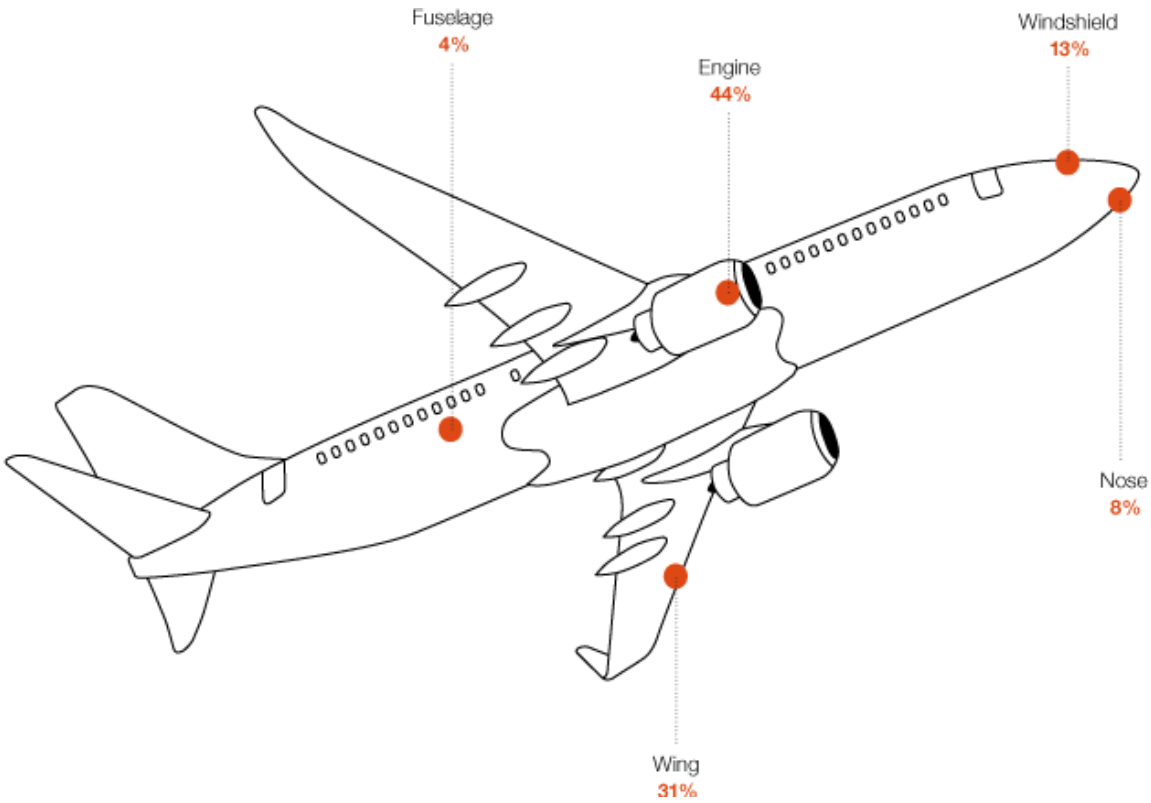

Figure 1.1 Susceptibility to foreign object impact (Image taken from [2])

Another well-known FOI incident occurred in January 2009; US Airways flight 1549 took off from LaGuardia Airport in New York City and struck a flock of Canadian geese during the takeoff. The bird ingestion caused both engines to fail simultaneously [5]. Fortunately, the debris of the propulsion system did not penetrate the cabin and the pilot was able to successfully perform an emergency ditching on the Hudson River without incurring any casualties.

1.1 Objective

To ensure passenger safety, the Federal Aviation Administration (FAA) requires engine manufacturers to strictly follow regulations regarding FOI scenarios and engine rotor containment [6–8]. These regulations require that an engine subject to bird ingestion should maintain adequate thrust to allow the aircraft to land safely. The design is also required to maintain the operating condition regardless of any ice ingestion. Additionally, the regulations demand for a stringent engine casing design to guarantee debris containment. The containment should include the

prevention of escaped blade fragments from penetrating through the structure of the casing in an event of component or system failure. In order to comply with the regulations, actual FOI tests have to be conducted to verify the damage tolerance within a propulsion system. Unfortunately, full-scale experiments are prohibitively expensive to perform under all FAA directed scenarios to guarantee reliability. Furthermore, it is extremely difficult to collect and post-process the result to understand all possible problems to improve the design.

In order to reduce costly experiments and provide more practical certification procedures, an explicit finite element framework is used to uniquely predict the damage progression within an advanced propulsion system caused by FOI. Most existing literature, except for studies from *CRASH* Lab [9–12], have focused on simple scenarios such as bird strikes on either flat plates or airframes [13–15], a single blade impact [16,17], or even a reduced structure with fewer fan blades [18], which still does not include a fully featured propulsion system for comprehensive damage investigation. By implementing detailed design, several problems which have never been introduced in the previous studies are identified, such as debris ingestion into low pressure compressor, ice particle distribution and possible fragments ingestion into LPC, casing abrasions and containment. Moreover, none of the current FOI work demonstrate consideration of air-structure interaction. The research presented here focuses on the development of a comprehensive, highly non-linear, multidisciplinary damage assessment strategy to accurately analyze the impact response of high-bypass propulsion systems subject to FOI, by incorporating the aerodynamic interaction with FSI strategies used for soft body impact investigations.

The goal of this study is to develop a novel high fidelity (highly detailed) computational methodology for:

(1) Develop a methodology to assess the dynamic response and damage progression sustained within the forward section of modern propulsion systems subject to both bird and ice ingestion.

(2) Coupling fluid and solid mechanics to develop a comprehensive multidisciplinary-multiphysics damage assessing methodology in order to characterize the mutual interaction between structural damage caused by soft body FOI and the resulting changes in fluid flow along the fan blades subject to FOI.

1.2 Analysis Methodology

Performing full experimental testing is prohibitively challenging in many respect. In particular, it is impossible to momentarily measure the fluid flow along the damaged system as the FOI is in progress. To overcome such obstacles, a computational methodology was developed and employed that takes advantage of continuous evolution of the relevant theories and recent improvements in computational power. In order to conduct such an analytical approach, understanding fluid flow characterization, multiple collision mechanics and interactions between objects was required to effectively assess the damage caused by FOI.

As indicated, two potential foreign objects, bird and ice, were selected for this study, as the two objects are the most common materials that can interact with an aircraft during its operation [3–5]. Because the mechanical strengths of both bird and ice are not fully defined, and relatively weaker than metal alloys or composite materials, a multidisciplinary study is required to computationally characterize their impact mechanics. FSI methodology and shock physics were extensively explored for predicting fluidic behavior of low strength projectiles at high speed impact. However, traditional finite element formulations are inadequate for predicting the complete FSI process. This is due to severe numerical instabilities associated with large mesh domain warping caused by fluidic deformation [19–21]. The instabilities include mesh entanglement, negative volumes, and zero-energy modes. To circumvent these limitations, an Arbitrary Lagrangian-Eulerian (ALE) and meshless Lagrangian formulation, were employed to supplement conventional approaches to solve an FSI problem.

In addition to the foreign object study, an advanced structure, fiber-reinforced polymer (FRP) material was also investigated to analyze the damage mechanics of modern propulsion system. For the modern propulsion system, carbon fiber reinforced polymer (CFRP) is used for the fan blade structure and Kevlar® is used for casing containment [22–25]. Hence, FRP damage modeling was also investigated and incorporated into the proposed methodology so that the full extent of post-impact damage in an advanced structural propulsion system could be quantified.

1.3 Dissertation outline

Diverse computational modeling methodologies were investigated and discussed in this work to highlight the foundations built for the developed methodology. Hence, a brief outline is provided in this section. Chapter 2 briefly discusses contemporary propulsion systems and the anticipated problems caused by the design. This chapter also encompasses the fan blades mechanics, current

regulations, problems associated with FOI, and soft body damage mechanics. In chapter 3, damage models used to predict structural responses are discussed as well as the equation of states that governs the fluidic deformation of soft bodies at the high speed impact. Chapter 4 contains element formulations, time step integration, and contact algorithms used within the finite element framework. Chapter 5 provides an overview of soft body projectile modeling methodologies and mesh dependency, as well as composite damage modeling strategies with validations. Discussions on the virtual model developed, damage assessment, and the subsequent issues discovered using the proposed damage methodology are presented in chapter 6. Chapters 7 and 8 address the capability to improve the design using the proposed methodology through the benefit of using a fully-parameterized damage assessing technique. Chapter 9 discusses the results of using the developed multidisciplinary FSI strategy to uniquely simulate the fluid field disturbance caused by FOI. Lastly, the summary and conclusion of the research presented and future work discussed in Chapter 9.

2 Background and Theory

Propulsion systems are integral to the operation of aircraft. In order for a jumbo-scale passenger aircraft to reach liftoff, the engine continually ingests large amounts of air and pushes it away to generate thrust. Among the different types of engines, high-bypass-ratio engines are some of the most suitable configurations, because of a higher efficiency and quieter operation than low-bypass engines. They offer a more comfortable flight experience to passengers. Such a jet engine is composed of several main components: the front inlet fan, casing, compressors, combustion chamber, turbines, and other control systems as shown in Fig. 2.1. All components must work together in unison for the thrust requirement to be met.

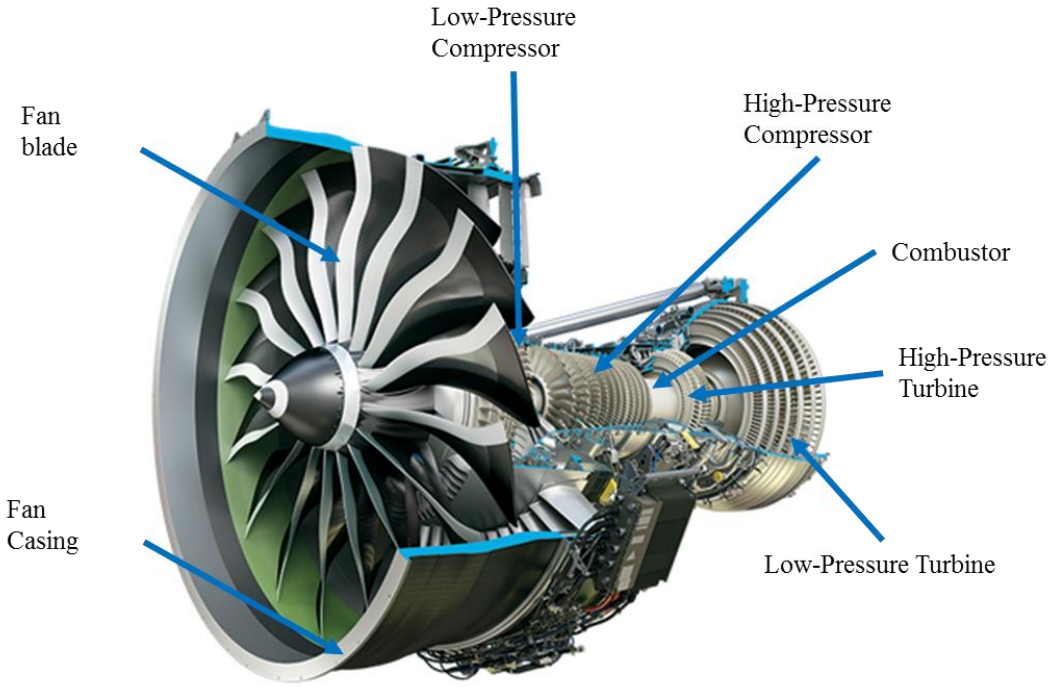

Figure 2.1. Schematic view of a high-bypass turbofan system (Image taken from [26]**)**

In order to improve the overall performance of propulsion systems, while complying with environmental regulations, aviation industry needs to continuously improve and optimize the use of different approaches. Among numerous improvement over the conventional design, the modern propulsion systems have achieved increased efficiency, performance and noise reduction by adopting CFRP structure fan blades, each with an aerodynamically optimized wide-swept design. An advanced fan design, can maintain the solidity, while using fewer blades. The weight of the forward assembly can be reduced, while the noise level is drastically dropped [27–29].

However, FRP has lower ductility that can cause sudden fracture under impact rather than yielding. Also, resin, which is used to cure fibers and fabricate the fan blades, is susceptible to wear, tear, and delamination around the edge. To solve these problems, titanium (Ti) alloy is foiled around the composite section to prevent degradation. Although CFRP is vulnerable, the demand for FRP has increased rapidly [30]. This increase has been partly due to FRP's relatively high strength-to-density ratio compared to that of metal alloys, of which the conventional blades are made [31]. Another reason FRP is employed is to reduce the engine mass. To satisfy the FAA regulation (FAR § 33.94), the fan casing is designed with Kevlar® due to its ballistic impact characteristics [32–34].

Because of its drastically more complicated microstructural architecture, the prediction of correct failure in FRP is significantly more difficult [35–37]. Due to the anisotropic mechanical properties caused by fiber and matrix, FRP laminates suffer from stiffness mismatch between the plies depending on their stacking sequence [31]. Hence, FRP damage models were further investigated and incorporated into the proposed methodology so that the full extent of post-impact damage in an advanced structural propulsion system can be quantified.

As mentioned, the two most common foreign objects, bird and ice, are investigated here. They are both capable of causing catastrophic damage on aircraft structures as well as the propulsion system, extenuated by the combination of rotational motion of the engine rotors and high flight speed of the aircraft. One such incident, which was occurred in September 2009, is shown in Fig. 2.2-(a). A B-737 operated by Germania Airline struck by a flock of starlings at approximately 300 *km/h* right side of the airplane. The airplane was able to return to the tarmac, but passengers sensed a sudden burst when the incident occurred.

Hail is usually created inside cumulonimbus clouds, which experience strong upstream wind due to the significant temperature differences (+20 $°C$ to -60 $°C$) along the altitude. Due to convection, large ice precipitation can float in the sky (3 *km* to 13 *km*) which is the normal altitude for most of the commercial aircraft. The damage caused by hailstorm is destructive in multiple ways, cars and residential areas are occasionally destroyed because of the mass and potential energy of hailstone. Although the potential energy is negligible between hail and aircraft at same altitude, the damage caused by ice impact is still considerably high because of the relative velocity between the hail and flight speed.

Another incident is shown in Fig. 2.2-(b), illustrating the result of an aircraft (flight number: N708AA) that flew through a hailstorm in 2006. The overall post-damage was considerable: the cockpit window was shattered and the radome was destroyed. Fortunately, the airplane was able to successfully land on the tarmac without any casualties.

(a) Bird ingestion into jet engine (b) Damage caused by hailstone

Figure 2.2. Picture of a plane subjected to bird ingestion (Image taken from [38]**) on the left and damage caused by hailstone impact on airplane radome (Image taken from** [39]**) on the right**

As shown, the projectile is subsequently subjected to large deformations and separation upon impact. The conventional finite element is unable to predict the material deformation accurately. Therefore, modern finite element methodologies aim to address this shortcoming by introducing fluidic deformation. Such a methodology was used to model a fluid field along the propulsion system using Multi-Material ALE element formulation.

2.1 Background of Damage Mechanics and Debris Containment

2.1.1 Mechanics of the Fan Blade

At the design stage of axial turbomachines, three types of loading conditions are very important: thermal, bending, and centrifugal. For the forward section, thermal loading is negligible. Bending loads become important when the blades interact with the both steady and unsteady fluid flows. The fan blade is slid into the blade hub, so that the assembly is loose and avoids over-constraining the fan blade. Bending loads on the fan blade can potentially be reduced by changing the aerodynamic design of the blade.

However, the centrifugal force is not avoidable even if the design is changed. When an object rotates at a constant angular velocity (ω), centrifugal force (F) develops orthogonal to the rotational motion at the root of fan blade as shown in Fig. 2.3. The centrifugal stress at the blade root depends

on three design parameters: density of material, geometric dimensions (primarily hub to tip distance), and rotational speed.

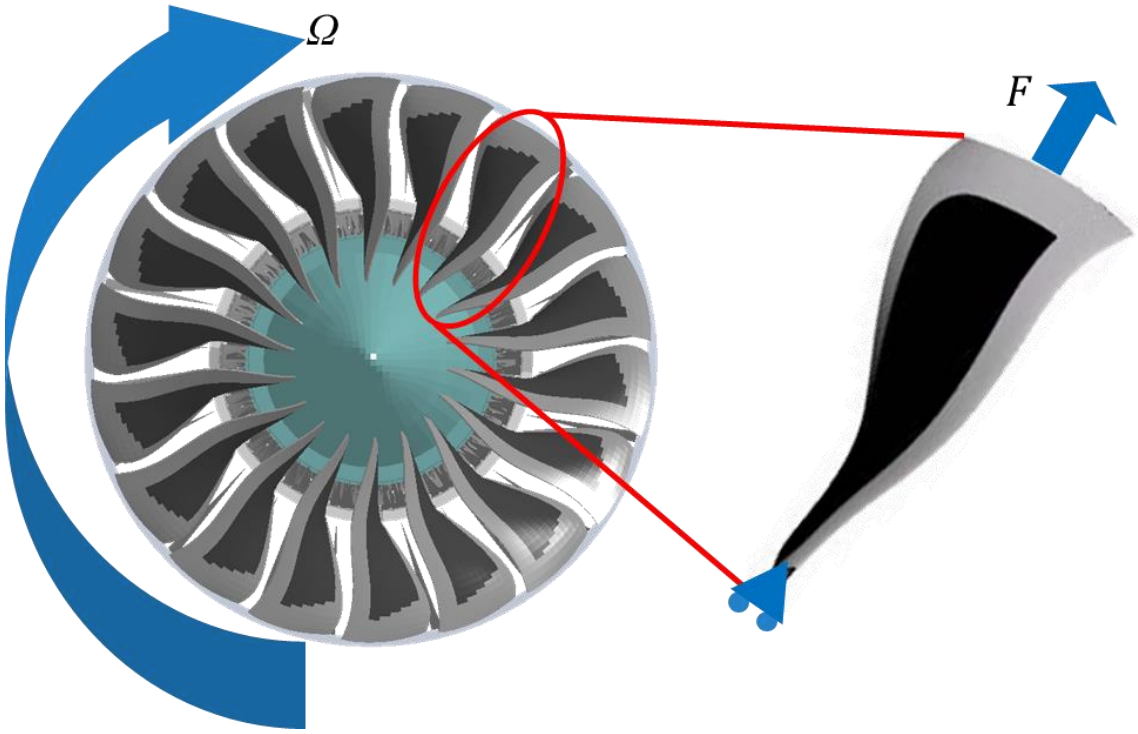

Figure 2.3 Schematic view of the centrifugal force (*F*) on fan blade with rotatioanl speed of ω

During takeoff, the front inlet section of a modern propulsion system can reach up to 2200 (230 *rad/s*) or 2700 (283 *rad/s*) revolutions per minute (*rpm*) depending on the design [40,41]. If a gearing system is adopted for the fan blade inlet section and multi-spool design, the operating *rpm* can be reduced compared to that of a traditional propulsion system. Despite the reduced *rpm*, centrifugal stress is still a great concern for developing high-performance turbofan system because the fan blade root section has to carry the entire loading. The schematic view of fan blade and blade hub assembly are shown in Fig. 2.4. The rotational stress (σ_r) on fan blade is evaluated by Eq. (1) [42]:

$$d(\sigma_r, A_b) = -(\rho_b, A_b, dr)\Omega^2 r \tag{1}$$

where A_b is local cross sectional area of blade, ρ_b is fan blade material density, Ω angular speed, and r is radius to the rotational center.

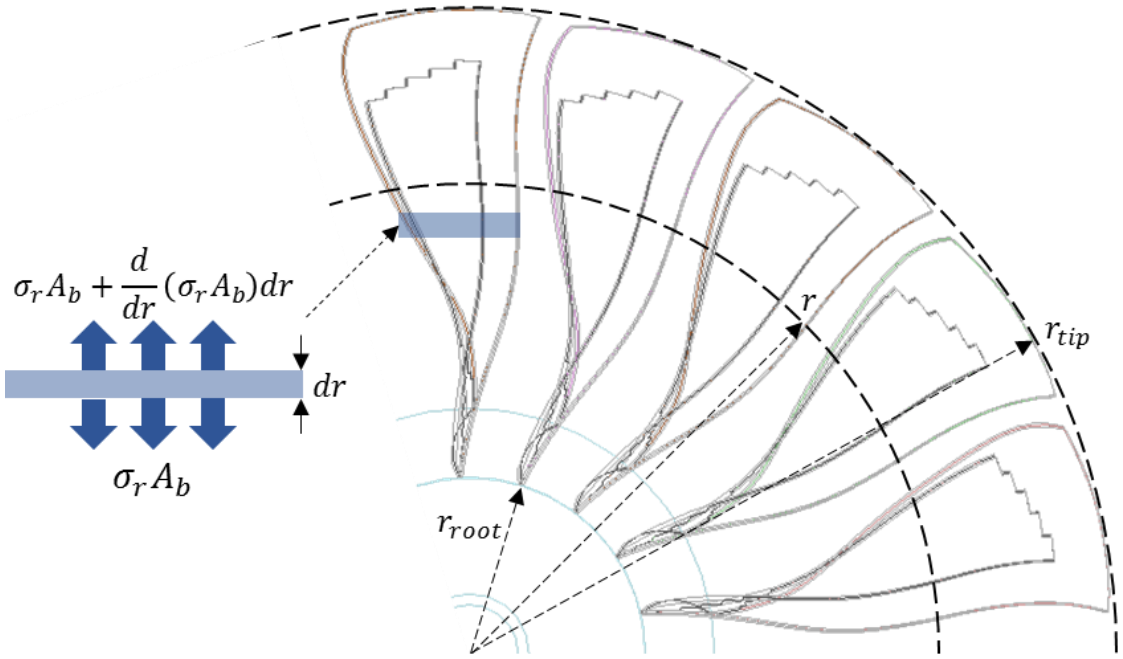

Figure 2.4 Schematic view of fan blades and blade hub assembly

Assuming A_b is not a function of r, the Eq. (1) becomes:

$$\frac{d\sigma_r}{dr} = -\rho_b \cdot \Omega^2 \cdot r \tag{2}$$

and integration with respect to r:

$$\int d\sigma_r = -\int (\rho_b \Omega^2 r) dr \tag{3}$$

If the integral bound is from the blade root to the blade tip, the Eq. (3) can be written as:

$$\sigma_{tip} - \sigma_{root} = -\frac{\rho_b \cdot \Omega^2}{2}\left(r_{tip}^2 - r_{root}^2\right) \tag{4}$$

Since the radial stress at tip (σ_{tip}) is zero, the blade root stress (σ_{root}) can be evaluated with following equation:

$$\sigma_{root} = \frac{\rho_b \cdot \Omega^2}{2}\left(r_{tip}^2 - r_{root}^2\right) \tag{5}$$

Assuming the mass of fan blade is:

$$m_{blade} = \rho_b \cdot A \cdot (r_{tip} - r_{root}) \tag{6}$$

The centrifugal fan blade root stress in Eq. (5) can be written in terms of mass as:

$$\sigma_{root} = \frac{m_{blade} \cdot \Omega^2 (r_{tip} + r_{root})}{2 \cdot A_{root}} \tag{7}$$

where A is the averaged cross sectional area of fan blade and A_{root} is the cross sectional area of blade root.

2.1.2 Soft Object Ingestion

According to the FAR § 33.76, the location of the bird impact is 50 percent or higher of the leading edge height of the fan blade as shown in Fig. 2.5 [8]. Considering the operating conditions of commercial aircraft, the recommended guideline for engine manufacturers is a projectile impact speed of 102 *m/s* (200 *knot*). When a single large bird or large flock of birds is ingested into the system, complete engine thrust loss is allowed. For small and medium size bird flocks, the subjected propulsion system must maintain 75 percent of take-off thrust with a momentary power output drop [8].

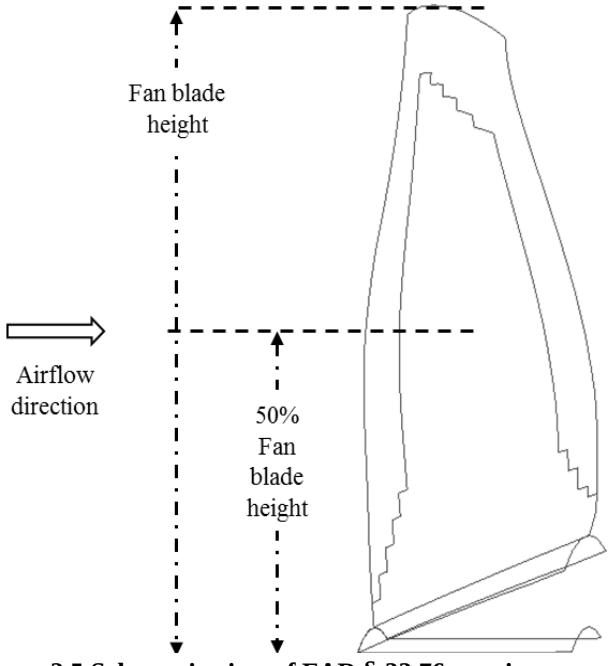

Figure 2.5 Schematic view of FAR § 33.76 requirement (Recreated based on [8]**)**

The jet engine is also required to be subjected to the ingestion of a large hailstone (~0.9 specific gravity) and maintain operational stability. The engine manufacturers are expected to design the engine to withstand an impact under the following conditions: the flight speed of aircraft at the

altitude of 4,500 *m* and the maximum power output operating condition. In order to satisfy the FAR § 33.77, the propulsion system may not suffer from unacceptable mechanical damage or huge thrust loss of upon the ice ingestion [43].

During the impact between the foreign object and the structure at high speed, a rapid loading is applied on both continua and such interaction is defined as impulse (*I*). Impulse is one of the shock loadings during which a force is exerted within an infinitesimal time window. Assuming an impact occurs at with given force *F(t)*, the impulse can be analytically evaluated using following Eq. (8):

$$I = \int_0^{\infty} F(t)dt \tag{8}$$

where the impulse throughout this calculation has the unit of $N \cdot s$. Figure 2.6 depicts a schematic view of when FOI occurs. Assuming the system is rotating while a foreign object is ingested, the object will be sliced as parabolic trajectory.

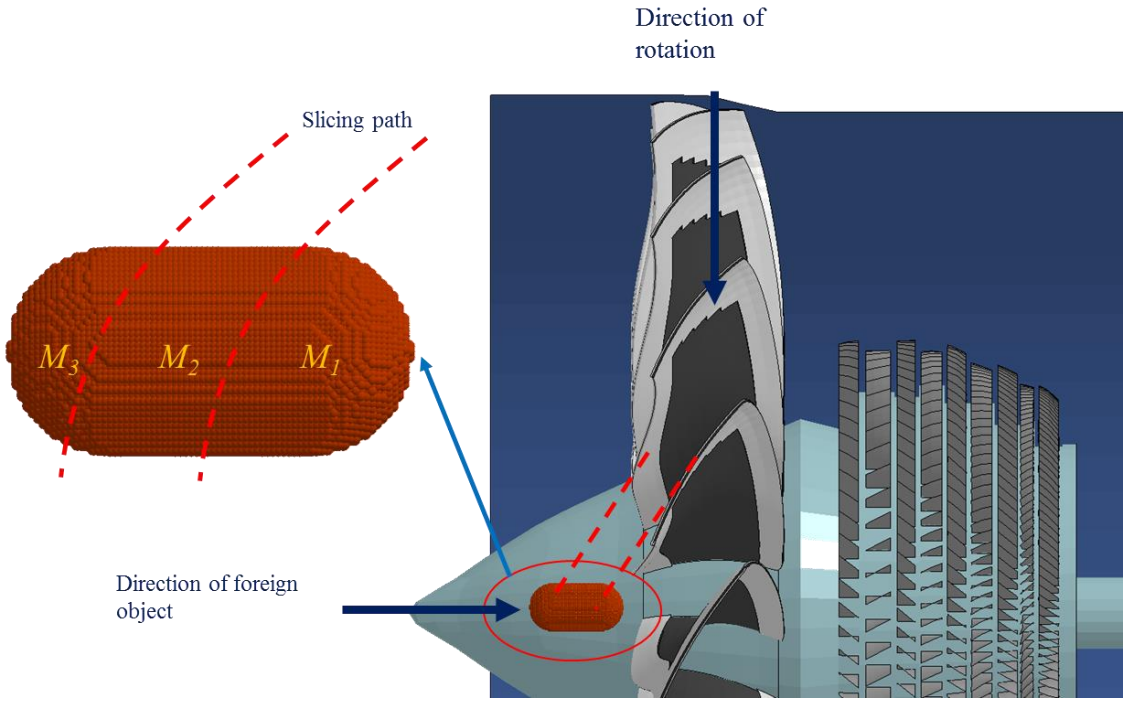

Figure 2.6 Schematic view of the interaction between a projectile with fan blades

When a foreign object is ingested, the tangential velocity of fan blade can reach the supersonic regime based on the impact location. Figure 2.7 shows the schematic diagram of relative velocity (v_r) between the foreign object and the fan blade based on the different impact locations. The main

difference between the locations is the relative velocity caused by the different tangential blade velocities (V_b).

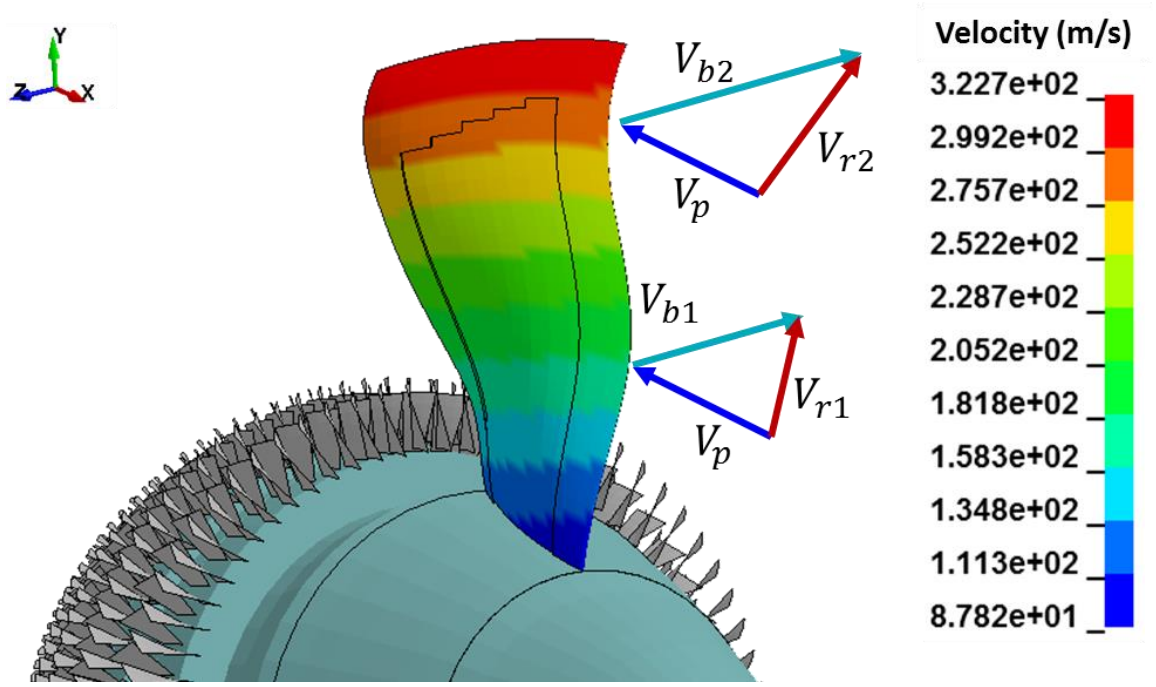

Figure 2.7 Schematic diagram of relative velocity between projectile and fan blade (V_r) as a function of different impact locations

Assuming the projectile speed is perpendicular with the tangential speed of the fan blade, the relative velocity (v_r) can be analytically calculated as:

$$v_r = \sqrt{V_p^2 + V_b^2} \tag{9}$$

If the ingested object dimensions are large enough to result in multiple pieces, a continuous interaction will occur and can cause further damage. Figure 2.8 shows a diagram of the interaction between fan blade and foreign object. Assuming the foreign object has a cylindrical shape, constant velocity for both fan blade and foreign object during the interaction, and rigid blade assumption, the sliced mass by interacting blade can be analytically calculated.

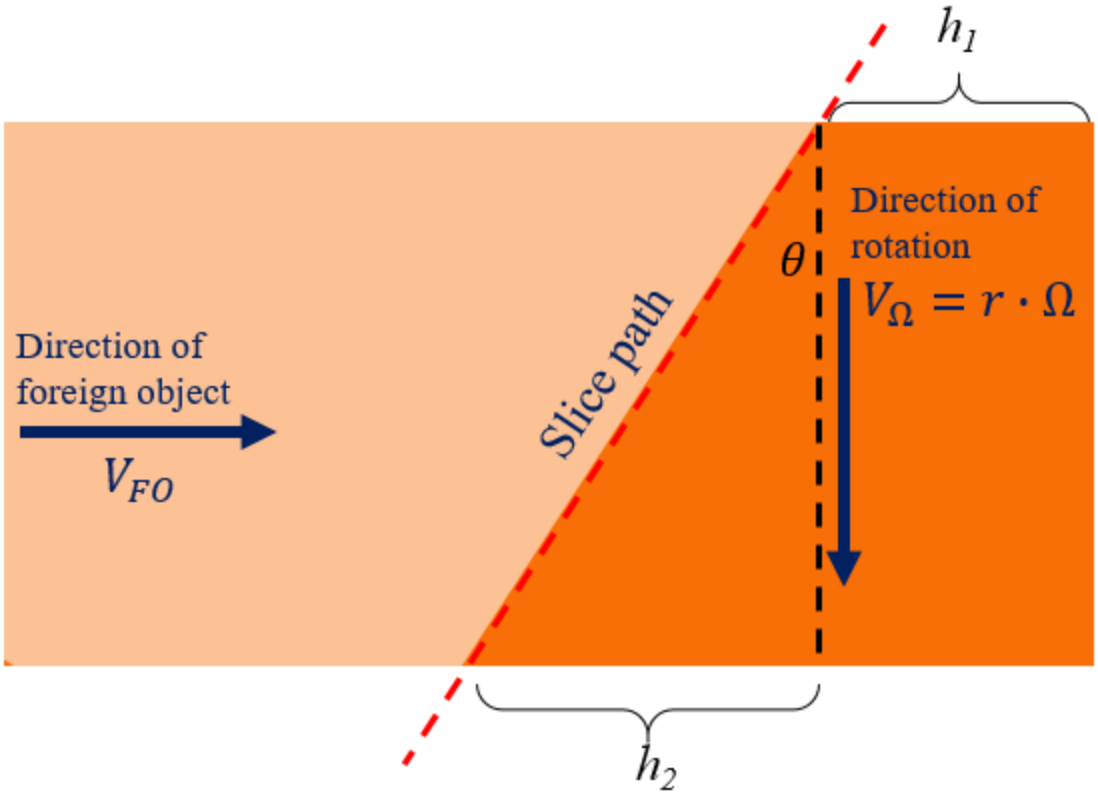

Figure 2.8 Detailed view of fan blade and foreign object interaction of cylindrical projectile

The angle (θ) is related with the relative velocity between the fan blade and foreign object. When the impact occurs at distance (r) from the center of rotation of the fan blade assembly, the slice angle can be calculated through using Eq. (16)

$$\theta = \tan^{-1}(V_{FO}/V_{\Omega}) \tag{10}$$

with the angle (θ), the sliced volume of cylinder can be calculated:

$$Q_{Slice} = \pi \cdot r_{cyl}^2 \cdot \frac{\{h_1 + (h_1 + h_2)\}}{2} \tag{11}$$

Since h_2 can be calculated by following equation:

$$h_2 = 2 \cdot r_{cyl} * \tan(\theta) \tag{12}$$

by substituting h_2 into Eq. (11), the sliced volume (Q_{Slice}) due to interaction can be calculated:

$$Q_{Slice} = \pi \cdot r_{cyl}^2 \cdot \left(h_1 + r_{cyl} \cdot \tan\left(Q_{FO}/Q_{\Omega} + \theta_{ba}(r)\right)\right) \tag{13}$$

$\theta_{ba}(r)$ is the angle of attach of fan blade at the distance of r from the center of rotation. Multiplying density of foreign object (ρ_{FO}) to the sliced volume from Eq. (13), the sliced mass (M_{FO}) can then be analytically calculated.

FOI causes additional loading on the blade, in the form of a bending load. In general, the fan blade suffers higher stresses under impact, compared with the centrifugal loading during the normal operating conditions. Upon impact, both projectile and the fan will experience significant amount of force due to momentum. The change in momentum during the impact is equal to $F \cdot \Delta t$, and the momentum can be simply derived by multiplying the projectile mass and velocity [44]. Hence, the change of velocity for the projectile is directly equal to the force exerted on the fan blade. The net force applied on the fan blade (F) can be analytically calculated through Eq. (17)

$$F = m_{FO} \cdot Q_{FO}/\Delta t \tag{14}$$

Combining Eq. (8) and (14), the overall impulse as a function of velocity change over time can be analytically evaluated:

$$I = \int_{t_1}^{t_2} F(t)dt \; = \int_{t_1}^{t_2} \left(m_{FO} \cdot a_{FO}(t)\right)dt \; = m_{FO} \cdot Q_{FO} \tag{15}$$

where $a_{FO}(t)$ is acceleration of foreign object as a function of time.

2.1.3 Fan Blade Out (FBO)

When FOI occurs, the target fan blade could detach from the fan assembly with high speed. The ejecta then becomes a threat to the rest of the aircraft [45] since it contains high kinetic energy and could penetrate the pressurized fuselage. Hence, all commercial engine manufacturers are required to successfully demonstrate the ability of their design to withstand FBO [6] by FAR § 33.94. Among multiple requirements, the baseline directive is to prevent fan case perforation in the

event of FBO during engine operation. When a fan blade is released during operation, it impacts with the engine casing with high kinetic energy as shown in Fig. 2.9.

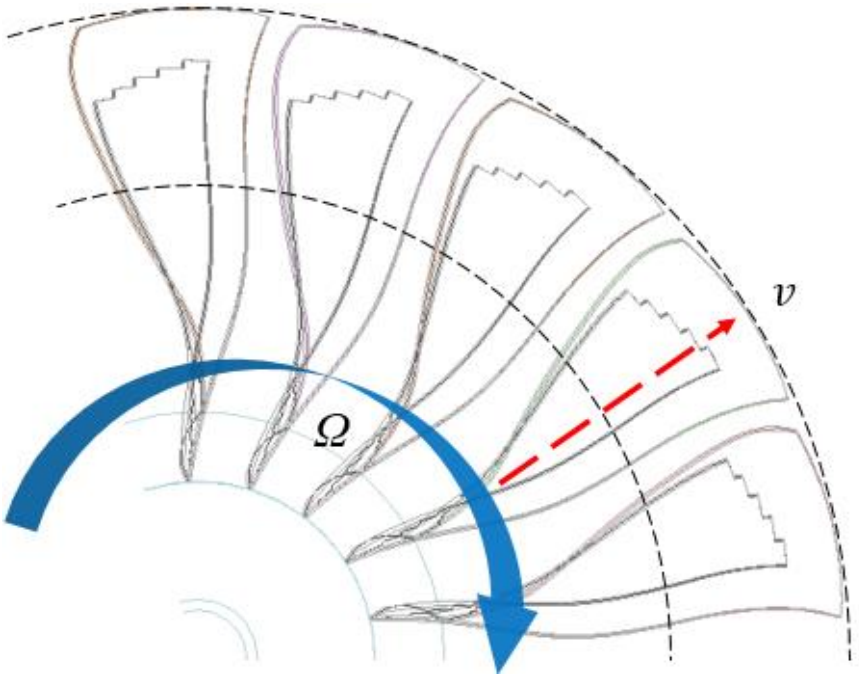

Figure 2.9 Schematic view of fan blade ejection

The translational speed of ejecta (*v*) can be found using Eq. (16):

$$v_{ejecta} = r * \Omega^2 \tag{16}$$

Assuming the radius (*r*), which is the casing radius of 1.52 *m*, the fan section speed of 2500 *rpm* (261.5 *rad/s*), and a lumped point mass of fan blade that is 15 *kg*, the kinetic energy of the fan blade can be calculated by following Eq. (17):

$$KE = \frac{1}{2} m * v_{ejecta}^2 \tag{17}$$

Based on this simplified analysis, the kinetic energy of the ejected blade is evaluated as 780 *kJ*. Once a fan blade is detached from the hub with such large kinetic energy, the casing is required to effectively arrest the blade. In addition to capturing the large kinetic energy, the fan case is also required to withstand the fan blade assembly and casing contact. After the blade is sheared off, an

eccentricity is induced on the entire rotating assembly, causing severe imbalance. The force induced by the rotating imbalance by missing single blade can be analytically calculated using Eq. (18)

$$F_{imbalance} = m \cdot e \cdot \Omega^2 \tag{18}$$

where e is eccentricity. Assuming the center of gravity of the fan blade is at 0.7 *m* from the rotating axis, the estimated eccentric force applied to the front fan hub will be 718 *kN*, assuming a single blade is lost during impact. This can cause a significant eccentric load to vibrate the front fan assembly. When the rotating imbalance occurs, the front fan assembly comes into contact with the fan casing. Controlling this is the other design criteria in addition to the fan blade ejection that needs to be addressed. As a result, the engine casing has to be strong enough to protect the fuselage in the event of FBO caused by FOI.

2.1.4 Fan Casing

In Mar. 2002, British Airways flight 268 was subjected to engine failure during flight. The airplane managed to successfully land in Sydney without fatalities [45], but according to the accident report, a fan blade from engine #3 suffered from fan blade failure. Figure 2.10 shows the ejected debris from the engine had penetrated the engine cowl, and was found over the entire plane: the leading edge, primary structure, and trailing edge flap of right-side wing with damage on the fuselage. Surprisingly the inspectors also found that debris from engine #3 was found at the intake cowl of neighbor engine #4.

As discussed, the fan blades in modern propulsion system employs a multi-spool system in order to reduce the front inlet fan section *rpm*. Consequently, the inlet diameter is increased to maximize the mass airflow through the system. The conventional fan casing, and even some of the modern propulsion system fan casings, is made out of homogeneous aluminum alloy as shown in Fig. 2.11-(a). However, the fan casing has very strict weight restrictions because the engine manufacturers have stringent fuel consumption and efficiency requirements of the system. Hence, designing a fan case with homogeneous block of metal alloy is not a fully optimized design approach, even though it is one of the most reliable ways to protect passengers from the ejecta.

(a) Damage observed at leading edge (b) Damage observed at fuselage

Figure 2.10 Post impact damage of the airplane after the engine failure (Image taken from [45]**)**

As a result, the casing is now developed using a hybrid design incorporating two different materials for improving the ballistic arresting characteristics and minimizing weight as much as possible. In order to satisfy the design requirement, the fan casing consists of two major structures: soft wall and hard wall casings (titanium alloy). The soft wall is mostly made out of a braided or weaved carbon fabric composite material at the outer perimeter of fan blade assembly in order to reduce the weight and achieve the high ballistic impact resistance [46,47]. The hard wall section covers the rest of section including the outer perimeter of the braided soft wall section in order to prevent a casing perforation during FBO incident as shown in Fig. 2.11-(b).

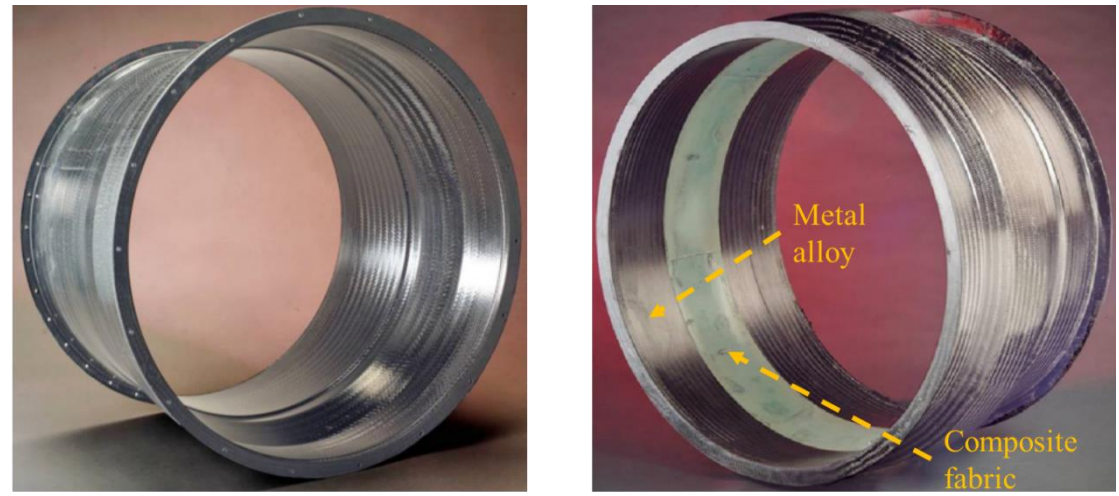

(a) Homogeneous hard wall fan casing (b) Hybrid material fan casing

Figure 2.11 Example of two fan casing designs (Images taken from [47]**)**

2.2 Soft Foreign Object

As mentioned, the mechanical strengths of both bird and ice are relatively weaker than any other airplane components including control surfaces or windshield. For this reason, a multidisciplinary approach is required to understand the impact mechanics. Soft body impact on deformable objects is a very complex phenomenon which cannot be described using a single set of equations. This problem is often defined as a fluid-structure interaction (FSI). Solid and fluid mechanics have to be coupled to properly capture the interaction of both the fluidic behavior of low strength materials and the dynamic response of the system after an impact incident. The fundamental of low strength projectile impact was initially proposed in 1978 by Wilbeck [48].

In Fig. 2.12, the time sequence for a soft body impact onto a compliant target is depicted. The soft body impact sequence over a deformable target is defined as: (a) initial impact, (b) shock propagation along the projectile and the target, (c) non-linear impact area growth, structural response, and damage initiation. The fluidization of soft body projectile simulated in the computational domain corresponded with the investigation done by Wilbeck [48]. Detailed results are discussed in later sections.

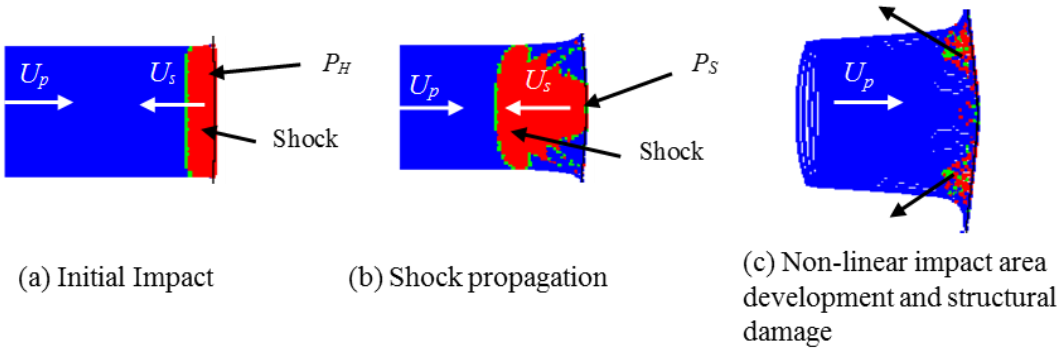

Figure 2.12 Sequential pictures of soft body impact on an elastic target from computational analysis

For a target made out of an elastic material, the response during the impact must be considered. Upon impact, the interaction between soft body projectile and structure results in two individual shockwaves to be generated at the interface, as shown in Fig. 2.12-(a). One is a shockwave through the projectile and the other is a shockwave that travels through the compliant target. The shock pressure (P_H), which is also known as Hugoniot pressure, sweeps through the projectile. This can be evaluated using the density and speed of sound of each material and the shock pressure can be analytically calculated by following Eq. (19) [49]:

$$P_H = \rho_p \cdot U_{s_p} \cdot U_b \cdot \left[\frac{\rho_t \cdot u_{s_t}}{\rho_p \cdot u_{s_p} + \rho_t \cdot u_{s_t}}\right] \quad (19)$$

where ρ_p is projectile density, U_{s_p} is a speed of sound of the projectile, U_b is relative projectile velocity against the target, ρ_t is target density, and u_{s_t} is speed of sound of the target. When the shockwave sweeps through the soft body projectile, the structure is destroyed and reduced to a bulk of water-like fluid for both bird and ice object as shown in Fig. 2.12-(b). Once the shockwave has passed through the continuum, presented in Fig. 2.12-(b), the fluidic bulk can then be assumed as a homogeneous non-Newtonian fluid as in Fig. 2.12-(c). Barber et al. [49]. also assumed the projectile turned into water-like fluid when it impacts on the target surface due to the sudden shock loading along the low strength projectile.

Due to the conservation of momentum, a chain of eddies constituting a larger ring vortex is generated around the outer edge of the front surface of the projectile Fig. 2.12-(c). This allows the homogeneous fluid body to dilate over the impact region as a result of the momentum of the projectile, while exerting dynamic loading onto the impact region. The dynamic loading decays out over the time interval considered as the change in the impulse of projectile. During the non-linear impact area development, the pressure on the target surface reaches the steady-state pressure (P_{ss}) at the impact location. The steady state pressure on the target surface can be calculated using Bernoulli's equation, and the stagnation pressure (P_{ss}) is written in Eq. (20):

$$P_{ss} = k \cdot \rho_b \cdot U_b^2 \quad (20)$$

where P_{ss} is the steady-state (stagnation) pressure applied on the target surface and k is compressibility of fluid.

2.2.1 Bird

For the certification procedure, the FAA lists four bird sizes based on the impact locations. Such impact locations are divided into windshield, wings, empennage and engines. As previously discussed, the FAA specifically requires manufacturers to perform a single 2.50 *kg* (or 5.51 *lbs.*) bird impact on both the cowl and fan blade for large diameter engines. The resulting damage should not impact on the structural integrity significantly so that the damaged system can generate continuous thrust generation after ingestion. In addition to the single bird requirement, a flock of

small or medium weight bird ingestion is also required to be tested based on the inlet throat area [8].

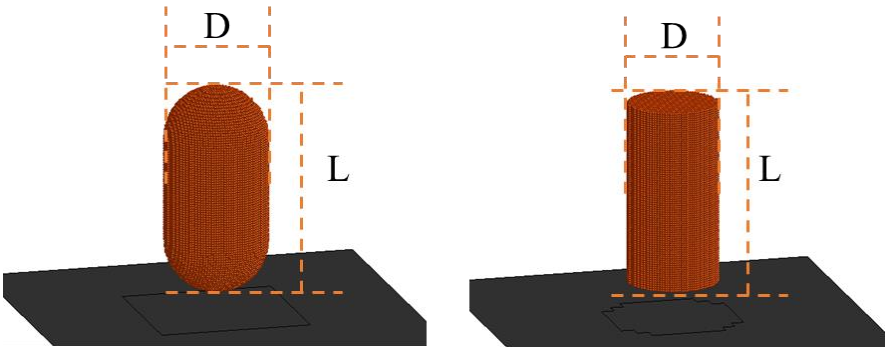

Figure 2.13 Two defeatured bird projectile shapes for computational analysis

Selecting an approximate bird geometry is important in the bird strike analysis, because the initial contacting surface area can affect the magnitude of shockwave trend during the impact. Hence, many projectile shapes have been explored in earlier studies and thoroughly discussed the change of force-time response on the target surface based on the geometry [50,51,14,52]. Those studies generally include cylinder, hemispherical cylinder, ellipsoid, or even fully featured bird model including internal structures such as bones and tissues. For this study, a defeatured 2.50 *kg* bird was created with two different cylinder variations (hemispherical-capped and flat-ended), which have been widely used in FOI analysis as shown in Fig. 2.13 [15,13,53,54]. The ratio between the length of the entire cylinder and its diameter were determined to be 2:1 to capture average bird body shapes and parameterize the dimension of cylinder based on the density and initial mass of projectile. Based on the predetermined projectile shape, aspect ratio (2:1), and density of bird, the projectile dimensions were determined by using following equations

For the cylinder projectile in in Fig. 2.13-(a):

$$D_{projectile} = \sqrt[3]{\frac{12 \cdot m_{bird}}{5 \cdot \rho_p \cdot \pi}} \tag{21}$$

For the hemispherical cylinder projectile in Fig. 2.13-(b):

$$D_{projectile} = \sqrt[3]{\frac{2 \cdot m_{bird}}{\rho_p \cdot \pi}} \tag{22}$$

where ρ_p is the density of projectile which is determined previously ($900\ kg/m^3$). Throughout the calculation, the dimension for each projectile calculated and tabulated in Table 2-1.

Table 2-1 Dimensions of low strength projectile for two shapes (m = 2.5 *kg*)

	Diameter (*m*)	**Length (*m*)**
Hemispherical Cylinder	0.128	0.257
Cylinder	0.121	0.242

In addition to the shape of bird, the material definition and following analytical derivation of bird projectile are equally important. Based on the previously addressed hypothesis, the density of homogeneous bird material was assumed to be a water-like Newtonian fluid. Because of the internal porosities regarding lungs and other light density substance, approximately 90% of the water density ($900\ kg/m^3$) was assigned to the virtual bird projectile model which had mass of 2.50 *kg*. The viscosity of the projectile was assumed as average human blood viscosity ($\mu = 4E^{-3}\ Pa \cdot s$ or $\nu = \mu/\rho = 3.8E^{-6}\ m^2/s$)., assuming the density of blood is $1.06E^3\ kg/m^3$. By establishing the bird substituent as a Newtonian fluid, the fluidic deformation of the bird and the corresponding nonlinear structural damage can be simulated.

2.2.2 Ice

Understanding the mechanical behavior of ice is very important for the damage prediction of the system upon the ice ingestion. Although it is one of the most commonly abundant materials, ice is environmentally sensitive, making the analysis difficult [55]. However, many researchers have investigated and concluded several of its mechanical properties. Table 2-1 shows typical mechanical properties of ice from several literatures [56–58]. The density changes of water from liquid state to solid state is up to 90%, when the ice is formed with well-organized crystalline structure. Since the mechanical properties of ice is stochastically determined by ambient conditions during formulation procedure, a fully dense ice crystalline structure material properties were selected to reduce the complexity of simulation while still predicting the worst case scenario.

Table 2-2 Mechanical properties of ice

	Gold [56]**, Arenson** [57] **at -5 ºC**	**Carney et al.** [58] **at -10 ºC**
Density, ρ (kg/m^3)	830 ~ 917	897.6
Young's modulus, E (GPa)	8.95 ~ 9.94	9.31
Poisson's ratio, ν	0.31 ~ 0.365	0.33

Ice, in general, is well known as a brittle material. Interestingly, this brittle behavior is not the only mechanical characteristic. According to earlier studies, ice can be deformed plastically in both tension and compression if any load applied on the specimen is sufficiently slow for ice to avoid from sudden fracture [59,60]. In addition to the earlier study, many other researches also insists ice can be a ductile material at very slow deformation and brittle under high strain rate [61–63].

Figure 2.14 schematically shows the relationship between the compressive strength (σ) and failure strain (ε) as a function of strain rate ($\dot{\varepsilon}$) [63]. The figure schematically represents that the failure of ice tends to be a ductile when a quasi-statically loading is applied. The peak compressive strength (σ) then progressively increases until the strain rate ($\dot{\varepsilon}$) reaches the transition between the ductile and brittle regime. Once the strain rate passes the border, the peak compressive strength (σ) decreases and failure response becomes brittle.

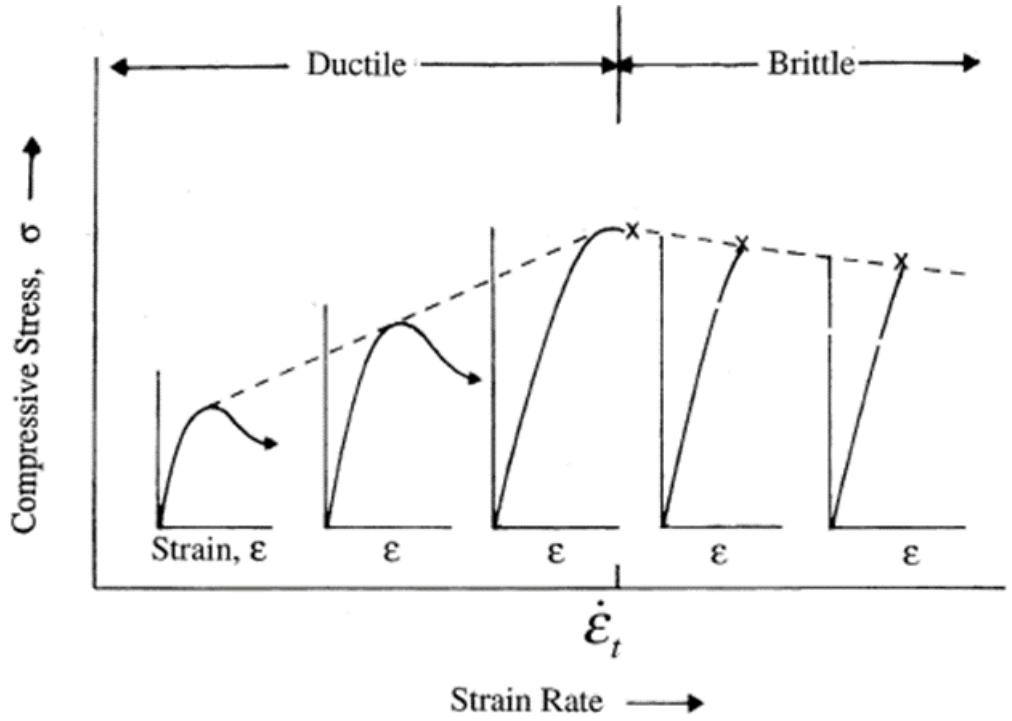

Figure 2.14 Schematic view of stress-strain rate relationship of ice (Image taken from [63]**)**

Such rate dependent mechanical characteristic has been analyzed, and analytical ice damage models proposed in previous research. Carney et al. [58] tabulated the relationship between stress scale factor and stain rate ($\dot{\varepsilon}$) based on the experimental result from Shazly et al. [64]. Kim and Keune [62] also proposed a stress-strain rate dependent ice material definition under the high strain rate loading condition.

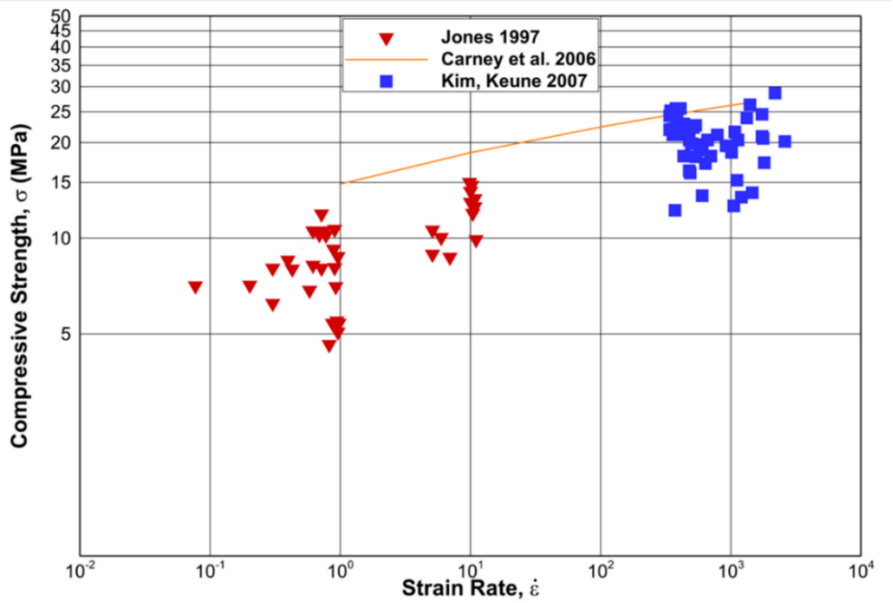

Figure 2.15 Compressive strength (σ) versus strain rate ($\dot{\varepsilon}$) relationship of ice (Data collected from [58,62,65]**)**

Figure 2.15 shows the change of compressive strength (σ) of ice with wide range of strain rate ($\dot{\varepsilon}$) reported by [62,65]. Instead of providing the compressive strength (σ) of ice with corresponding strain rate ($\dot{\varepsilon}$), Carney et al. [58] reported a set of stress scale factor at multiple strain rate to interpolate the mechanical strength of ice which is tabulated in Table 2-3. The scale factor was determined based on the experimental result provided by Shazly et al. [64], which was based on the static compressive strength of 14.8 *MPa* and the analytical strain rate property is plotted in Fig. 2.15.

Table 2-3 Tabulated relationship between strain rate and stress scale factor(Data collected from [58]**)**

Strain rate (S^{-1})	Stress scale factor	Strain rate (S^{-1})	Stress scale factor
1.0	1.00000	600.0	1.71287
10.0	1.25660	700.0	1.73005
100.0	1.51320	800.0	1.74493
200.0	1.59044	900.0	1.75805
300.0	1.63532	1000.0	1.76979
400.0	1.66768	1100.0	1.78042
500.0	1.69255	1500.0	1.81498

Indeed, the proposed virtual ice model contains many unknown parameters which could potentially result in an inaccurate simulation because implementing experimental measurement equipment on the ice is difficult. In addition to the implementation, the mechanical properties of ice can be easily influenced by the experimental environment as discussed. Since the existing mechanical properties of ice are very limited, another numerical modeling strategy was also investigated to reduce the complexity of input parameters.

As shown in Fig. 2.16, the most commonly used ice model (combination-1) is using the solid ice model with the tabulated equation of state (EOS), which will be discussed in later. However, establishing the pressure-volumetric strain of ice to establish the Tabulated EOS is extremely difficult. To reduce the complexity, the same assumption that was developed in the bird impact analysis was employed to create a new way to make an ice model for the high speed impact scenario. As with the high speed bird impact, the FSI approach was employed because the mechanical strength of ice is also weaker than that of airplane structure,

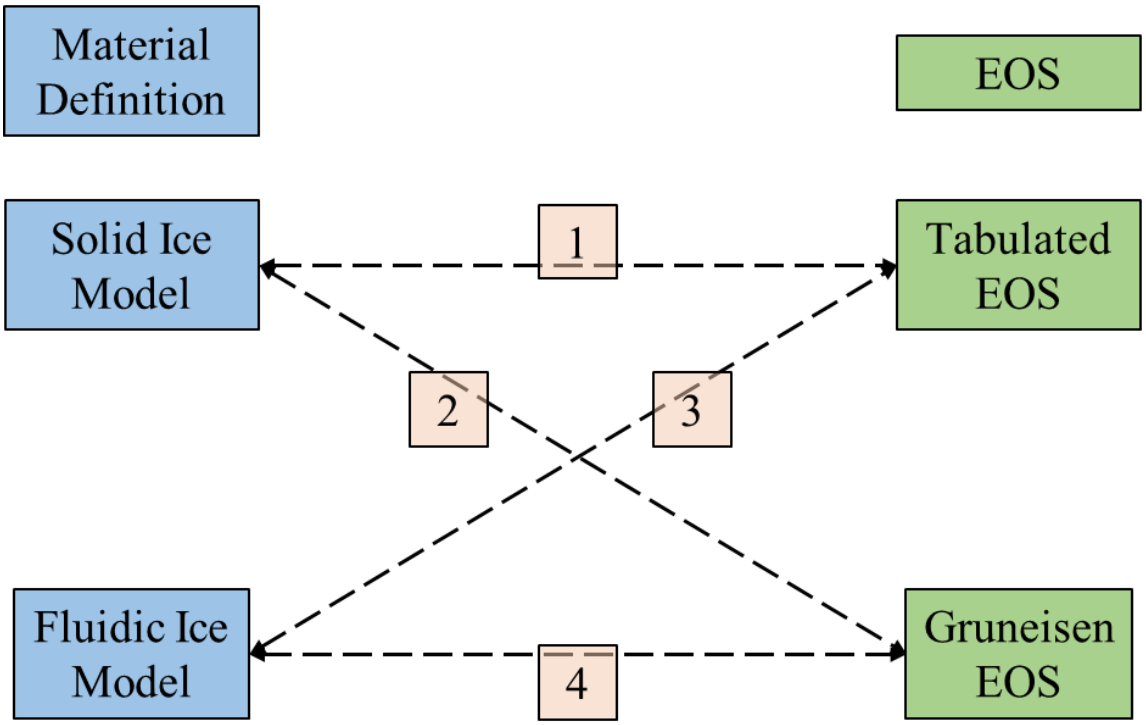

Figure 2.16 Schematic diagram of the modeling combinations for a high speed ice impact simulation

Upon the impact, the shock will be generated at the interface, continue to sweep through the projectile, and turn the ice projectile into disintegrated particles due to the sudden pressure rise.

The difference between the bird and the ice is the viscous effect on the target surface after impact. Unlike to a non-Newtonian bird constituent, the viscous effect of ice fragmentation on the target surface is negligible. Hence, ice material is modeled as an inviscid for the further investigation. If the ice fragments do not have negligible tensile strength between each particle with an inviscid property, the deformation of ice projectile at high speed impact can be simulated with same methodology used in bird strike analysis. In order to develop the high speed ice impact model, the modeling combination-4 in Fig. 2.16 was used for this study. Additionally, a parametric study between the material definitions and the EOS was also explored to investigate the influence of each computational approach.

3 Material Theories

3.1 Isotropic Damage Model

Material failure is the main concern, since it predicts the condition under which material fails due to diverse loading conditions. The basic types of material failure are classified as either deformation or fracture. Deformation includes time independent (elastic and plastic deformation) and time dependent (Creep). Fracture is divided into static loading (brittle and ductile) and cyclic loading (fatigue) [66].

For the comprehensive FOI analysis, two damage models for metal alloys are employed. In order to reduce the computational expense, linear elastic-plastic hardening damage model is used to calculate the stress-strain response for some of the engine components. Figure 3.1 shows a schematic stress-strain response of a metal alloy of both an experimental (actual) and a simplified bi-linear computational model.

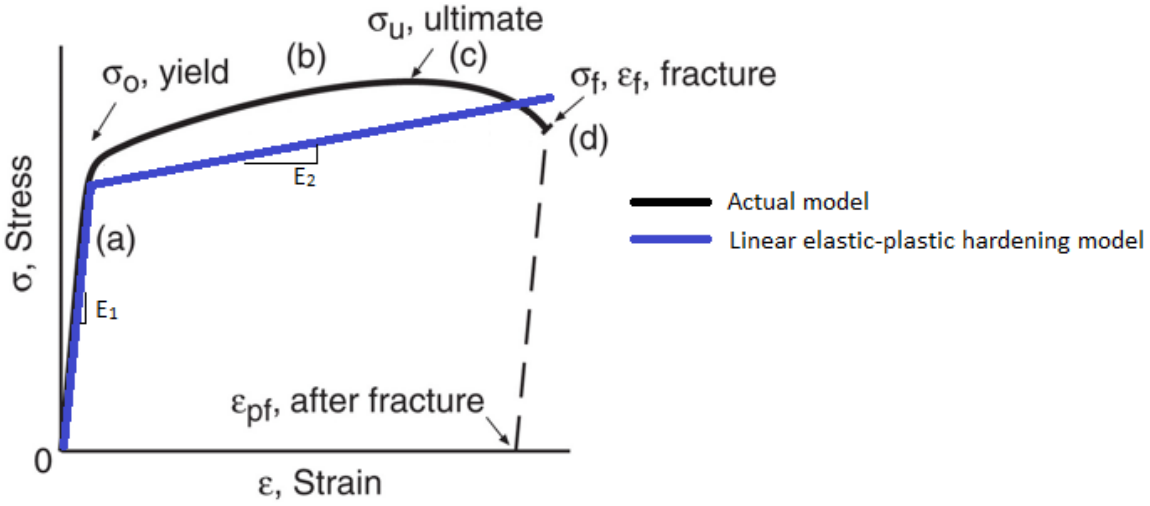

Figure 3.1 Stress-strain curve comparison between linear elastic and plastic hardening model (black) and linear elastic-plastic hardening model (blue)

Although the non-linear response of the actual material does not exactly match the response of the computational model, the differences in stress-strain response of both damage models within the elastic regime (a) is negligible. However, the stress-strain correlation of the computational damage model becomes different from the actual stress-strain response once plastic deformation occurs (b)-(c). The linear elastic-plastic hardening equation is shown as in Eq. (23)

$$\sigma = \begin{cases} E_1 \cdot \varepsilon_e & (\sigma \leq \sigma_o) \\ E_2 \cdot \varepsilon_p + \sigma_o & (\sigma > \sigma_o) \end{cases} \quad (23)$$

where E_1 is the elastic modulus, E_2 is the simplified plastic hardening modulus, σ_o is the yield strength, ε_e and ε_p are the elastic and the plastic strain respectively. By calibrating the plastic hardening modulus, the ultimate tensile strength (σ_u) of the computational damage model is made to be the same as that of the actual material response. In the computational domain, the material failure is represented by a simple element deletion when the maximum element strain reaches the failure strain (ε_f) [67].

3.2 Composite Model

Carbon fiber reinforced polymer (CFRP) is popular due to its high strength to density ratio, so it is widely selected to design a lightweight structure with higher stiffness. Another well-known the composite material is woven aramid-epoxy composite (also known as Kevlar®). The woven aramid-epoxy composite does not have as high a stiffness as CFRP, but is also widely used for shielding applications which requires high ballistic characteristics. Consequently, both composite materials are widely used over the modern advanced high-bypass propulsion engines in terms of improving the efficiency and the safety.

Unidirectional carbon fiber/epoxy (IM7/8551-7) is one of the widely used pre-impregnated composite materials that aviation industries has been investigated and uses to fabricate the composite fan blade [68,69]. Using a complicated fiber orientation, the carbon fiber fan blade can endure the high centrifugal loading with significantly less material than metal alloy, even though it has a complicated aerodynamic swept geometry. The woven aramid-epoxy composite is also used to design the casing to protect the fuselage from any high speed debris caused by a FBO incident.

The downside to FRPs is their extremely complicated damage prediction which is caused by mismatching stiffness between each individual plies. The mismatching stiffness is a unique characteristic for laminated composite with anisotropic plies, where individual plies have different fiber orientations based on the stacking orientation. Because of the mismatching stiffness between plies and fiber-epoxy construction, the composite laminate has multiple damage configurations: (1) matrix cracking, (2) fiber breakage, and (3) fiber-matrix shearing [37,70]. Figure 3.2 shows a schematic pictures of an example laminated composite which has a $[0/90]_s$ stacking sequence, where the major failure modes are shown.

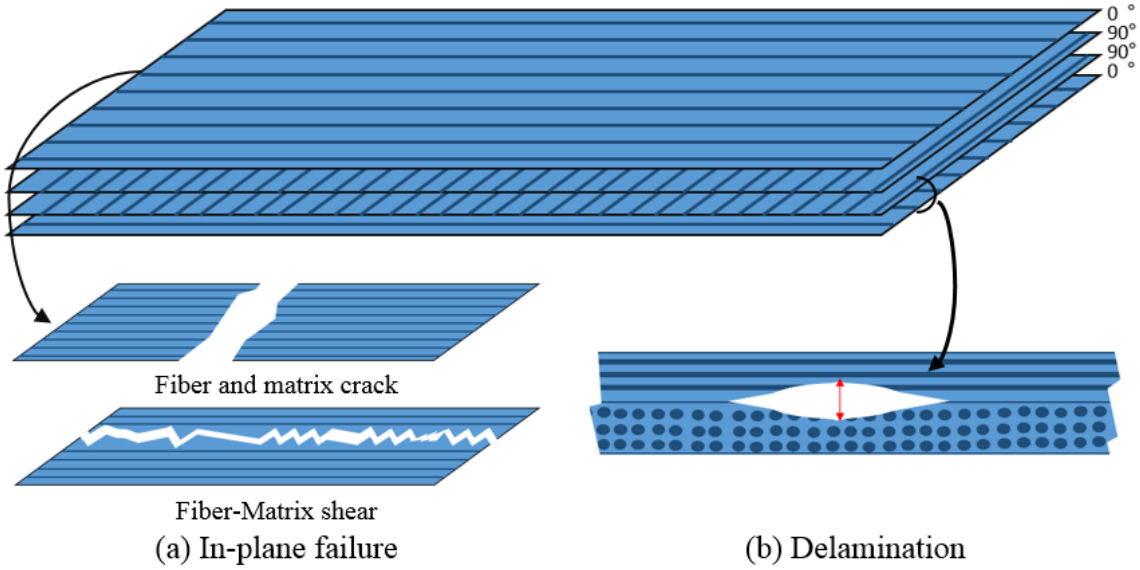

Figure 3.2 Schematic image of composite laminate $[0/90]_s$ and typical failure modes

For the damage prediction of composite material, many failure criteria were developed throughout the mid to late 1900's, such as the Tsai-Wu model in 1970 [71], Chang-Chang model in 1986 [36], and the more recent models such as Daimler-Pinho model (2006) [72,73]. While many more have been developed, the Tsai-Wu and Chang-Chang composite damage models are among those that have been implemented into common finite element analysis (FEA) software. Although listed damage models do not predict a perfect representation, they are widely used for initial estimates of the highly non-linear dynamic damage mechanics of composite laminate.

In this study, two different modeling methodologies were employed in order to able to simulate the FOI into propulsion system. Fan blades were macroscopically created based on a fully integrated quadrilateral element (shell). In accordance with the representative volume element (RVE) theory, the constitutive composite fan blade material definition was developed. For the damage prediction, Chang-Change damage model [36] is employed. Each element is designed to include a through-thickness integration point in order to virtually represent the number and orientation of each plies.

On the other hand, the soft casing is designed based on the mesoscale methodology. Figure 3.3 illustrates one of the examples of soft casing models and interlaminar bonding conditions used for this analysis. The computational model developed in this study is designed to capture continuum mechanics with inter-ply separation. Here, the continuum approach is used to model each individual ply layer. This has the benefit of being relatively computationally inexpensive as well as having a direct physical analog that can be experimentally tested. Despite the number of simplifying

assumptions inherent to the continuum approach, it has been successfully implemented by many groups in the past [32,74–76].

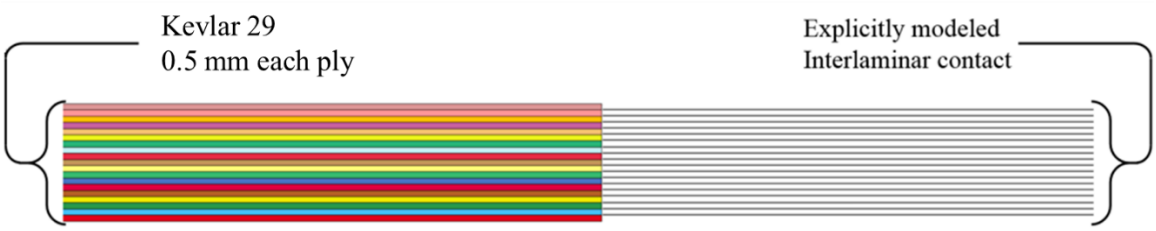

Figure 3.3 Schematic view of mesoscale soft casing modeling methodology

For the fan blade composite damage model, the Chang-Chang mixed criterion is selected in order to define the failure considering both fiber and matrix individually. The model assumes that the unidirectional fiber reinforced composites has a transversely isotropic (x_2=x_3) behavior along the fiber direction (x_1). The analytical composite model allows the calculation of stress and damage correlation of the fiber and the matrix separately to determine the damage condition of an individual ply. The failure of the composite laminate is numerically written as Eq. (24)-(27) [35,36]:

For the matrix failure modes:

Tensile

$$\varepsilon_{mt}^2 = \left(\frac{\sigma_{bb}}{Y_t}\right)^2 + \left(\frac{\sigma_{ab}}{S_c}\right)^2 \tag{24}$$

Compressive

$$\varepsilon_{mc}^2 = \left(\frac{\sigma_{bb}}{2S_c}\right)^2 + \left[\left(\frac{Y_c}{2S_c}\right)^2 - 1\right]\left(\frac{\sigma_{bb}}{Y_c}\right)^2 + \left(\frac{\sigma_{ab}}{S_c}\right)^2 \tag{25}$$

where subscript *a*, *b*, and *c* are equivalent to x, y and z. Another subscript t and c is the tension and compression correspondingly. The fiber direction is *a*, while *b* and *c* are the matrix direction and through-thickness direction, respectively. σ_{aa} is the longitudinal stress of each layer, σ_{ab} is the shear stress of each layer, Y_t and Y_c are the transverse tensile and compressive strength of matrix, and S_c is the shear strength of the matrix in the xy-plane.

For the fiber failure modes:

Tensile

$$\varepsilon_{ft}^2 = \left(\frac{\sigma_{aa}}{X_t}\right)^2 + \beta\left(\frac{\sigma_{ab}}{S_c}\right)^2 \tag{26}$$

Compressive

$$\varepsilon_{fc}^2 = \left(\frac{\sigma_{aa}}{X_c}\right)^2 \tag{27}$$

where X_t and X_c are longitudinal tensile and compressive strength of fiber material.ε_m is a failure parameter that determines the occurrence of matrix cracking, and ε_f is the failure parameter for the fiber. Damage occurs when the damage parameter (ε) is equal to or greater than unity.

Alternatively, another composite damage model was investigated. Tsai-Wu failure criterion evaluates the damage based on the stresses in each orthotropic orientation, which is similar to the von-Mises stress criterion. Tsai-Wu failure criterion is written as [71,77]:

$$F_1\sigma_1 + F_2\sigma_2 + F_{11}\sigma_1^2 + F_{22}\sigma_2^2 + F_{66}\tau_{12}^2 - \sqrt{F_{11}F_{22}}\sigma_1\sigma_2 < 1 \tag{28}$$

where F_i the material property which is tension and compression strength in both the longitudinal and transverse directions. F_{ij} is the maximum shear strength of anisotropic material. The combination of stresses becomes unity when a failure occurs. As shown in the numerical correlation, the individual stress components are mutually interacting each other. As a result, the primary failure mode becomes inherently difficult to identify and the damage model yields more conservative damage prediction.

For the casing, a comprehensive 3-D anisotropic damage model was selected to represent the composite. Unlike the Chang-Chang failure model, the 3-D anisotropic model is not based on phenomenological observations that reduce the problem using simplifications such as plane stress theory. This model considers failure in a three-dimensional stress space where the ultimate failure and damage are purely driven by strain. The damaged compliance matrix is given by Eq. (29), where E is Young's modulus, ν_{ij} is Poisson's ratio, G_{ij} is shear modulus, and d_{ij} is the damage parameter [31,67].

$$[S_{ij}]^{dam} = \begin{bmatrix} \frac{1}{E_1(1-d_{11})} & \frac{-\nu_{21}}{E_2} & \frac{-\nu_{31}}{E_3} & 0 & 0 & 0 \\ \frac{-\nu_{12}}{E_2} & \frac{1}{E_2(1-d_{22})} & \frac{-\nu_{32}}{E_3} & 0 & 0 & 0 \\ \frac{-\nu_{13}}{E_1} & \frac{-\nu_{23}}{E_2} & \frac{1}{E_3(1-d_{33})} & 0 & 0 & 0 \\ 0 & 0 & 0 & \frac{1}{G_{23}(1-d_{23})} & 0 & 0 \\ 0 & 0 & 0 & 0 & \frac{1}{G_{13}(1-d_{13})} & 0 \\ 0 & 0 & 0 & 0 & 0 & \frac{1}{G_{12}(1-d_{12})} \end{bmatrix} \quad (29)$$

where

$$d_{ij} = max\left[d_{ij}, d_{ij}^{c}\left[\frac{\varepsilon_{ij} - \varepsilon_{ij}^{th}}{\varepsilon_{ij}^{c} - \varepsilon_{ij}^{th}}\right]\right] \quad (30)$$

where, ε_{ij} is the strain, superscript *c* represents the critical value, and superscript *th* represents the damage threshold value.

These critical and damage threshold strains are user-defined, where the threshold value represents the lowest strain value at which damage can start to occur and the critical value represents the strain at which the selected property can no longer increase in damage. The formulation of the damage parameter ensures that any damage inflicted remains present throughout the simulation. This is a reasonable assumption in impact analysis because there is negligible unloading within the time window of interest. This damage parameter is active in both tension and compression and updates based on the component strains

3.3 Cohesive Zone Modeling

Delamination occurs because of the miss-matching stiffness caused by different fiber orientations based on the designed stacking sequence. To simulate the delamination between composite plies, the cohesive zone model (CZM) is selected to assign the mechanical connection between each plies. CZM is the modern applications which is developed by understanding fracture mechanics.

A. A. Griffith initially proposed the fracture mechanics by using energy methods to consider existing micro cracks in solid continuum [66,78]. Then the work was revisited by G. R. Irwin [79,80], who employed energy methods to consider the law of thermodynamics to predict failure

by external loadings. These works proposed the definition of the strain energy release rate (G), fracture toughness (K_c), stress concentration factors (K) and the mutual relationship among each other to analytically predict the material response of a continuum which has preexisting crack. Numerous researchers have investigated the ballistic response of the composite model, developed their computational model using CZM, and successfully validated their simulation against experiments [32,81].

In general, the fracture mode is categorized into Mode I (crack opening damage), II (in-plane shear damage) and III (out-of-plane shear damage). In computational applications, two major damage modes are implemented to predict damage. The fracture mode I computes the damage caused by through-thickness tensile loading. The fracture mode II deals with the in-plane shear stress, resulting from interlaminar shear loading. The fracture mode III is very similar to the mode II, but it is initiated by the out-of-plane shear damage [82].

Figure 3.4 shows a schematic diagram about the bilinear stress-displacement model and mixed mode to represent the comprehensive material response. The energy release rate of mode I is completely independent from the energy release rate of mode II. However, typical delamination of the composite laminate caused by impact is always a result of a combination of mode I and II. Hence, the mixed mode is introduced in the damage model. To capture a comprehensive failure, bilinear mixed-mode stress-displacement model is selected to have a constitutive material response from both normal and shear stress.

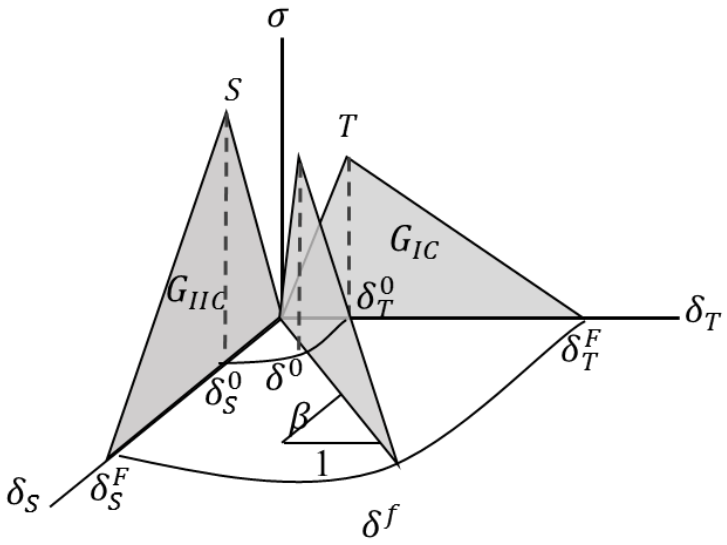

Figure 3.4 Bilinear mixed-mode stress-displacement diagram (Image recreated based on [77]**)**

As an additional way to model the delamination, the Dycoss Discrete Crack Model [83] was applied to assign the interlaminar bonding shown in Fig. 3.3. This model works in both tension and compression, with shear (σ_{ij}) and normal (σ_{ii}) failure criteria that govern interface strength as shown in Eq (31).

$$\left[\frac{max(\sigma_n, 0)}{\sigma_N}\right]^2 + \left[\frac{\sigma_s}{\sigma_S - sin(\theta) \cdot min(0, \sigma_n)}\right]^2 = 1 \tag{31}$$

where σ_N is the normal failure stress and σ_S is the shear failure stress of interlaminar bonding. This model allows separation to be calculated on a continuous scale from 0 to 1, where 0 represents full adhesion and 1 represents full separation. This can emulate the elastic and plastic response of interlaminar interaction based on given loading conditions. In addition, an energy release rate is assigned in both normal separation (Mode I) and in-plane shear separation (Mode II), allowing the delamination to propagate from the initiation zone.

3.4 Equation of State

In the previous discussion, it was shown that a shockwave is generated when a soft object impacts on an elastic hard surface. Indeed, a shock wave is generated when a disturbance of energy flow occurs in any object. The shockwave is caused by the energy wave moving faster than the speed of sound of the continuum including gas, liquid and solid phase in the event of the impact. Unlike some equilibrium conditions, which obeys the mass, momentum and energy conservation law, shock dynamics is not a linear phenomenon and consequently does not necessarily obey the momentum and energy conservations [84,85]. This often violates pressure-volume (*p*-*Q*) path and rather jump from initial to final state directly. A linear interpolation between initial and final state is called the Rayleigh line in *p*-*Q* relationship. Such sudden *p*-*Q* nonlinear relationship is also known as a "jump". When it occurs, the shock increases pressure, density and temperature within infinitesimal regime.

The required input parameters are empirically evaluated by measuring the particle velocity (U_p) and shock front velocity (U_p) and speed of sound of a material (C_0) Their analytical relationship can be written as:

$$U_s = C_0 + S \cdot U_p \tag{32}$$

where s is experimentally derived curve fitting constant. By using $U_s - U_p$ relationship, the Rankine-Hugoniot *p-V* correlation can be evaluated. Although this provides a sufficient result to predict the ideal shock dynamics, several equation of states were explored and employed in order to calculate a full set of state variables at each time step and accurate physical representations during the high speed impact.

3.4.1 Tabulated Equation of State

Because of the highly non-linear behavior of soft body object, the Tabulated equation of state (EOS) is considered to numerically represent the constitutive material states; pressure, density, and temperature. The parameters are tabulated based on empirical observations. Based on the experiment, the volumetric strain, temperature rises and the corresponding pressure are measured in order to establish the mutual relationship. The Tabulated EOS is defined as written in Eq. (33) [67]:

$$P_{EOS} = C(\varepsilon_v) + \gamma \cdot T(\varepsilon_v)E \tag{33}$$

where *C* and *T* are tabular coefficients which are empirically evaluated, ε_v is natural log of the volumetric strain ($ln(Q/Q_0)$), γ is the Gruneisen constant, and *E* is the internal energy. Figure 3.5 shows an example of pressure-volumetric strain relationship for loading and unloading conditions.

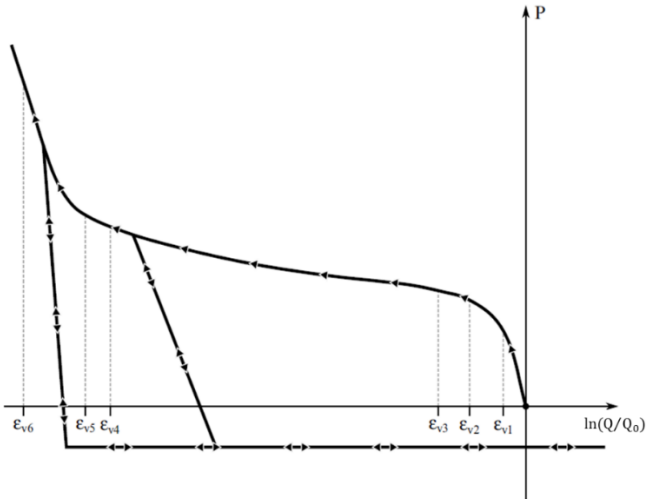

Figure 3.5 Pressure versus volumetric strain curve for Equation of state [67]

The Tabulated EOS has a positive pressure in compression but a negative volumetric strain (ε_v) because the volumetric ratio (Q/Q_0) is always below than 1 under the compressive loading. The bulk unloading modulus is provided to estimate the unloading behavior of ice material according with the peak volumetric strain (ε_v).

3.4.2 Linear Polynomial Equation of State

Using the state variables (p, ρ, and T), the EOS calculates a constitutive mathematical relationship of a homogeneous material by the law of thermodynamics. The most simplistic and widely used equation of state is the linear polynomial. The linear polynomial has the third order pressure-volume relationship and the second order of pressure-internal energy correlation. The EOS is written in Eq. (34).

$$P_{EOS} = C_0 + C_1\mu + C_2\mu^2 + C_3\mu^3 + (C_4 + C_5\mu + C_6\mu^2)E \tag{34}$$

where $\mu = \rho/\rho_0 - 1$, $C_{\#}$s are the empirical coefficients evaluated by experiment, E is the internal energy ($C_p \cdot T$), ρ_0 is the initial fluid density and ρ is the modified density of the material upon any compression or tension. C_1 is bulk modulus, e.g. 2.2 *GPa* for water. For example, a fluid model obeys Boyle's law can be represented, using zero for all constants except C_0 and C_1. Assuming the initial density is a constant and both C_0 and C_1 are set as 1 to make the linear polynomial EOS algebraically equal to the ideal gas equation. Ideal gas equation can be also derived by applying C_0-C_3 and C_6 equal to zero, specify C_4 and C_5 as 0.4, and the specific heat of ideal gas as shown in Eq. (35).

$$P/\rho = Constant \tag{35}$$

3.4.3 Mie-Gruneisen Equation of State

Mie, in 1903, founded a high temperature equation of state of solid [86]. In 1912, Gruneisen improved Mie's equation to calculate the density and the internal energy to the solid state continuum under hydrostatic pressure [87]. In this study, the Mie-Gruneisen (M-G) EOS is used to

estimate the dynamic response of a fluid as well as a solid under the high velocity impact scenarios. Upon impact, the projectile's kinetic energy is converted into a sudden pressure rise. This pressure directly affects both the fluidic projectile and the solid continuum target, resulting in massive deformation. The M-G EOS can predict shock, pressure-volume relationship, and internal energy of the homogeneous material. A non-linear pressure-volume relationship can be mathematically captured using the third-order slope correction.

The M-G EOS is defined for compressed material as [88]:

$$p = \frac{C^2\rho_0\mu\left[1+\left(1-\frac{\gamma_0}{2}\right)\mu-\frac{a}{2}\mu^2\right]}{\left[1-(S_1-1)\mu-S_2\frac{\mu^2}{\mu+1}-S_3\frac{\mu^3}{(\mu+1)^2}\right]} + (\gamma_0 + a\mu)E \tag{36}$$

Under expansion:

$$p = \rho_0 C^2\mu + (\gamma_0 + a\mu)E \tag{37}$$

where μ is the relative density ratio ($\mu = \rho/\rho_0 - 1$), C is the speed of sound of the material, $S_{1\text{-}3}$ are the empirical Hugoniot slope constants for the pressure-volume relationship, γ_0 is the Gruneisen gamma, a is the first order dimensionless empirical volume correction factor, and E is the internal energy.

3.5 Fluid Body Deformation Model

Unlike solid structures, fluid has no mechanical properties such as elastic modulus, shear modulus or yield strength. Instead, the predominant contribution of a fluid body deformation is shear force, a phenomenon that cannot be easily simulated by conventional solid mechanical FE analysis. A Newtonian fluid model, which is linearly proportional to the strain rate in shear direction, is selected to calculate the Newtonian viscous shear stress for the fluidic deformation of soft body projectiles

To assign a fluidic deformation using the structural analysis framework, a null material model, designed to calculate deviatoric stress based on the strain rate of the fluid body, is selected and shown in the following Eq. (38) [67].

$$\sigma'_{xy} = 2\mu \cdot \dot{\varepsilon}_{xy} \tag{38}$$

where σ'_{xy} is the deviatoric viscous stress, μ is the dynamic viscosity, and $\dot{\varepsilon}_{xy}$is the deviatoric strain rate. In order to the compute volumetric strain and the corresponding pressure of the fluid body, an EOS is employed. Combined with the EOS, this fluid material definition can calculate total stress within the continuum as shown in Eq. (39).

$$\sigma_{xy} = \sigma'_{xy} + P \cdot \delta_{xy} \tag{39}$$

where *P* is the hydrostatic pressure calculated by EOS, and δ_{xy} is the Kronecker's delta. By adding the principal hydrostatic stress of fluid body with deviatoric viscous shear stress, a full set of stress tensors for the infinitesimal fluid body can be calculated.

4 Computational Models

To assess the dynamic response and damage progression due to an FOI event onto a full-scale contemporary propulsion system, an explicit finite element analysis tool, LS-Dyna, is extensively utilized. The time explicit integration numerical scheme was used because it tends to be more suitable for highly non-linear problems such as impact and crash than the implicit integration scheme.

For the structure of the engine, two conventional finite element formulations (solid and shell) were utilized for efficiency. By doing so, the computational effort is controlled within a reasonable range without compromising the accuracy. Although the listed element formulations are generally robust, both formulations can result in inaccurate solutions or numerical instabilities with the large deformation or domain separation [89–91]. Such instabilities are expected when a soft body object comes in contact with a propulsion system at high speed. Hence, newer element formulations, Arbitrarily Lagrangian-Eulerian (ALE) and Smoothed Particle Hydrodynamics (SPH), are explored in this chapter.

4.1 Shell Element Formulation

The quadrilateral element is the simplest element which has four nodes on each corner. Because of the relatively low computational expense, the quadrilateral element is widely used in much research. Figure 4.1 shows a coordinate system of the quadrilateral element (4-noded) with the reduced integration point and the corresponding boundaries. The shape function N_1 to define node 1 should not influence nodes 2, 3, and 4.

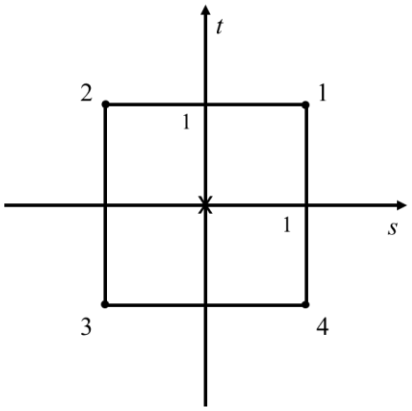

Figure 4.1 Schematic view of a 2-D quadrilateral element (4-noded) with a reduced (1) integration point

To numerically allow the influence of shape function for node 1 to be 0 for the other nodes, a simple equation was derived, $(1+s)(1+t)$, then divided by 4 to be normalized. It was so that N_1 can be equal to 1. Based on the same mathematical approach, the rest of the nodes of the quadrilateral element are defined by the equations shown below:

$$\mathrm{N}_1(s,t) = \frac{(1+s)(1+t)}{4} \tag{40}$$

$$\mathrm{N}_2(s,t) = \frac{(1-s)(1+t)}{4} \tag{41}$$

$$\mathrm{N}_3(s,t) = \frac{(1-s)(1-t)}{4} \tag{42}$$

$$\mathrm{N}_4(s,t) = \frac{(1+s)(1-t)}{4} \tag{43}$$

Even though the under-integrated quadrilateral element can deliver the solution with less computational expense, it has accuracy problems because of the overly simplified element calculations. As an example, some of the "zero-energy" mode deformation, also known as hourglass mode deformation, is illustrated in Fig. 4.2.

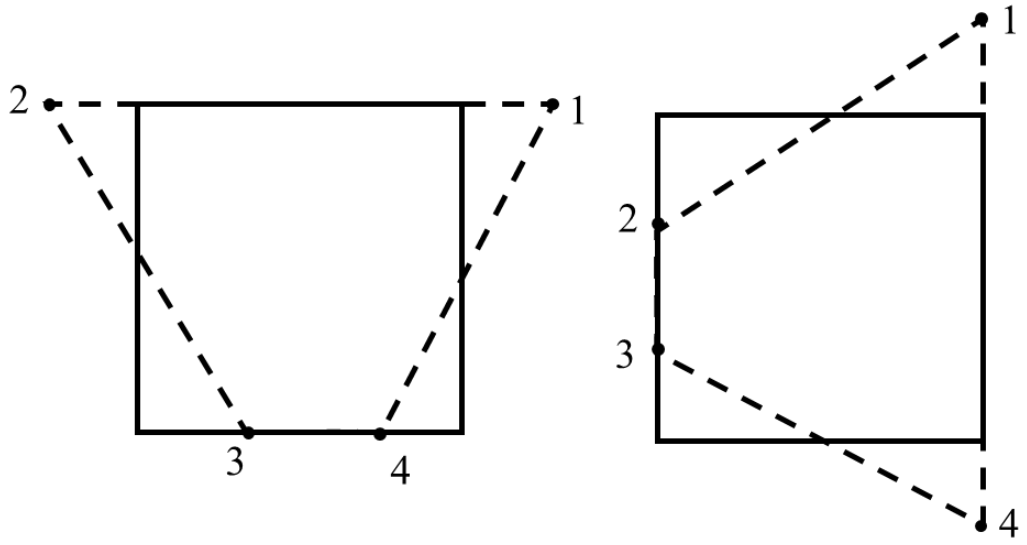

Figure 4.2 Zero-energy (Hourglass) deformation mode of a quadrilateral element

The hourglass mode commonly occurs when the quadrilateral element is defined with reduced integration point, because of the insufficient Gauss point implemented in this reduced integration quadrilateral element. Deformation shapes shown in Fig. 4.2 are subject to bending loads which have no strain in computational domain. This is because the under-integrated quadrilateral element only has a single Gauss point at the center of the element, and the single Gauss point is the only sampling point of the integration rule. Consequently, such deformation modes do not provide any resistance to applied loads and reduce the accuracy.

As an example, an inaccurate computational result is shown in Fig. 4.3-(a). The fixed boundary condition was applied on the left edge and a tensile loading using prescribed displacement was applied on right side edge. The shear-locking from Fig. 4.2 is evident in Fig. 4.3-(a) in the form of the trapezoidal shaped elements. Comparing to Fig. 4.3-(b), which implements the fully-integrated quadrilateral element, the deformation caused by tensile loading is more unrealistic when the hourglass occurs.

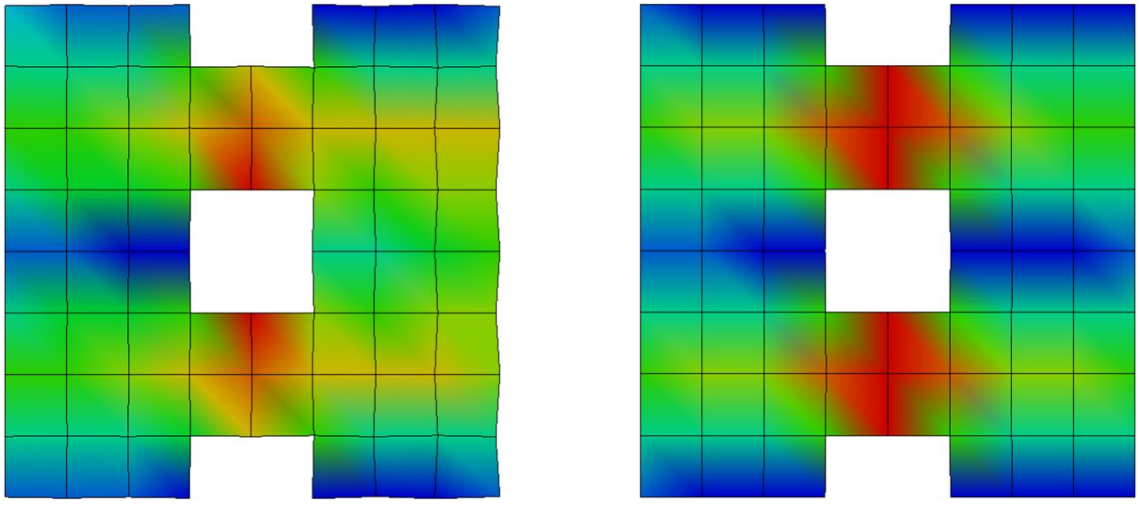

(a) Reduced quadrilateral element (b) Fully-integrated element

Figure 4.3 Tensile loading simulation results for both (a) the reduced quadrilateral element and (b) the fully integrated element

In addition to the qualitative result, the accuracy of the quantitative result is also compromised. Figure 4.4 plots the energy distribution due to the tensile loading. Hypothetically, the total energy is always equal to the summation of the kinetic energy and the internal energy of the entire simulation domain when the hourglass energy does not exist. However, Fig. 4.4 implies that hourglass energy is a significant percentage of the total energy in Fig. 4.3-(a).

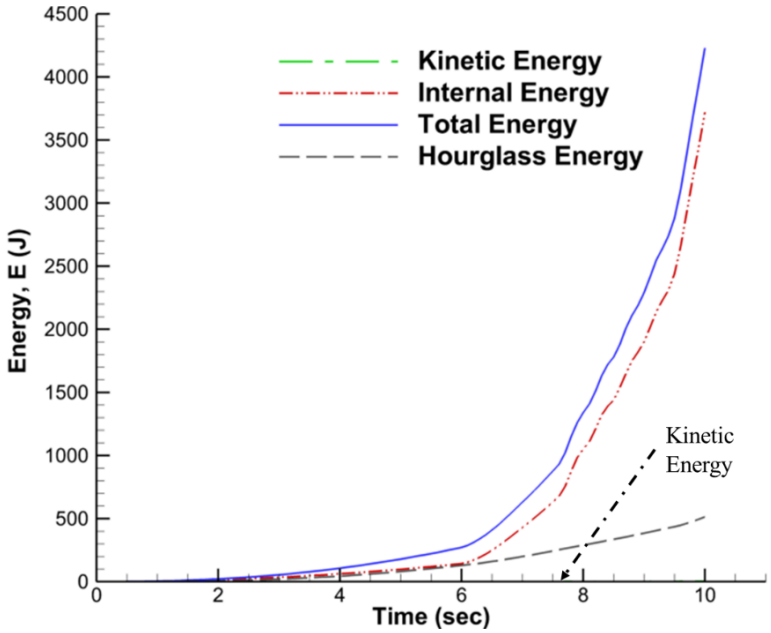

Figure 4.4 Energy plot of the quasi-tension test using the reduced quadrilateral element

The hourglass mode can propagate throughout the mesh and produce false results since the total energy is dissipated through the virtual deformation. Ideally, the suggested hourglass energy is less than 10% of the peak internal energy [92,93]. However, this is still high when an analysis is associated with either impact or crash scenario. Assuming all the kinetic energy is converted into the internal energy during impact, 10% of the total initial kinetic energy is considerable and could cause additional damage to the structure. In short, the quadrilateral element formulation with an under-integration scheme, without additional hourglass control, requires either more integration points or higher order shape function to improve the accuracy.

For most aerospace applications, almost all the structures are thin enough to analyze them using the plane stress assumption since such thin structures are not normally considered to carry a through-thickness stress. So utilizing the quadrilateral element with under-integration is inevitable to design an aerospace structure in terms of the computational efficiency, even though it is apodictically detrimental for the accuracy. One way to avoid hourglassing is to use triangular shell element. Triangular elements do not exhibit hourglassing, but the shear locking can occur [94,95]. When shear locking occurs, the continuum becomes overly stiff and the final result is inaccurate.

Using an hourglass control scheme is alternative solution to mitigate the zero-energy mode deformation which requires an additional computational expense. Another way is using *h* (mesh) and *p* (polynomial order of the shape function) refinements. Both methods inherently increase the computational expense, but can reduce the hourglass energy and improve the solution accuracy. The other way is using the fully-integrated quadrilateral element as shown in Fig. 4.5.

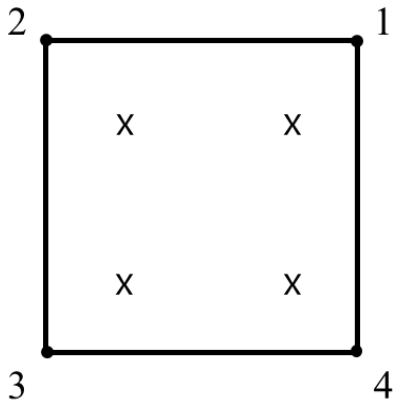

Figure 4.5 Schematic diagram of a quadrilateral element (4-noded) with the fully integrated points (4 Gauss point)

By allocating four integration points, the virtual deformation caused by insufficient Gauss point can be eliminated. Consequently the fully integrated element formulation provides an enhanced strain formulation and a computational expense which is much higher than the under-integrated quadrilateral element (approximately 2.5 times the computation time required by the reduced quadrilateral shell element [96]). More details of the element formulations can be found in Cook et al. [95] and some other publications [89,97].

4.2 Solid Element Formulation

Instead of using the plate theory implemented in 2-D element formulations, the 3-D element formulations can directly calculate the through-thickness stress without additional numerical schemes in commercial finite element code. By implementing the 3-D element, a detailed damage mechanics, such as through-thickness, ply failure, and delamination can be predicted which are not nearly impossible with 2-D element formulations.

The hexahedral element is one of the most frequently selected elements which has 8 nodes on each corner and a single integration point at the centroid of the cube as shown in Fig. 4.6. This element formulation and is very similar to the quadrilateral element with reduced integration point (1 Gauss point) in terms of the computational expense and accuracy. Aforementioned, the under-integrated element formulation, which is 8 nodes hexahedral element in this case, requires relatively low computational expense, but has potentially unphysical modes of deformations caused by the hourglass. As a result, the hourglass takes away from the initial energy of the simulation domain and cause less deformations.

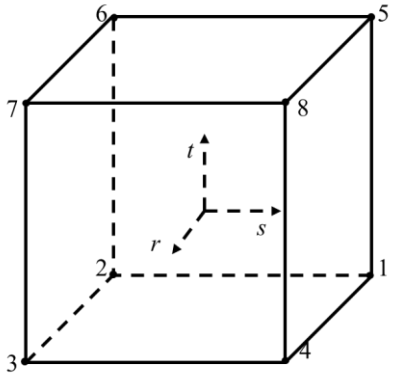

Figure 4.6 Reduced integrated hexahedral element (8-noded)

Alternative solid elements, tetrahedral elements and pentahedral (wedge shape) elements, are also available. As discussed in the previous section, these elements also have the shear locking issue. Thus both elements contribute an unrealistic stiffness to the mesh and directly impact the quality of solution.

In the same manner, the hexahedral elements also include 8 Gauss points inside and become a fully integrated element. Figure 4.7 shows a 8-noded fully integrated hexahedral element. By implementing the eight integration points, the element becomes more suitable to capture large deformations, such as foam and rubber deformations and impact simulations, but it is approximately four times more expensive. To minimize the computational expense, LS-Dyna also implements the selectively reduced element, which utilizes both the reduced and full integration formulations, to save computational costs while preventing hourglass deformations.

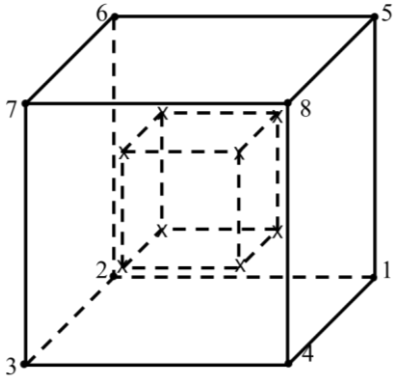

Figure 4.7 Fully integrated hexahedral element (8-noded)

4.3 Arbitrary Lagrangian-Eulerian (ALE)

Although the traditional finite element (FE) method is a powerful tool for most structural analysis applications, the results can become inaccurate when large deformations and mesh separations occur. When such results occur in conventional element formulations, such as Lagrangian and Eulerian, the analysis will often deliver inaccurate solutions or even fail to converge to a solution. Such numerical errors are associated with zero-energy modes, mesh entanglement, and severe element deletion, which directly impact the quality of the results. In order to accurately predict fluidic behavior using a structural solver, multiple methodologies have been addressed.

Arbitrary Lagrangian-Eulerian (ALE) is a methodology that has been specifically designed for FSI [98] and metal forming [99] which are subjected to large deformations. ALE was initially proposed by Noh [100] and Trulio [101] and has since been implemented by researchers including Hughes et al. [102] (1981) and more recent research [103] (2014). Schematically, the ALE formulation allows the ambient Eulerian mesh deforms using the Lagrangian scheme, and the advection within the Eulerian domain occurs to capture the deformation of materials inside.

ALE kinematics works in two steps: the explicit normal Lagrangian calculation, and the rezoning (advection) step. An explicit Lagrangian calculation is conducted until the mesh is distorted, then the distorted mesh is smoothed out by advection. Using the advection algorithm to periodically morph the distorted mesh, conservation of mass and momentum in the Lagrangian domain is ensured [104]. Because of this arbitrary mesh advection, the computational accuracy of ALE is significantly influenced by the mesh rezoning algorithm. Currently, LS-DYNA implements two advection algorithms. One is the donor cell scheme, which provides the first order accuracy and a high dissipation [105,106]. The other algorithm is named as Van-Leer scheme. This advection algorithm is very conservative and provides the second order accuracy. In addition to the high accuracy, the Van-Leer algorithm has monotonic behavior which does not introduce an artificially high value in the next time step. In this study, Van Leer mesh advection [107], a second order monotone upwind discretization algorithm, is selected to obey the conservation laws while mesh remapping occurs. The conservation equations for mass and momentum in ALE scheme can be written as:

$$\left.\frac{\partial \rho}{\partial t}\right|_{ref} + (v_m - \hat{v}) \cdot \nabla(\rho) = -\rho \nabla \cdot v \tag{44}$$

$$\rho\left(\left.\frac{\partial v}{\partial t}\right|_{ref} + \left((v_m - \hat{v}) \cdot \nabla\right)v\right) = \nabla \cdot \sigma + \rho\vec{f} \tag{45}$$

where subscript ref is the reference domain, v_m is the material velocity inside of CLE mesh, $\hat{v}$ is the ALE mesh grid velocity σ is the Cauchy stress tensor, and f is body force. The right hand side of the equation is in Eulerian spatial form whereas the ALE conservation equation is represented on left hand side. Because the ambient mesh motion does not affect the simulation result, only the acceleration a and velocity v in the Lagrangian domain are required to capture the deformation. ALE formulation of acceleration can be derived as:

$$a = \left.\frac{\partial v}{\partial t}\right|_{ref} + (v_m - \hat{v})\frac{\partial v}{\partial x} \tag{46}$$

As a result, the structural solver can represent a fluidic behavior using ALE formulation, an example of which is shown in Fig. 4.8. The figure illustrates the use of the ALE method for modelling a hollow ball dropping into a box of water, with gravity applied over the domain to produce the buoyancy effect necessary to capture a comprehensive FSI. In addition to the gravity, "no slip" boundary conditions are applied around the mesh boundary for the simulation to define the boundary condition as a container. By doing so, the water deforms within the defined mesh when the ball came into contact. Because of the initial potential energy, the water sloshes with balls until the energy damps out.

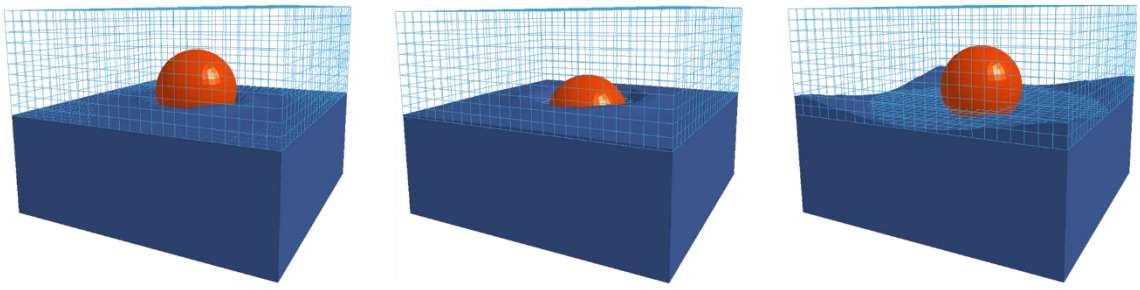

(a) Initial contact (b) Submerging (c) Buoyancy effect

Figure 4.8 An example of ALE method for a water impact simulation

These advection algorithms conserve the internal energy throughout the simulation by employing the EOS. However, the kinetic energy is not natively conserved since the algorithms are initially focused on conserving the total momentum. This might cause some issue where the simulation has a predefined total energy such as explosions, and new algorithms are continuously developed to improve the solution by conserving the total energy.

4.4 Hourglass Control Models

Because of their low computational expense, the under-integrated shell and solid elements are widely utilized. However, many computational models require additional supplements because of the accuracy issues associated with the hourglass deformations. Hourglass control was developed as a remedy for such under-integrated elements, but it can become a double-edged sword if misused.

The hourglass control models are developed based on either the viscous or stiffness forms. The viscous method uses a nodal velocity which helps to reduce hourglass deformations by generating hourglass forces. Because of the viscous-based formulation, it is recommended for a simulation associated with high velocity or high strain rate problems such as high speed impacts, ballistics, and even explosions. On the other hand, the stiffness-based formulation uses a nodal displacement that contributes to mitigate hourglass modes. Hence the hourglass algorithm generates hourglass forces proportion to the nodal displacement; these methods are suitable for relatively low speed scenarios including quasi-static tension tests, low speed cyclic loading simulations, and low speed crash scenarios.

Proposed methodologies are able to reduce the total amount of hourglass deformations without a considerable increase in computational cost. However, the hourglass control models tend to make the continuum artificially stiffer, so an adequate hourglass model setting is required. In addition to the artificial stiffness, the hourglass can influence the ALE formulation by adding shear stiffness. Hence, a fluid simulation using ALE is required to have no hourglass control to avoid inaccurate solutions.

4.5 Smoothed Particle Hydrodynamics (SPH)

As another way to overcome the previously stated shortcomings of traditional FE, SPH was addressed in order to analyze its ability to capture a large deformation observed in fluidic motions. The most apparent difference between the conventional element formulation and SPH is the absence of an ambient mesh grid. Instead of discretizing a continuum with a finite mesh, the object is defined by a set of volume-less particles. Absence of the ambient grid enhances the stability of the simulation result by avoiding numerical errors caused by large deformation or separation of mesh. Lucy [108] and Gingold & Monaghan [109] initially proposed SPH to analyze the physics

behind galaxy evolution. Since then, the methodology has been improved and successfully broadened to variety of fluid and solid mechanics applications [110–112]. In SPH, each particle discretizes the volume of a continuum (Ω) with an arbitrary radius (r), with the mass of each particle located at the node. As shown in Fig. 4.9 the influence from neighboring particles j to particle i changes based on the distance. The influence on the particle i is inversely related to distance, with magnitude of influence increasing as particles move closer together, and vice-versa for further particles. Eventually the influence from neighboring particles becomes zero when they are separated by more than twice the smoothing length ($2h$) in order to reduce computational expense.

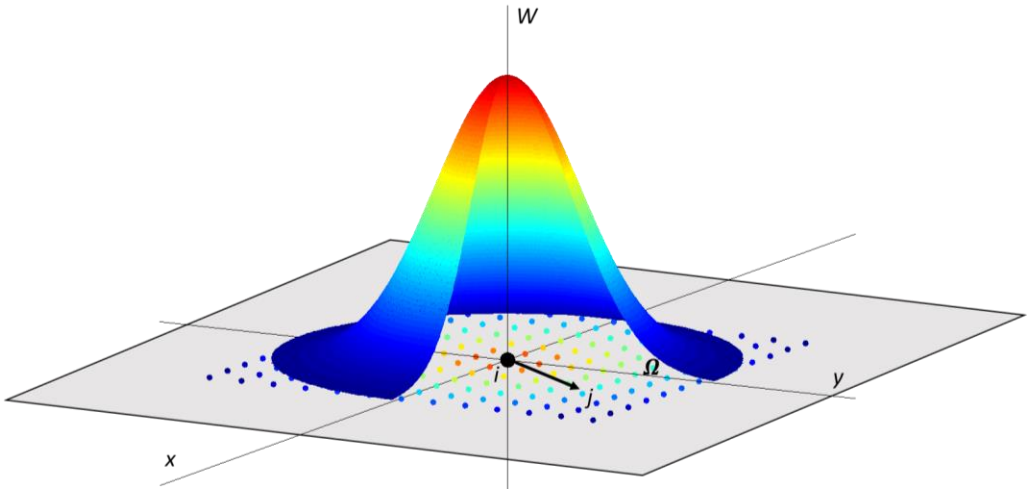

Figure 4.9 Representation of particle influence on surrounding neighbors in SPH

To calculate the interaction between the particle (i) and neighbor particles (j), a kernel function, also known as smoothing function or smoothing kernel function, is employed in order to define the magnitude of influence for all SPH particles [112–114].

$$f(x) = \int_{\Omega} f(x')\,\delta(x - x')dx' \tag{47}$$

where f is a three-dimensional position function and δ is the Kronecker's delta, and it becomes unity when $x = x'$ and zero for $x \neq x'$. By replacing with a smoothing function $W(x - x', h)$, which is not the Kronecker's delta, the Eq. (47) can be written as:

$$< f(x) >= \int_{\Omega} f(x')\,W(x - x', h)dx' \tag{48}$$

where

$$\int_{\Omega} W(x - x', h)dx' = 1 \tag{49}$$

h, is the smoothing length which is a width of the kernel function. Eq. (48) is called as smoothing kernel function with the notation of the angle bracket (<*f(x)*>) [114]. As a kernel function *W*, it is required to satisfy with few conditions. The first requirement is the normalization condition, which states that the integral of the kernel function must be equal to unity. The next condition is the Kronecker's delta condition when the smoothing length becomes to zero, and this numerical correlation is shown in Eq. (50):

$$\lim_{h \to 0} W(x - x', h) = \delta(x - x') \tag{50}$$

In LS-Dyna, the cubic B-spline piecewise kernel function, which is one of many SPH algorithms, is implemented [77,115]. Because of the continuity within the range between 0 to 2, the function is optimized to govern the particle interaction. In addition to the continuity, the function truncates the interaction once the *x* becomes larger than 2 for saving the computational expense. The cubic B-spline piecewise kernel function is described as shown in Eq. (51):

$$W(x, h) = \frac{C}{h^d} \begin{cases} 1 - \frac{3}{2}x^2 + \frac{3}{4}x^3 & for\ |x| \leq 1 \\ \frac{1}{4}(2 - x)^3 & for\ 1 \leq |x| \leq 2 \\ 0 & for\ 2 \leq |x| \end{cases} \tag{51}$$

where *C* is a dimensional constant which depends on the dimension of the particle approximation and *d* is the number of dimensions in space.

To govern the particles by fluid mechanics principles, the particles are required to obey the continuity equations (mass, momentum, and energy) and Navier-Stokes (N-S) equations. Additionally, the particle density approximation is extremely important since it governs the particle distribution and the smoothing length development. There are two main approaches to define density in SPH; the first one is a summation density approach, and the other is the continuity density approximation [112]. LS-DYNA implements the latter methodology. So, the particle approximation is based on the continuity equation in fluid dynamics as well as N-S equations. The

momentum equation is also developed similar to the continuity density approach. Both equations are shown respectively in Eq. (52) and (53):

$$\frac{d\rho_i}{dt} = \rho_i \sum_{j=1}^{N} \frac{m_j}{\rho_j} \left(v_i^\beta - v_j^\beta\right) \frac{\partial W_{ij}}{\partial x_i^\beta} \tag{52}$$

$$\frac{dv_i^\alpha}{dt} = -\sum_{j=1}^{N} m_j \left(\frac{\sigma_i^{\alpha\beta}}{\rho_i^2} + \frac{\sigma_j^{\alpha\beta}}{\rho_j^2} + \pi_{\alpha\beta}\right) \frac{\partial W_{ij}}{\partial x_i^\beta} \tag{53}$$

where ρ is the fluid density, $\sigma^{\alpha\beta}$ is the shear stress of particle and $\pi_{\alpha\beta}$.is the artificial viscosity for compression of a continuum using quadratic equation.

4.5.1 Artificial Viscosity for Smoothed Particle Hydrodynamics (SPH)

As discussed in section 3.4, a shock is a rapid rise of pressures which is associated with a nearly discontinuous jump from the initial to the final states. The discontinuity requires an additional equation to simulate, since the extreme nonlinearity of shock causes an unphysical oscillation near the shock regime in the simulation result. To damp out the unrealistic oscillation in the analysis, the artificial viscosity was initially proposed by von Neumann and Richtmyer [116]. Consequently, an artificial viscosity is also implemented for the analysis stability when a shock is introduced. Many different forms of artificial viscosity have been proposed [113,117,118], but the standard Monaghan artificial viscosity model [117], which is similar to the bulk viscosity was selected as shown in (54):

$$\pi_{\alpha\beta} = \begin{cases} \dfrac{-a\bar{c}_{\alpha\beta}\mu_{\alpha\beta} + b\mu_{\alpha\beta}^2}{\rho_{\alpha\beta}}, & v_{\alpha\beta}r_{\alpha\beta} < 0 \\ 0, & v_{\alpha\beta}r_{\alpha\beta} \geq 0 \end{cases} \tag{54}$$

where $\mu_{\alpha\beta} = \frac{h \cdot v_{\alpha\beta} \cdot r_{\alpha\beta}}{r_{\alpha\beta}^2 + .001 \cdot h^2}$

a and b are the constants for artificial viscosity, $\bar{c}_{\alpha\beta}$ is the average speed of sound for particles α and β, and $r_{\alpha\beta}$ is the distance from particle α to β. If the particles are in tension ($v_{\alpha\beta} \cdot r_{\alpha\beta} \geq 0$), there is no shock event presents, which makes the artificial viscosity vanishes. When the particles are under compression ($v_{\alpha\beta} r_{\alpha\beta} < 0$), the artificial viscosity is activated. To avoid an undefined solution, $0.01h^2$ is added to the denominator while $\mu_{\alpha\beta}$ is calculated.

4.5.2 Time Step Integration in SPH

For the shell and solid element, the time step size is evaluated by dividing the characteristic length of element by the corresponding speed of sound defined by material selection. The speed of sound is calculated by:

$$c = \sqrt{\frac{E}{\rho(1-\nu^2)}} \tag{55}$$

where E is the young's modulus, ρ is the density of material, and ν is the Poisson's ratio. Having numerous time step sizes according to the number of elements in the simulation domain, the minimum value over the entire element becomes the governing time step size for the next iterations as shown in Eq. (56):

$$\Delta t^{i+1} = TSSFAC \cdot min(\Delta t_1, \Delta t_2, \Delta t_3, \dots, \Delta t_{\#\ of\ element}) \tag{56}$$

where i is the i_{th} iteration and $TSSFAC$ is the time scale factor for computed time step, which has a range from zero to 0.9. When a high speed impact or hypervelocity impact occurs, the time step is required to be substantially low enough to converge to a solution.

The SPH does not have a characteristic length like other element formulations. Therefore, the time step of SPH is derived by using the smoothing length. Typically, the smoothing length is a time-dependent variable that is constantly updated based on the particle allocation of the previous time-step. However, during the first time-step, LS-Dyna uses the initial smoothing length to define the neighboring particles. Using the smoothing length, the time-step of explicit SPH simulation is determined by using Eq. (57):

$$\delta t = C_{cfl} Min(\frac{h_i}{c_i + v_i}) \quad (57)$$

where C_{cfl} is Courant-Friedrichs-Lewy (CFL) constant for stability of the explicit time integration solution. c_i is the average material speed of sound of particle i and v_i is the particle i velocity. Because CFL condition suggests the maximum allowable smallest time-step, the smallest value is selected to determine the initial time-step [119]. After the initialization, the smoothing length is iteratively updated based on the divergence of particle velocity to find another optimal smoothing length [117]. While the new smoothing length is calculated and employed to determine the time-step for next iteration, the default smoothing length is scaled from 0.2 to 2 to maintain a constant number of particles within each particle's smoothing length during the calculation instance [21,120].

4.6 Stress Initialization for Rotational Object

When a dynamic analysis includes steady-state loading, such as a rotating fan blade, gravity initialization, or pre-tensioned bolt, the steady-state loads have to applied on the object in advance [121,122]. Without stress initialization, the analysis will contain unrealistic energy oscillations rather than a quasi-static response.

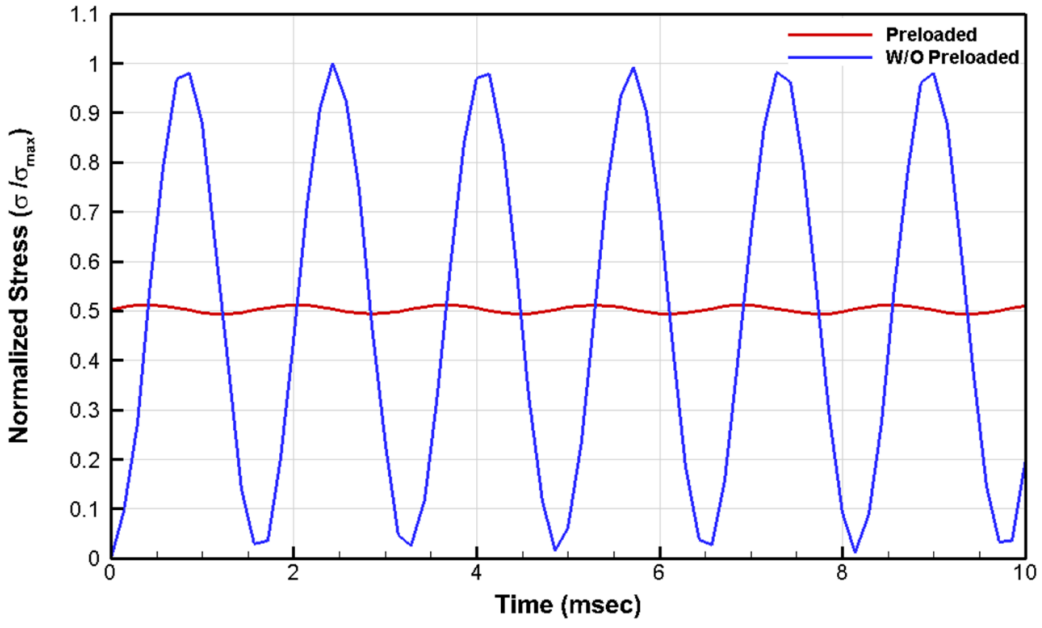

Figure 4.10 von-Mises stress of a spinning disk with constant angular velocity (normalized with maximum stress without preload)

As an example, Fig. 4.10 shows the stress oscillation of a steady-state spinning disk with and without stress initialization. As shown, the average of two normalized radial stresses are very close to each other, however the plot shows a distinctively different trend: the stress oscillation. The simulation without preload shows the significant normalized stress oscillation compared with the preloaded simulation. The fluctuation of stress is also qualitatively observed in the simulation result. As shown in Fig. 4.11, the rotational stress of the disk starts zero initially, then the regime of maximum stress is propagating toward the outer disk at 1 *msec*. Then the stress contour plot shows the correct stress distribution momentarily at 2 *msec*, which is also equally observed in Fig. 4.10.

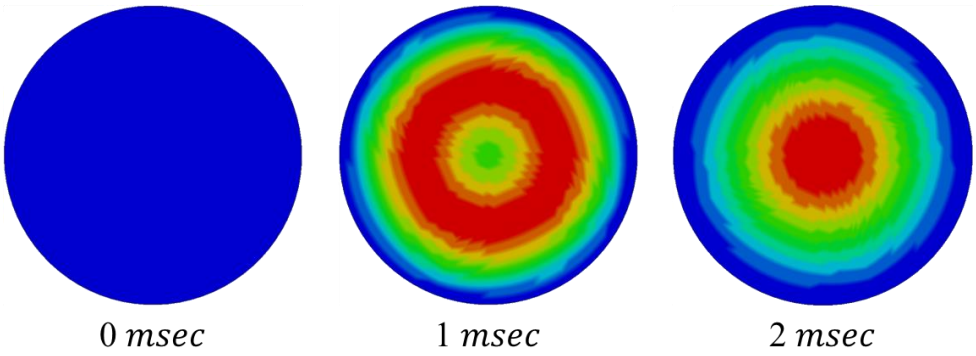

Figure 4.11 Stress oscillation of a steady-state spinning disk without stress initialization

This stress oscillation is never damped out and continuously observed throughout the entire simulation. Because of the significant stress fluctuation without the stress initialization, the FOI simulation without preloading can cause more damage than what should be present. Hence, stress initialization is required to be performed prior to the FOI scenario to improve the fidelity of the FOI analysis. In LS-Dyna, the stress initialization is implement and named as dynamic relaxation, and it is implemented for the implicit and explicit analyses. During the explicit dynamic relaxation procedure, the oscillatory (distorted) kinetic energy is monitored prior to the transient dynamic analysis. Since it is a separate set of computation from the actual transient analysis, an additional computational expense is applied to the overall investigation. The dynamic relaxation in LS-Dyna [77] is developed based on the work of Underwood [121] and Papadrakakis [123].

The algorithm is developed by using the total energy and the approximated kinetic energy using a rigid body assumption. The distorted kinetic energy is calculated by subtracting the kinetic energy evaluated by using rigid body motion from the total energy of the entire simulation domain iteratively until the distorted kinetic energy reaches to an assigned tolerance. The tolerance is computed by the current distorted kinetic energy dividing by the initial distorted kinetic energy.

After the preloading procedure finishes, the steady-state stress and strain of rotating assembly is embedded to the input file to avoid repetition for further investigation.

4.7 Contact in Finite Element Analysis

The general idea of contact is to allow the interaction between more than two finite element parts. Initially, the contact (or impact) algorithms were proposed by Hughes et al. [124] and the methodology has been applied to modern finite element framework. In accordance with the development of other element formulations, the contact algorithm is also improved to encompass other contacting cases such as SPH to Lagrangian and ALE or Eulerian to Lagrangian. The contact algorithms include major interactions that are observed in the real world such as impact, friction, spot weld, and adhesion.

Among many contact algorithms, the penalty-base contact algorithm is widely selected. When contact occurs, a virtual spring, which is elastic and activates for only compression loading conditions, is generated between all penetrating nodes on master parts to the contact nodes on slave parts in normal direction to the master to prevent penetrations of the nodes on the slave part through the surface of master elements. Then the artificial spring constants are continuously updated based on the contact condition and added to the stiffness matrix directly at each time step to calculate the contact force and corresponding displacement [77].

In the FOI analysis, multiple contact algorithms are required. The primary contact scenario throughout the simulation is the soft body projectile and the propulsion system structure. Then, the internal components are subjected to contact with each other as triggered by the dynamic responses. Such internal contact can occur without additional support when contacting parts have similar densities. However, when dissimilar materials come into contact, considering ice or bird contacting with the engine structure in this study, the contact algorithm requires additional stiffness in order to successfully calculate the contact between each body. To alleviate such stiffness discrepancy between soft body and structure, additional stiffness is introduced by using the nodal mass of slave material and the current time step with the given scale factor for the simulation stability.

5 Preliminary Validation and Verification of Computational Model

A proper mesh density is investigated in this chapter to maximize the solution accuracy without the excessive computational expense. Aforementioned, the post-impact behavior of two FOI candidates (bird and ice) are extremely similar to that of a fluid; the bird constituent becomes a non-Newtonian fluid and the ice material becomes a group of inviscid particles. Hence, a multidisciplinary approach is thoroughly developed to capture the fluid-structure interaction (FSI).

Since both FOI candidates are expected to suffer from large deformations and domain separations upon the impact, SPH formulation was selected to capture the fluidic deformation caused by the interaction. To isolate the computational error caused by the particle density, a simulation uncertainty analysis was conducted. In order to quantify the mesh dependency, the distance between particles (pitch) was changed within the same volume in order to maintain a consistent projectile mass. Using the uncertainty analysis methodology, the force discrepancy caused by different mesh densities was quantified and the errors among different mesh densities are measured. Throughout the analyses, the particle densities for two projectiles were determined. Having investigated the mesh dependency, an extensive code verification and validation was conducted to verify the FSI methodology. A brief composite damage modeling result is also discussed in this chapter. The detailed discussion of ALE and composite casing design are discussed in Appendix.

5.1 Bird

5.1.1 Model Verification

A code verification of the fluidic modeling methodology using SPH was conducted. To do so, the distance between particles (pitch) was changed within the same volume with the M-G EOS and viscous fluid model as previously mentioned. The impact velocity (V_c in Fig. 2.7) was selected based on the relative velocity between that of the aircraft and the fan blade's tangential speed, assuming the impact location of 75% from the hub at the leading edge of the fan stage. As a result, the projectile impact velocity was set at 228 *m/s*. Given the reported dimensions of the soft body impact shown in Fig. 2.13, and the varying particle densities, a comprehensive code verification,

including the grid resolution and *Norm* studies, was conducted by simulating the soft body projectile impact onto a flat compliant surface. Table 5-1 lists the relationship between computational expenses versus particle density in each case.

Table 5-1 Number of SPH particles used at each pitch and corresponding computational time

Pitch (mm)	Number of Particles	Computational time (sec)
10	2,714	62
8	5,261	86
7	7,889	116
6	12,488	173
4	42,381	552
3	100,430	1,371
2.5	173,536	2,517
2	339,889	5,743
1.5	804,632	11,838

Figure 5.1 shows a force time plot of multiple mesh densities; each result equally filtered at 10 kHz using a low-pass filter to minimize the artificial numerical noise. The filtration frequency of raw data was selected by applying the fast Fourier transform (FFT) response to the raw data and evaluating the frequency candidates. The peak frequency candidates were then selected to remove the artificial noise,

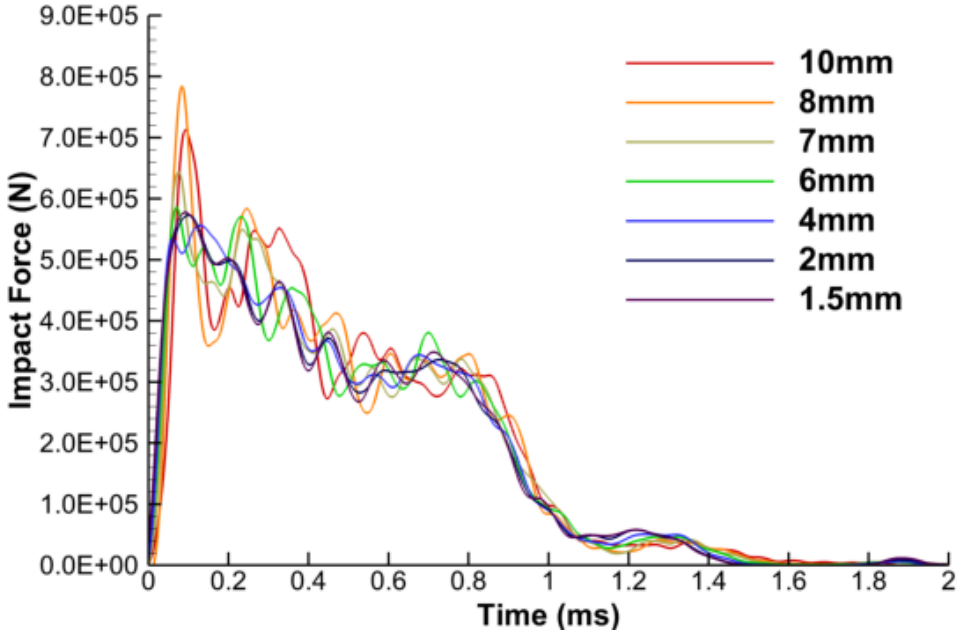

Figure 5.1 Force time plot of the low strength projectile for multiple mesh densities

The filtered mesh density considerably affected both the magnitude of initial peak force and the unloading behavior. The peak force converged progressively to that resulting from the highest mesh, as the magnitude of oscillation lessened with incremental increase in particle density. To maintain the quality of the simulation, while optimizing the computational cost, a computational error quantification analysis was conducted to find a mesh dependency for further analysis and corresponding additional computational expense. Eight pairs of mesh (*h*), with nine different particle densities, were created, run, and compared as presented in Table 5-2.

The *L_2Norm* is one of the most widely used methods in computational fluid dynamics (CFD) to determine the quality of the analytical result among different mesh densities [125]. To quantify the discrepancy of result among different mesh densities, the impact force on target surface was measured at each time step and processed using Eq. (58):

$$L_2Norm = \left(\frac{\sum_{n=1}^{N} \left(F_{coarse,n} - F_{fine,n}\right)^2}{N} \right)^{\frac{1}{2}} \tag{58}$$

where *N* is the number of time steps, *F* is the force for both coarse and fine mesh at each time step. Due to the absence of an exact solution, the force measured from the finer mesh was substituted into Eq. (58). In Fig. 5.2, the data for *L_2Norm* and the computational increment versus mesh pair is plotted, while also tabulated in Table 5-2.

Table 5-2 Computational time increase, and *L_2Norm* at each mesh pair (*h*)

h	**Mesh Pair**	**Time Increase (sec)**	***L_2Norm***
1	(10, 8.0)	24	943
2	(8.0,7.0)	30	676
3	(7.0,6.0)	57	771
4	(6.0,4.0)	379	655
5	(4.0,3.0)	819	347
6	(3.0,2.5)	1146	276
7	(2.5,2.0)	3226	229
8	(2.0,1.5)	6095	170

From the graph, it is evident that the computational cost exponentially rose as the particle density increased. However, the rate of convergence dropped beyond the mesh pair # 6. Although monolithic convergence did not occur at the second mesh pair, the force discrepancy between each mesh pair decreased gradually with the increasing particle density. However, the magnitude of the

L_2Norm decrement became gradually negligible for the finest resolution to compare with the coarsest particle density.

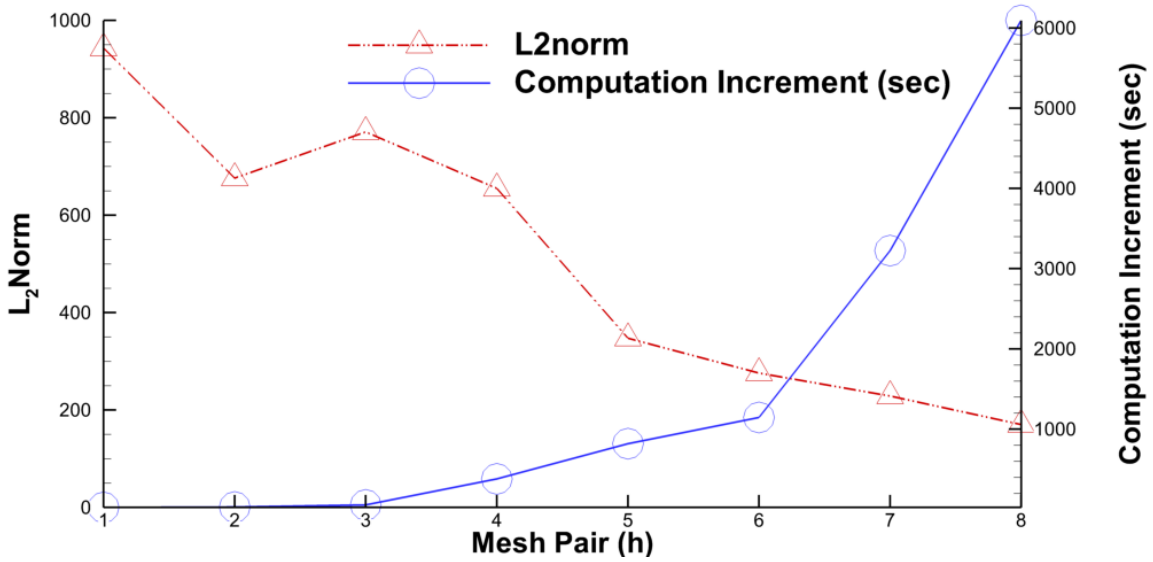

Figure 5.2 *L_2Norm* and computation increment as a function of mesh pair (*h*)

For quantitative comparison between the convergence characteristics of each computational model, numerical uncertainty analysis was conducted to quantify the numerical error; such as discretization error and truncation error. Roache [126] initially proposed the use of grid convergence index (*GCI*) for computational analysis in order to systematically quantify the numerical errors of computational model for both CFD and other disciplines. Celik et al. [127], then proposed the details of a procedure to assess a code verification with a uniform methodology.

The *GCI* calculation is based on the grid refinement factor (r) and simulation solution (ϕ) and quantify the solution accuracy with given set of result. To find *GCI* of the computational model, the apparent order (p), approximated relative error (ε_a), and grid refinement factor are required. The observed order (p) is evaluated by using following equations (59)-(61):

$$\varepsilon_a^{21} = \left|\frac{\phi_1 - \phi_2}{\phi_1}\right| \tag{59}$$

$$p = \frac{\left|\ln\left(\frac{\varepsilon_{32}}{\varepsilon_{21}}.\left(\frac{r_{21}^{p}-s}{r_{32}^{p}-s}\right)\right)\right|}{ln(r_{21})} \tag{60}$$

where $\varepsilon_{32} = \phi_3 - \phi_2$, $\varepsilon_{21} = \phi_2 - \phi_1$, $s = 1 \cdot sign(\varepsilon_{32}/\varepsilon_{21})$, $r_{32} = h_3/h_2$, $r_{21} = h_2/h_1$, and subscript 1, 2, and 3 represents fine, medium, and coarse mesh density respectively. Using the calculated observed order of accuracy (*p*) and approximated relative error, the *GCI* of presented computational model is evaluated as shown in Eq. (61):

$$GCI_{mid}^{32} = \frac{1.25 \cdot \varepsilon_a^{32}}{r_{32}^p - 1} \tag{61}$$

For the presented FSI methodology using SPH element formulation, the peak forces for particle pitches of 8, 4, and 2 mm were selected to determine the convergence trend. Table 5-3 shows the tabulated results from the *GCI* analysis. *N* is the number of particles at each mesh resolution and *F* is the reaction force on target surface.

The apparent order of accuracy (*P*) was evaluated as 3.5, which is higher than the theoretical order of accuracy for typical finite element discretization schemes. The solution displays monotonic convergence to the highest mesh density, with the numerical uncertainty of 4.9% from the coarse mesh to the medium sized grid. On the other hand, the *GCI* was reduced to 0.41% when considering the medium to fine mesh densities. Therefore, based on the *GCI* study, the 4 mm particle spacing was selected and used for further analysis.

Table 5-3 Computational error for particle densities of 8, 4, and 2 mm. The subscript (3, 2, and 1) are coarse, mid, and find mesh resolution respectively.

N_1, N_2, N_3	**339809, 42381, 5261**
r_{21}, r_{32}	2, 2
F_1	572,502
F_2	552,574
F_3	784,335
P	3.529
e_a^{21}	0.328%
e_a^{32}	4.106%
GCI_{21}	0.411%
GCI_{32}	4.930%

5.1.2 Parametric Study of Pressure Cutoff

A low strength fluidic projectile resists volumetric expansion, as observed after the initial contact with a surface. The expansion threshold applied is defined by adding a pressure cutoff (PC). A parametric study was conducted to simulate the effect of the PC both qualitatively and quantitatively.

In Fig. 5.3, particle distributions after impact for multiple PCs have been depicted. Since the resistance against dilation does not exist when PC is set to zero, the particles are dispersed widely and symmetrically which is qualitatively close to an inviscid fluid deformation as shown in Fig. 5.3-(a). Such particle behavior changes once the PC becomes non-zero, particle cluster starts forming when the PC is assigned. As the value increases, the post deformation shape of soft body projectile becomes more like that of the Newtonian fluid body which is also qualitatively presented in Fig. 5.3-(c).

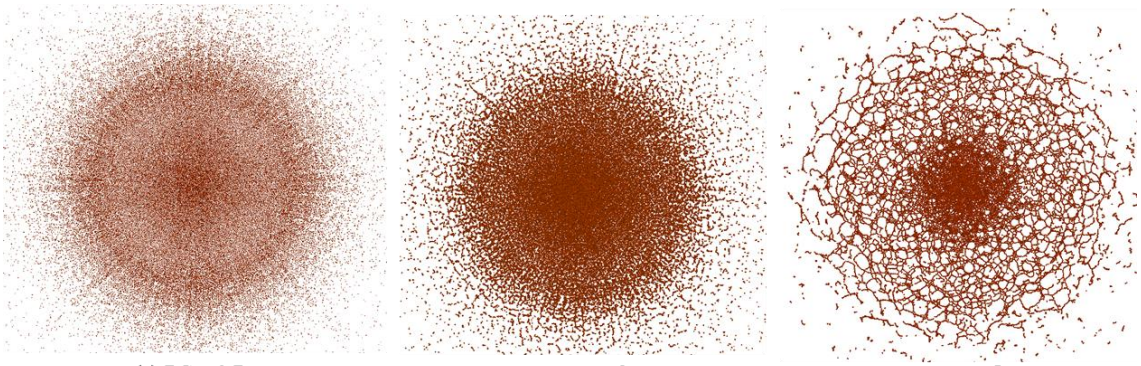

(a) PC = 0 Pa (b) PC = $5.E^5$ Pa (c) PC = $5.E^7$ Pa

Figure 5.3 Particle distributions as a function of pressure cutoff (m=2.5 *kg*, V= 228 *m/s*)

In addition to the qualitative damage prediction, the phenomenon is also important since the momentum transferred by a group of particles is larger than that of an individual particle. In short, a clumped particle can cause a larger continuous damage on the secondary target surface to compare with the single particle impact. Hence, proper selection of the PC value is imperative in order to predict an accurate fluidic behavior to the soft body projectile.

Although the particle scattering appears significantly different, the quantitative data does not vary noticeably. Figure 5.4 highlights the force time graphs for a range of PC values. The initial loading path on the target surface and the discrepancy of initial peak forces is negligible. The continuous unloading path and the impact time window for all three models are extremely similar to each other. One difference is that the soft body projectile with higher PC (50 *MPa*) undergoes

more vigorous force fluctuations after the initial impact due to particle clumping as shown in Fig. 5.3-(c).

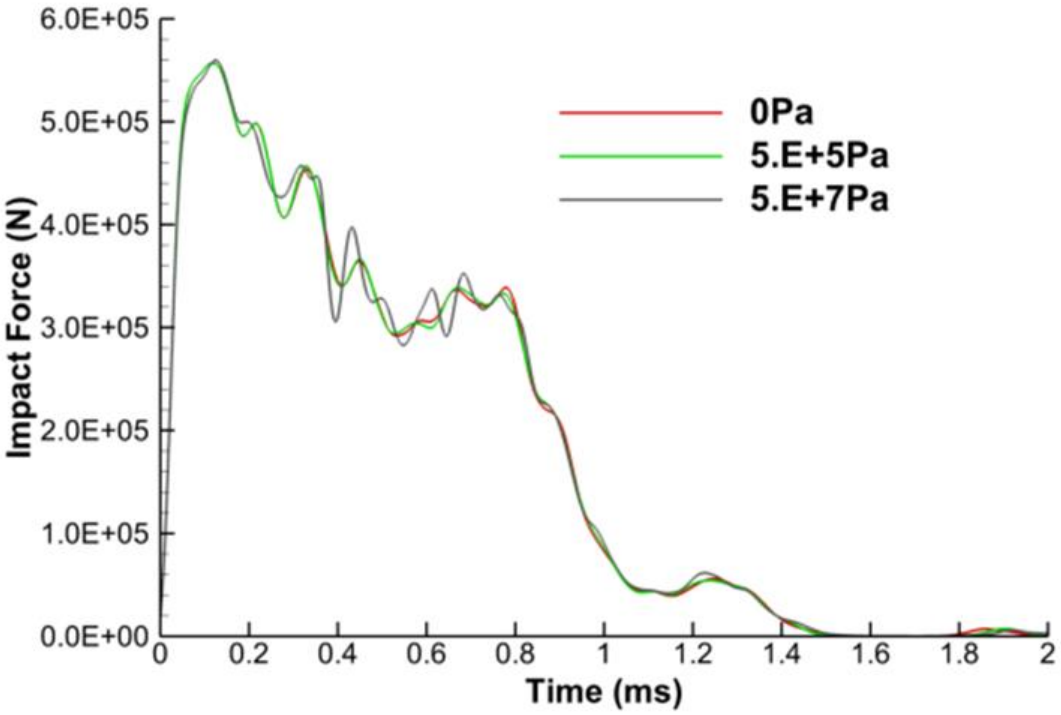

Figure 5.4 Force-time history of soft projectile impacts with 3 different PCs (m=2.5 *kg*, V= 228 *m/s*)

Even though the overall result was quantitatively remained similar by defining a PC on a low strength fluidic projectile, the computational cost slightly increased (~5%). The simulation stability was compromised as the PC value became excessively large. This was caused by the confliction between the resistance against dilatation which lead to prevent a separation of projectile particles during the impact and the conservation law which continuously requires a separation among each particles. By considering both stability of simulation and more realistic particle distribution after the impact, the PC is set as 50 *MPa* for the comprehensive FOI analysis.

5.1.3 Validation of Soft Body Impact Model

The virtual projectile model was compared against physical experiments. Seidt et al. [128] conducted a ballistic impact test using gelatin to represent a soft body projectile. The dimensions of the projectile in the experiment were 3.175 *cm* (1.25 *in*) in diameter and 7.62 *cm* (3 *in*) in length. Figure 5.5-(1) shows the initial contact between projectile and target surface. Upon the initial

impact, an initial shockwave was generated at the impact zone, sweeping through the projectile. The non-linear contact area growth on the target surface is observed in Figs. 5.5-(2), and (3). The impact time window in the experiment was reported as 0.5 *ms*, while the simulation predicted the contact duration as 0.47 *ms*.

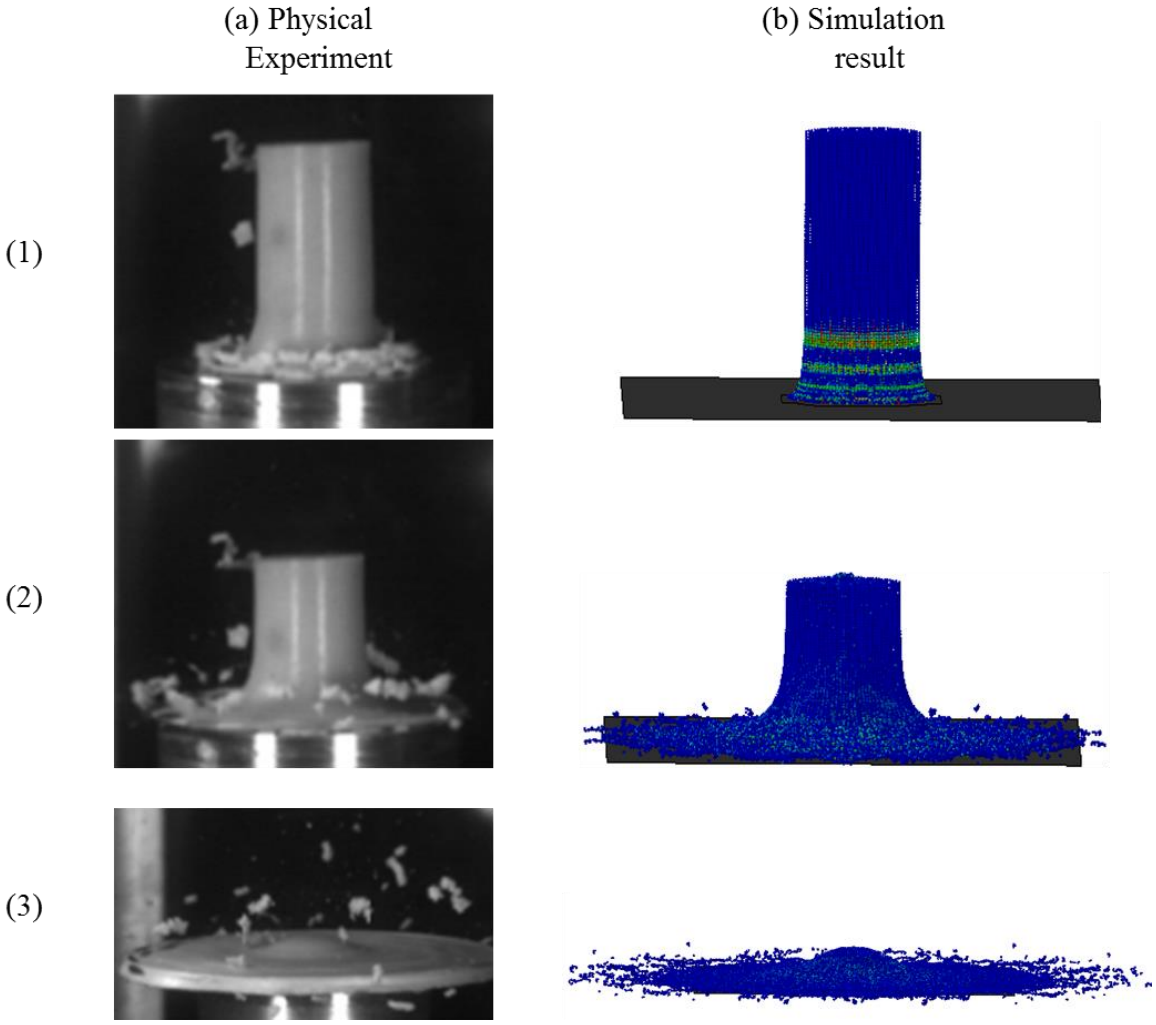

Figure 5.5 Qualitative comparison between (a) physical experiment [128] **and (b) simulation**

The peak force measured in the simulation was 71,200 *N*, while the corresponding reading during the experiment was reported as 65,000 *N* (14,500 lb_f). The discrepancy between the simulation and experimental peak impact forces was approximately 9% which is considered to be within an acceptable range. Further, impulse (I) was calculated analytically in order to be compared with the simulation data. The impulse of the target surface is determined using Eq. (62):

$$I = \int_{t_1}^{t_2} F(t)dt \tag{62}$$

where *F* is the force as a function of time on the target surface. The force response of the target surface during the impact is presented in Fig. 5.7 (cylindrical projectile). The numerical integration of the force time response is conducted using the Simpson's rule. Based on the initial conditions of the test, the momentum of the projectile is equal to 8.79 *N·s*. By integrating the force over time in the simulation, the impulse on the target surface can be determined as 8.78 *N·s*. This value is in high agreement with that of the physical experiment with only 0.11% deviation from the physical experiment.

5.1.4 Parametric Study of Projectile Geometry

The details of other tentative bird geometry and the shape effect is thoroughly investigated by Nizampatnam [14]. During the course of this program, the effects of the projectile geometry were briefly investigated. In this study, two defeatured bird projectile shapes, which are a cylindrical projectile with hemispherical cap on both side and cylindrical projectile, were selected as shown in Fig. 5.6.

The qualitative results of the soft body impact of two candidate projectile shapes were considered as presented in Fig. 5.6. Due to the differences in their geometries, the impact time windows were slightly modified, with no considerable change in their deformation mechanics and the qualitative particle scatter. Although the difference in qualitative results between the candidate shapes are negligible, a significant quantitative difference between the two simulations was observed.

The propagation and magnitude of the shock were significantly different from each other because of the shape of the projectile. Geometrically, the hemispherical cylinder projectile has more gradual contact area development at the interface rather than that of the cylindrical projectile. Hence, a sharper Hugoniot shock (P_H) was induced on the entire contact surface of cylindrical projectile in the quantitative result. But, the Hugoniot shock (P_H) was induced at the localized (or tip) of the hemispherical cylinder projectile, causing the shock to be more gradually developed as the contact area increased.

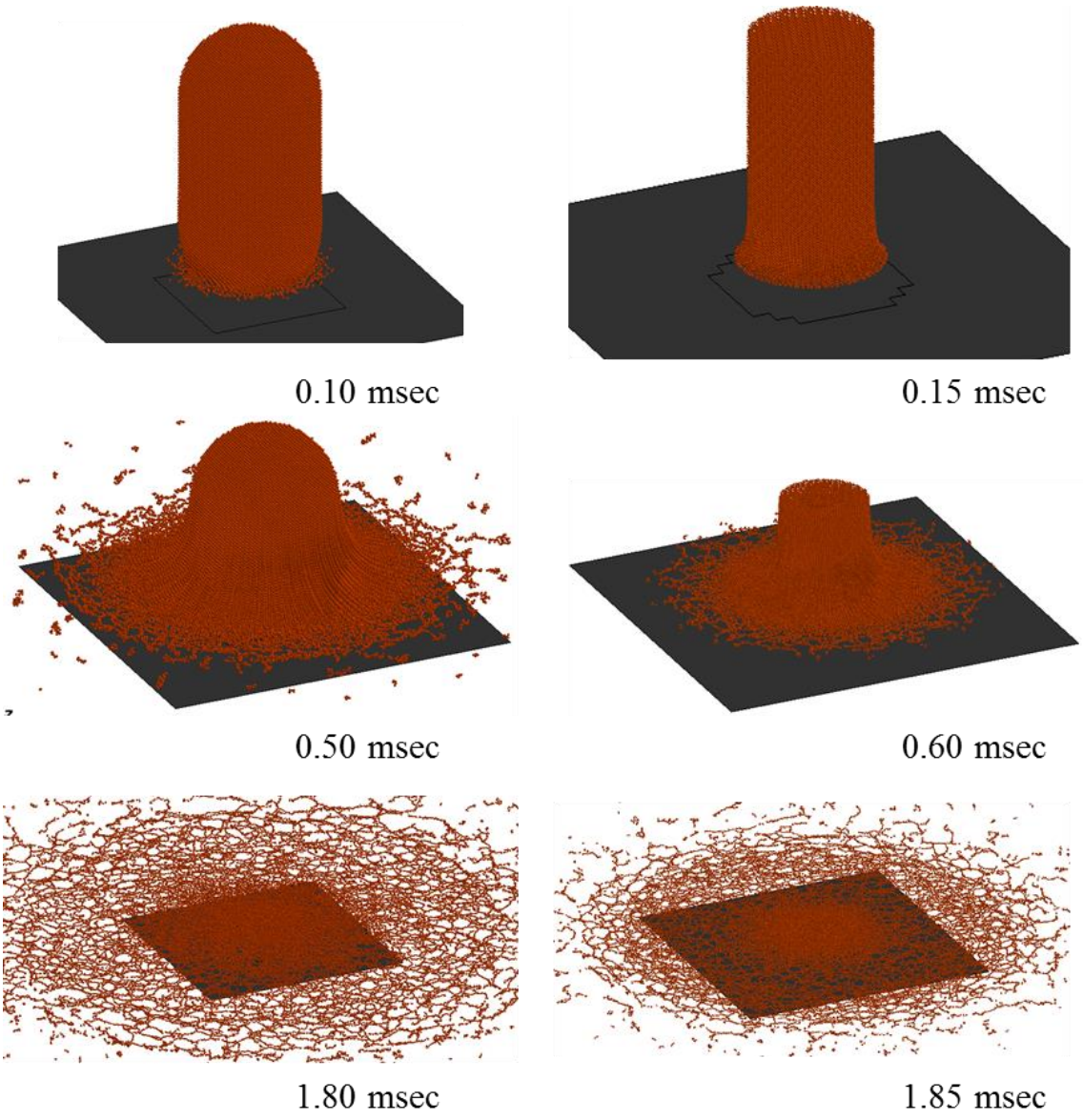

Figure 5.6 Qualitative results of soft body impact simulation of two candidate projectiles (*m*=2.5 *Kg*, *V*= 228 *m/s*, and *PC* =50 *MPa*)

Figure 5.7 shows the trends of the force induced on the target surface over time. Because of the shape of the projectile tip, the initial peak force of the cylindrical projectile was measured several times higher than that of the hemispherical cylinder projectile as previously discussed. However, the average pressure during the unloading stage of the cylinder projectile was determined to be smaller than that of the hemispherical projectile. This was caused by the relationship between the induced shockwave as a function of the shape of the projectile head and the PC assigned for the bird substance.

Aforesaid, the PC of the virtual bird was defined as 50 *MPa* which is a fraction of Hugoniot shock pressure (P_H) of analytical calculation. The analytical shock pressure (P_H) for the projectiles at the moment of initial contact with the aluminum target was calculated as 287 *MPa*, based on Eq. (19). The simulation predicted the P_H of cylindrical projectile as 264 *MPa* with the error of 8% within entire contact surface and travels through the rest of the continuum. During the impact, the majority of continuum suffered from the larger magnitude of shock pressure threshold and most of the particles were separated. The shock pressure (P_H) for the hemispherical cylinder was 277 *MPa*, which is only 3.4% from the analytical value, is very localized and most of the continuum was gradually disintegrated with the combination of the shock pressure (P_H) and stagnation pressure (P_{SS}).

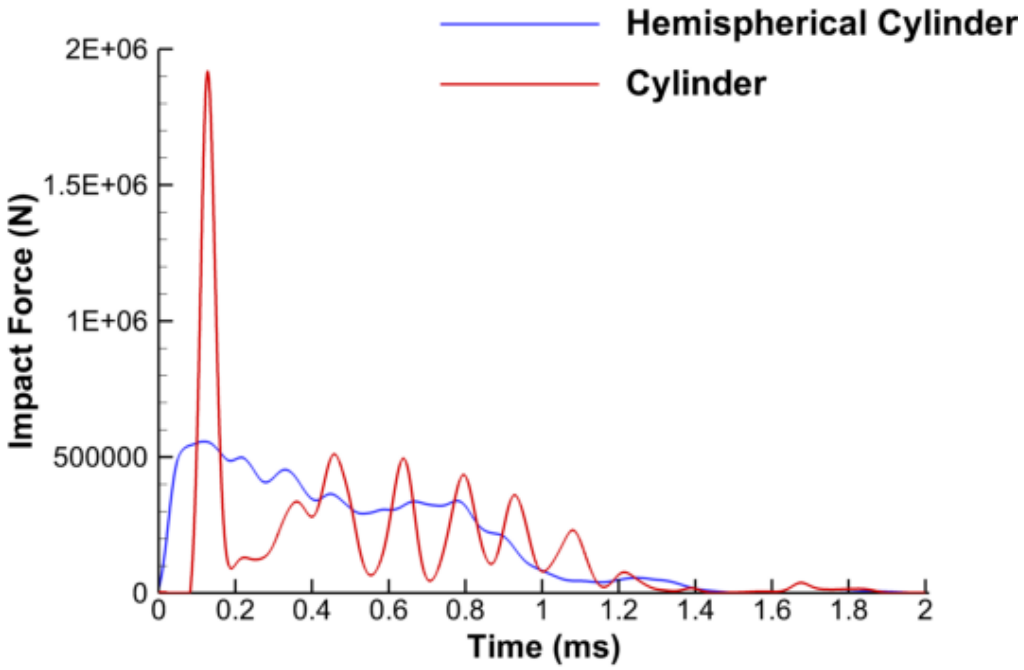

Figure 5.7 Force-time history of two candidate projectiles (*m*=2.5 *Kg*, *V*= 228 *m/s*, and *PC* =50 *MPa*)

As another validation, the impulse values of both candidate projectiles were compared using Eq. (62). Analytically, the initial momentum for both cases were 568 *N·s*. The simulation result predicted the impulse of both projectile very close to the analytical calculation. The impulses on the target surface for the hemispherical cylinder and cylindrical projectiles were calculated as 558.67 and 569.66 *N·s*, respectively. To compare the trend of impulse for both geometries, it was normalized as shown in Eq. (63):

$$I_{norm} = \frac{I}{m_{bird} * V_{bird}} \tag{63}$$

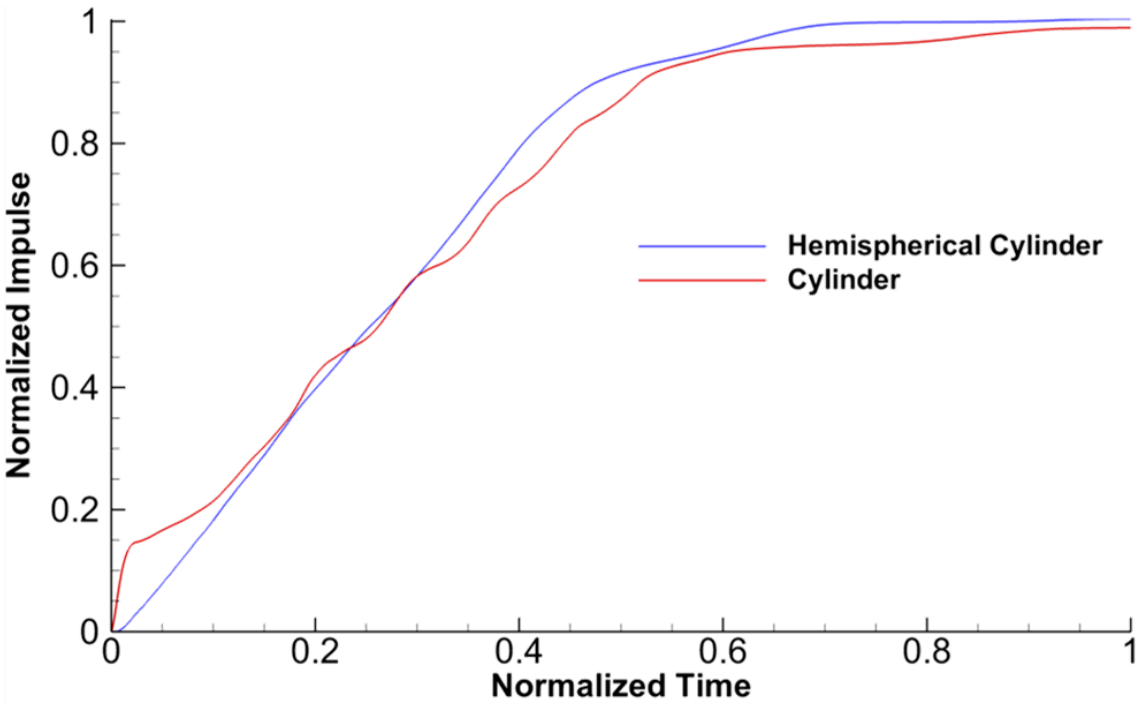

Figure 5.8 Normalized impulse of two candidate projectiles (*m*=2.5 *Kg*, *V*= 228 *m/s*, and *PC* =50 *MPa*)

Figure 5.8 shows the impulse of both projectiles after normalization. As shown in the graph, the impulse of the cylindrical projectile on the target surface initially increases more rapidly than the impulse of the hemispherical projectile. On the other hand, the load applied on impact surface was more linear when the hemispherical projectile was employed. The rate of impulse increase of the cylinder projectile after the initial contact was less steep than that of the hemispherical cylinder projectile. It was observed that the hemispherical cylinder was able to consistently exert a higher magnitude of loading on the target surface, resulting in the same total impulse as that of the cylindrical projectile, without prompting any severe changes in the Hugoniot shock levels. Therefore, the hemispherical cylinder shape was selected for full-scale bird ingestion simulations

5.2 Ice

5.2.1 Model Verification

As a prerequisite procedure to conduct comprehensive ice ingestion analyses, a proper particle density for ice model was evaluated to maintain the fidelity of the simulation. The same computational model verification methodology, previously explored, was applied to assess the numerical uncertainty of the solid ice model and optimize the particle density for the

comprehensive FOI analysis. The solid ice damage model (combination -1 in Fig. 2.16) was thoroughly discussed with the material definitions by Carney et al. For the detailed discussion of solid ice damage model, readers are commended to review the work by Carney et al. [58]. The series of ice impact experiments was used to validate the ice model for both qualitatively and quantitatively in the later this chapter. Pereira et al. [129] created several ice projectiles with multiple ice crystalline lattice structures, controlling the volume and mass of each projectile constant, to conduct impact tests from the speed of 91 *m/s* (300 *ft/s*) to 213.36 *m/s* (700 *ft/s*). One of the important conclusions in the study was that ice crystalline structure did not significantly influence on the acquisitioned results [129].

The dimensions of the cylindrical projectile used for the ice impact experiments were 1.75 *cm* (0.6875 *in*) in diameter, and 4.22 *cm* (1.66 *in*) in length. The impact velocity for the ice impact model verification was set at 152.4 *m/s* (500 *ft/s*), which matches one of the experiment cases. The same modeling methodology was employed to vary the particle densities as described in the previous section. Corresponding with the reduced projectile size, the pitch was varied incrementally from 0.25 *mm* to 5 *mm*. The particle densities and the corresponding computational times are listed in Table 5-4.

Table 5-4 Number of SPH particles, and computational time of ice model at various particle spacing

Pitch (mm)	Number of Particles	Computational time (sec)
5.0	108	79
4.0	142	80
2.0	1,342	96
1.5	3,248	133
1.0	10,320	309
0.5	80,665	2,354
0.4	157,304	5,460
0.3	371,817	15,632
0.25	644,228	34,673

As noticed in previous section, the computational expense was exponentially increased as the particle density to describe the ice model was increased. Such correlation is also shown in Table 5-4. Figure 5.9 shows the force time response of the proposed mesh densities which were equally filtered at 25.6 *kHz* using low pass filter. The general trend of force time plot is similar to the previous analysis. The magnitude of peak forces was converged toward to the highest mesh density solution. Not only the peak force, but the fluctuations during the unloading were also converged to the highest mesh density result.

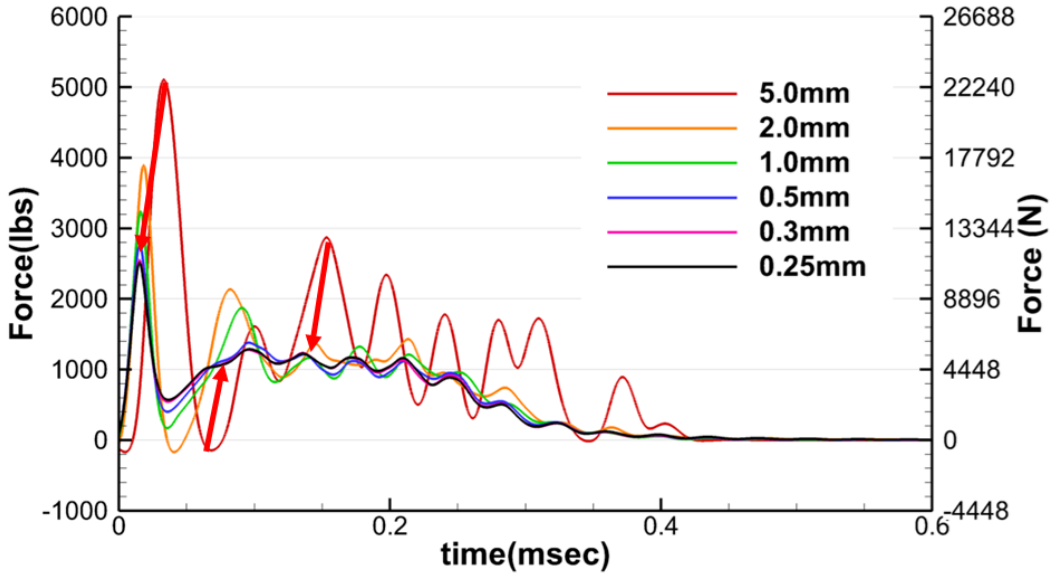

Figure 5.9 Force time histories of ice impact simulations for multiple mesh densities at 500 *ft/s* (152.4 *ft/s*)

Eight mesh pairs (*h*) were created with nine different mesh densities were created for the L_2Norm analysis using Eq. (58): Interestingly, the similitude between the bird and solid ice impact model was observed during the analysis. Figure 5.1 shows the relationship between each mesh pair (*h*) and both L_2Norm as well as incremental computational expense. As we observed, the computational expense exponentially increased along each increment of mesh density, while the effectiveness of increasing mesh density gradually decreased beyond. The force discrepancy between each mesh pair became effectively negligible beyond the 5th mesh pair. The computational expense is dramatically increased after 6th mesh pair as well.

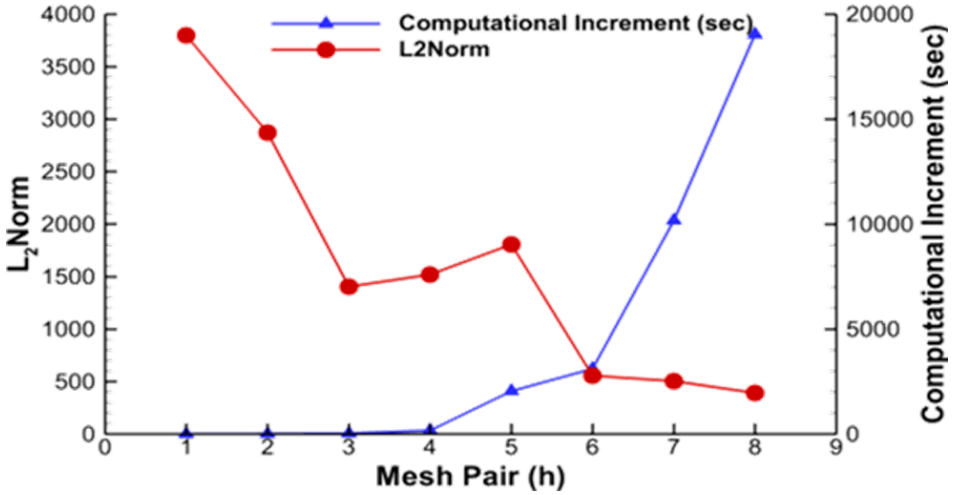

Figure 5.10 L_2Norm and computational increment versus mesh pair (*h*)

For the computational uncertainty analysis of the solid ice impact model, the *GCI* analysis was conducted using Eq. (59)-(61). The peak forces of 1, 0.5, and 0.25 *mm* particle spacing simulations were used to quantify uncertainty in the computational analyses and the result is tabulated in Table 5-5.

Table 5-5 Computational error for ice model. The subscript (3, 2, and 1) are coarse (1 *mm*), mid (0.5 *mm*), and find (0.25 *mm*) mesh resolution respectively.

N_1, N_2, N_3	**644228, 157304, 10320**
r_{21}, r_{32}	2.480, 1.600
F_1	11,191
F_2	12,295
F_3	14,410
P	2.048
e_a^{21}	9.862%
e_a^{32}	17.20%
GCI_{21}	2.274%
GCI_{32}	13.290%

The observed order of accuracy (*P*) of solid ice high speed impact model was evaluated to be 2.048. Considering the theoretical order of SPH formulation (2nd order), the ice impact simulation exhibited the proper order of accuracy. The approximated analytical error for the coarse-to-medium mesh pair (e_a) was 17.20%, and 9.86% for the medium-to-fine mesh pair which were relatively larger than that of the bird model. Similarly, the computational uncertainty (*GCI*) was observed higher than that of the previous model. The *GCI* for the coarse-to-medium pair was evaluated as 13.290% and 2.274% for the medium-to-fine mesh pair. Considering the additional computational expense between 0.5 *mm* and 0.25 *mm* and 2.274% of convergence toward the highest mesh resolution, the 0.5 *mm* particle distance was selected for the comprehensive ice-ingestion analysis.

5.2.2 Parametric Study of Material Definition and EOS

As previously discussed, an alternative way to simulate the high speed ice impact scenario was explored in this chapter. As shown in Fig 2.16 in section 2.2.2, the solid ice material damage model with the Tabulated EOS (combination -1) and the fluidic ice model with Gruneisen EOS (combination -4) were primarily discussed in this chapter. Additionally, sensitivity analyses for both the material definitions and EOS were conducted in order to check the influence on the simulation result by changing the inputs. The post processed data for the sensitivity analyses and all the impact velocity scenarios are thoroughly provided in Appendix-A.

Figure 5.11 is the force time plot for both the solid ice damage model and the proposed ice damage model at three different impact speed. The overall differences between two damage models are the initial peak force and the unloading path. Generally, the fluidic ice model presented higher initial contact force at all the impact speeds. More dynamical response along the unloading sequence was predicted with the fluidic ice damage model. At the impact speed of 91.4 *m/s* (300 *ft/s*) in Fig. 5.11,the peak impact force was measured for 7100 *N* (1600 lb_S) using the proposed methodology, and the solid ice model induced 5300 N (1150 lb_S) force at the target surface. The peak impact force was approximately 40% more intense to compare with the conventional model. Not only the peak force, the steady state (or stagnation) force time response on the target surface was also noticeably changed by using different damage models. Instead of the piece-wise response observed in solid ice mode, the oscillation of force after the initial contact becomes more dynamic when the fluidic ice damage model was implemented.

A similar force time trend was observed when the impact speed increased to 152.4 *m/s* (500 *ft/s*). The conventional solid ice damage model calculated the peak impact force as 10089 *N* (2252 lb_S), and the peak force of proposed ice model was measured as 12371 N (2781 lb_S). The initial impact force measured using fluidic ice definition was over predicted by 22 %, though the discrepancy in both models was reduced noticeably. The impact time window for both simulations was equally reduced to compare with the 91.4 *m/s* (300 *ft/s*) case, because the ice particle dispersion after the shock disintegrate the ice projectile occurred more rapidly due to the higher impact speed.

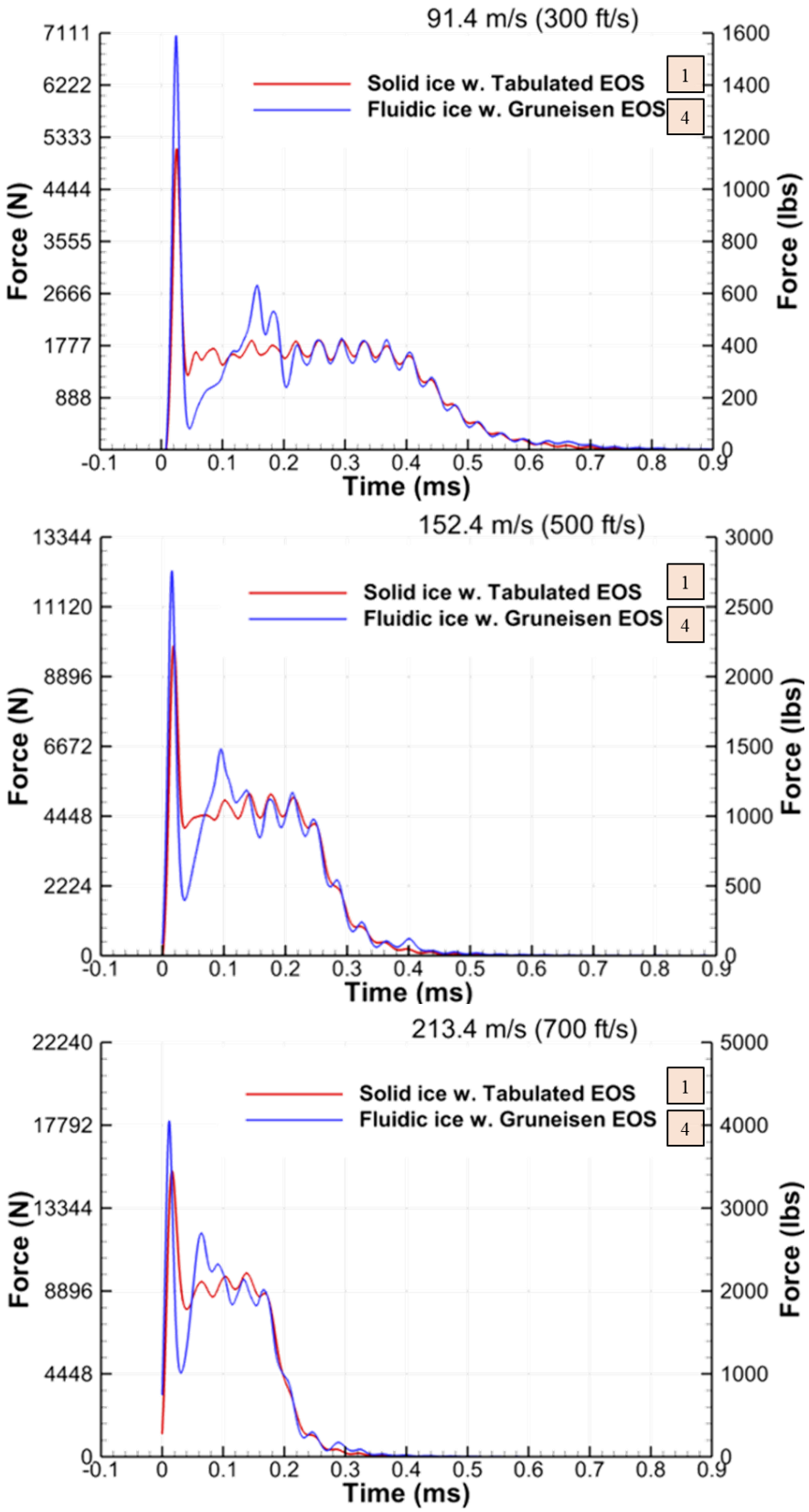

Figure 5.11 Force-time plot of high speed ice impact simulation for both computational model at multiple impact speeds

When the impact speed set as 213.4 *m/s* (700 *ft/s*), the fluidic ice damage model with Gruneisen EOS predicted consistently higher impact force than that of the solid ice damage mode with the Tabulated EOS. The peak impact force of proposed ice model at the target surface was measured as 18044 *N* (4057 lb_S), while the solid ice damage model with the Tabulated EOS calculated the impact force as 15369 *N* (3455 lb_S). As shown in Fig. 5.11, the discrepancy in impact force between two damage model was decreased to compare with the slowest impact scenario (~17%), yet the difference was still considerable. The impact time window was reduced corresponding to the impact velocity.

Throughout the sequence of analyses, the overall conclusion was the similitude between two distinctively different high speed ice impact damage models. Although the complexity of fluidic ice damage model and input parameters is significant less than that of the constitutive solid ice damage model, both the qualitative and the quantitative result were not considerably different from each other especially. This is caused by the fluidization of ice projectile at high speed impact at higher strength target surface, which is similar to the soft body impact. As an example, the qualitative result of the fluidic ice damage model is presented in Fig 5.12 and that of the solid ice damage model is presented in Fig. **Error! Reference source not found.**.

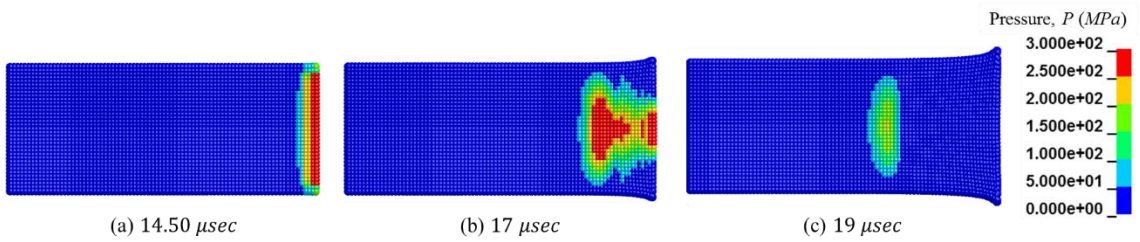

Figure 5.12 Sequence of shockwave propagation through ice projectile during the initial impact

The sequence of pictures shown above resembles with the damage mechanics of the soft body projectile shown in Fig. 2.12 in section 2.2. This implies that damage evolution similar to the bird impact can be expected especially when the mechanical strength of the projectile is weak, such as ice. Considering the impact surface is steel, the Hugoniot shock pressure (P_H) is analytically derived as 400 *MPa* when the initial contact occurs. As expected, the fluidic damage model assessed the initial shock pressure as 403 *MPa*. As the shock travels through the projectile, the peak pressure progressively decayed out, though the pressure was still well exceeding of the mechanical strength of ice and disintegrated the ice projectile into a group of particles. On the other hand, the peak pressure was calculated as 68.5 *MPa* and it swept throughout the entire projectile without any

reduction of the stress. This unique prediction was prompted since both the material definition of the solid ice damage model and the Tabulated EOS forced the peak pressure to be clipped off.

5.2.3 Model Validation

For the computational model validation, two ice damage models were compared to the physical experiment. Currently existing publications do not provide both qualitative and quantitative data thoroughly. Hence, the validation of proposed computational models was mainly referred by the work done by Pereira et al. [129]. Figure 5.13 shows a force-time history based on one such experiment with ice impacting the target at 213.36 *m/s*. All other the impact velocity scenarios are discussed in Appendix-A. In the experiment, a unique modal response was observed, which was not represented in the simulation. The oscillation had a period of 0.16 *ms* approximately, which is equivalent to frequency of 6250 *Hz*. According to the document, the experimental results included three unique resonance frequencies at approximately 4,400, 6,500, and 13,000 *Hz* [129].

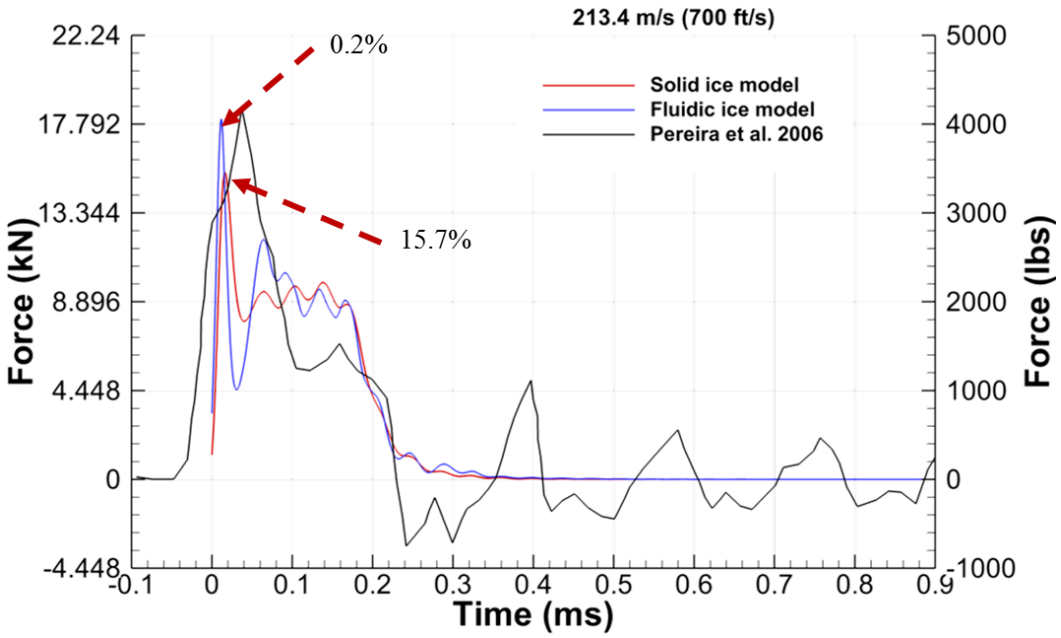

Figure 5.13 Force-time history for both computational models and comparison to the experiment [129] **(*V*=213.4 *m/s*)**

This implied that one of the modal responses of the test rig (6250 *Hz*) was blended into the force time result. According to the experimental result, the peak force was observed approximately 18237 *N* (4100 lb_S). The proposed (fluidic) ice damage model calculated the initial impact force as 18015 *N* (4050 lb_S) which was 0.2 % while the solid ice damage model predicted around 15370 *N*

(3455 lb_S) and the percent error was 15.7 %. To validate the simulation data with experimental results, impulse (I) was analytically calculated using Eq. (62). Based on the test setup (m= 9.0413 g and V= 213.36 m/s), the momentum of the projectile was calculated to be 1.92 $N{\cdot}s$. By integrating force over time in the computational analysis, the impulse on the target surface was found to be 1.911 $N{\cdot}s$ for the fluidic ice damage model, which has only 0.5% error when compared to the physical experiment. The impulse of the conventional ice damage model also evaluated as 1.90 $N{\cdot}s$.

In addition to the quantitative comparison, the simulation result was compared with the experiment and presented in Fig. 5.14. Both figures show the same stages, before the initial contact with target surface (a), the shock propagation and fragmentation (b), nonlinear contact area development and steady state loading phase (c), and the completion of impact (d). Before the impact occurs (1-(a)), the ice projectile is mostly intact and perfectly transparent. Due to the limited frames, the progressive damage evolution along the ice projectile was not provided, though the projectile became opaque after the shockwave swept through and disintegrated the projectile (2-(a)). Due to the projectile's momentum, the ice fragments continuously traveled toward the target surface which induces the stagnation pressure at the interface. Also the contact area between the projectile and target grew radially (3-(a)). The projectile is completely destroyed and the fragments are dispersed from the target surface (4-(a)).

Summarizing the sequence of analyses, the material definition of ice did not influence both the peak force magnitude and steady-state response significantly according to Appendix-A. However, the force time response was significantly changed by implementing two different EOSs, since the shock response of projectile upon impact is defined by the state variable calculated by EOS. The difference mainly caused by the lack of understanding the ice.

Hence, a proper selection of suitable EOS and material definition is necessary for the high fidelity damage assessment of FOI into a propulsion system. In recent research, the shock pressure of conventional solid ice damage model with the Tabulated EOS was governed by purely empirical observation as discussed previously. Therefore, the material properties at the regime beyond the investigation is either clipped off or extrapolated with a set of numerical correlation developed based on experiments which still required many assumptions. In contrast, the fluidic ice damage model with Gruneisen EOS does not require these empirical parameters, and predicted more reasonable shock dynamics including the magnitude of Hugoniot shock and pressure dissipation as the shock propagated. Considering the motivation of proposed ice damage modeling methodology, further comprehensive FOI analysis was developed based on the fluidic ice damage model with Gruneisen EOS.

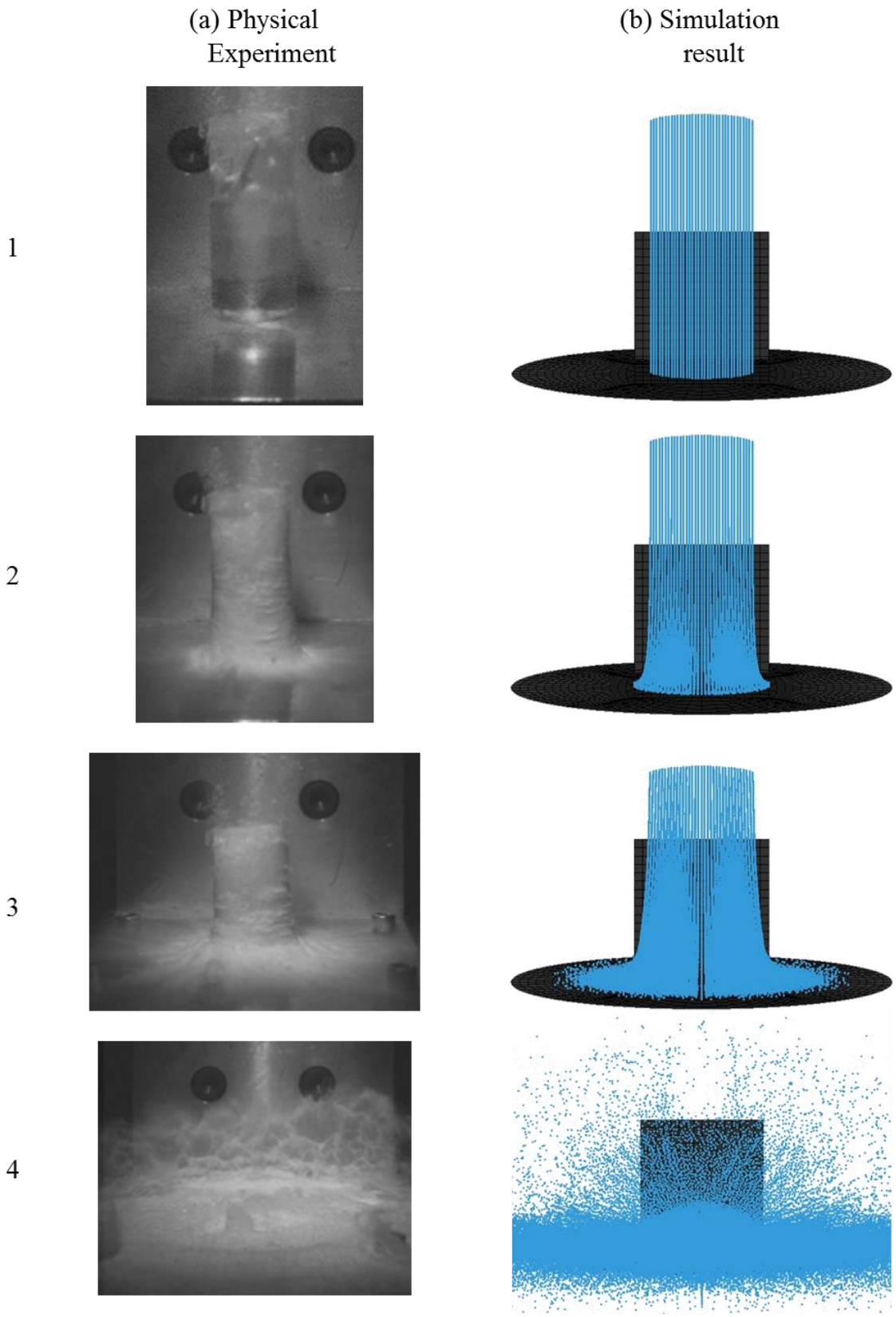

Figure 5.14 Qualitative comparison of ice impact scenario between (a) physical experiment [129] **and (b) fluidic ice damage model**

The motivation of this section is to introduce a new, significantly less intricate ice damage model developed through this studies. Not only the reduced complexity, but also the improved damage prediction help enhance the fidelity of the traditional damage predictions. By revisiting the damage mechanics of soft body projectiles such as bird, a new hypothesis to be used for ice impact scenarios was developed. This hypothesis and its subsequent numerical representation developed was thoroughly investigated by comparing it with existing models, as well as physical experiments. It was shown that the new fluidic ice damage model can assess the damage caused by a high speed ice impact with higher accuracy, contributing to future aerospace propulsion and structural design.

5.3 Composite Model

5.3.1 2-D Composite Damage Modeling for Fan Blade

In order to verify the 2-D composite damage modeling methodology, which is implemented to model the composite fan blade for FOI analysis, a composite coupon tension experiment was conducted. Composite strips were subjected to tensile loading using an Instron machine at Virginia Tech, which can apply up to 50 *kN* referring to the ASTM standard D4018-99 [130]. All the test articles were 0.308 *m* in length and 0.0254 *m* in width, and it was composed of 4 plies with the orientation of $[0/90]_S$. To comply with the tensile loading experiment standard, the specimens were required to be trimmed into a dog bone shape. However, in this experiment, the original specimen shape was used without modification, since any cutting or additional treat on the specimen might cause unexpected matrix (resin) deterioration. Figure 5.15 shows one of the composite test samples used in the experiment.

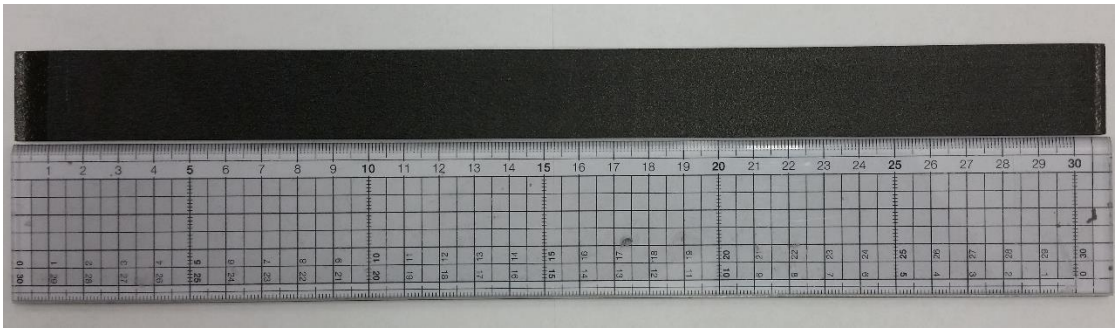

Figure 5.15 Composite strip used in the experiment

Since the original geometry of sample specimen was used without any modification and the material strength of the composite material, applying a tensile load was challenging since it slipped during the experiment. The first composite sample slipped during the experiment. However, the specimens were also required to avoid extremely high pressure at the grip, since it could cause damage on the matrix or fiber and the catastrophic failure at the vise than the composite specimen center. By sacrificing the first sample, an alternative mounting method was used to hold the specimen firmly. As a solution, all the composite specimens were vised with an 80 grit sandpaper in order to prevent any slipping during the experiment as shown in Fig. 5.16. Based on the test standard recommended by ASTM, four samples were subjected to a quasi-static load with a displacement rate of 2 *mm/min*.

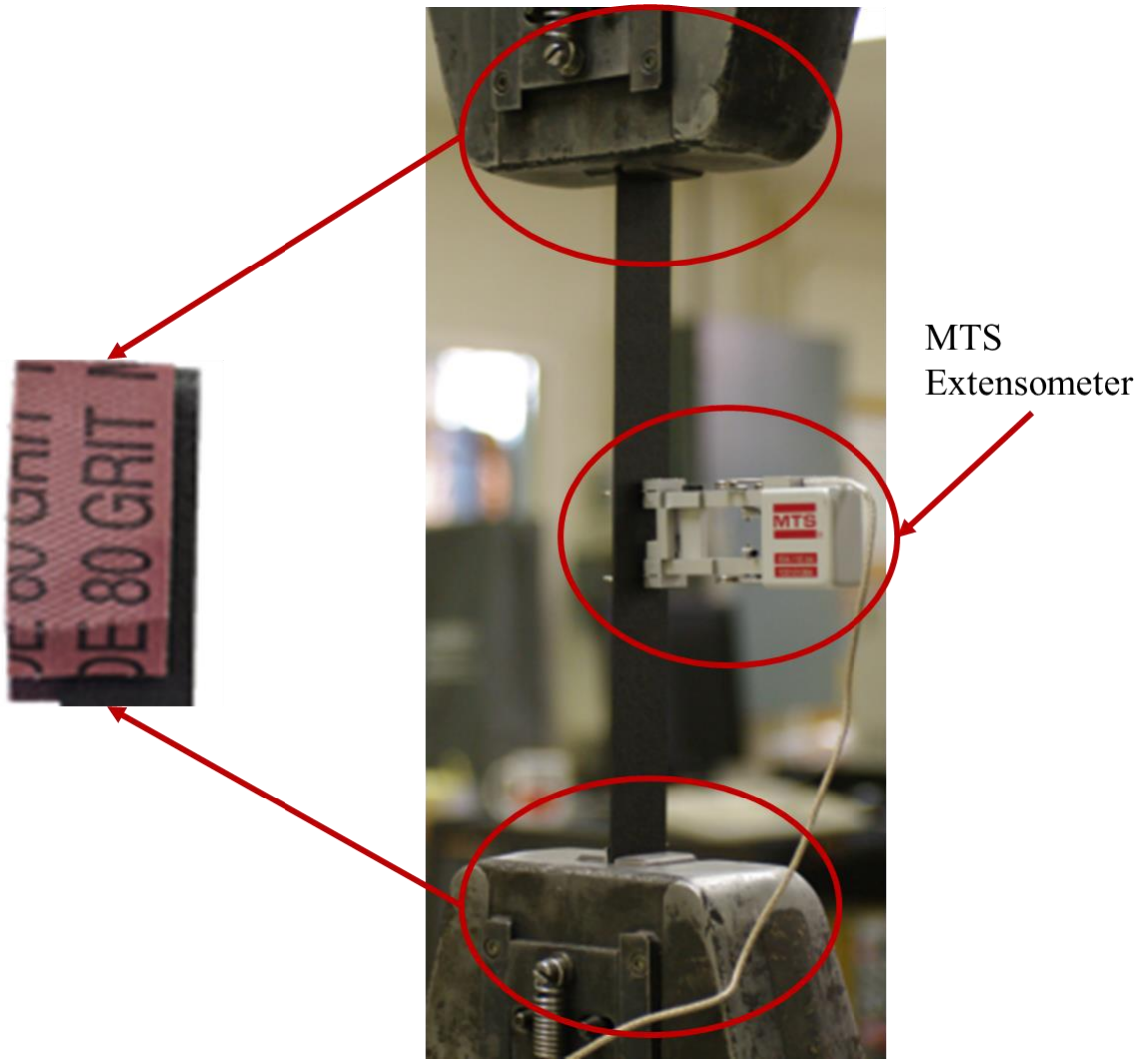

Figure 5.16 Setup for tensile experiment using Instron machine. An extensometer is mounted on composite specimen vised with 80 grit sandpaper

Because of the deflection of the cross member of the Instron machine under such high load, a precise displacement was not feasible to measure using the load cell displacement. To measure the displacement, an extensometer was mounted near the center of composite to measure the deformation throughout the experiment as shown in Fig. 5.16. The result of five composite loading experiments is presented in Fig. 5.17. As previously discussed, the failure of experiment was plotted as Test 1. The loading was successfully applied on specimen to 600 *MPa* before the specimen started to slip. The other test articles were successfully elongated up to 0.012 of the average strain.

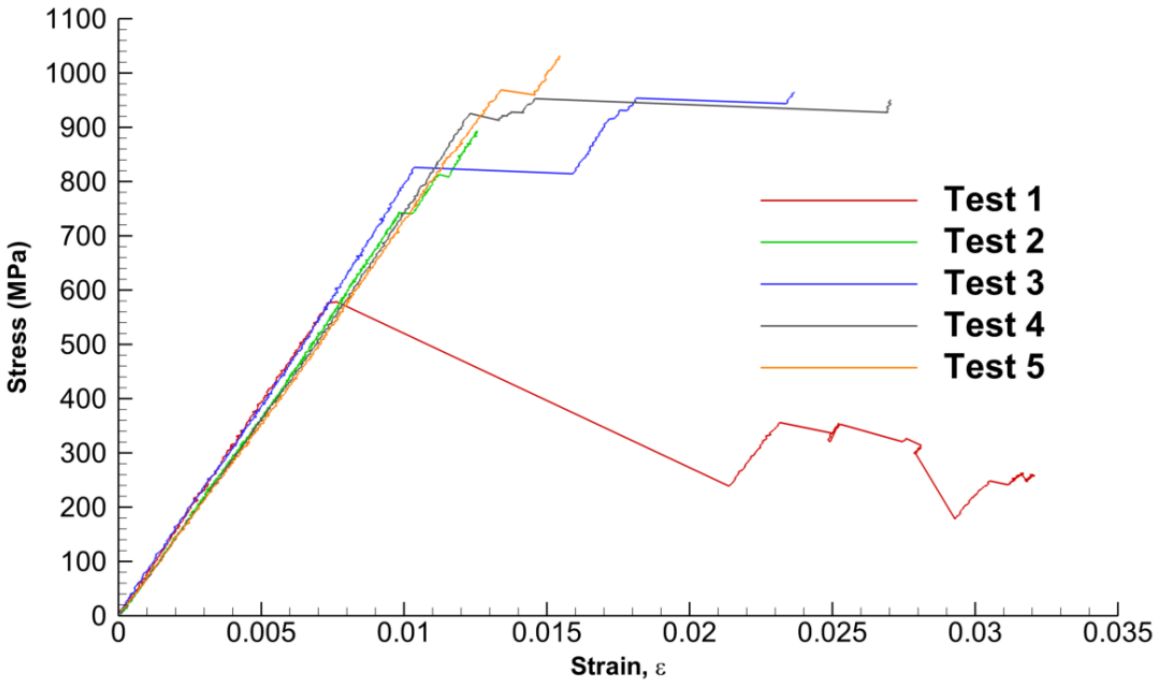

Figure 5.17 Stress vs. strain response of composite specimens under uni-axial tensile loading test

As shown in Table 5-6, the average effective modulus of the specimen was calculated as 76.24 *GPa* and yield strength of 859.1 *MPa* throughout the experiment. The standard deviations for each result were 2.18 *GPa* and 103.9 *MPa*, respectively. Including the first experiment, the young's modulus (*E*) was very consistent throughout the test. However, the yield stress of each material was slightly inconsistent.

Even excluding the Test 1 case, the Test 2 sample was extremely underperformed to compare with the other samples. It might be caused by an imperfection when the sample was fabricated. The experimental result was used to compare with the simulation result in order to verify the composite

shell modeling methodology which is equally used for the composite fan blade on the propulsion system.

Table 5-6 Stress-strain responses of graphite composite tension test

	Modulus, *E* (*GPa*)	**Yield Stress, σ (*MPa*)**
Test 1	78.20	N/A
Test 2	75.58	734.7
Test 3	78.67	815.6
Test 4	75.28	921.2
Test 5	73.44	964.7
Average	76.24	859.1*

(* Does not include Test 1)

Using the experimental setup, a corresponding computational model was developed to verify the composite damage modeling methodology which is later implemented to define the composite fan blade. To simulate the stress-strain response of composite under tensile loading, the Chang-Chang damage criterion was selected as discussed in section 3.2. Considering the boundary condition of the tensile loading experiment, all nodes at the bottom of element were fixed (*x*, *y*, *z*, *Rx*, *Ry*, *Rz* =0) as shown in Fig. 5.18.

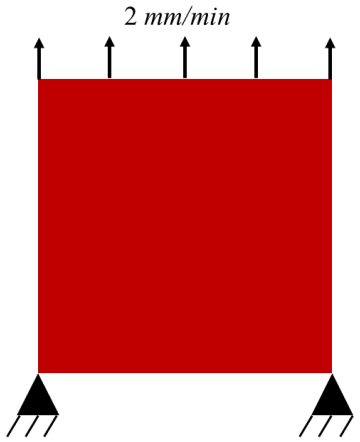

Figure 5.18 Schematic diagram of tensile loading simulation with fixed boundary condition and the same loading case

Not only the fixed boundary condition, but the same amount of quasi-static loading, which was used in the experiment, was also applied at the top of the element. The element was generated using fully-integrated 4-noded quadrilateral element to prevent a zero-energy mode deformation. Also, the finite element model had $[0/90]_S$ stacking sequence with a set of typical graphite fiber reinforced polymer material definition provided [31]. The tensile loading simulation was conducted

using both shell and solid element formulations. The stress-strain response of each element formulation is plotted in Fig. 5.19.

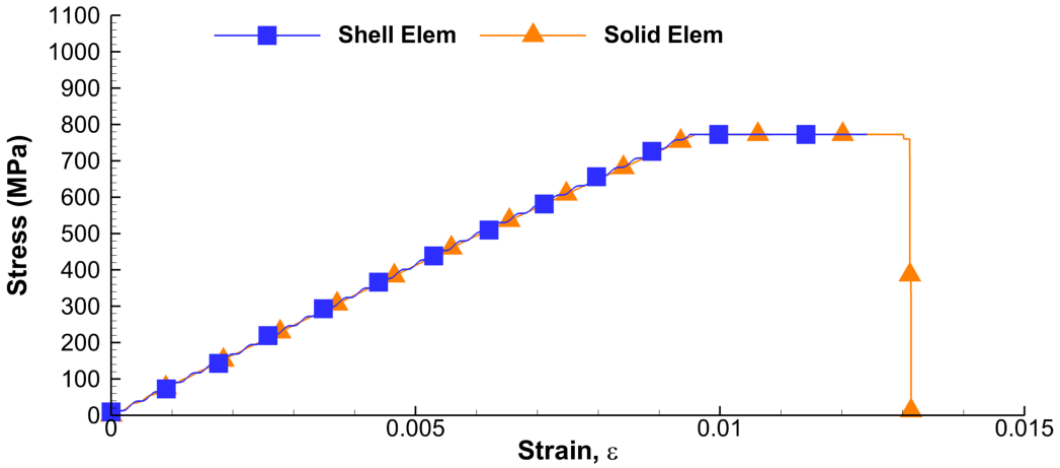

Figure 5.19 Stress vs. strain response of virtual composite specimens under uni-axial tensile loading simulation for both shell and solid element

Table 5-7 tabulates the stress-strain response of averaged experimental results and simulation results. In general, the simulation result was correlated well in terms of both young's modulus and yield stress. The shell element slightly over predicted the young's modulus about 6.3% and the solid element was 4.4%. The yield strength of both element formulation was off by approximately 11%, which is moderately high.

Table 5-7 Comparison between the physical experiments and computational analyses using two element formulations (shell and solid)

	Modulus, *E* (*GPa*)	**Yield Stress, *σ* (*MPa*)**
Shell	81.40	765.8
Solid	79.77	797.7
Avg. Exp.	76.24	859.1

Although such noticeable discrepancy, the composite damage model was considered to be acceptable since the material definition was defined based on the generic properties of each ply provided by textbook [31] rather than the lumped properties of four ply laminate properties evaluated using the classic laminate theory (CLT). Hence the composite damage modeling methodology was successfully evaluated, it was then implemented to assign the stress-strain response and damage prediction for the composite fan blade subjected to the FOI.

5.3.2 3-D Composite Damage Modeling for Casing design

Even though the 2-D composite damage modeling methodology is robust in terms of accuracy and computational expense, it is impossible to characterize the through-thickness damage mechanics. Therefore, a 3-D composite damage model was investigated in order to develop and verify the mesoscale soft casing modeling methodology as discussed in Fig. 3.3. After the methodology was developed, nineteen plies of Kevlar® 29 were subjected to a 146 m/s impact by a hemispherical nose-shaped projectile as shown in Fig. 5.20.

To minimize the computational expense, a quarter-symmetric modeling methodology is used. The details of the experimental setup and result are thoroughly discussed in the experimental work by Gower et al. [32].

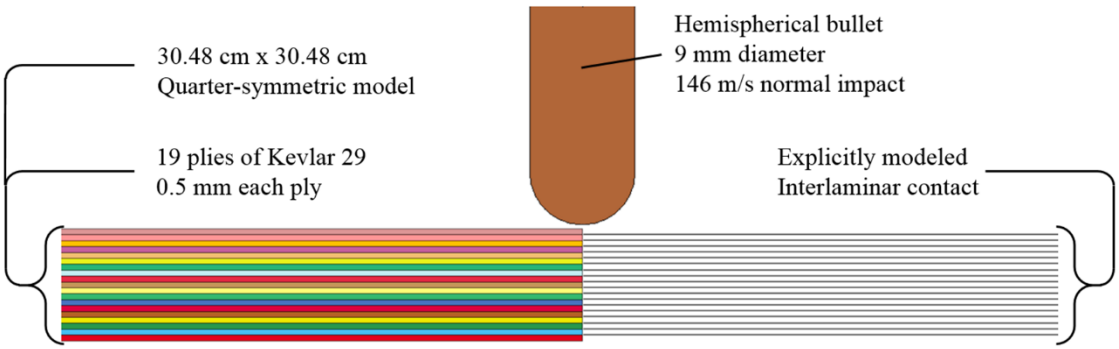

Figure 5.20 Schematic view of high speed (146 m/s) projectile impact on 19 ply Kevlar® simulation corresponding with the experiment conducted by Gower et al. [32]

The dynamic damage evolution and corresponding delamination of the plies is demonstrated in Fig. 5.21. Four instances are sequentially provided to understand four stages of projectile arrest involving lamina damage initiation and evolution as well as delamination. From these sequential shots, it was observed that the plies were initially deformed corresponding with the impactor tip shape in Fig. 5.21-(a). Kinetic energy of the projectile was then transformed into a shockwave and the shockwave propagated along the Kevlar® plies initiating deformation of the continuum and delamination, which is represented as red, near the impact regime. Because of the time required for the shock to propagate through the thickness direction, the delamination at the top surface is slightly more extended that at the bottom surface

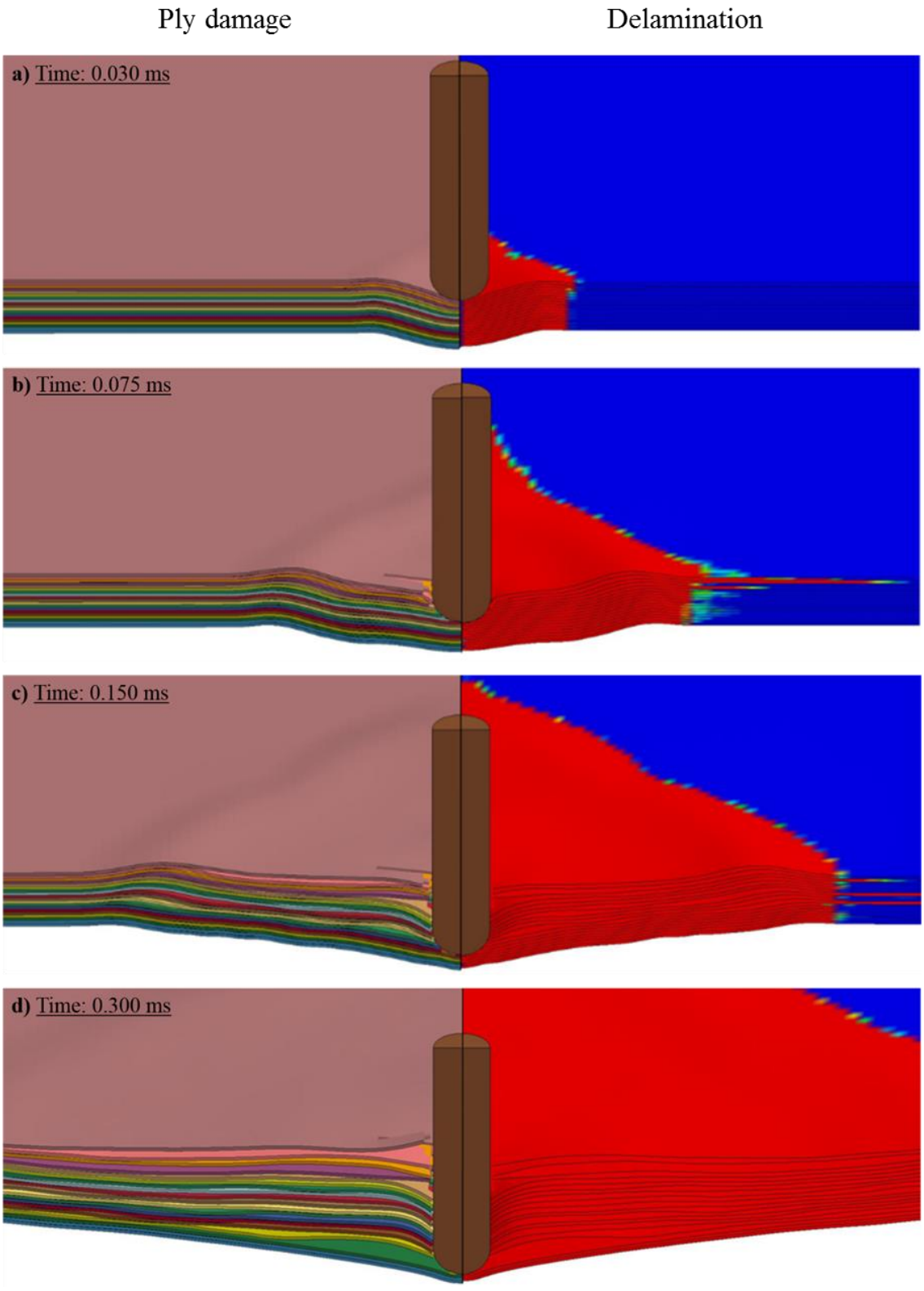

Figure 5.21 Progressive damage evolution of Kevlar® (on the left) and delamination propagation at each ply interface (on the right). Blue represents intact interface and red implies fully separated interface

The ply continuum damage progressively developed as the time elapsed. The stress near the impact regime was well in excess of material strengths and caused a failure as shown in 5.21-(b), In this moment, almost instantaneous failure in multiple plies was observed which allowed the projectile to advance through the composite laminate. As seen, this initial failure was caused by the shear stress caused by localized high speed loading due to the projectile rather than the tensile failure. While the projectile was damaging the ply and pushing the following laminas, its kinetic energy was dissipated which resulted in significant reduction of projectile speed. The pushing phenomenon caused a sudden extreme delamination between top two laminas and the rest of plies.

Continuously, the bullet had penetrated through more plies as shown in Fig. 5.21-(c), At this stage, the ply failure was prompted by exceeding the tensile stress of the composite as opposed to the shear stress, which was the predominant failure mechanism previously. This tensile driven failure mode contributed more kinetic energy absorption to compare with the shear driven ply failure. As well as the energy absorption caused by ply deformation, the delamination was consistently propagated to dissipate additional kinetic energy from the projectile. Finally, in Fig. 5.21-(d), the projectile was fully arrested, therefore there was no further penetration observed. Before the projectile came to a complete stop, the residual energy of both projectile and laminate pushed the bottom few laminas backward. As observed, the area of delamination continued to evolve due to the relative motion of the plies instead of the projectile motion. Another important phenomenon was fiber wrapping around the projectile. Because of this wrapping, the friction between the projectile and Kevlar® assisted in the projectile arrest.

Figure 5.22-(a) shows the backface displacement of the simulation for the three different failure methods, which are the 3-D orthotropic damage model, Chang-Chang and Tsai-Wu, as well as the experimental result. Chang-Chang composite damage model successfully arrested the projectile as the experiment stated, though the damage model over predicted the back face displacement. As discussed in section 3.2, Tsai-Wu anisotropic damage model predicted more conservative result than the Chang-Chang. As a result, both damage models were overly predicted the back face displacement even though they successfully arrested the projectile. The 3-D anisotropic model matched the experimental result with the highest level of similarity, because the damage model includes progressive softening effect of composite laminate corresponding with the damage evolution of the plate as well as the through-thickness damage degradation, Hence, the virtual composite laminate becomes relatively more ductile to compare with the other models, which helps to arrest the projectile with similar back face displacement to the experimental result.

A primary difference between the experiment and each of the computational results was the initial rate of backface deflection and post damage response of Kevlar® laminate. The rate of

backface deflection was slightly under predicted to compare with the experiment. After the projectile was fully arrested and the laminate began the unloading phase, the laminate in computational domain elastically responded which caused a slight decrease in backface displacement. In the physical experiment the backface displacement was almost steady state since there was no significant residual strength of material in the damaged specimen.

Figure 5.22-(b) shows the energy distribution between the projectile, Kevlar®, and external dissipation up to the full arrest of the impactor. According to this plot, the total energy of the entire simulation domain was conserved. It is not exclusively included in the plot, but the projectile kinetic energy was converged to zero when it was fully arrested. Based on the observation, the majority of initial projectile kinetic energy (~89%) was dissipated through both the internal (laminate deformation) and delamination energy. The delamination mechanics is an important since it is one of the ways to dissipate the initial kinetic energy. The distinctive composite damage mechanics was investigated by several researchers. Work done by Iremonger et al. and by Lee et al. emphasized the importance of delamination area in projectile arrest [131,132]. The remaining energy is transformed into the friction between the projectile and laminate. These relative percentages of absorbed energy closely match analytical predictions by Naik et al.[133].

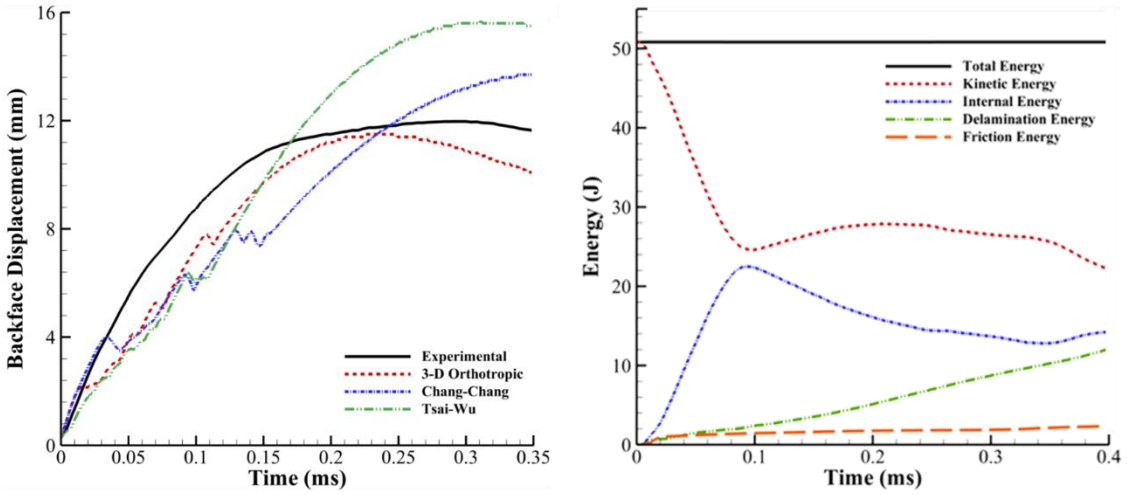

(a) Back face displacement (b) Delamination

Figure 5.22 Comparison of backface displacement versus time for the selected failure methodologies (a), and the energy distribution over the entire simulation domain

Further investigations concerning model verification, mesh study, and additional validations are provided in Appendix-B. Even though the rate of deflection was under predicted, the maximum backface displacement was substantially close to the experimental result. In addition to the quantitative similitude, the simulation result successfully predicted the sequence of damage

evolution upon the high speed impact. As a result, many failure modes, such as a shear driven ply failure near the impact regime, delamination, and tensile lamina failure, were identified during the impact incident

In accordance with the structural design of modern high-bypass propulsion system, both 2-D and 3-D composite damage modeling were selected. In order to reduce the computational expense, the advanced fan blades were developed using 2-D composite damage model, because the through the thickness damage prediction was not the primary concern during FOI incident. On the other hand, 3-D damage model was employed to design the casing to capture the through-thickness damage progression upon FBO incident.

6 Comprehensive Damage Investigation for Soft Body FOI into a High-Bypass Propulsion System

As discussed, the propulsion model developed during this study was based on the contemporary fan blade design. Figure 6.1 shows the comparison between the real fan blade model [134], which is currently in service, and the virtual fan bladed which was created for the high fidelity damage analysis for FOI scenario. Figure 6.1-(b) depicts of the composite section of the fan blade. The advanced aerodynamic shape fan blade is also shown in Fig. 6.1-(c). The virtual fan blade was created with the height of 1 *m* and the distance from the rotational center to the fan blade tip (r_{tip}) was measured as 1.42 *m*. In order to comply with the modern fan blade design, the fan blade structure is made out of the combination of CFRP and titanium alloy foil around the edge of fan blade in order to prevent any deterioration of the composite section of fan blade by small object such as small pebbles on tarmac.

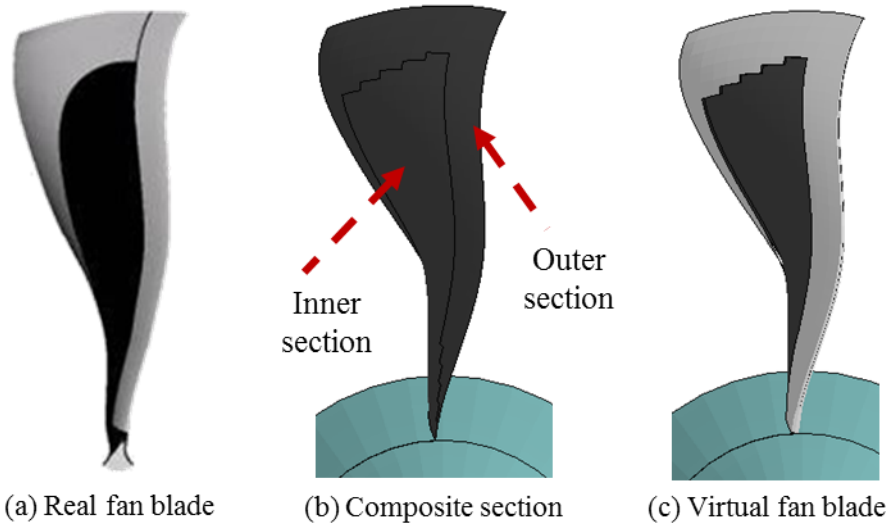

Figure 6.1 Comparison between the actual fan blade and the virtual fan blade; original model (a) [134]**, composite section of the virtual fan blade (b), and fully assembled virtual fan blade(c)**

For the composite section of fan blade, a unidirectional carbon fiber/epoxy (IM7/8551-7) is selected because of its relatively higher fiber stiffness, strength and damage tolerance compare with the others such as AS4 or other typical fibers [135]. The fiber volume fraction of composite laminate was assumed as 60% in the comprehensive analysis. The lay-up sequence of composite

section was preliminary developed as $[(90^{o}{}_{3}/0^{o})_{4}/90^{o}/0^{o}]_{S}$ which had total 36 plies, where the 90º is referring to the radial direction of fan blade.

However, the preliminary lay-up did not have a sufficient bending and shear resistance. Therefore, an alternative lay-up design was investigated. The alternative fan blade layup was selected based on the preceding research done by Miller et al. [69]. The fan blade was made out of two different stacking up sequences. One is used for the inner section fan blade where the majority of the radial stress is supported, and the other is used for the outer section of the fan blade as shown in Fig. 6.1-(b). For the FOI damage analysis, 50 plies were assigned for the inner section. For the outer perimeter of fan blade, 28 plies were used. In the front inlet section, eighteen fan blades were attached to the blade hub as shown in Fig. 6.2.

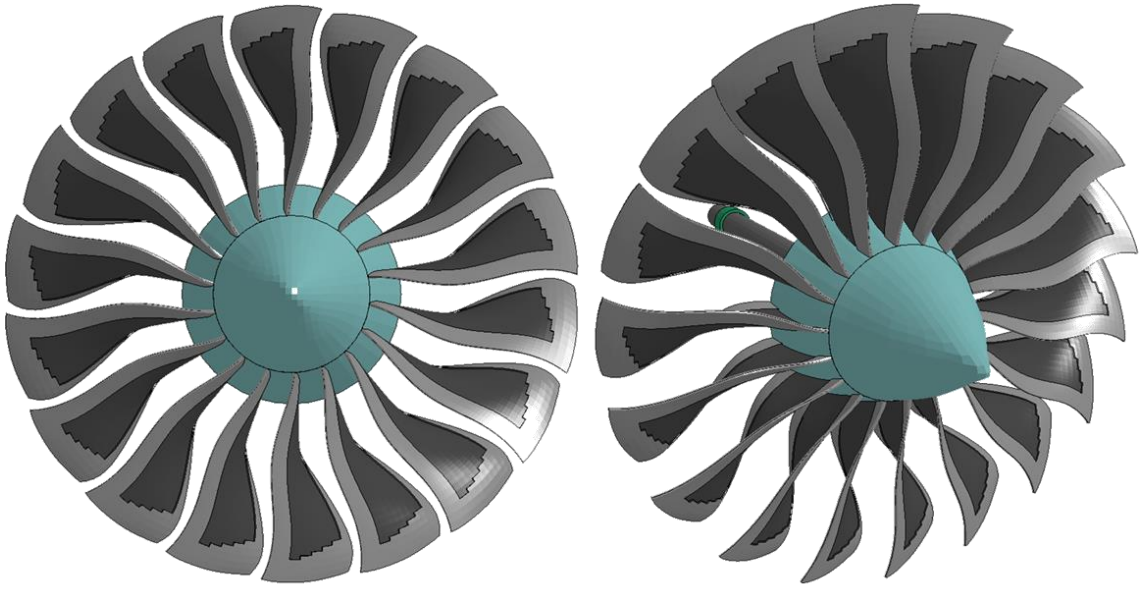

(a) Front view (b) Isometric view

Figure 6.2 Front inlet fan assembly of virtual high-bypass turbofan engine

In addition to the modern fan blade design, a low pressure compressor (LPC) was also developed and included in the detailed model to achieve a high fidelity numerical simulation. A four-stage LPC, with inlet guide vane (IGV), was designed to complement the model. Considering the rotational speed of the assembly, the J-C damage model was selected to model the compressor blades (rotor and stator) as well as the IGV.

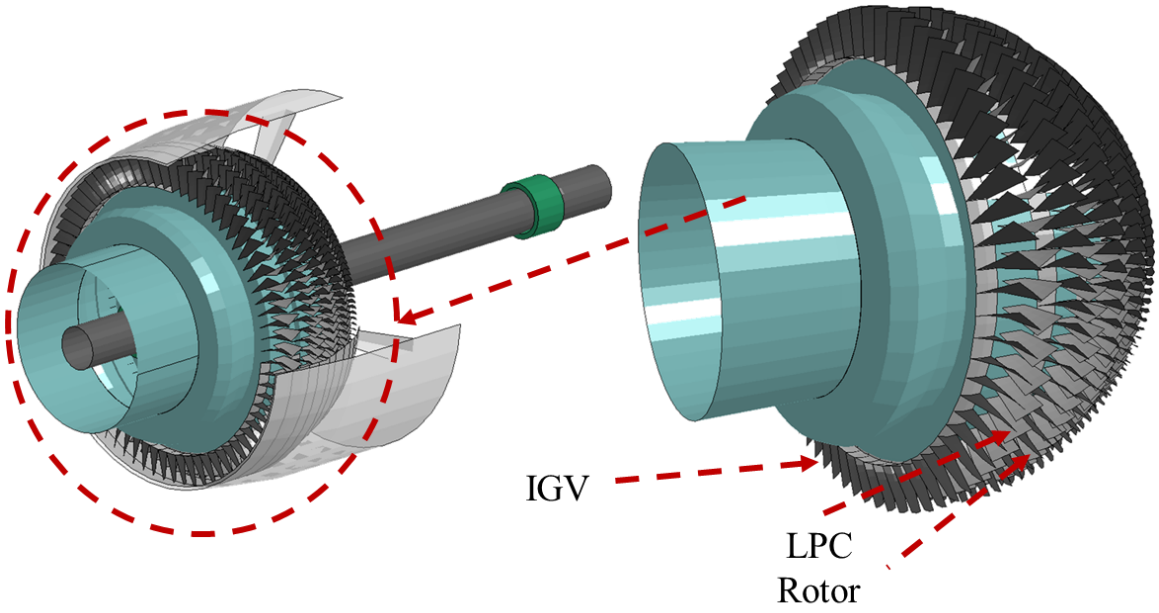

Figure 6.3 Isometric and side view of Low pressure compressor

After the front inlet section and LPC model were developed, they were assembled to the LPC drive shaft. The relative motion of the hub was directly connected to the deformable shaft for the comprehensive damage response of a propulsion system subject to FOI. To retain the rotational motion, the drive shaft had a three bearing system as shown in Fig. 6.4. By having two thrust bearings at the front and one ball bearing in the end, the translational motion of the assembly was restricted.

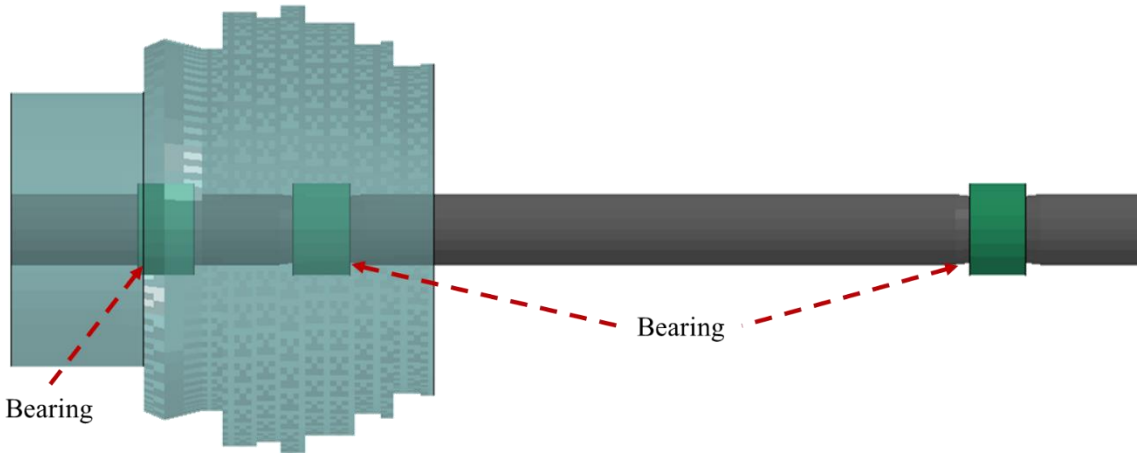

Figure 6.4 Blade hub, LPC rotor, and main shaft assembly with 3 bearings

The operating condition of the front fan assembly and LPC section was assumed to be rotating at approximately 2166 *rpm* (226.8 *rad/s*) [40,41]. A full assembly of the virtual propulsion system which includes the front inlet section, LPC, casing, shaft, and bearings is shown in Fig. 6.5.

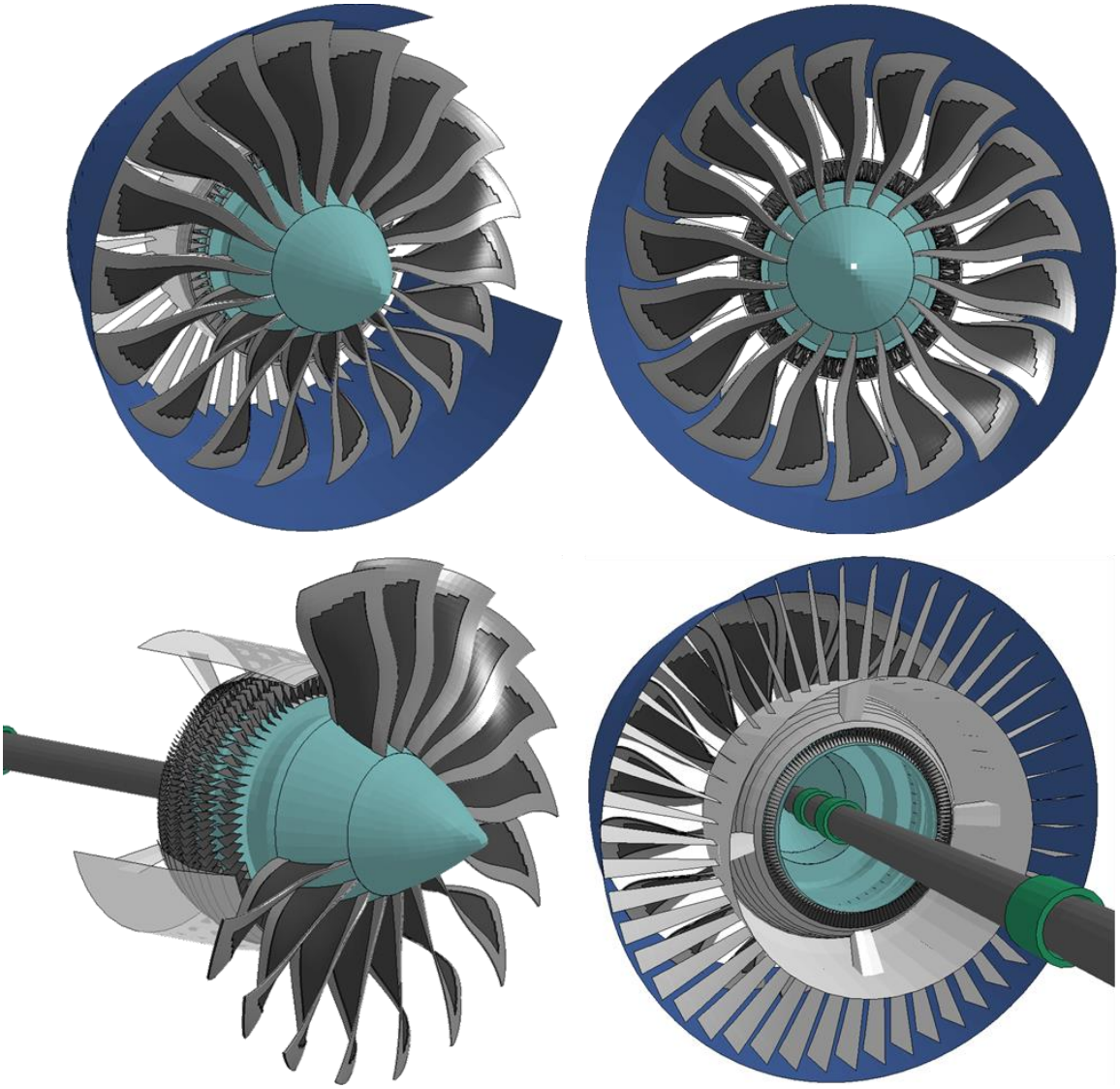

Figure 6.5 Isometric view, front view, cutaway side view, and back side view of virtual high-bypass turbofan engine

The casing, as discussed in section 2.1.4, was modeled to improve the simulation fidelity. Considering the fan blade impact speed when FBO occurs, the material of casing was defined as Al-6061 and implemented with the J-C damage model for the hard casing design. In order to minimize the computational expense, both shell and solid elements were used depending on the

interaction between the fan blades and casing. As shown in Fig. 6.6, solid elements were allocated where the fan blade could either contact or impact when FOI occurs. Later, the hybrid casing design will be discussed to compare the performance of damage arrestment and the weight of the hybrid casing against the conventional hard casing design.

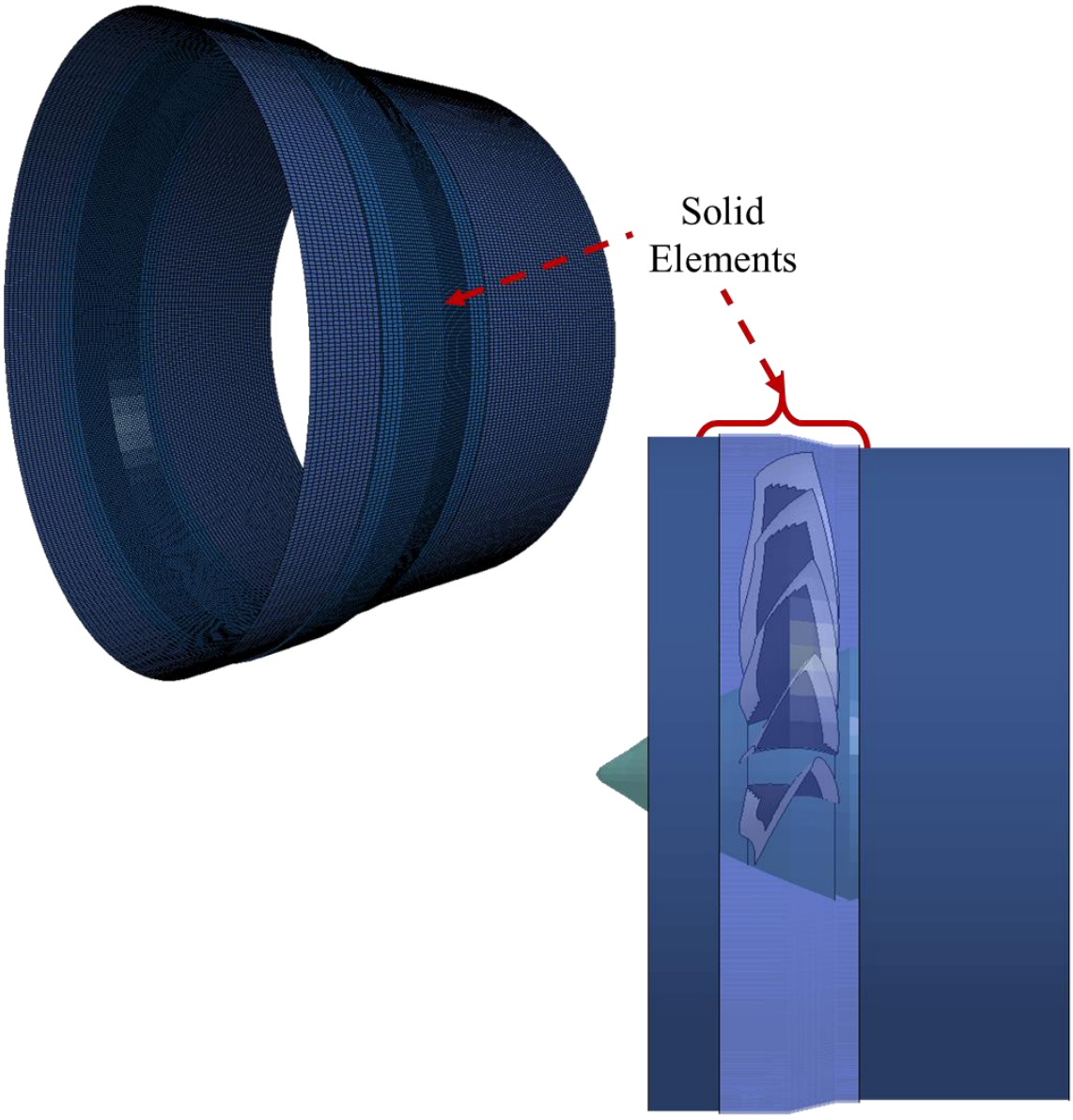

Figure 6.6. Computational model for fan casing using both shell and solid element formulations

6.1 Validation of Virtual Engine Model

Validation of the virtual model was required to ensure the accuracy of the simulation results. For the preliminary validation, the tangential velocity and blade root stress (σ_{root}) were analytically calculated and compared with the simulation results using a simple rectangular fan blade rotating at a constant speed. As discussed in Section 4.4, the stress initialization is essential to correctly calculate the centrifugal stress along the fan blade for a steady-state rotating object. Shown in Fig. 6.7, is a virtual fan blade with a simplified rectangular geometry for a validation with the analytical prediction. The fan blade material was Ti-6Al-4V and the rotational speed was set at 226.8 *rad/s*.

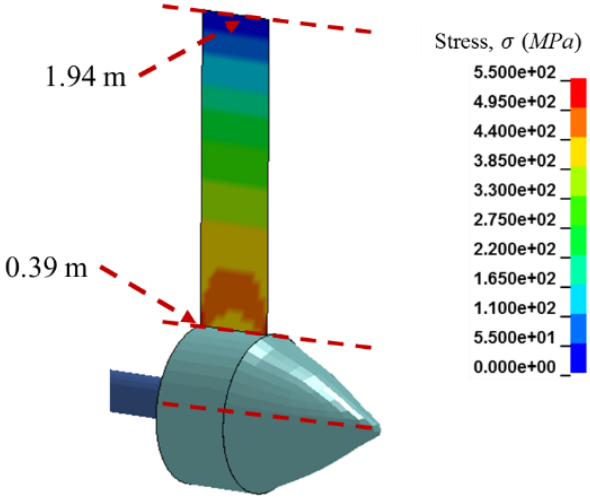

Figure 6.7 Stress distribution for simple fan blade rotating at a constant angular speed of *ω = 226.8 rad/s*

Based on the analytical stress evaluated using Eq. (3), the blade root stress was calculated at 411 *MPa* while the simulation result predicted approximately 415 *MPa*. This resulted only in 1 *%* error from the analytical calculation. In the computational model, the fan blade hub was modeled as rigid and the deformable fan blade was fixed to the hub. With this boundary condition, the Poisson's effect was restricted at both the leading edge and the trailing edge roots. Consequently, the blade root stress at both locations were calculated and found slightly (415 *MPa* vs 411 *MPa*) higher than the analytical solution.

After the analytical validation with simple case, the fan blade root stress was simulated using the actual geometry that was used for the further comprehensive damage investigation using the developed methodology. The height of the virtual fan blade was approximately 1 *m* and the radius of front inlet section of virtual propulsion system was 1.42 *m*. Considering the structural geometry,

the analytical tangential velocity was calculated to range from 90 *m/s* to 322 *m/s*. The simulated velocity was closely matched with the analytical calculation as shown in Fig. 6.8-(a).

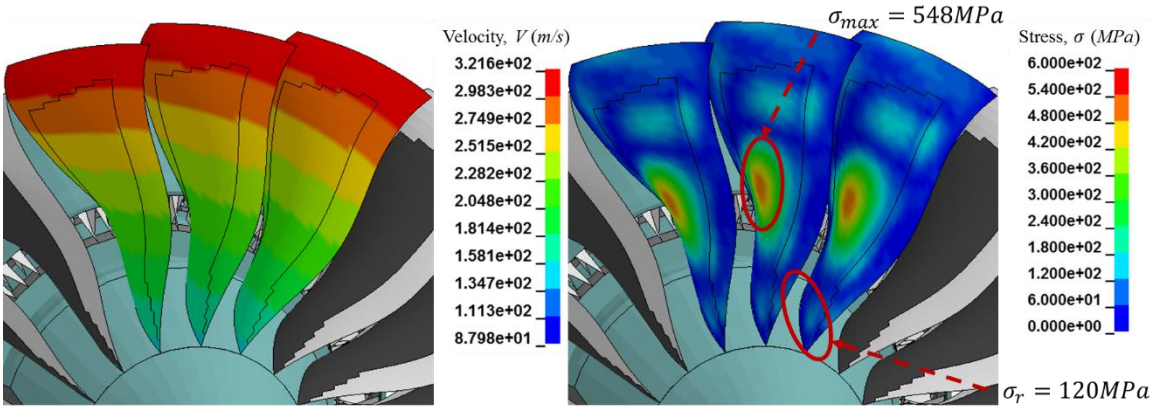

(a) Velocity magnitude (b) Averaged blade stress

Figure 6.8 Tangential velocity (a) and averaged stress among the entire plies (b) (*ω = 226.8 rad/s*)

The fan blade root stress was analytically calculated and compared against the computational result. To alleviate the stress fluctuation as discussed in section 4.6, the stress initialization was conducted for the entire rotating parts, including fan the blade assembly, LPC components, bearings and shaft, in advance of the comprehensive analysis.

Figure 6.8-(b) shows the maximum stress among the composite plies during the steady state rotational motion. The result was slightly different due to the orthotropic material for the fan blade. Some of the plies, which had fiber orientation along the radial direction, carried higher than the analytical prediction because of the stiffness of fiber. For the ply had the fiber orientation along the radial direction, the maximum root stress among the composite plies was measured approximately 227 *MPa*. By averaging among the entire plies, the averaged blade root stress on composite section was measured approximately 120 *MPa*, correlating well with the simplified analytical prediction.

Interestingly, the maximum stress was occurred at the center of the fan blade. At the center of fan blade, the maximum stress among the composite plies (through-thickness direction) was measured as high as 548 *MPa*, which was even five times greater than the blade root stress. The averaged stress of entire plies at the corresponding location was approximately 198 *MPa*. Such a sudden localized stress at the center of advanced aerodynamic fan blade has been reported in existing research, though both works were conducted using slightly different aerodynamic designs [136,137]. Considering the different geometry, the stress at the center of fan blade reported in the literature [137] was reasonably similar to the simulation result shown in Fig. 6.8. By overarching the projectile modeling methodologies and composite damage models, a comprehensive dynamic

damage response was simulated and damage mechanics of an advanced propulsion system subjected to FOI were assessed.

6.2 Bird Ingestion Scenario

The simulated impact scenario complied with the Federal Aviation Regulation (FAR) § 33.76. According to the regulation, the engine, which has the inlet throat area greater than 3.90 m^2, must sustain the structural integrity required for continuous thrust generation after ingesting a single large bird or flock of medium size bird (~1.15 *kg*) [8].

Based on the FAA regulation, the full scale FOI comprehensive simulation was generated using a single 2.5 *kg* bird at the ingestion speed of 330 *km/h* (92 *m/s*) which is equivalent to the take-off speed of a large size passenger aircraft. For the damage analyses, three different impact locations were selected; the blade root, 50% of the blade height (regulation requirement), and fan blade tip which are 0.3, 0.5 and 0.75 *m* from the fan blade root, respectively. Figure 6.9 depicts the simulation setups for three different ingestion scenarios.

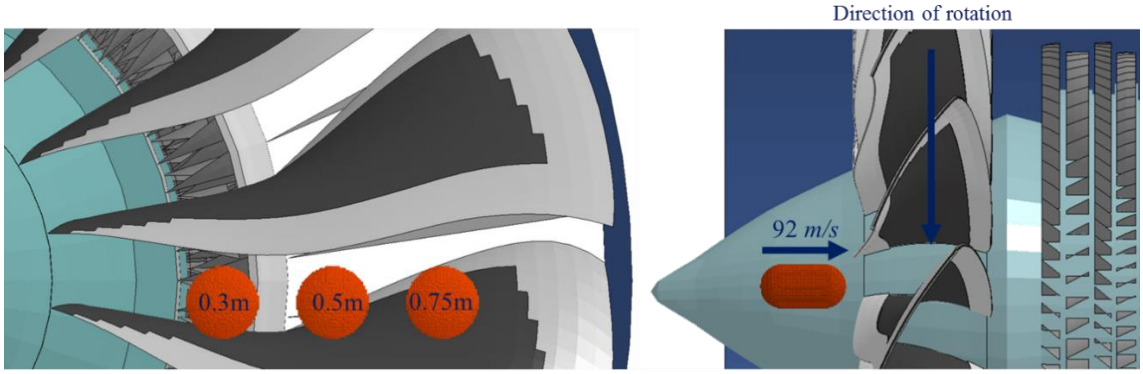

Figure 6.9 Simulation setup for the comprehensive FOI simulation Three impact locations (a) and bird ingestion condition (b)

6.2.1 Initial Contact and Damage Initiation

Figure 6.10 depicts the dynamic response of the propulsion system to bird ingestion. As shown in Fig. 6.10-(a), the initial contact between the bird and the target fan blade occurred near the root of the blade, just above the leading edge. While the stress distribution along the rest of the fan blade

diminished in the positive radial direction toward the blade tip, the target blade was subjected to a sudden shock loading due to the interaction near the impact area. The shock pressure then traveled along the leading edge, producing a high stress regime as shown in Fig. 6.10-(a). In addition to the shock loading, the blade root suffered from a large bending load because of the rotational inertia of target fan blade. Because of the inertia, the fan blade bent toward the rotational direction, which lead to occurrence of even greater stresses at the root near the impact regime. Because of the highly compressive loading at the impact location, the leading edge section was structurally damaged, yet the bending motion of fan blade was not severe enough to cause FBO.

At the point of initial impact, the lumped bird material was sliced by the first target fan blade (Fig. 6.10-(a)). Immediately after the initial contact, the back side (pressure side) of the adjacent fan blade impacted with the second half of the bird material. The bird interaction in this incident involved both a bisecting motion with the secondary target blade leading edge as well as a blunt impact with the rear face of the blade as shown in Fig. 6.10-(b). The remaining bird material continued to contact with the third target blade. Both first and second target blades interacted with relatively large portions of bird to compare with the third blade, however, the second fan blade was hit by bird most heavily.

The subjected fan blades sustained severe deformation and damage due to both impacts as shown in Fig. 6.10-(c). The figure shows a fan blade immediately after the initial loading and no significant damage is observed at this time. However, the damage progressively developed due to the continuous centrifugal motion of fan assembly and prompted the leading edge to eventually fail. As shown in Fig. 6.10-(d), some sections of the leading edge on the two blades has deteriorated, though no further damage evolution was observed after several rotations.

Even though no catastrophic structural failure was observed, wide spread fiber compressive failure was observed after the impact. Fiber tensile failure was also predicted at the root of two target blades. Complex damage (matrix tensile and compressive failure) was predicted near the impact interface. Overall, the comprehensive FOI damage assessment methodology predicted that a minor structural disintegration was predicted where a 2.5 *kg* impacted at 0.3 *m* at the blade root.

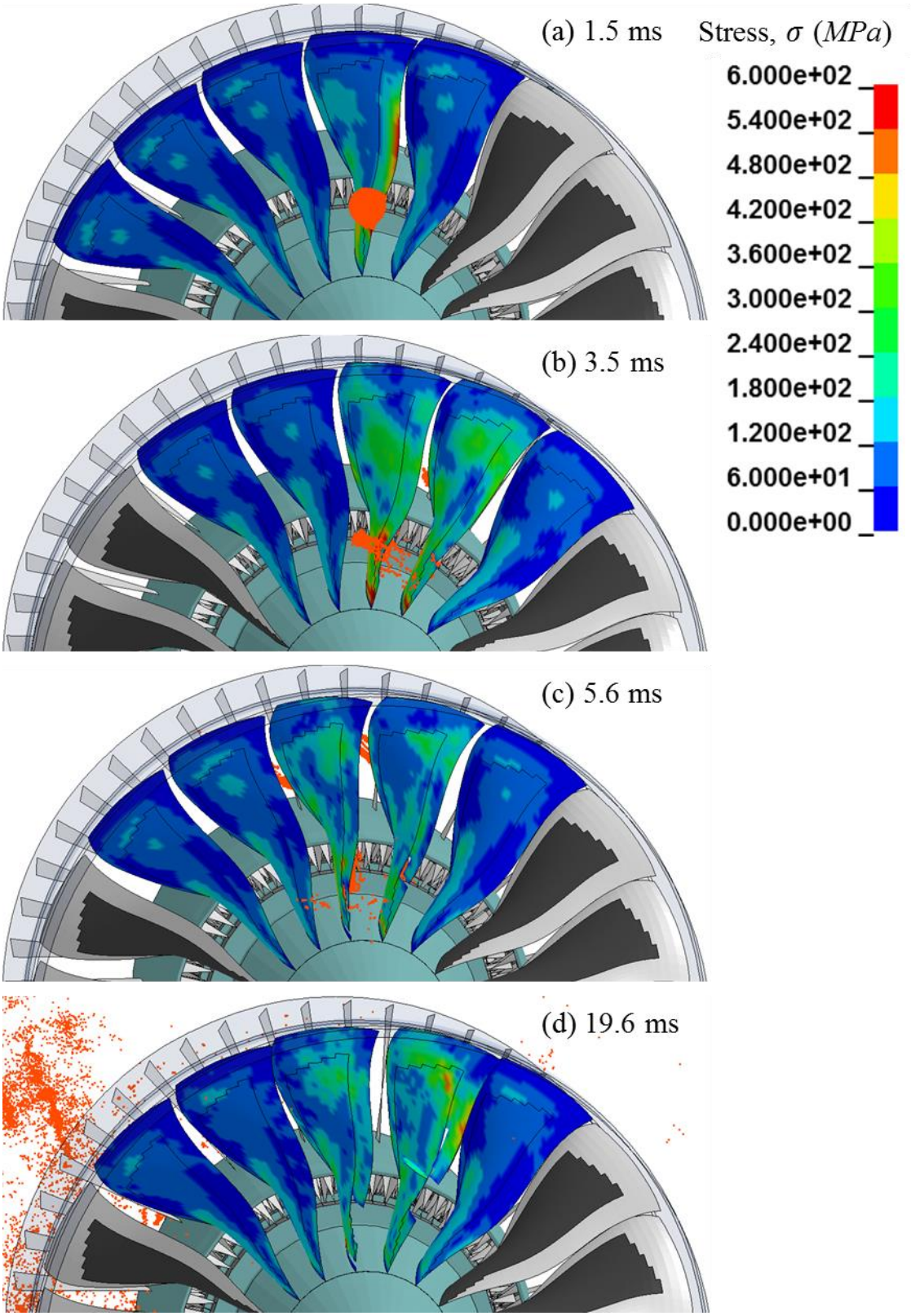

Figure 6.10 Sequence of von-Mises stress contour plots of propulsion system after bird ingestion at 0.3 *m* from the blade root. Screenshot rotated corresponding to target blades

The force-time history from the interaction between the bird and fan blades is presented in Fig. 6.11. As discussed, the bird was dissected into two major and one minor portion. According to the simulation results, the initial impact force on the first target blade peaked at 138 *kN* and the second target blade peaks force measured approximately 160 *kN* continuously. The impact window of the second fan blade was slightly longer than that of the first blade since the largest portion of bird contacted with the face of the second blade.

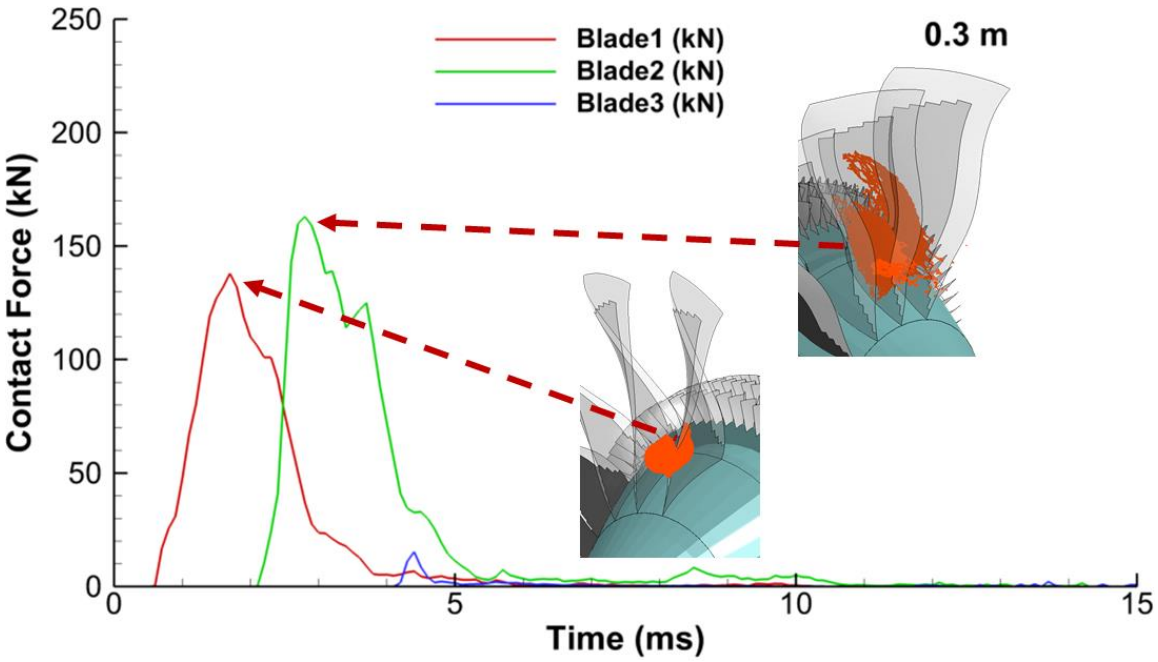

Figure 6.11 Force-time plots of the bird material impacted with multiple fan blades (at 0.3 *m*)

The impulse of this FOI scenario was calculated as 456 $N \cdot s$ considering the bird mass and relative velocity magnitude at the moment of impact. The impulse was normalized using the analytical calculation and shown in Fig. 6.12. The plot shows that approximately 47.1% of the bird material came into contact with the first blade, while 57.5% and 0.2% of the remaining contacted with the second and third impacting blades, respectively. From both force time history and normalized impulse plot, the second target blade is proven to be subjected to higher loading. Even through the similar magnitude of damage was observed for both impacted blades as shown in Fig. 6.10-(d), the bird only initiated a crack on the first blade but did not cause an immediate break. On the other hand, the heavier impact resulted in immediate fracture on the second impacted blade.

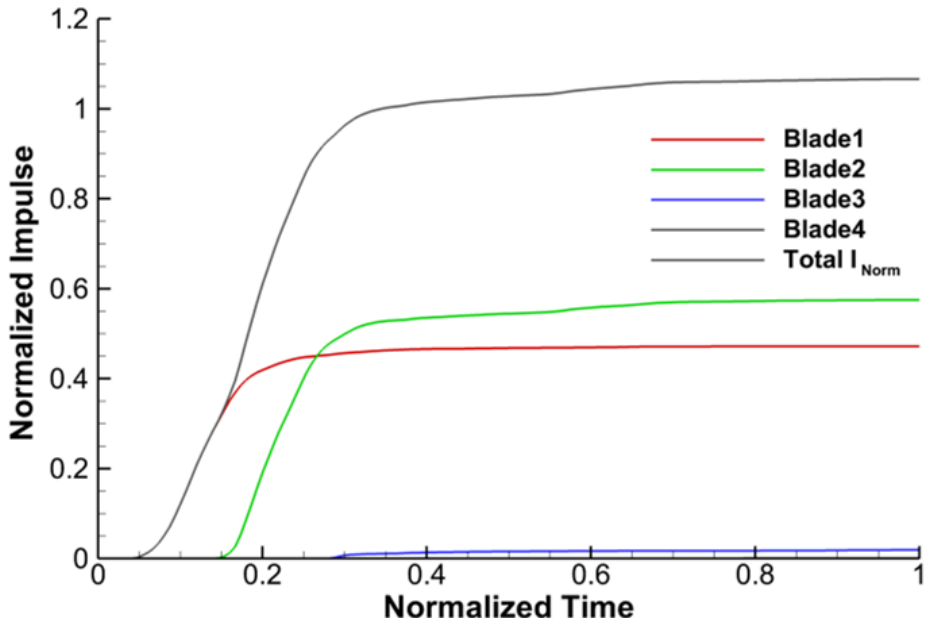

Figure 6.12 Normalized impulse of each impacted blades (0.3 *m*), The impulse is normalized based on analytical calculation ($I_{analytic}$=456 *N·s*)

Figure 6.13 shows the damage mechanics when the impact occurred at 50 % of blade height. The sequence of comprehensive von-Mises stress contour plots of the entire propulsion system is shown in section 0. In short, the damage mechanics predicted throughout the simulation resemble the previous impact scenario. As previously observed, the initial contact between the bird and the target fan blade induced a sudden shock loading at the impact area and traveled along the leading edge as shown in Fig. 6.13-(a). The bird and structure interaction continuously occurred with the following blade as seen in Fig 6.13-(b). The second blade, which suffered from the highest impact loading, was noticeably bent backward by the bird, subjecting it to an additional high stress at the blade root. Unlike to the previous scenario, the impact caused immediate fiber and matrix failure due to the compressive loading and damaged the entire leading edge of fan blade as observed in in Fig 6.13-(c).

After several rotations, the damaged leading edge section was completely detached from the main section of fan blade and the fragment was lodged between the adjacent fan blade and the casing (Fig 6.13-(d)). As observed in previous ingestion scenario, some of the bird material directly ingested to LPC section. Because of the distance from LPC to the impact location, a smaller amount of the bird material traveled into compressor to compare with the previous FOI scenario. Even though the amount of ingested debris was reduced, the result still implies the importance of the comprehensive damage methodology for FOI. Although one of the debris from the second fan blade caused severe damage on the adjacent fan blade, the entire fan assembly was able to maintain a continuous revolution.

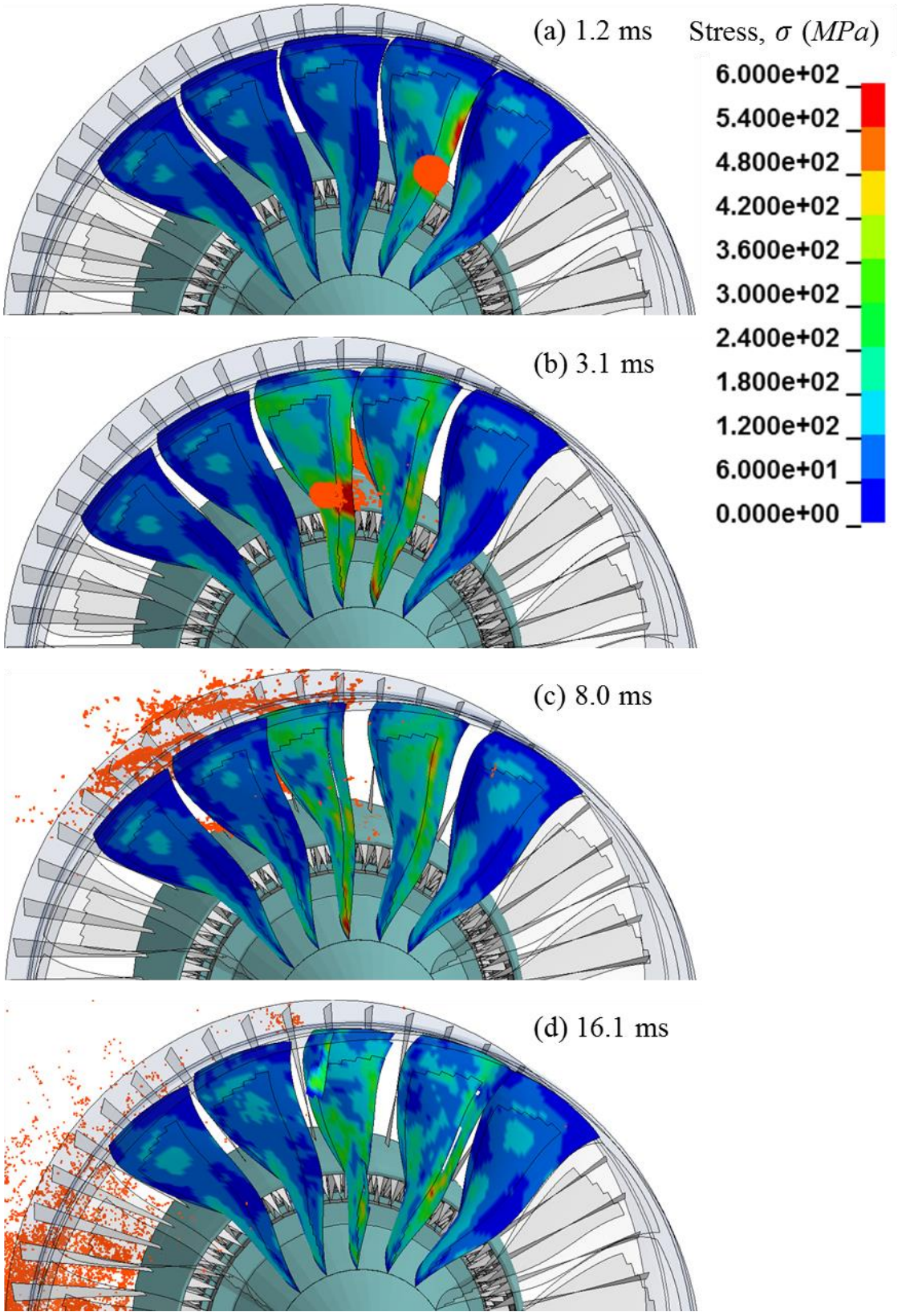

Figure 6.13 Sequence of von-Mises stress contour plots of propulsion system after bird ingestion at 0.5 *m* from the blade root. Screenshot revolved corresponding to target blades

The corresponding force-time history is presented in Fig. 6.14. Similar to the 0.3 *m* impact scenario, the bird interacted with three fan blades. The second fan blade was once again most heavily hit by the bird. Because of the fan blade fragmentation due to the interaction, the casing was also subjected to the impact. The mass of the fragmentation was 0.760 *kg* and the impact velocity was approximately 250 *m/s*. Because of the fragment size, the contact force was not high enough to penetrate the fan casing and the system was able to sustain continuous rotation.

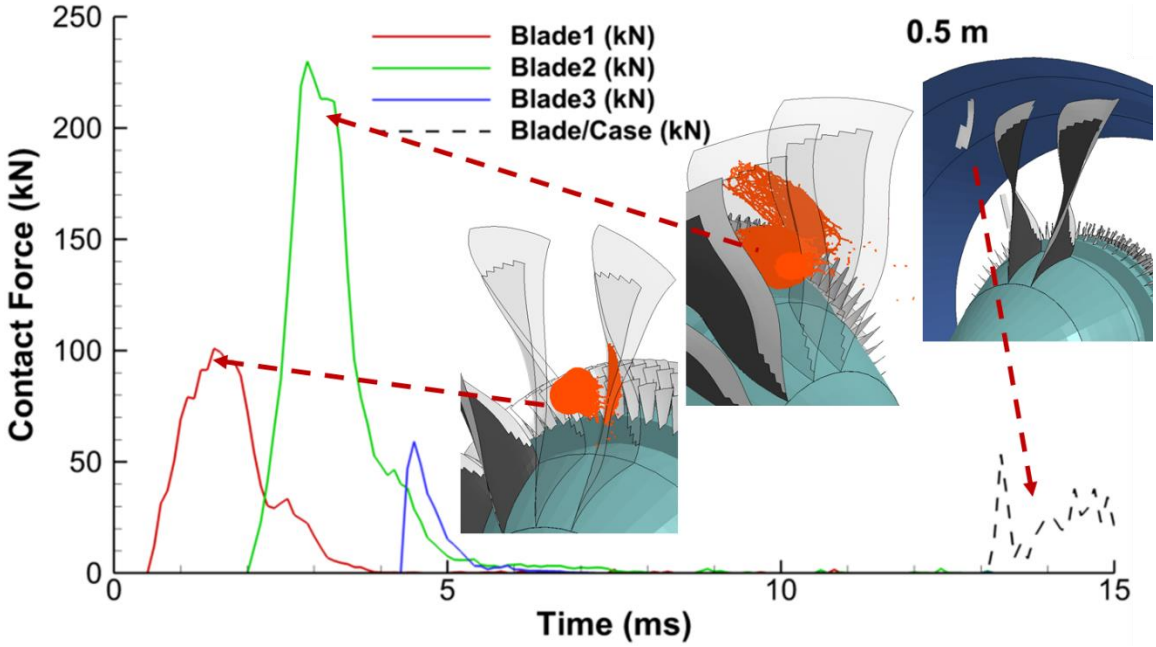

Figure 6.14 Force-time history caused by the interaction between bird and fan blades as well as casing and fan blade fragment (at 0.5 *m*)

Figure 6.15 shows the damage process when the impact location was defined as 75% of the blade height. Although the interaction between the bird and fan assembly was similar to the previous two cases, shown in Fig. 6.15-(a) and (b), the damage mechanics present were different. Because of the distance from the impact location to the blade root, a high bending load was applied to the blade root and caused fiber compression at the trailing edge section near the root while fiber tensile failure simultaneously occurred at the leading edge section. As a result, an immediate detachment occurred on the second target blade during the impact as presented in Fig. 6.15-(c). Because of the centrifugal force, the bird material did not make contact with the LPC. Figure 6.15-(d) shows the progressive damage evolution after the debris came in contact with the neighboring fan blade. The debris was lodged between the adjacent fan blade and the casing, prompting severe stress response on the entire front fan assembly.

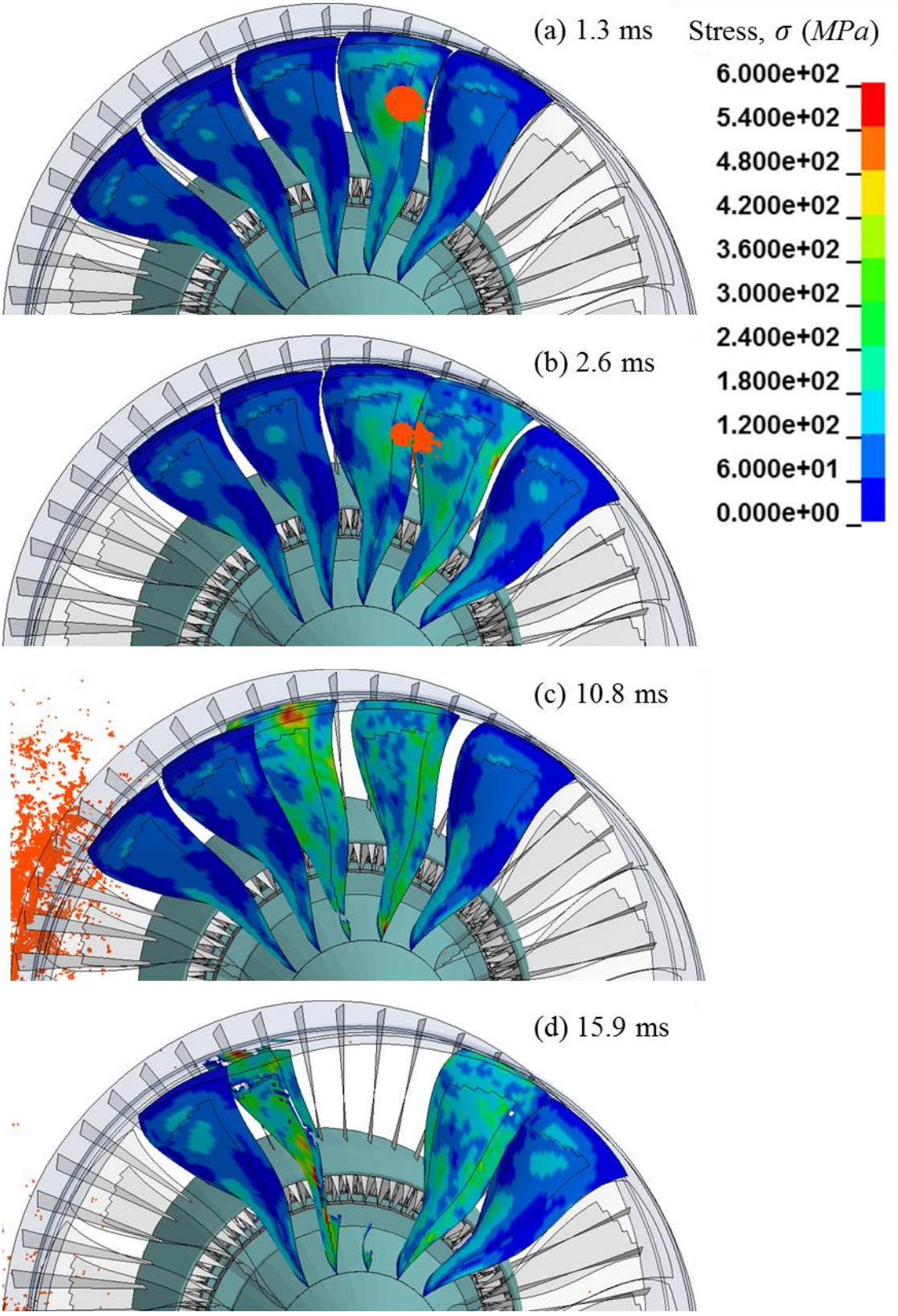

Figure 6.15 Sequence of von-Mises stress contour plots of propulsion system after bird ingestion at 0.75 *m* from the blade root. Screenshot turned corresponding to target blades

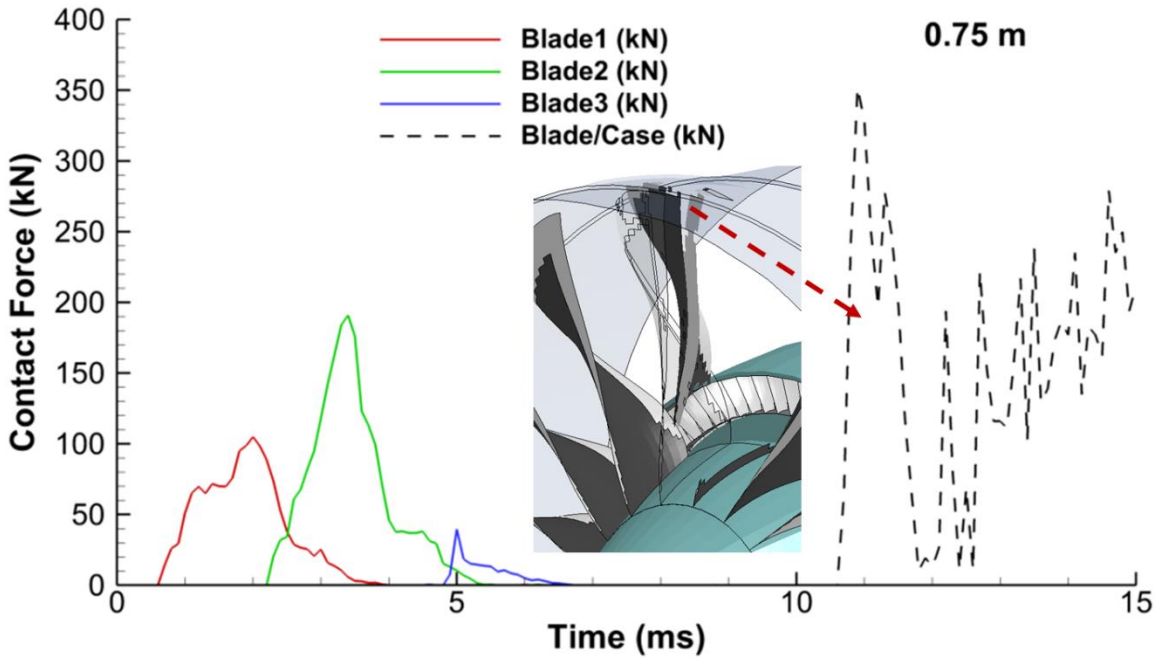

Figure 6.16 Force-time history between bird and fan blades as well as casing and fan blade ejecta (at 0.75 *m*)

The force-time plot between the bird and fan blades is presented in Fig. 6.16. Similar to the previous investigations, the bird interacted with multiple fan blades as well as producing an intense impact on the second fan blade. Interestingly, both the force magnitude and the impact window were noticeably less than that of the previous FOI scenarios. This result was caused by the advanced aerodynamic fan blade design. Because the fan blade is designed to reduce the bending load induced by the interaction between fluid and structure, the interaction between the bird and fan blade was less than the analytical prediction. As a result, the load caused by impact was not severe enough to damage both target blades by the interaction with the bird constituent. Yet, the continuous operation caused the fan blade detachment after the impact.

As seen in Fig. 6.17, the total impulse for both 0.5 *m* and 0.75 *m* cases, the total impulse was gradually decreased as the impact location getting further from the blade root. However, the first target blade, in these impact cases, was subjected to blade detachment due to the combination of damage magnitude caused by FOI and continuous rotation after the impact.

The debris mass was approximately 10 *kg* and the relative impact velocity with the adjacent blade varied from 320 *m/s* (blade tip) to 113 *m/s* (blade root). Because of the debris mass and speed, the contact force between casing and fan blade was several times higher than that of the one between the bird and fan assembly as seen in Fig. 6.16. As the fan assembly continued to rotate, this interaction caused further severe abrasion and containment failure.

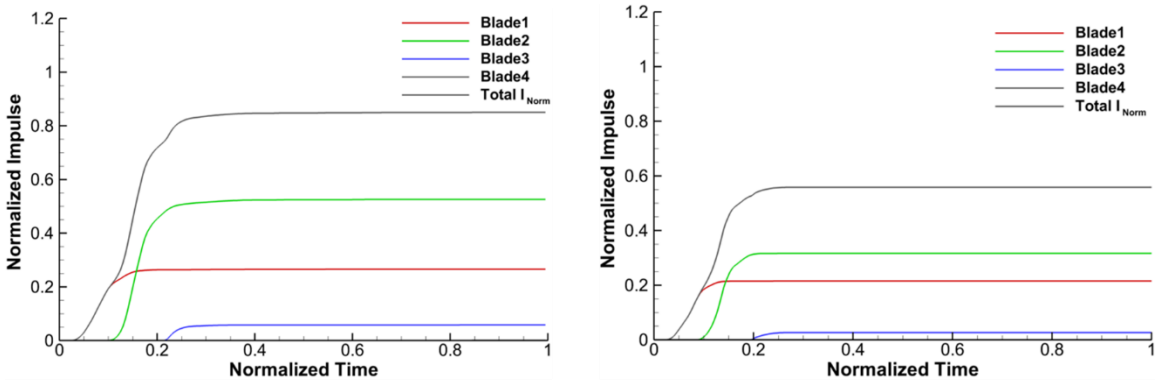

(a) 0.5 *m* impact (b) 0.75 *m* impact

Figure 6.17 Normalized impulse for both FOI simulations (0.5 *m* and 0.75 *m*). The impulses of each subjected component are normalized based on analytical results for each individual impact scenario. (546 *N·s* and 670 *N·s* respectively)

6.2.2 Detailed Damage Investigation

In this section the comprehensive FOI damage investigation is extended to address some other post-impact features. Currently, there is a handful of research on the public domain discussing the post-FOI structural response. Most existing research focuses on the impact dynamics of a single blade [53,138,18]. In this section, a thorough investigation was conducted to address several important features, including damage classifications of the impacted composite fan blade, debris containment, and post-impact response of the subjected engine.

Fiber-Matrix Failure Mode during Impact. Previously, a comprehensive investigation was conducted to show the stress distribution along the fan blades, force-time history, and impulse. However, the damage mechanics of composite are more complicated than that of isotropic materials. Figure 6.18 shows four composite damage modes upon impact by a 2.5 *kg* bird at 0.3 *m* (Fig. 6.10). The figure was created by averaging each damage mode over all of the plies, regardless of the ply orientation. Clearly, the primary damage mode on the target fan blade was compressive failure for both fiber and matrix induced by the slicing trajectory along the leading edge and the through-thickness interaction on the pressure side of fan blade. As a result, the failure caused by compressive loading for both fiber and matrix propagated out on the subjected fan blades (Fig. 6.18-(b) and (d)). The damaged area from this FOI scenario was similar for both impacted blades. This is because of the similar magnitude of momentum was applied on both target fan blades as shown in Fig. 6.12.

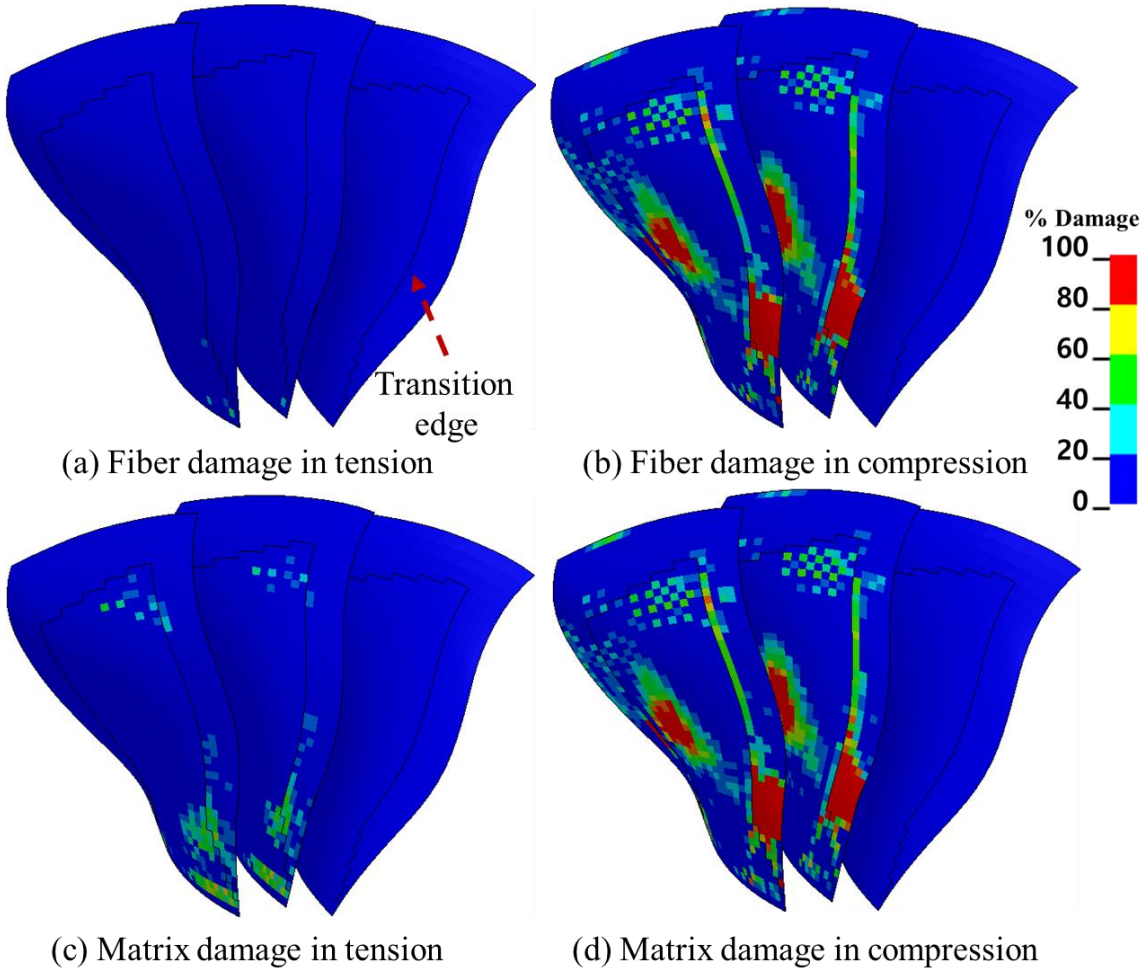

Figure 6.18 Damage mode on composite section of fan blade hit by a 2.5 *kg* bird (0.3 *m*)

Interestingly, one of the most severely damaged regimes was observed along the thickness transition edge where the thick main composite section interfaced with the thin blade edge section. Due to the bending load that pushed the blade backward, the matrix was disintegrated due to the tensile loading near the leading edge section at the root (Fig. 6.18-(c)).

Figure 6.19 presents the structural integrity of composite fan blade after FOI occurred at 50% leading edge height. The damage mode across the target blade was similar to the 0.3 *m* impact case. Yet, the damage magnitude in this FOI scenario was different, since the magnitude of momentum applied on each blade was not equal to each other. The momentum discrepancy is previously shown in detail in Fig. 6.14. Another important issue is the interaction between fan blade and casing. Because of the greater distance from the blade root to impact location, a larger bending load was applied, causing the target fan blade to elongate more than in the previous FOI scenario. As a result, the simulation result presented additional damage on the tip of impacted fan blades.

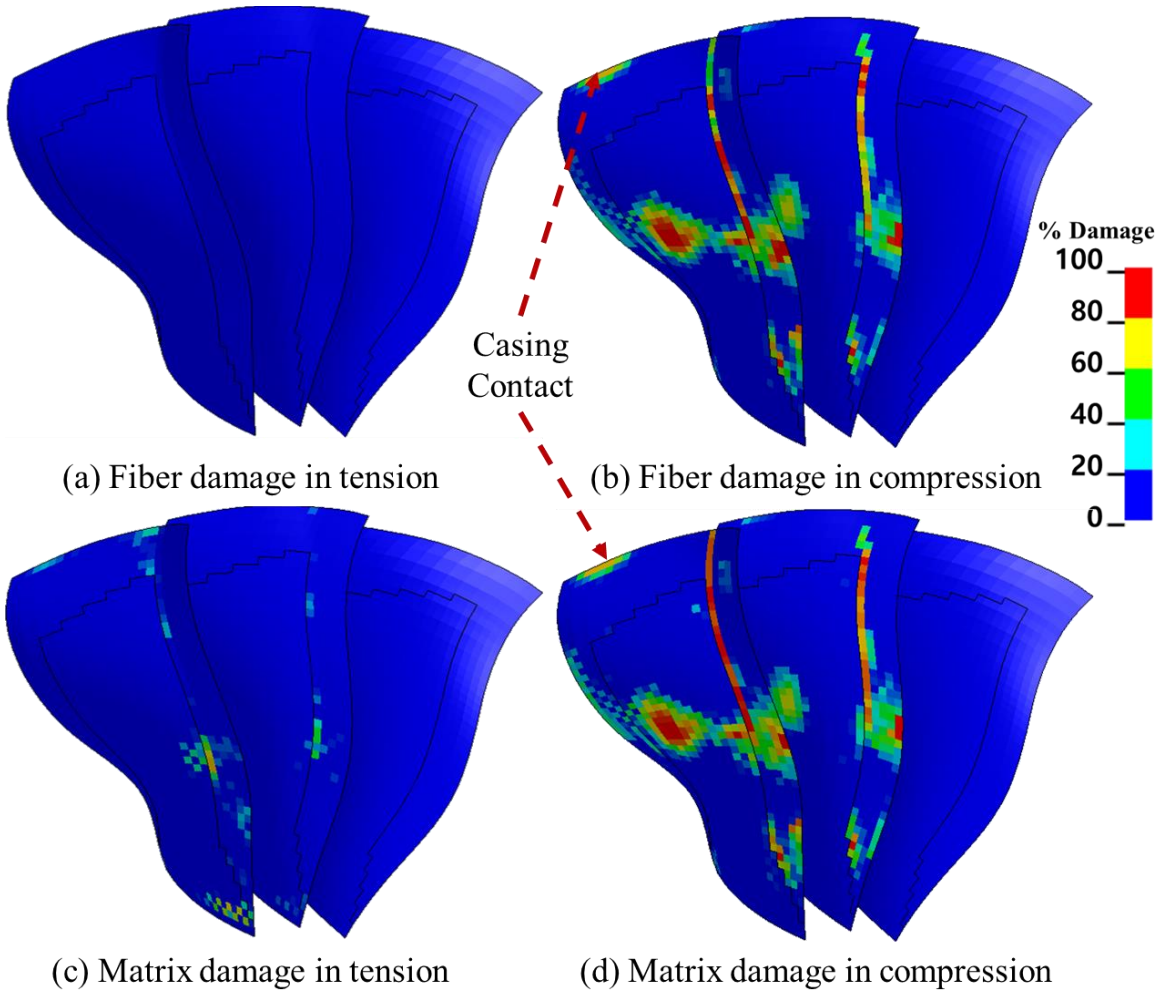

Figure 6.19 Damage mode on composite section of fan blade hit by a 2.5 *kg* bird (0.5 *m*)

The damage modes of the 0.75 *m* impact case deviated from the previously discussed scenarios and led to FBO, despite the reduce impact intensity as discussed in Fig 6.16. As seen in Fig. 6.20-(b), the magnitude of compressive failure, which was triggered by foreign object impact, was less than what was observed in the two previous investigations. However, the larger bending load applied at the trailing edge section of the second impacted fan blade root caused a major fiber and matrix disintegration due to the compressive loading.

Meanwhile, the bending motion applied by the projectile caused a large magnitude of tensile loading on the leading edge section of the blade root. Because of the progressive failure, the cross sectional area of the blade root continued to narrow, further increasing the stress at the root due to the centrifugal force. Consequently, the second target blade was detached from the inlet fan assembly which initiated damage evolution from casing interaction.

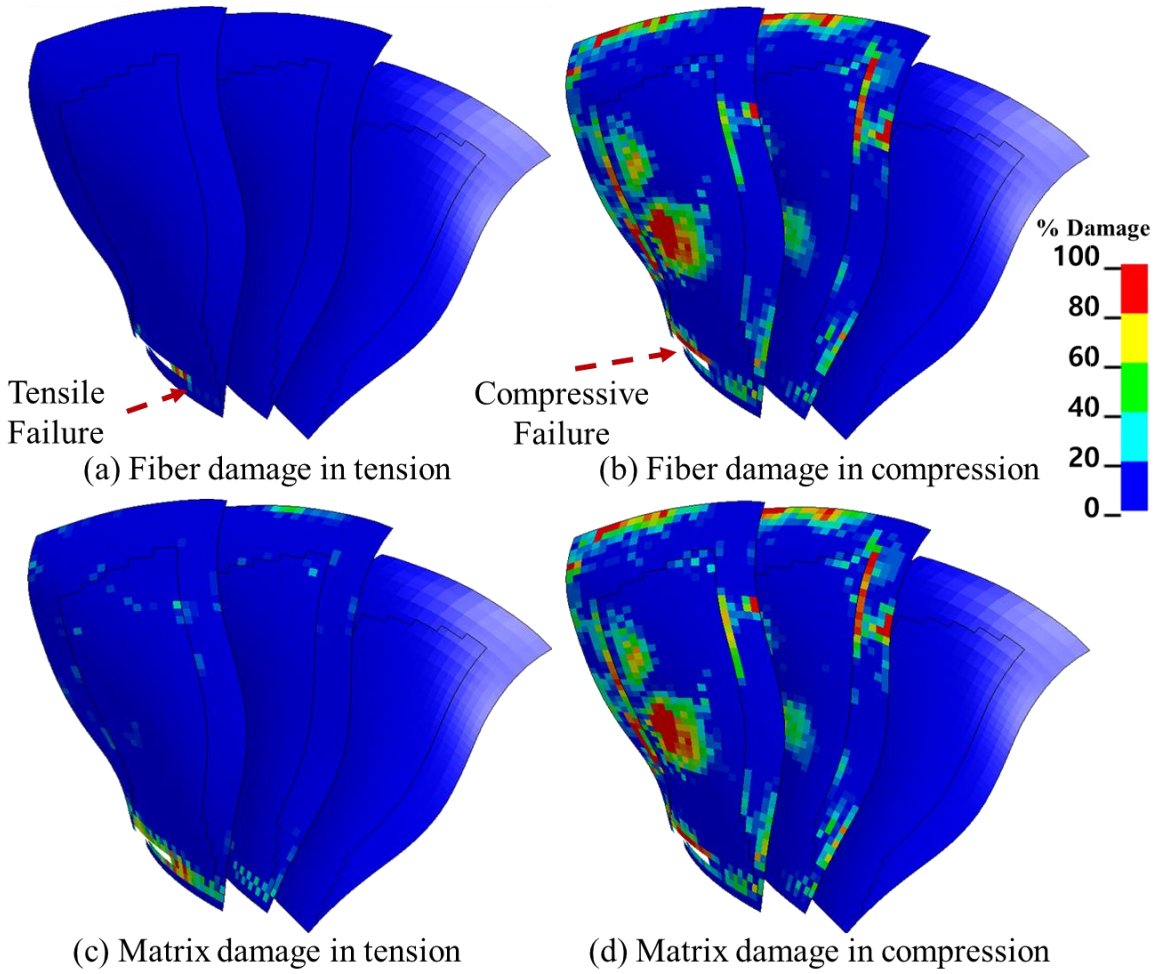

Figure 6.20 Damage mode on composite section of fan blade hit by a 2.5 *kg* bird (0.75 *m*)

Damage Evolution and Casing Penetration. When a fan blade detachment occurs, a progressive damage evolution and larger magnitude of damage is expected because of the continuous interaction between the remaining structure and the ejected fan blade. In this section, the damage progression due to FBO and casing damage evolution are addressed to help develop an alternative solution for an effective debris containment casing design. The casing thickness around the fan section was designed as 1.25 *cm* and 1 *cm* for the rest of the structure. As discussed, the second target fan blade was not directly damaged from FOI for the 0.75 *m* leading edge height impact scenario yet it was subjected to an impact with the ejected fan blade. Thus the magnitude of damage caused on the fan casing was much more severe than the other two cases, even intense enough to breach the casing.

Figure 6.21-(a) shows the damaged engine after a blade piece is lodged between the casing and adjacent fan blade during an FOI at 0.75 *m*. The piece was caught between the casing and adjacent blade, contributing to the drastic bending load on the latter. This load was caused by friction

between the casing and the ejected fan blade. Since the fan blades are not capable of withstanding such high bending loads, the exerted stresses contributed to further blade shear off, increasing the eccentricity of the system.

As seen in Fig. 6.15, the ejected fan bladed maintained its original mass at the moment of impact with the adjacent fan blade. Figure 6.21-(b) presents one of two penetrations on the thick section (around the fan assembly) of casing caused by an initial interaction between the ejected fan blade and the adjacent fan blade, while the ejected fan blade contacted the second blade and casing and progressively abraded, a severe bending load was applied to the adjacent blade. In addition to the abrasion, the fan assembly begins to eccentrically rotate due to the effect of mass redistribution through the ejected and the lodged fan blades. Such a comprehensive damage response provoked additional blade detachment (the adjacent fan blade) and caused an additional casing breach as shown in Fig. 6.21-(c).

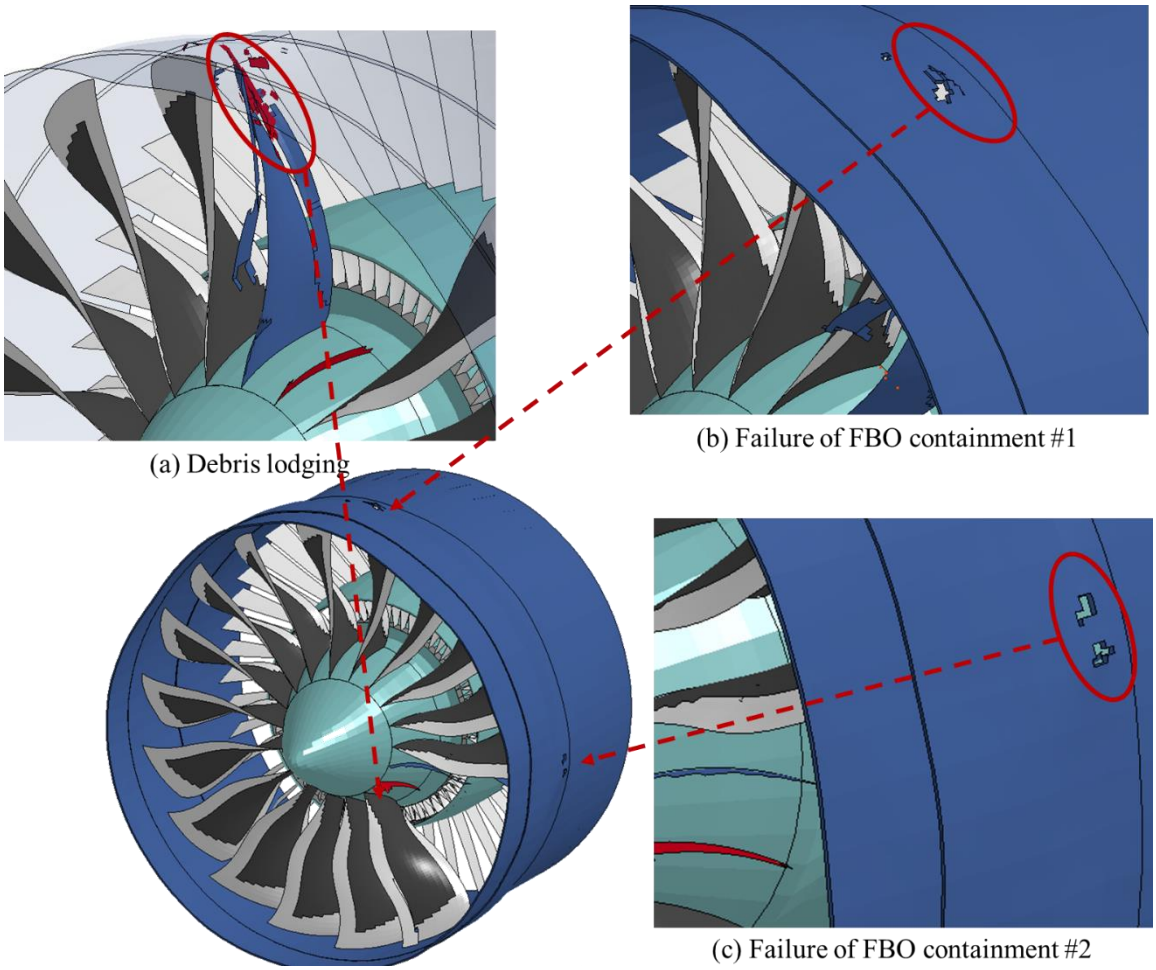

Figure 6.21 Lodged fan blade between the casing and adjacent blade (a), and casing damage due to FBO (b and c). The red fan blade was impacted by a bird and the blue fan blade was adjacent fan blade (2.5 *kg* bird impacted at 0.75 *m*)

Figure 6.22 shows a trace of the fan assembly after FOI for the 0.75 *m* leading edge height impact when FBO occurred. The plot includes both the center coordinate of the fan assembly (red) and four circumferential nodes (blue) at the center of the rotational axis. The outward spiraling implies that the intense interaction between the damaged fan assembly and casing leads to damage escalation as the fan assembly continues to rotate.

As seen in the plot, the vibration caused by FOI has an amplitude in the order of a centimeter, which becomes even larger due to the two FBO incidents. The first detachment (second impacted blade) triggered severe vibration on fan assembly by contacting with the neighboring fan blade and casing. The off-axis rotation then progressively worsened due to the adjacent fan blade detachment.

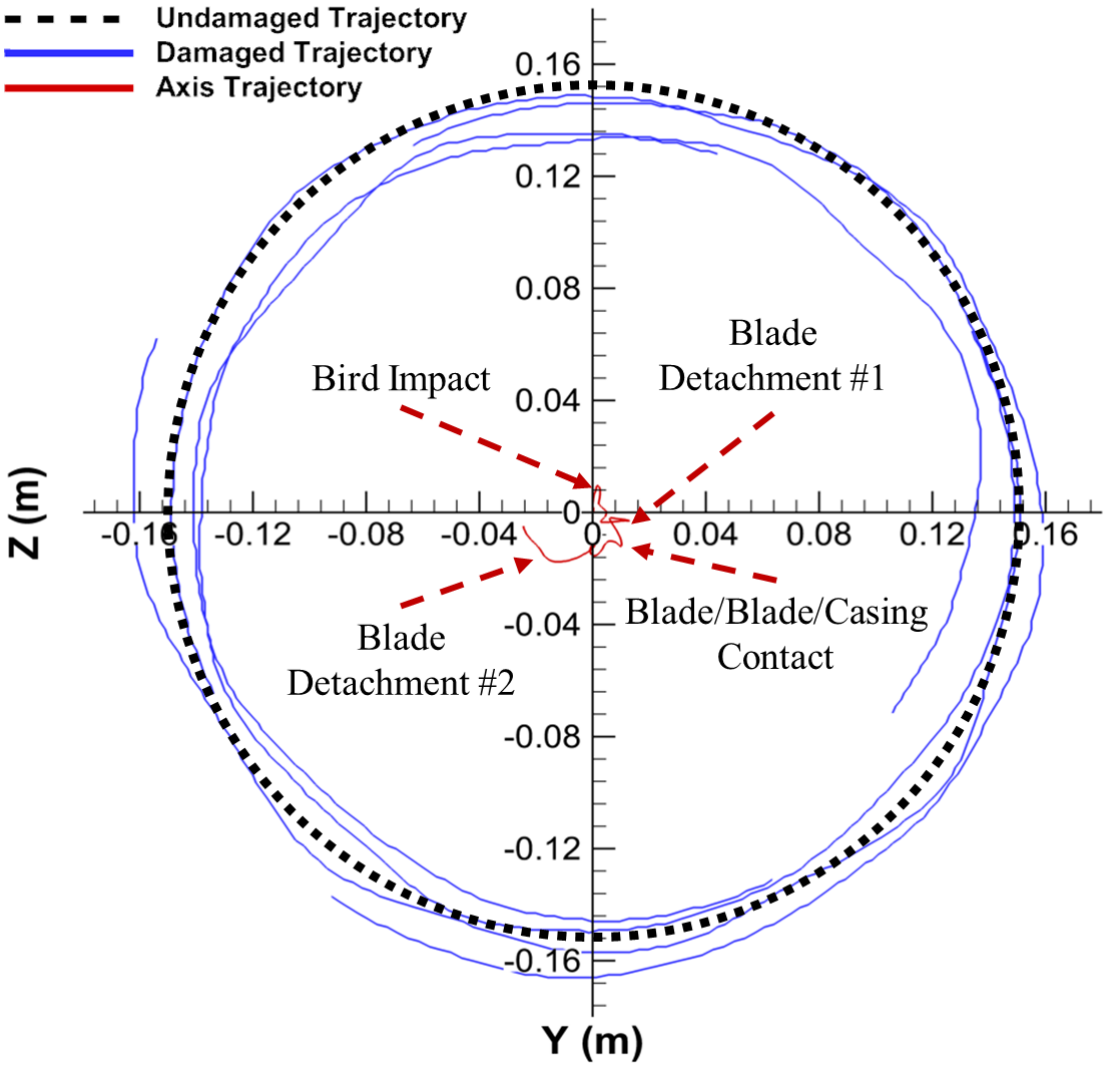

Figure 6.22 Trajectory of damaged fan assembly due to FOI (2.5 *kg* bird impacted at 0.75 *m*)

The instability caused by the imbalance of the system resulted in unaffected fan blades to also come into contact with the casing. Due to FOI, the rotational axis can shift from its original position. Considering the tight tolerance between the blade and casing designed to keep the pressure behind of the fan section, an undesired vibration could trigger a catastrophic failure on the propulsion system.

Debris Ingestion into LPC. Even in the case of successful damage arrestment, as observed in the first two scenarios, another issue to be considered is debris ingestion into the LPC following the bird-fan assembly impact. The ingested debris and fragments into LPC have the potential to cause compressor stall [139,140], which will directly impact the thrust production, as well as the overall yaw and roll of an otherwise stable aircraft, due to sudden discharge of pressurized air from the damaged engine.

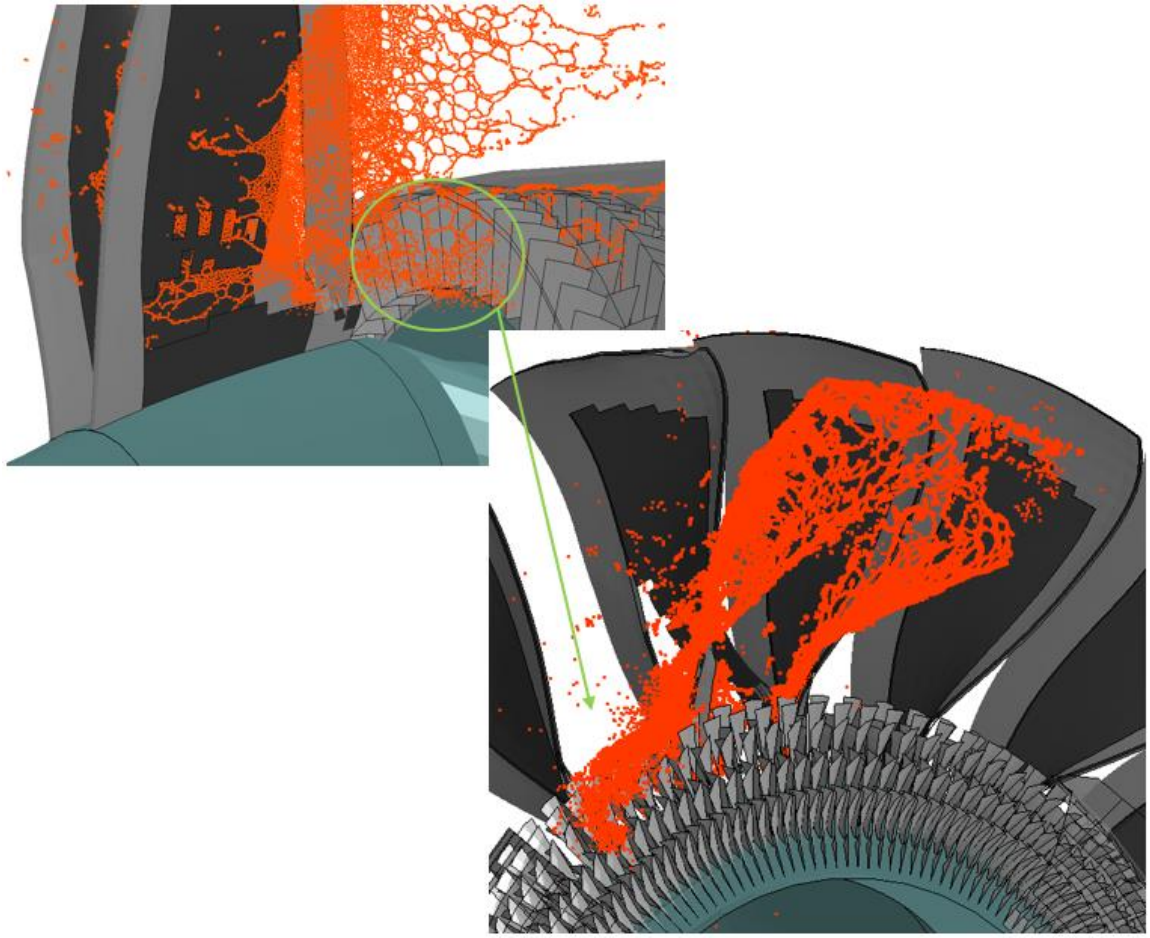

Figure 6.23 Bird debris ingestion into LPC (2.5 *kg* bird impacted at 0.3 *m*)

As depicted in Fig. 6.23, most of the bird material was ejected through the bypass, as a result of the larger radial velocity induced by the fan assembly. Yet, some debris was still directed into the LPC. The figure depicts a section of the debris as it moves through the IGV stage, before getting ingested by the LPC. Even if the engine survives the initial impact, there would still be a possibility of compressor stall caused by large amount debris ingestion, as it gives rise to an off-design operating condition.

6.3 Ice Ingestion Scenario

Combining the comprehensive FOI damage modeling methodology and the developed ice model, the study of dynamic response of propulsion system subjected to hail ingestion is discussed. In addition to the hail ingestion, ice ingestion to LPC also explored in this section.

Hail Impact onto Fan Blades. The damage assessment methodology was employed to investigate the dynamic response of a jet engine subjected to a large hailstone ingestion. A comprehensive investigation was created based on a normal flight altitude of a large commercial passenger aircraft. For the damage analysis, two fully dense 6.8 *cm* diameter hailstones (each roughly the size of a softball and the density of 897.6 kg/m^3) were created to hit a high-bypass propulsion system in sequence at 560 *mph* (250 *m/s*). With the given flight condition, the propulsion system was producing the maximum thrust and the fan assembly was rotating at 2166 *RPM*. As shown in Fig. 6.24, the hailstones were approximated as spherical masses and struck the fan section at 0.4 and 0.5 *m* from the blade root.

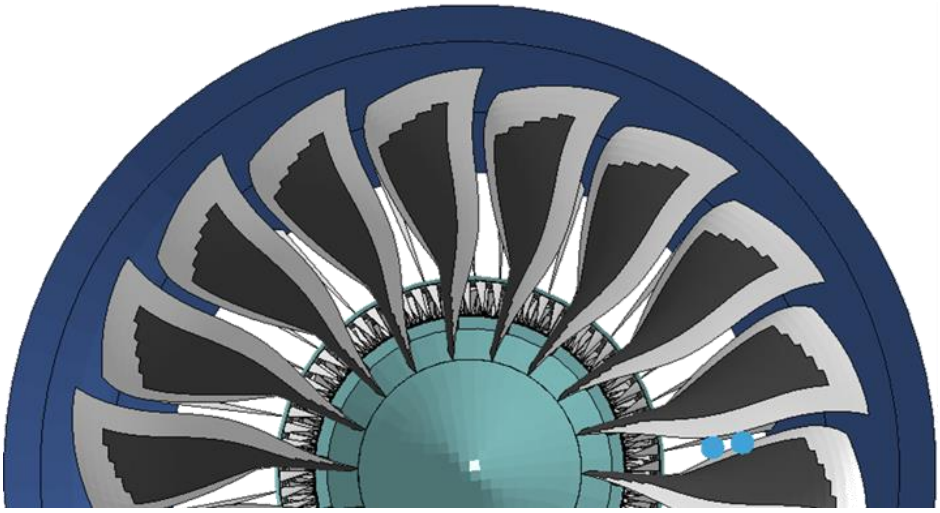

Figure 6.24 Full-scale ice ingestion model (m_{ice}=147 *g* and V_{ice}=250 *m/s*)

Because of the hail size, it was able to impact on either the leading edge of fan blade or main fan blade section. Hence, the initial impact surface was changed to assess the damage caused by each impact. First of all, the leading edge impact scenario was assumed and the resultant composite damaged mode due to the ice impact was presented.

Figure 6.25 shows the damage of composite fan blade caused by ice impact on the fan blade leading edge. The impact angle was perpendicular to the leading edge. Because of the mass of the projectiles (147*g* x2), the damage on the fan blade was not significant. Fiber damage was not detected in any ply orientation. Nevertheless, the matrix structure was disintegrated due to the compressive loading, regardless of the ply orientation. The damage on 90˚ ply was the most severe to compare with any other directions. The damage area and magnitude gradually reduced as the ply orientation approached 0˚. The damage trend was caused by a composite laminate fabricated using anisotropic material. Since the fiber has a higher impact resistance than the matrix, the damage magnitude of the 0˚ ply was less than the 90˚ ply.

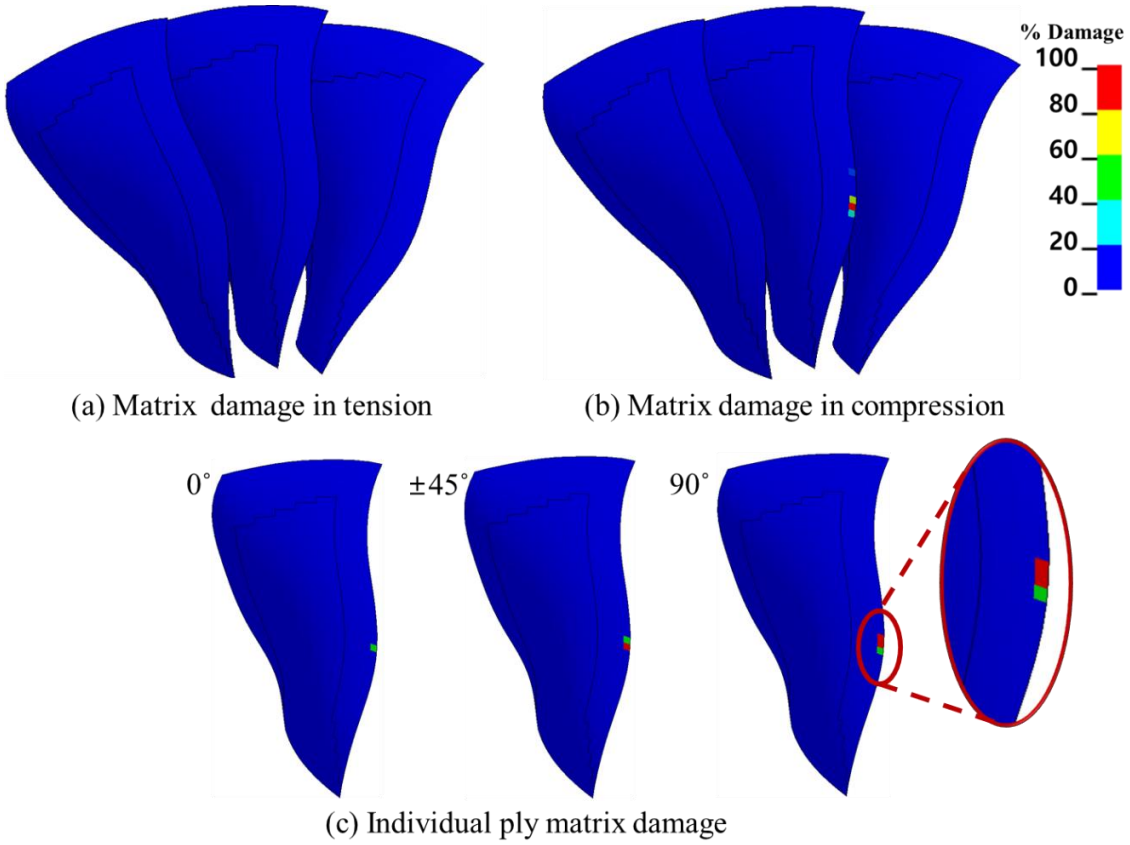

Figure 6.25 Averaged matrix damage of composite fan blade due to hail impact by tensile loading (a), compressive loading (b), and damage on each ply based on the fiber orientation (c), where 0˚ is the fiber orientation corresponding to the radial direction (leading edge impact).

For the impact that occurred on the main section of composite blade, the damage trend was noticeably different. Unlike the leading edge impact scenario, the damage magnitude was greater on the 0˚ plies than for the 90˚ plies as shown in Fig. 6.26. The impact load on the structure was combined with the existing centrifugal stress to cause minor matrix deterioration. No further damage development occurred after impact due to the continuous operation throughout the simulation.

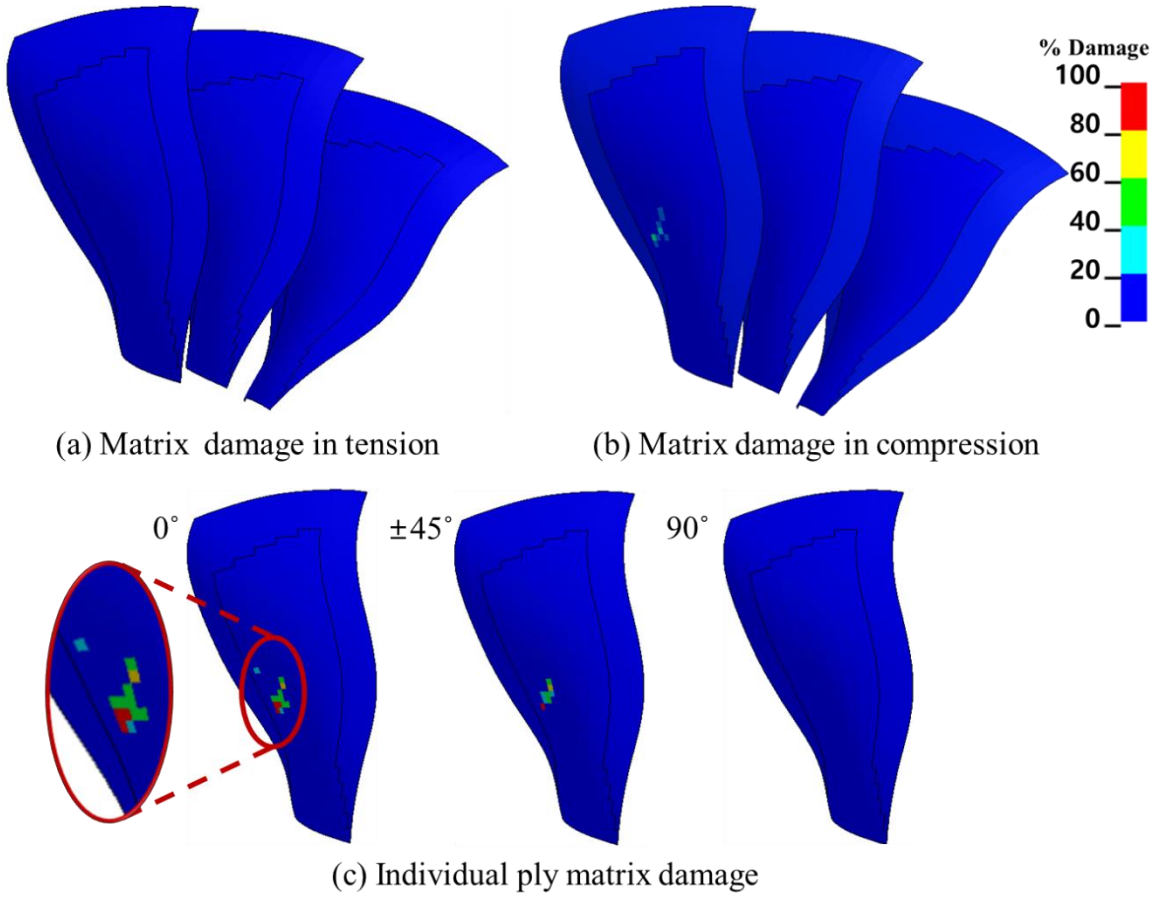

Figure 6.26 Averaged matrix damage of composite fan blade due to hail impact by tensile loading (a), compressive loading (b), and damage on each ply based on the fiber orientation (c), where 0˚ is the fiber orientation corresponding to the radial direction (pressure edge impact).

Ice Debris Ingestion into LPC. Based on the previous investigation, it was concluded that a large size hail impact did not compromise the fan blade structure. However, it was observed that some of the ice fragments were ingested into the LPC. The ice fragment ingestion or small size ice crystal ingestion can have a significant impact on the engine performance, as a result, current research is directed toward understanding the ice accretion on high-bypass jet engines [141,142].

Not only is the engine subjected to a super-cooled high water content environment, but the ice crystals or hail fragment ingestion into LPC accelerates the ice accretion and impacts the aerodynamic performance [143]. Hence, the impact location was radially increased using numerical investigation in order to identify the threshold distance for ice fragment ingestion into LPC. The simulation setup is shown in Fig. 6.27.

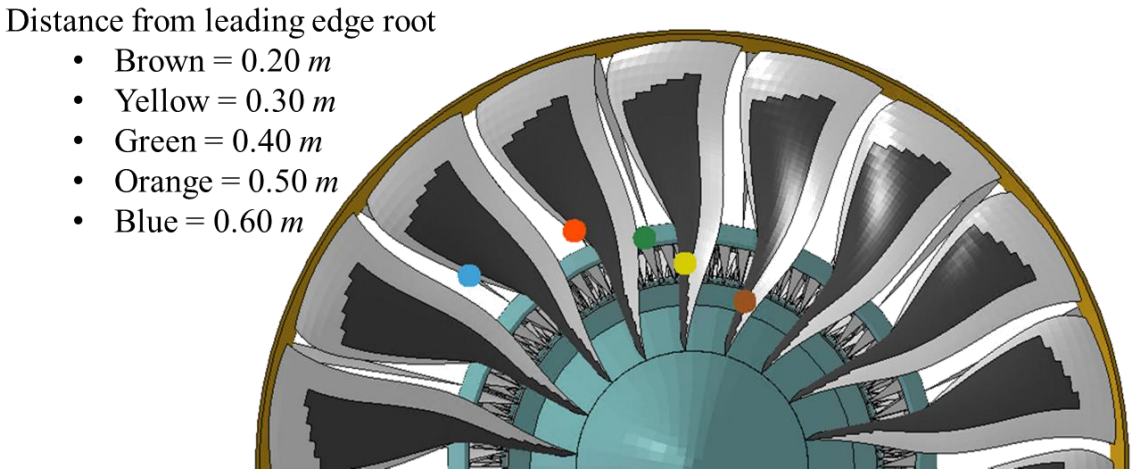

Figure 6.27 Simulation setup to identify the threshold distance for hail fragment ingestion (Projectiles are color coded to identify the distance from blade root)

Figure 6.28 shows the ice crystal distribution after hail impact with the fan blade for all five impact scenarios. When a hailstone impacted at 0.2 *m* leading edge height, the majority of ice crystals were directly ingested into the LPC. Approximately 77.4% of the original mass of the hailstone was ingested through the compressor. According to the simulation, 62.2% of hail fragments went into the LPC when the hail impact occurred at 0.3 *m* leading edge height. The amount of ingested fragments becomes significantly less when the impact distance is greater than the 0.3 *m*. When hail impacted at 0.4 *m* of the leading edge height, only 12.3% of ice crystal was ingested into LPC. For the remaining two impact locations, the amount of ice crystal ingestion was negligible.

During the investigation, it was observed that the large amount of ice fragments ingestion caused a sudden stress on the compressor blades. Also, the relative velocity between the naturally formed hailstones and flight speed at normal cruising altitude is fast enough to occasionally cause a hailstone to directly impact the LPC. Therefore, direct hail ingestion simulation is investigated in the next section.

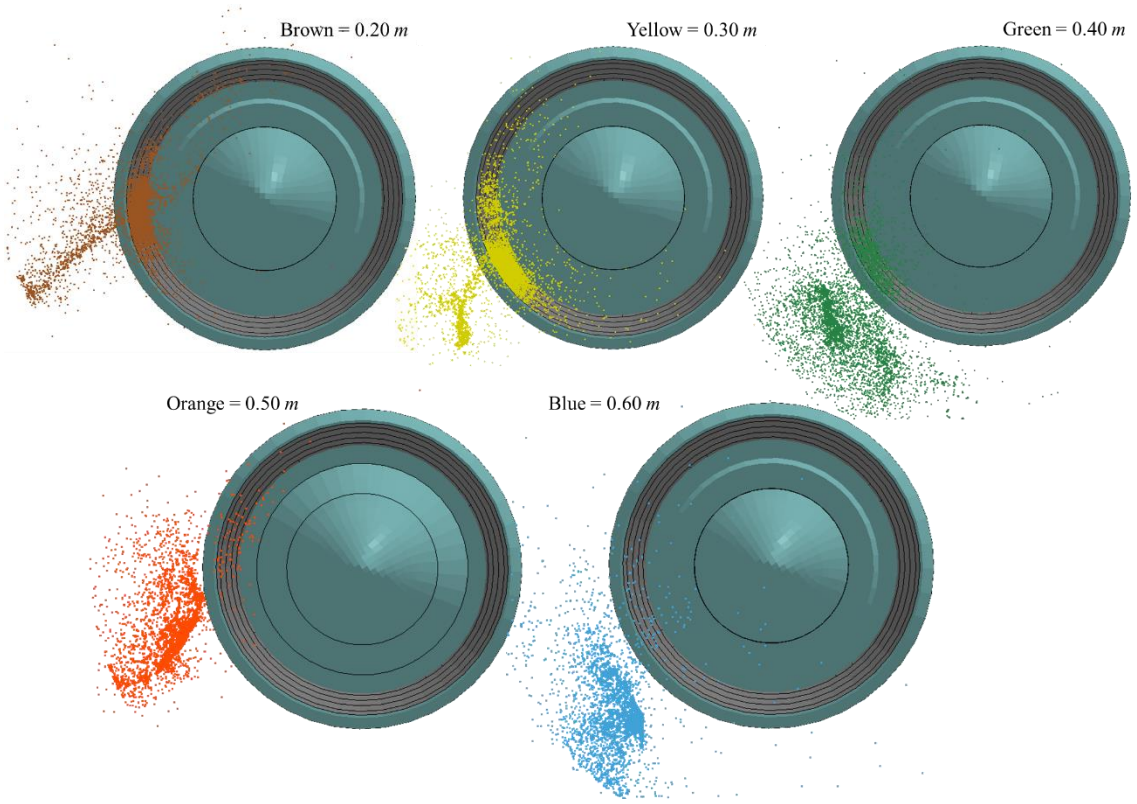

Figure 6.28 Fragment distribution after hail impact and the ice crystal ingestion into LPC at various ingestion location (m_{ice}=147 g and V_{ice}=250 $m/$)

Direct Hail Ingestion into LPC. Although numerous ways to mitigate the ice formation within a high-bypass engine have been implemented, several occurrences of ice accretion have been reported during normal operating conditions at high altitude in past two decades. Regardless of the engine generation, no high-bypass engine can be exempted from ice crystal icing. It occurs at the inlet, fan, spindle, and IGV. Among multiple locations, ice accretion on the LPC is one of the major design concerns, since it directly impacts the system performance [142,143].

Not only the performance degradation, but also the accreted ice ingestion to LPC could be an issue since the ice slabs won't make contact with fan blades and will be traveling at the ingestion speed directly into on compressor blades. Based on LPC accretion assumption, a corresponding simulation was created to assess the damage caused by impact. As depicted in Fig.6.29, four ice slabs were created in-between the IGVs. The ingestion velocity of ice slabs to LPC was set as 250 *m/s*. The dimension of each ice slab was 6 *cm* x 2.2 *cm* x 3.0 *cm* and the total ingested ice mass was 130 *g*.

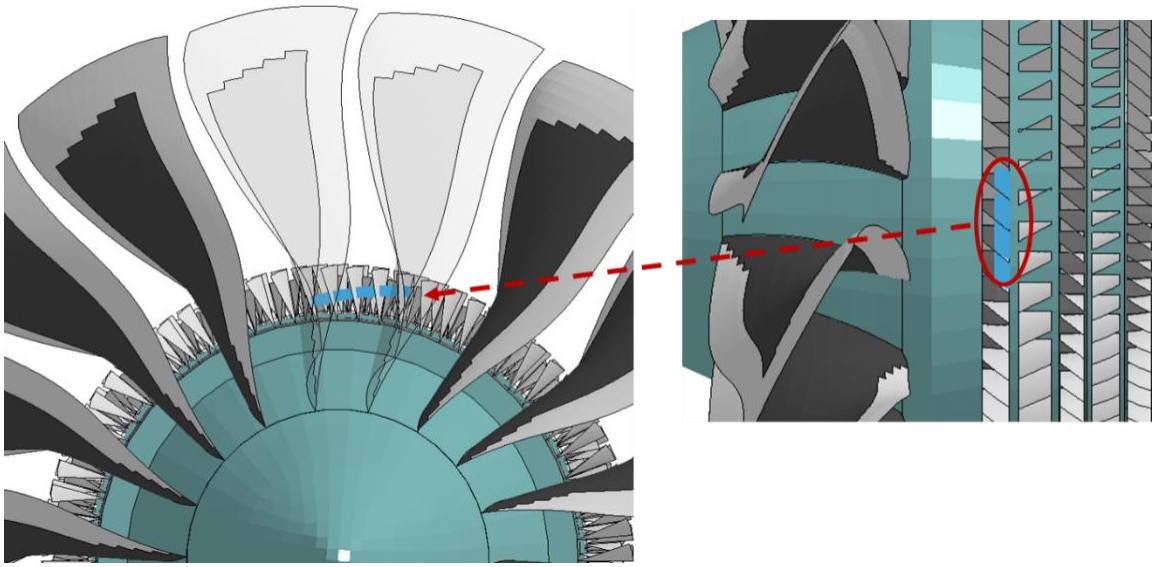

Figure 6.29 Simulation setup for ice ingestion from IGV to the LPC

The structural response on the LPC due to ice slabs ingestion is presented in Fig. 6.30. Considering the mechanical strength of compressor blades, the structural response was limited to within the elastic regime. The highest stress occurred on the stator behind of the 1st stage compressor because the ice particles were accelerated by the interaction.

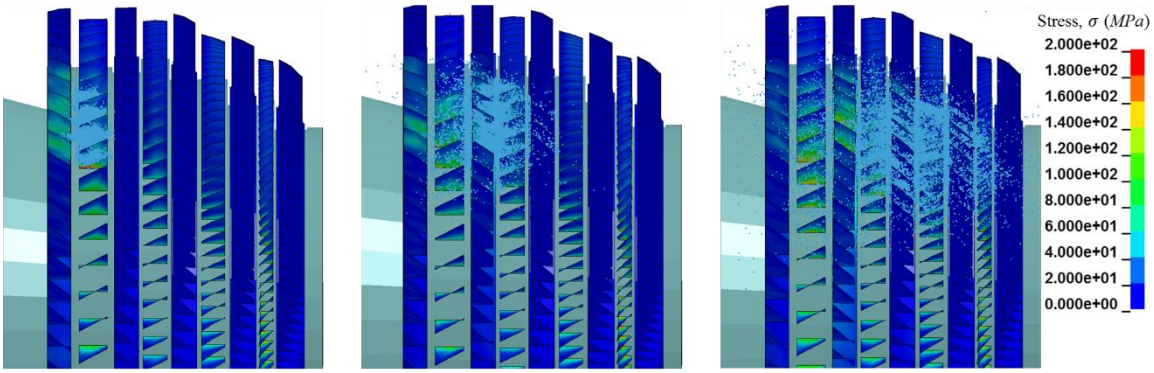

(a) 0.2 *ms* (b) 0.7 *ms* (c)1.5 *ms*

Figure 6.30 Sequential image of ice slab ingestion and ice particle trajectory through LPC

The investigation result did not predict any damage caused by ice impact. However, one of the experiments reported in literature discussed a minor structural damage caused by ice/water ingestion into a jet engine that could potentially cause operating instability and blade damage [144]. According to their investigation, 83 *g* of ice triggered the engine to flame out, and damage was observed on the axial compressor blades, which was caused by direct ice ingestion and flame out. Overall, the ice/hail ingestion into a propulsion system did not exhibit the same level of damage as

was observed for the bird ingestion scenario. Yet the subjected system still suffered from a minor damage such as matrix deterioration, which would require attention eventually.

6.4 Summary of Work

In this chapter, a comprehensive FOI damage methodology developed is discussed, verified by quantifying the computational uncertainty, and partially validated against several existing experiments. By combining the partially validated and fully verified modeling techniques, this unique damage assessment methodology was successful in performing nonlinear dynamic damage analysis and effectively capturing the comprehensive response of a propulsion system subject to a soft body FOI. Additionally, a fully parameterized virtual propulsion model based on the current FAA regulations was developed for this study. The computational work thoroughly presented the detailed structural response, as well as highlighting some important phenomena such as fiber/matrix disintegration, eccentricity, casing abrasion, and debris ingestion into the LPC, which was not addressed in past studies.

7 Analysis of an Alternative Design for Damage Mitigation Using the Developed Methodology

In this section, the comprehensive FOI damage assessing methodology was extensively employed to develop a virtual model to arrest damage caused by impact using the baseline virtual model which complies with the current regulation. In an effort to computationally examine the performance of a hybrid casing in arresting FBO, three casing designs were developed and assessed using the comprehensive FOI methodology developed in this study. Additionally, an alternative fan blade design was investigated to improve the impact resistance by hybridizing metal alloy and composite materials.

7.1 Performance Evaluation of Debris Arrest for Soft Casing Design

Research into ballistic-related applications has generated many practical arrestment solutions such as bullet proof jackets, bumper shields, and even aerospace applications. As known, aramid based composite materials tend to have high ballistic resistance [145,146], yet are considered to have low abrasion resistance [147]. Because FOI tends to apply a combination of both ballistic loading and abrasion to the casing, it is important to design a casing to withstand the high loading with the minimum additional weight.

In order to develop a new casing design to successfully contaminate the damage caused by FBO, a hybrid structure using both aluminum and Kevlar® was developed and investigated arrest using the comprehensive damage assessment computational methodology. Since Kevlar has different damage mechanics than an isotropic material, three different hybrid casing designs were created as shown in Fig. 7.1.

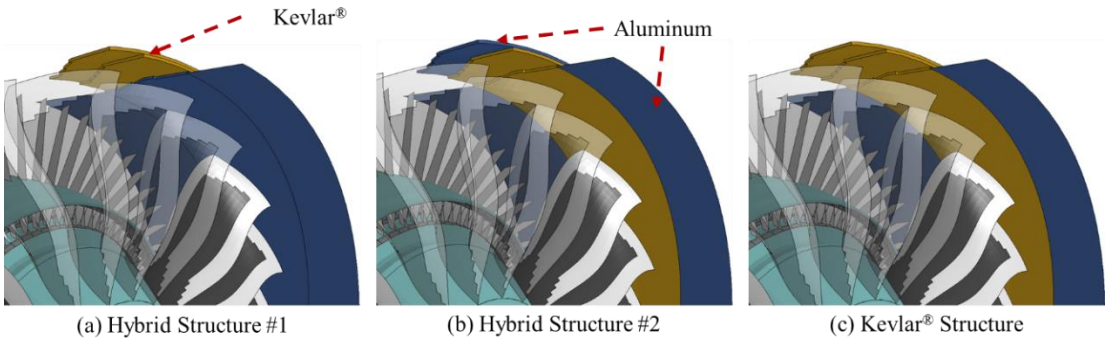

Figure 7.1 Three alternative casing designs (Blue = Aluminum, Yellow = Kevlar®)

Kevlar has low resistance against abrasion but high ballistic performance, so the two hybrid casing designs used Kevlar both inside and outside of thick section of aluminum casing to evaluate the FBO arrest performance. Similar to the high speed impact investigation in section 5.3.2, each element layer representative of Kevlar was 1.25 *cm* by lumping 25 plies of Kevlar (0.5*mm* thick each ply) to save the computational expense. The third candidate was developed using only 75 Kevlar plies (3.75 *cm* thickness) around the inlet fan assembly and no metal alloy was allocated. For all of the hybrid casing designs, the thin casing section, this is not directly involved in the FBO was reduced by 2 *mm* which ended up with 8 *mm* thick of aluminum. Fig. 7.1 shows the three casing design candidate where each layer of the yellow mesh represents 25 plies of Kevlar and the blue mesh around the fan blade is 1.25 *cm* of aluminum.

Each layer of casing design was bonded using the 3-D composite damage modeling methodology which was previously discussed in section 5.3.2. Fig.7.2 shows a cutaway view of one of the hybrid casing designs developed for the investigation. Both green and red layers represent the computational representation of interlaminar bonding. The additional weight required to develop the first hybrid casing design (#1) was approximately 50 *kg* by adding Kevlar laminate around the casing.

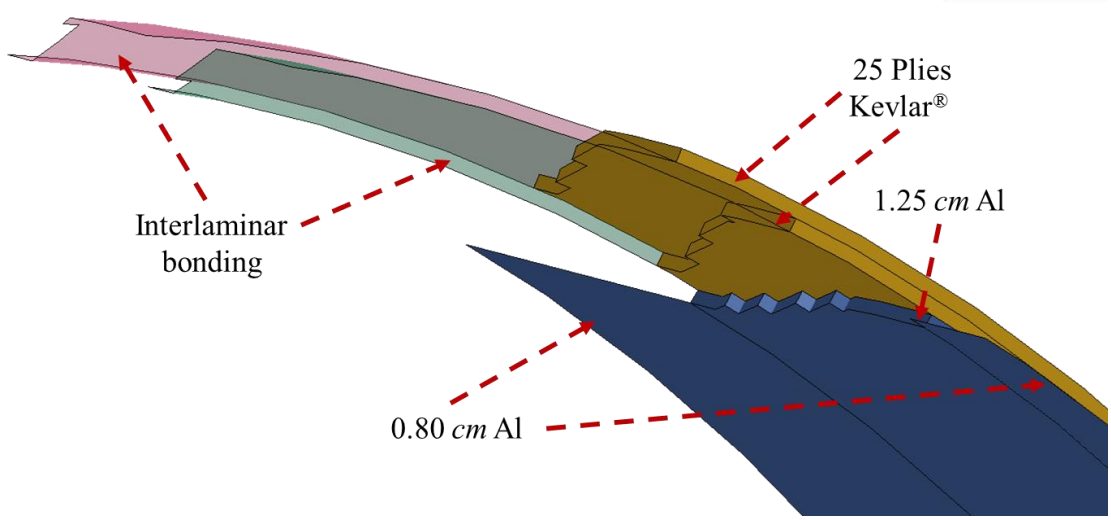

Figure 7.2 Cutaway view of a hybrid casing design for FBO arrest solution

The FBO scenario was based on the same setup as previously discussed. A 2.5 *kg* bird was ingested at the same speed into the same high-bypass commercial jet engine. The impact location was set as 0.75 *m* leading height while the system was operating 226.8 *rad/s*. The damage evolution sequence due to the casing and blade contact is presented in Fig. 7.3. As soon as the detachment occurred, the ejected fan blade started contacting with the inner surface as shown in Fig. 7.3-(a).

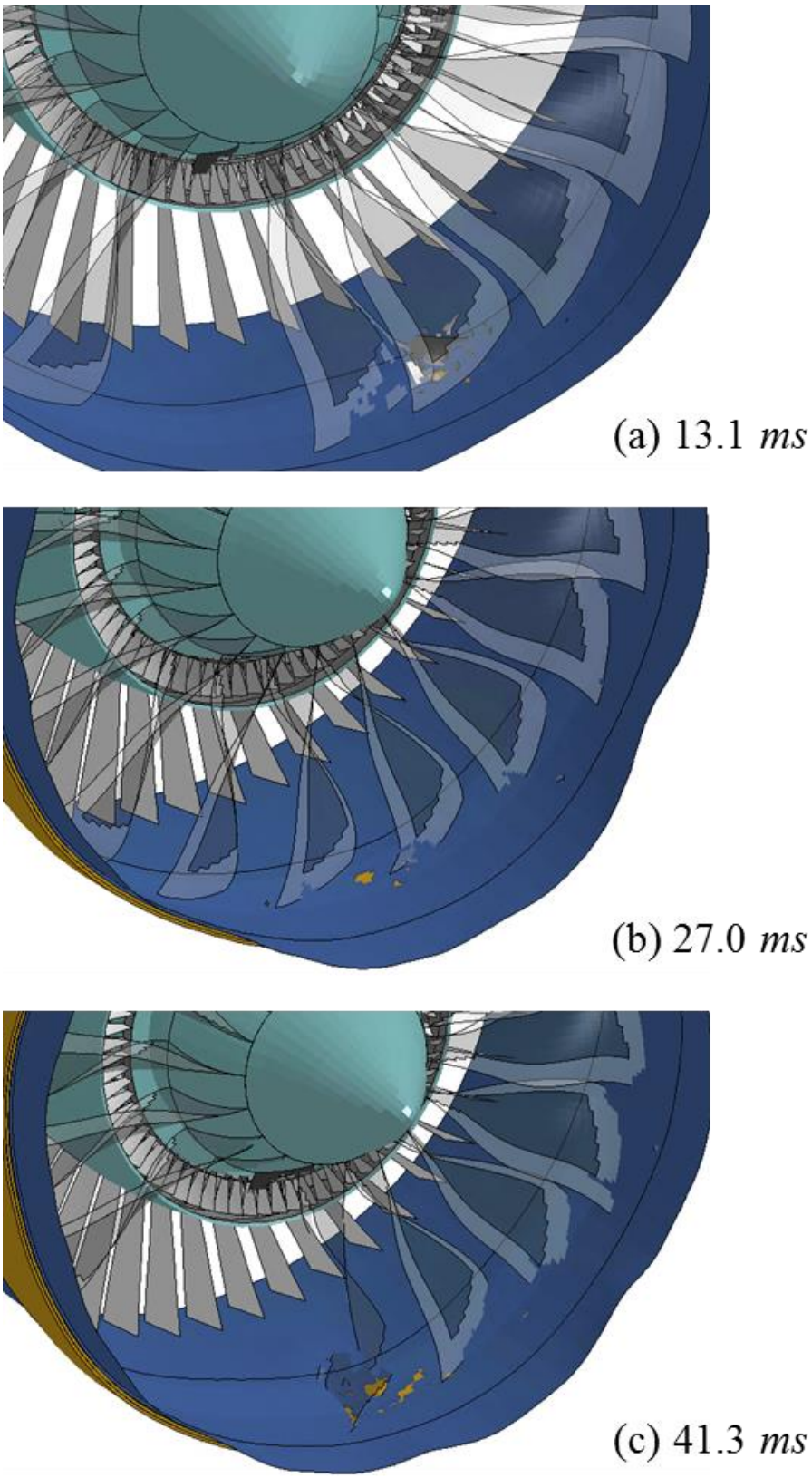

Figure 7.3 Damage evolution on a hybrid casing design (#1) from FBO. Fan blades were transparent to represent the damage evolution on fan casing

As shown, the ejected fan blade contacted with the adjacent fan blade. As a result of the continuous rotation of the fan assembly, the ejected fan blade contacted with the adjacent fan blade and casing simultaneously. This complicated interaction induced a continuous damage evolution on fan casing. The structural response throughout the operation is shown in Fig. 7.3-(b). No further damage evolution on both the casing, yet the tip of the fan blades was deteriorated due to the vibration of fan assembly and casing deformation. Figure 7.3-(c) shows the primary damaged area of the fan assembly after several revolutions following FBO.

Overall, the casing contact with fan assembly was a result of the combination of the ejected fan blade and eccentricity of fan assembly from FBO. The structural response provoked contact of all the blade tips with casing, as a result, the tip of every fan blade was severely eroded. Figure 7.4 shows such damage on both fan assembly and casing after the damaged system after several revolutions.

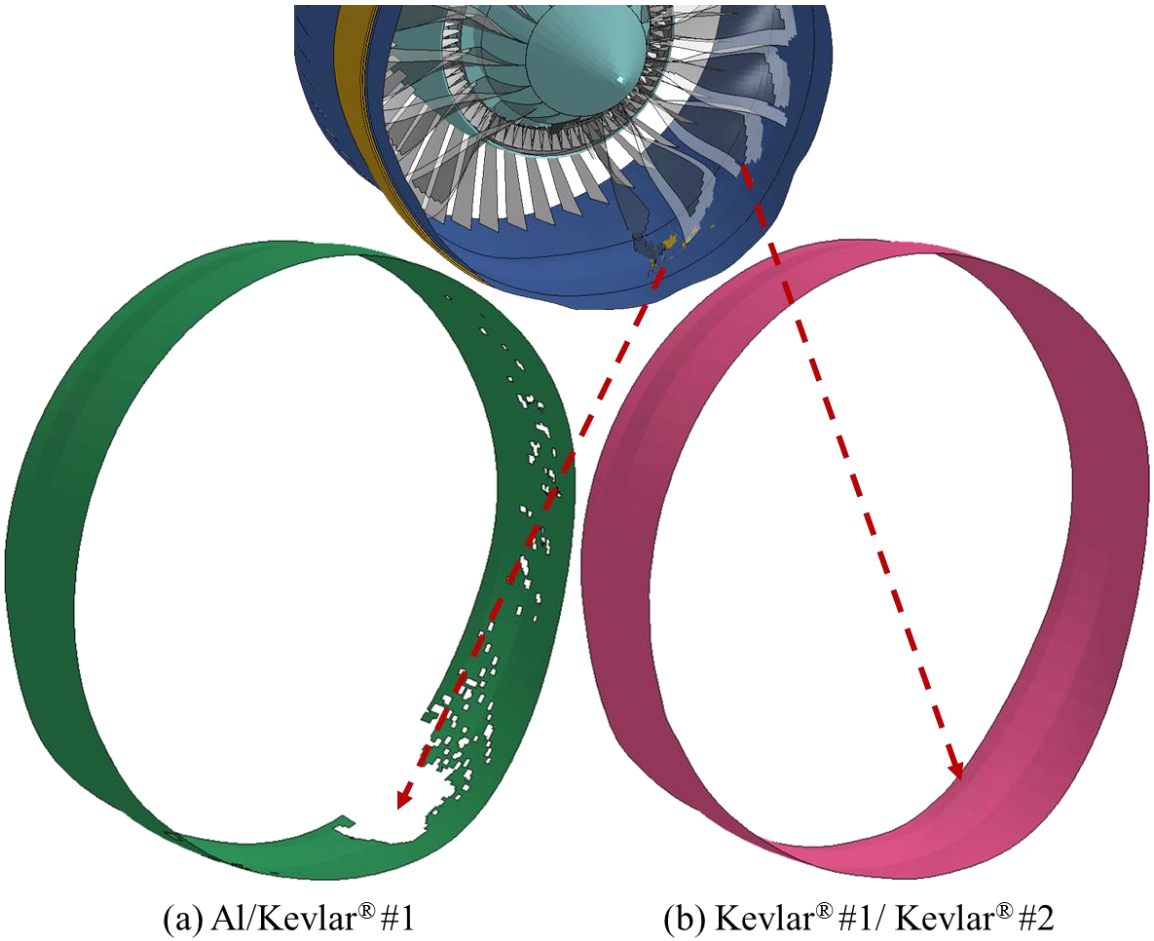

Figure 7.4 Damage on both fan assembly and hybrid casing due to FOI and area of delamination occurred by the interaction between fan assembly and casing

The abrasion was not as significant as what was predicted in Fig. 6.21. The aluminum layer was compromised due to the first FBO as observed. However, the first Kevlar laminates successfully arrested the further damage development, with some damage was detected in mesoscale level. Aforesaid, when impact occurs to a composite laminate, one of the important impact energy absorbing mechanisms is delamination.

The delamination area shown in Fig. 7.4-(a) was measured to be approximately 0.32 m^2 due to the interaction between the fan assembly and hybrid casing. The area of delamination was approximately 6% of its entire interface area (5.47 m^2) when it was intact. The second interlaminar bonding remained undamaged throughout the investigation as depicted in Fig. 7.4-(b). The hybrid structure was able to absorb approximately 24.2% of total energy of system by dissipating it through delamination and the friction between fan assembly and casing.

Next, the hybrid casing design #2 was investigated to evaluate the FBO arrest performance. The same impact scenario was selected in this investigation. Figure 7.5 shows a sequence of damage progression caused by the continuous rotation of fan assembly after FOI. One of the noticeable differences from the #1 hybrid casing design was the immediate failure on the most inner Kevlar layer upon impact.

As shown in Fig. 7.5-(a), the ejected fan blade immediately caused the first Kevlar layer failure. The broken blade was lodged in between the casing and adjacent fan blade during rotation, which magnified the casing abrasion. Because of the low abrasion resistance, both Kevlar layers along the contact regime were completely compromised as presented in Fig. 7.5-(b). Additionally, both laminates were detached from the outer aluminum section and warped away from the aluminum section of the hybrid casing. Due to the tight tolerance design, the warping triggered a wide range of damage on the Kevlar layers by the subsequent fan blades' slicing motion. Consequently, the structural response led to wider range of abraded area than the #1 hybrid casing design.

The image shown in Fig. 7.5-(c) presents the damage on the hybrid casing after several rotations. Because of the cutting damage caused by tip of fan blade assembly, the first layer of Kevlar was stripped off where the first ejected fan blade impacted. The interaction between the Kevlar layer and fan assembly continued to amplify the damage. Such damage progression contributed to a wider area of delamination to compare with the #1 hybrid casing design.

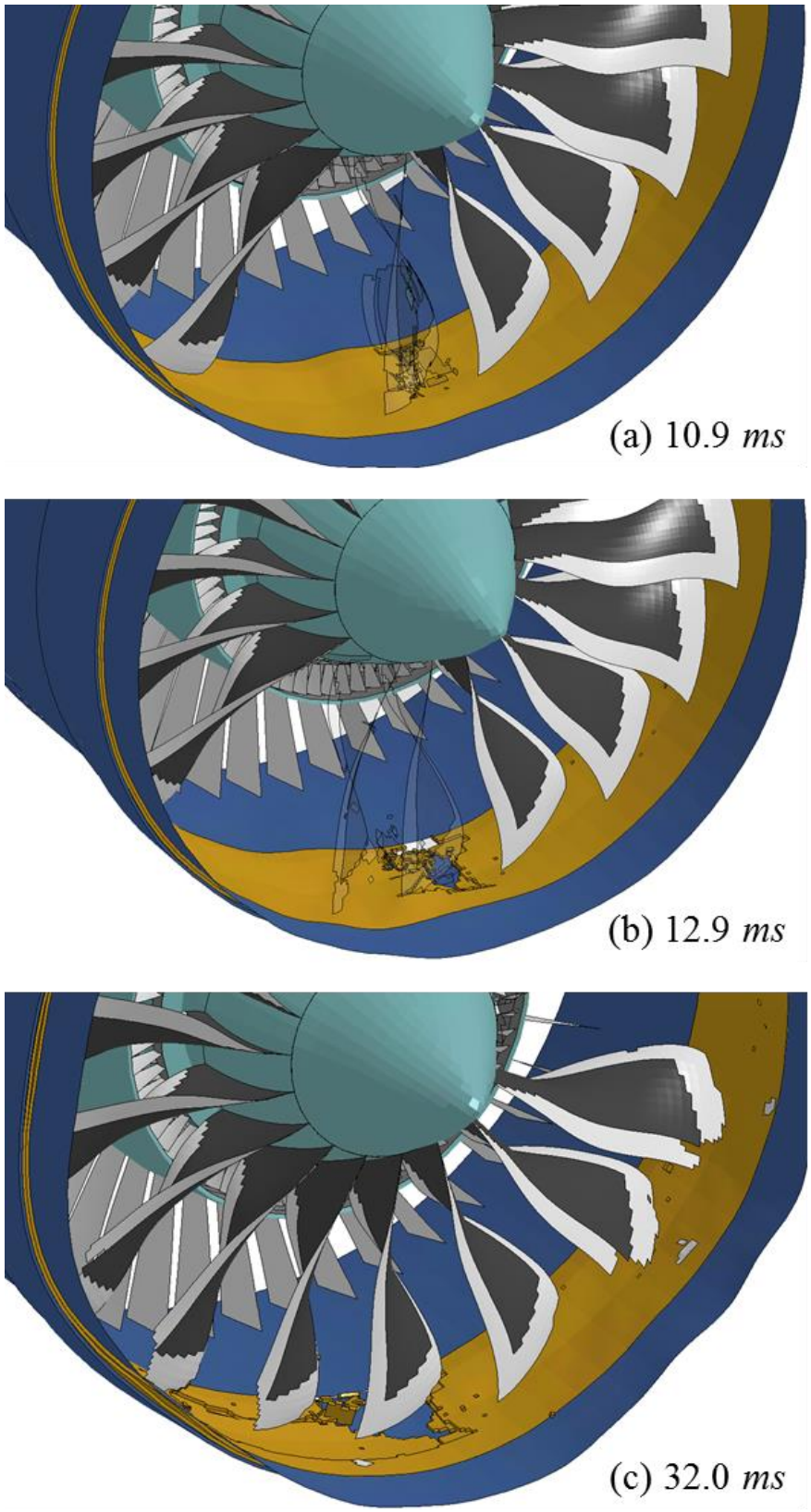

Figure 7.5 Damage response on a hybrid casing design (#2) from FBO. Fan blades were transparent to represent the damage evolution on fan casing

The hybrid casing model #2 was overall successful in arresting any subsequent damage on propulsion caused by FBO. However, the system was subjected to greater magnitude of damage due to the inner Kevlar layer entangling with the entire fan assembly. Figure 7.6 shows a closer view of the damage on the #2 hybrid fan casing after several rotations. As seen from the simulation result, the damaged area was widened and the damage on the fan blades was also much more severe to compare with the #1 hybrid casing design.

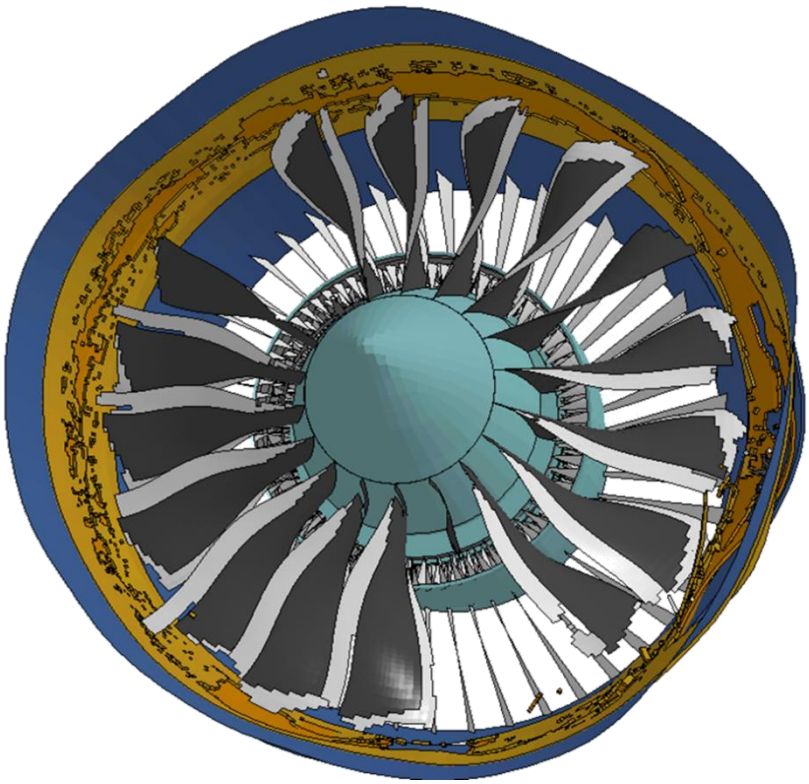

Figure 7.6 Damage on hybrid casing #2 caused by FBO

Last, the structural response of #3 casing design which used only Kevlar layers was investigated upon FBO. The initial contact between casing and blade debris caused an immediate failure on the casing as depicted in Fig. 7.7-(a). Then the interaction among the adjacent fan blade, debris, and the fabric thick section of casing magnified the damage on the casing as previously observed in the other casing design (#2). Figure 7.7-(b) shows the Kevlar slicing damage mode caused by the fan blades. Because of such severe interaction, both inner layers were eroded and the abrasion was widely observed. As shown in Fig. 7.7-(c), the damaged area was broadened as a result of continuous fan rotation. Eventually, the contact between the fan casing and the fan blade applied high bending load on the fan assembly and one of the severely damage fan blade detached and became an additional fragments impacting on the pre-damaged structure.

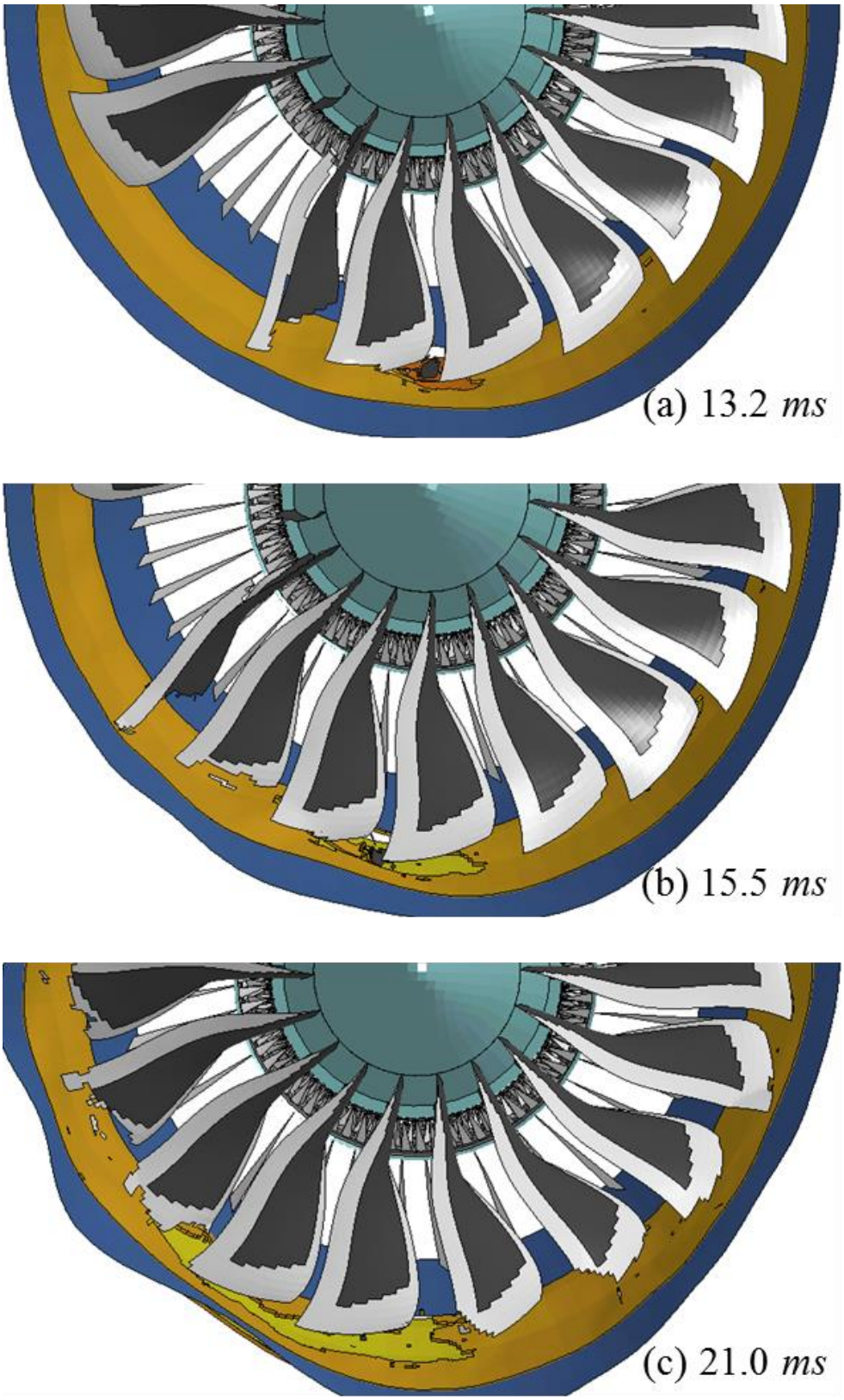

Figure 7.7 Damage response on a casing design (#3) from FBO

Catastrophic damage on the fan casing was produced by the additional FBO. The following image shows the failure of debris containment after additional FBO occurred. As seen in Fig. 7.8, the detached fan blade managed to impact a previously damaged section of casing. Because the casing material was already severely abraded by continuous interaction with fan assembly, the rest of the structure was completely compromised upon the secondary impact.

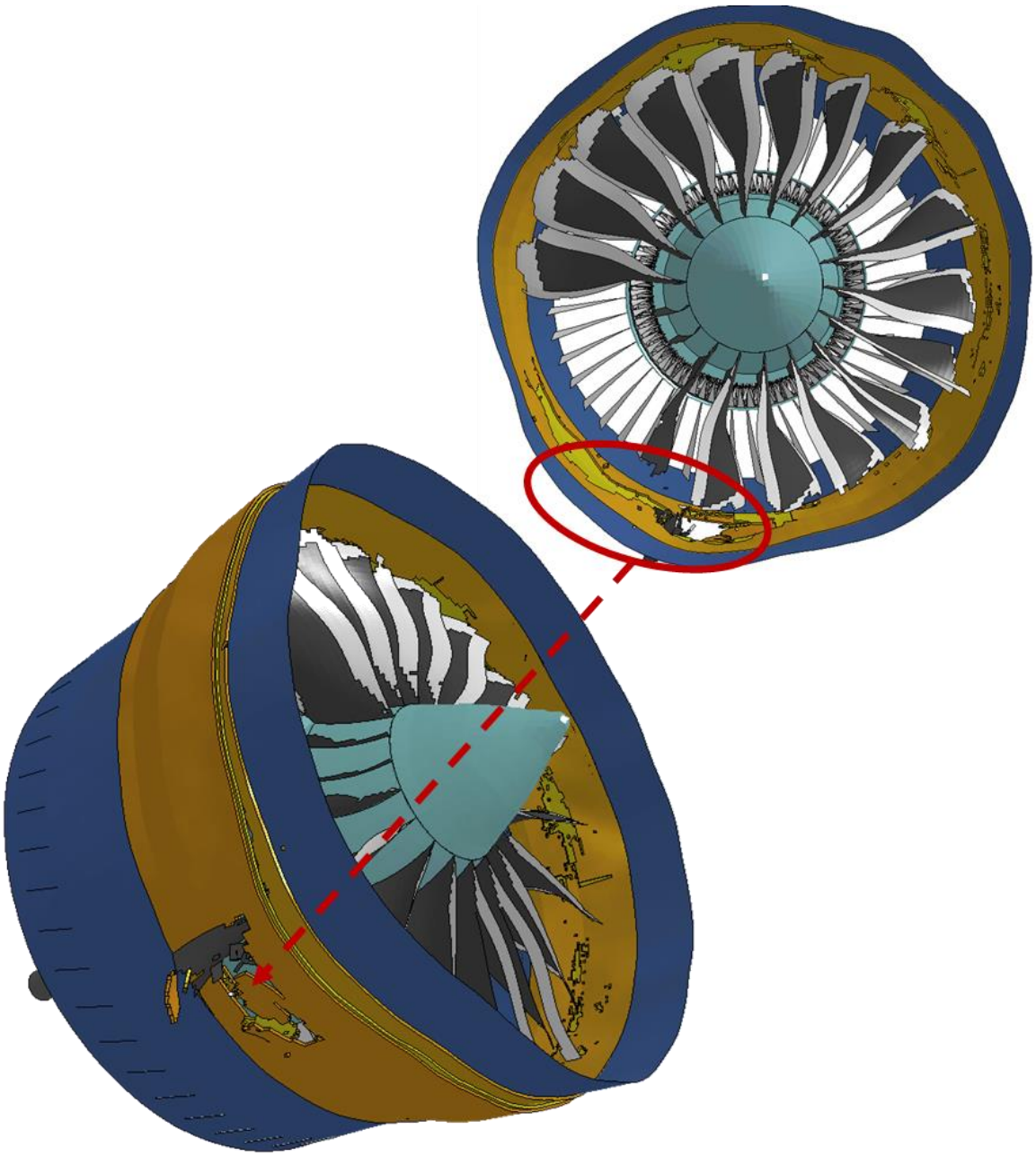

Figure 7.8 Failure of debris containment of #3 casing design after FOI

Such failure of debris containment is undesirable, hence the #3 casing design failed to comply the requirement. Alternatively, the other two fan casing designs successfully arrested the debris created by FOI despite the high debris speed and severe fan assembly and casing contact. The conventional design, which was discussed in previous FBO investigation section, required an additional 130 *kg* of aluminum material to ensure the successful debris containment. On the other hand, both hybrid casing designs only required an additional 50 *kg* of Kevlar layers to ensure the passenger safety from FBO incident. Although both hybrid casing design successfully arrested debris, the damage containment of the system was superior when the inner layer was made out of Kevlar.

7.2 Investigation of an Alternative Fan Blade Design

As discussed, the primary damage mechanic caused by FOI is compressive failure for both the fiber and matrix near the impact regime. The fan blade subjected to the combined loading condition near the blade root eventually failed due to radial stresses from continuous rotation after the impact. Such damage progression is caused by the reduced residual post-impact strength. The vulnerability of the post-impact residual strength of CFRP is also well-known in both tensile and compressive loadings [148,149]. In order to compensate for these issues, much research has been conducted in past decades to develop a unique design to elevate the post-impact residual strength. Stitched composites are a potential solution to ensure the mechanical strength of damaged composite structures after failure by reinforcing the inter-laminar bonding with stitches in the through-thickness direction [150–152]. However, the stitching on composite panels prohibits the delamination which inherently causes more localized failure near the impact regime and reduces the ballistic performance [146].

After the investigation of the damage mechanics of composite material and alternative designs, a new fan blade design was proposed by adjacent a metal alloy with composite material. Since the primary damage mode of composite fan blade is caused by compressive load, a titanium sheath was developed to replace the leading edge composite section in order to mitigate the compressive failure caused by impact. In order to keep the surface continuity, the titanium leading edge was designed using a 8 *mm* thick Ti-6Al-4V as shown in Fig. 7.9. The rest of the fan blade sections, which are the main section and edge section, remained constant such as the individual ply thickness, stacking sequence, and damage model. The additional weight assigned to develop the alternative design was approximately 15% of its original mass, increasing the mass of each blade by 1.7 *kg*. The alternative

fan blade structure was then subjected to the same impact conditions previously used for the FOI investigation to compare the damage susceptibility with the original design.

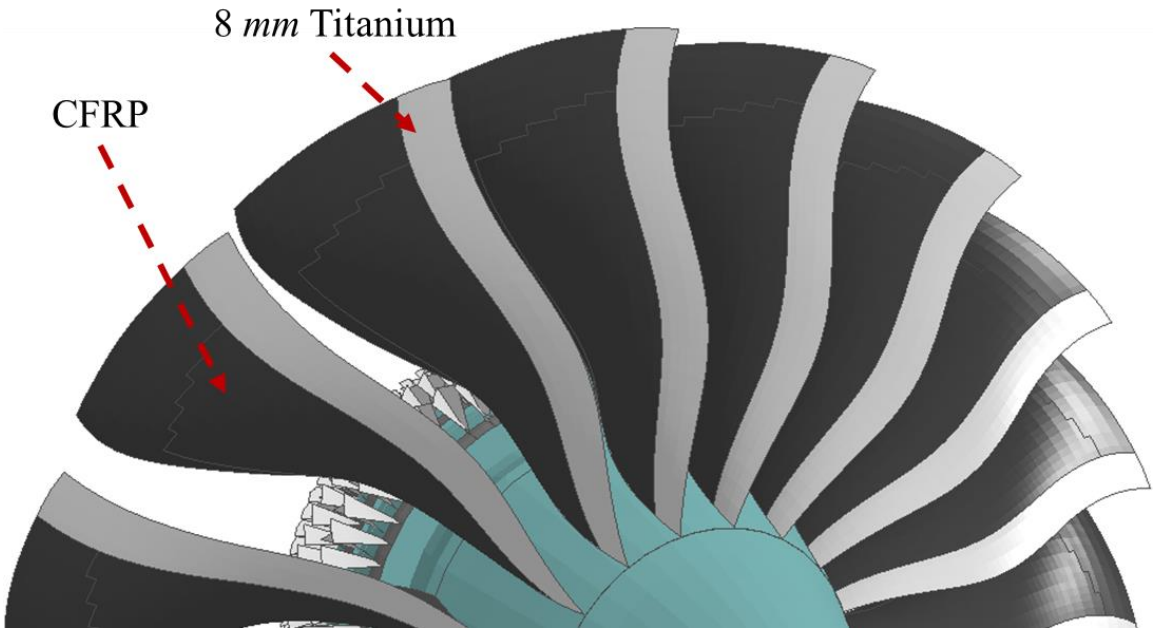

Figure 7.9 Alternative fan blade design for high FOI resistance performance

First, the 0.3 *m* impact scenario was simulated with the same condition as seen in Section 6.2.1. Figure 7.10 shows the elastic and plastic strain on the fan blade after a 2.5 *kg* bird impact at the same conditions as previously discussed. Because of the averaged young's modulus of composite section was relatively close to that of the titanium alloy, a smooth strain distribution was observed along the interaction as shown in Fig. 7.10-(a). As shown, the most heavily impacted fan blade suffered from a large deformation near the blade root. The strain predicted near the leading edge blade was 1% which is significant for carbon fiber material.

The titanium edge of heavily impacted fan blade was subjected to a plastic deformation as presented in Fig. 7.10-(b). Yet, the sheath was able to resist against the leading edge failure due to the impact loading which was observed in Fig. 6.10. Because the plastic deformation was limited within the titanium edge, the post-impact fan blade structure was still intact and the simulation result was presented the possibility of continuous operation after the impact.

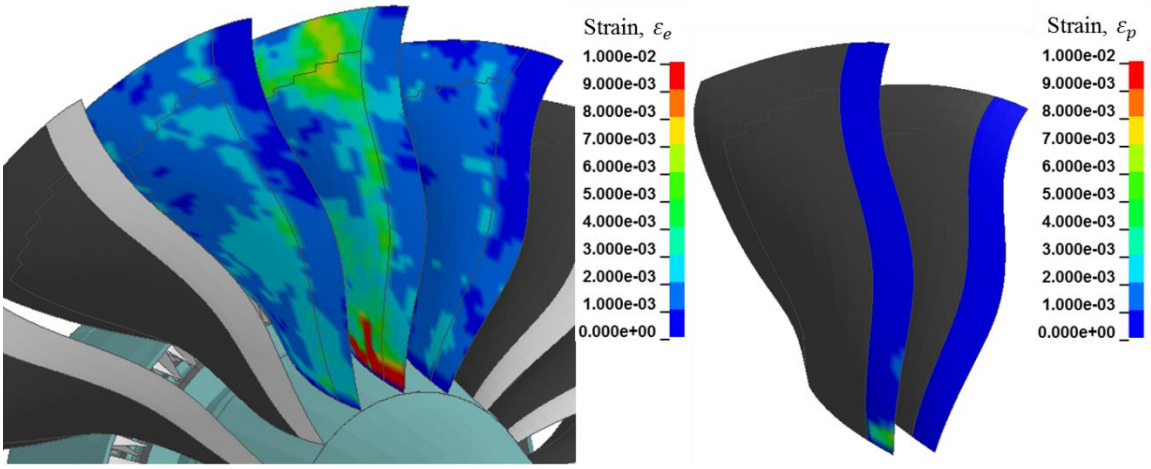

Figure 7.10 Post impact elastic (a) and plastic (b) strain response along the fan blade after impact occurred at 0.3 *m* leading edge height (*m*= 2.5 *kg*, *v*= 92 *m/s*)

Figure 7.11 shows the three major damage modes occurred on composite section of the two heavily impacted fan blades without averaging to show a clear damage path on the structure. As seen, the impact loading was still intense enough to disintegrate some of plies' fiber and matrix micro-structure, yet the titanium leading edge prevented any complete material failure. As the sequences of pictures implies, the most severely damaged location was at the blade root near the leading edge section behind of the titanium sheath. Because of the direct contact with the projectile, the structural disintegration was initiated near the impact regime and propagated along the high stress regime due to centrifugal loading. After some of the fibers failed, tensile matrix failure was initiated near the blade root of heavily impacted fan blade.

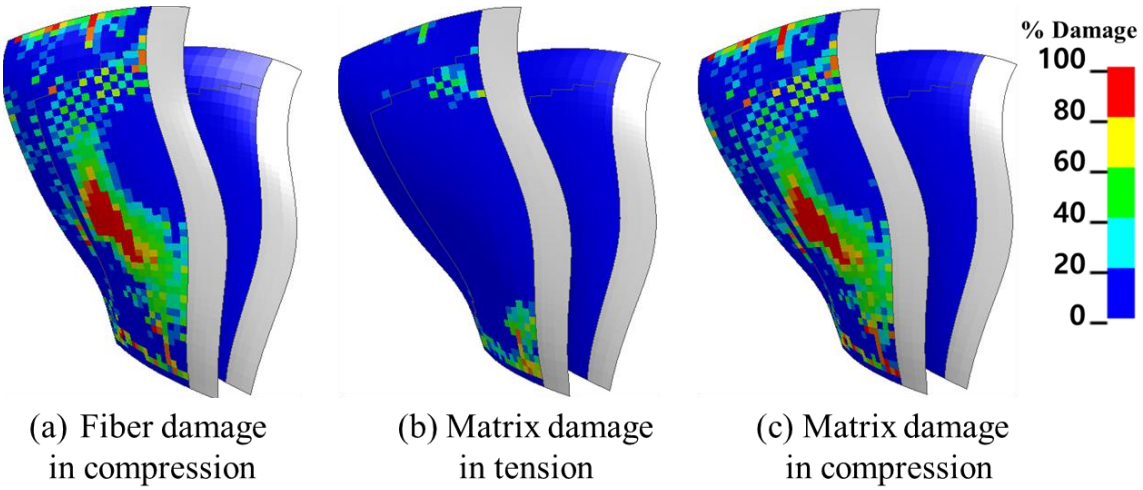

Figure 7.11 Damage mode on composite section of fan blade hit by a 2.5 *kg* bird (0.3 *m*)

Next, another impact scenario was investigated. As previously, a bird was impacted on leading edge at 0.5 *m* from the blade root. Similar to the first impact investigations, the most heavily impacted fan blade was subjected to the highest loading. The contact regime with a bird projectile in this simulation was wider to compare with the earlier case. The broadened contact area increased the bending load applied to the leading edge part of fan blade root as seen in Fig. 7.12-(a). Additionally, the impact applied more intense compressive loading on the trailing edge to compare with the 0.3 *m* impact case which resulted in failure as shown in Fig. 7.12-(a). Other than the failure that occurred at the trailing edge, the stress propagation along the composite section of fan blade was resembled with the damage signature from previous case. As expected, the plastic deformation on titanium leading edge occurred near the impact regime as well as at the blade root as shown in Fig. 7.12-(b).

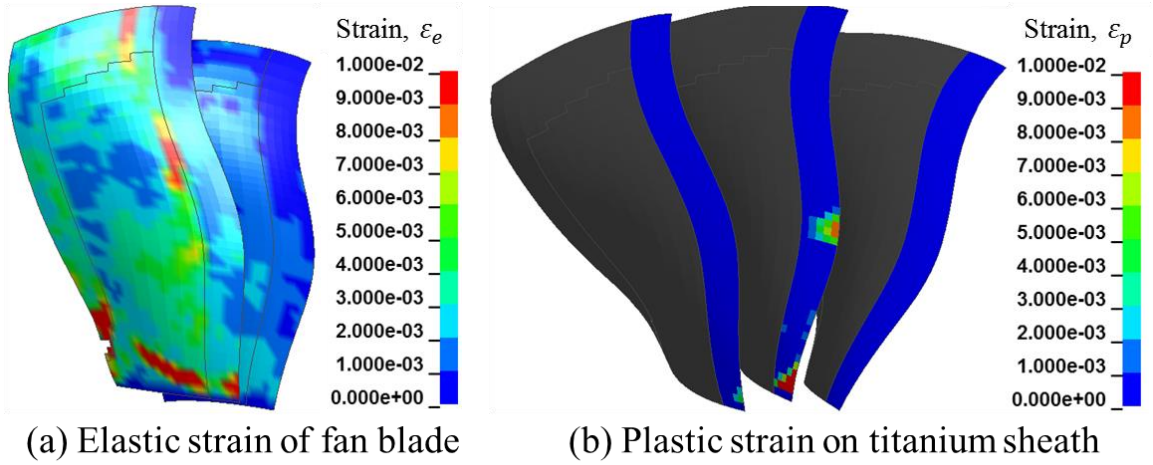

Figure 7.12 Post impact elastic (a) and plastic (b) strain response along the fan blade after impact occurred at 0.5 *m* leading edge height (*m*= 2.5 *kg*, *v*= 92 *m/s*)

To compare with the original design, the post-impact structural damage was reduced. As seen in Fig. 6.13 in section 6.2.1, a 2.5 *kg* bird damaged two of the original fan blade leading edge near the impact regime. Overall, the titanium leading edge was improved crashworthiness of fan blade successfully up to 0.5 *m* leading edge height impact.

Although the impact resistance performance was noticeably improved by hybridizing the titanium sheath with the existing composite structure, the new design was not able to prevent FBO when a projectile impacted at 0.75 *m* from the fan blade root. The impact triggered a negligible plastic strain on the titanium sheath to compare with two previous impact scenarios. As was observed with the original design, the extended moment arm caused immediate composite section failure from the trailing edge near blade root during the impact as presented in Fig. 7.13-(a).

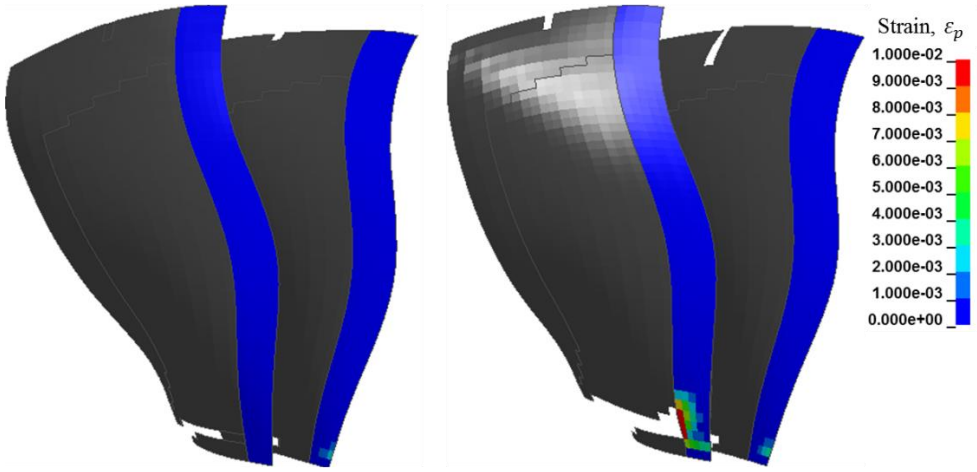

Figure 7.13 Plastic strain on the titanium sheath at the moment of impact (a) and after continuous rotation after impact (b) occurred at 0.75 *m* leading edge height (*m*= 2.5 *kg*, *v*= 92 *m/s*)

The reduction of impact load as well as the target fan blade ejection was discussed in section 6.2.1 when the impact occurs at 0.75 *m*. In short, the initial contact caused an immediate failure near the trailing edge at the blade root due to the bending load, which progressively developed due to the continuous rotation. The similar damage mechanics was occurred for the new composite-alloy hybrid design. The titanium leading edge was initially able to resist the damage propagation, but eventually failed due to the combination of continuous rotation and contact between fan blade and casing. Because titanium sheath was resisting the separation unlike to the composite fan blade thanks to its ductility, the ejected fan blade was gradually impacted on the casing and the complete separation was occurred when the damaged fan blade started contacting with the casing. The titanium sheath assisted the casing FBO arrestment by gradually distributing the fragmentation over the wider range of casing.

In order to overcome the shortages of using composite material for fan blade design, a hybrid metal and composite structure was proposed in this chapter. By adding 15% more weight, the new design was able to improve the crashworthiness of propulsion system up to an impact scenario up to 0.5 *m*. More thorough research including the fabrication methodology must be investigated to finalize the proposed model. Currently, a complete bonding assumption was used for the analysis, but for the actual production, stitching between titanium leading edge section and composite main section or using an adhesive material to bond both structure would be a proposed methodology to hybrid two structures. By using the comprehensive FOI damage assessment methodology, the proposed hybrid metal composite fan blade design was successfully developed and the impact resistance was computationally evaluated.

8 Simulation of Fluid Field along Propulsion System and Damage Investigations

Many preceding studies have attempted to capture the dynamic response and damage mechanics of fan blades subjected to impact. However, seldom is the entire propulsion system subjected to FOI, and to the author's knowledge, no studies thus far have considered the effects of air flow over the subjected system. Coupling fluid and solid mechanics into a single domain has been the goal for the computational analysis community. Even though hybrids of fluid and solid mechanical solvers exist, most of the methodologies solve the problem in two separate domains by assuming either a rigid body assumption for fluid analysis or the absence of fluid in structural analysis. The fluid field along the propulsion system was modeled by tightly coupling both disciplines into a single domain finite element framework. The ALE methodology is uniquely implemented to simulate the fluid flow along the advanced modern air-breathing propulsion system.

ALE is one of the most successful methodologies in the finite element domain for capturing large deformations of solid objects and fluid mechanics using the mechanical solver [153,154]. The ALE formulation was compared to other existing fluid solvers and preceding experiments, with the results presented in Appendix-C.

By coupling the fluid field modeling methodology, with structural solver a comprehensive FSI study was attempted to simulate any additional damage on the structure caused by including the interaction between fluid and structure. Additionally, any fluid disturbances caused by fan blade deformations or fluttering were captured. For the fluid model, the air was assumed as the ideal gas. In order to define the ideal gas, the Linear Polynomial EOS and fluid body deformation model were selected. Table 8-1 shows the mechanical definition for the air model used for the computational investigation.

Table 8-1 Material definition of the ideal gas at 1 *atm*

	Air
Density, ρ (kg/m^3)	1.20
Dynamic viscosity, μ ($Pa \cdot s$)	1.746e-005
Gas constant, γ	1.4
Pressure, P_a (kPa)	101.325

8.1 Simulation Results of Air Flow along Fan Assembly

The simulation setup is shown in Fig. 8.1. To model the ALE in front of the engine, approximately 1.5 million ALE elements were created. The stress initialization was applied in advance of the comprehensive FSI investigation. The air ingestion speed was set same as the bird ingestion speed (92 *m/s*).

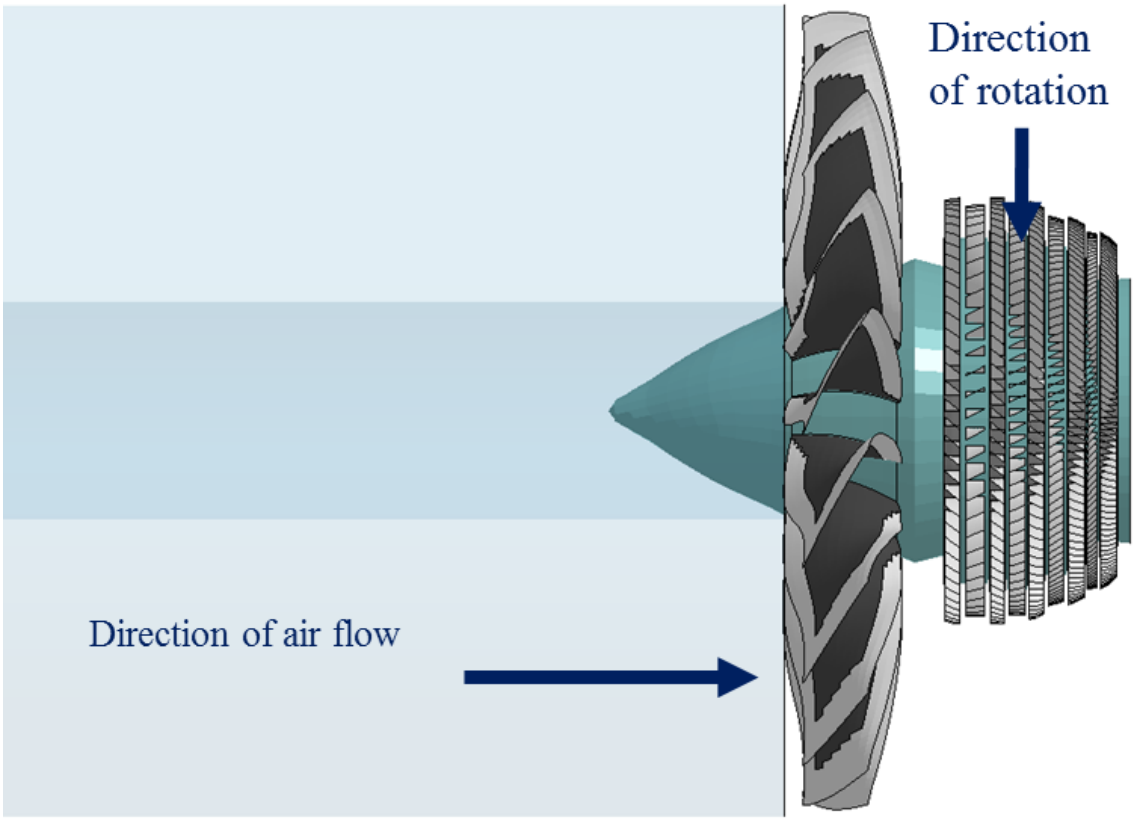

Figure 8.1 Simulation setup using comprehensive FSI for high-fidelity FOI damage assessment

In order to make contact between ALE formulation and the conventional finite element Lagrangian formulation, a penalty based contact was selected using the penalty based contact. Typically, the recommended penalty stiffness is adequate for most FSI problems when both fluid and structure materials do not have a drastic density disparity. For example, FSI problems such as an aircraft water ditching simulation [155] or crash landing on soil simulation [156] do not require additional modifications from the recommended setup.

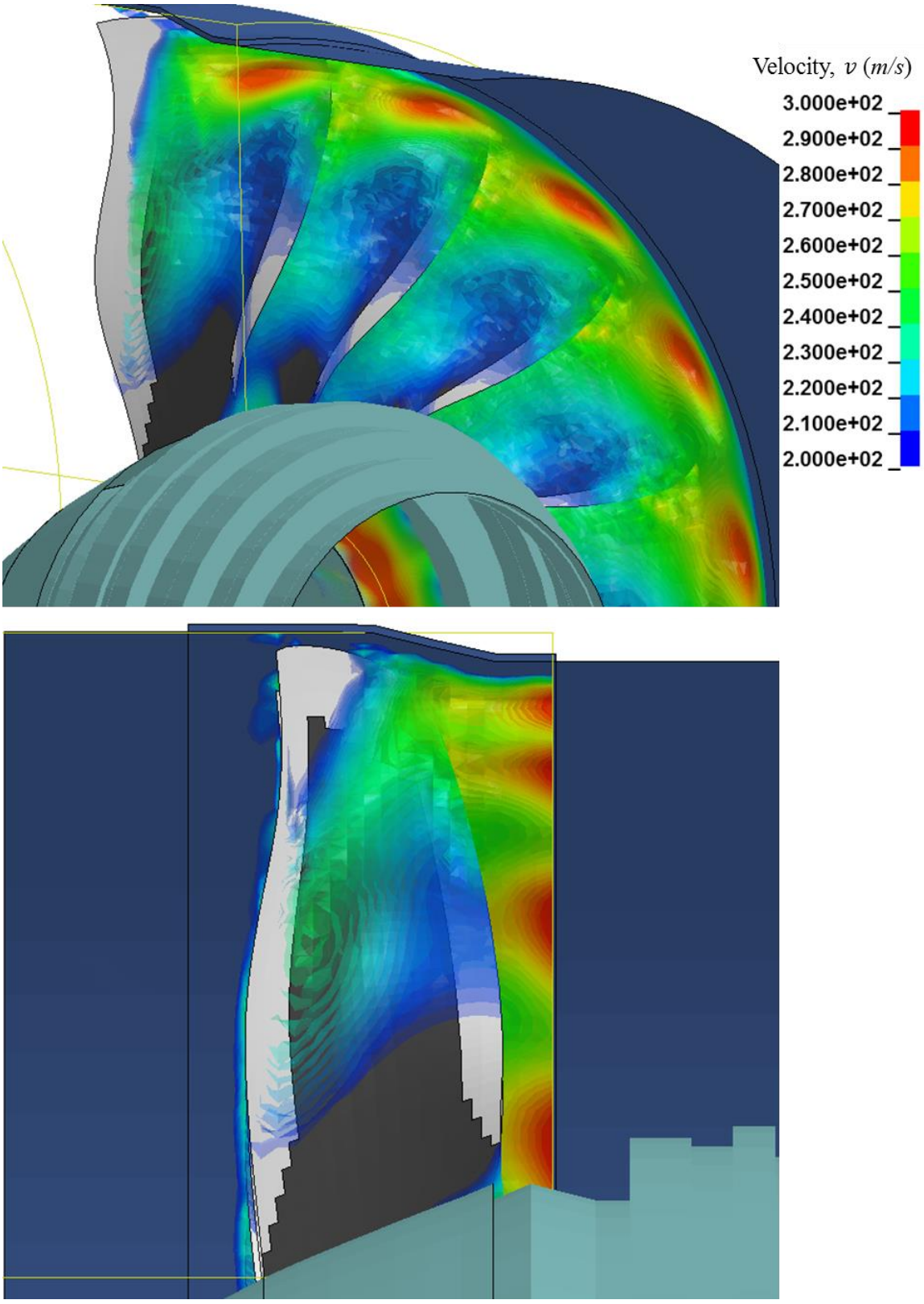

Figure 8.2 Air flow velocity along the front fan section using 3-D comprehensive FSI methodology (back isometric view (top) and side view (bottom))

However, the density difference between the structure and air is significant. Such density disparity, in this analysis, often caused "out-of-range velocity" errors on ALE elements near the interface and failed to converge to the solution. Because of the severe disparity of density between air and CFRP materials, the penalty scale factor was modified from the recommend value to avoid simulation divergence. First, the air flow along the deformable structure simulation result is shown in Fig. 8.2. The corresponding energy plot calculated from the simulation is provided in section 0. The penalty based contact accelerated the fluid velocity as shown in the velocity isosurface plot.

The fluid velocity behind of the fan blade ranged from 156 to 271 *m/s* at the blade root and tip, respectively. The comprehensive FSI methodology was also able to interact with the casing. Because of the narrowed section of the casing (behind of the fan blades), the air speed near the tip regime was accelerated up to 320 *m/s*. The amount of force applied on the entire fan assembly was measured to compare the simulation result to the commercially available jet engines. The overall thrust generated by the entire inlet assembly was approximately 200 *kN*. Although the simulation was performed by using the defeatured fan blade geometry, the magnitude of thrust value measured from the simulation result was corresponded with commercial jet engines' thrust production by their inlet fan section [26,41].

This proposed methodology was able to capture the pressure rise coefficient of fan blade. As a benefit of using the penalty based contact with the proposed comprehensive FSI methodology, not only the acceleration of airspeed, but the pressure rise across the fan blade of the virtual propulsion system used for the investigation was calculated. According to the simulation result, the pressure behind of the fan blade was measured as 154 *kPa* near the tip regime as seen in Fig. 8.3. Based on the initial boundary conduction mentioned above, the pressure coefficient of the virtual fan blade was evaluated as 1.5.

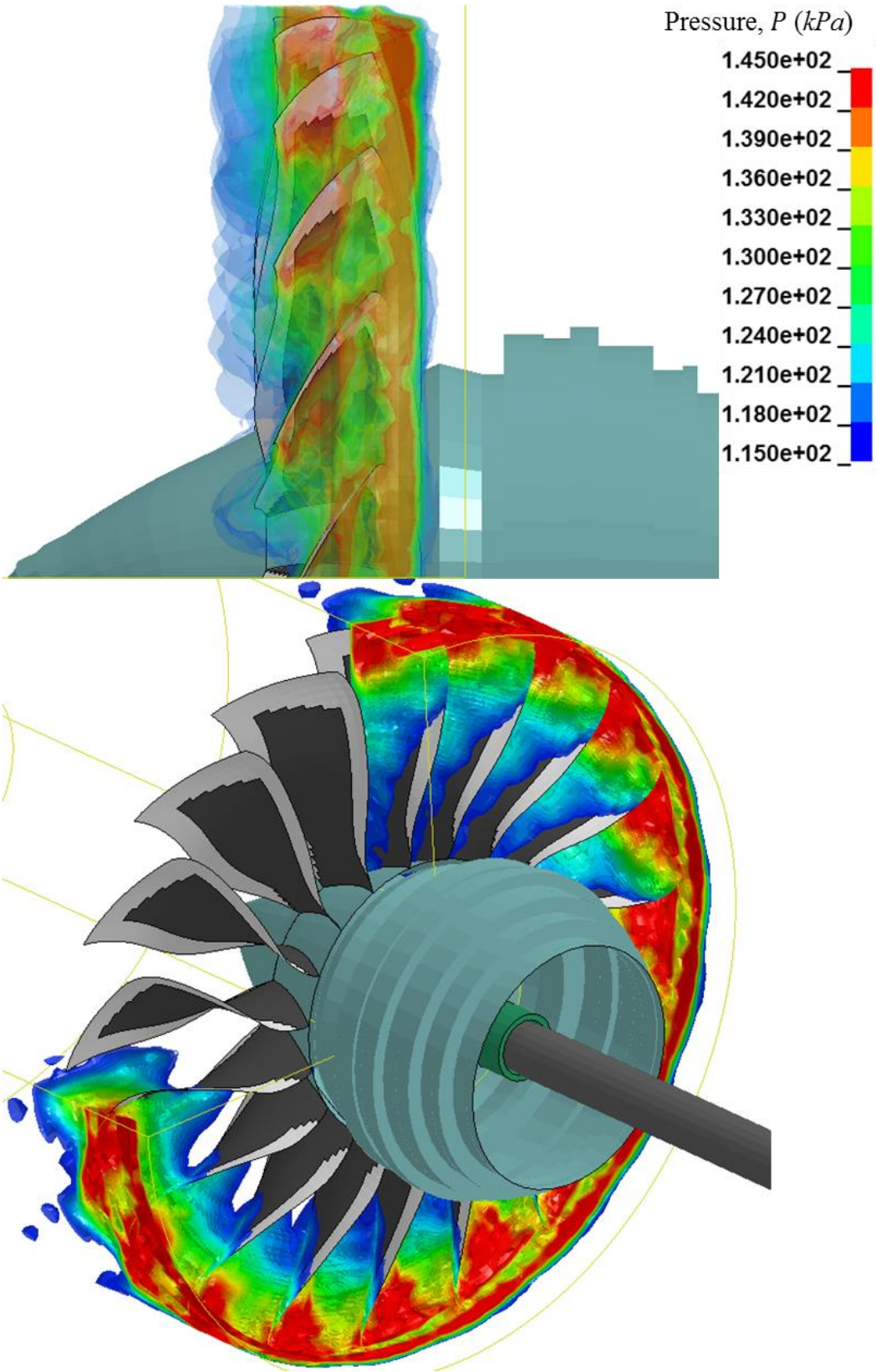

Figure 8.3 Pressure isosurface plot behind of the front fan section

Additional bending loads were expected due to the interaction between air and structure, which is important since the additional aerodynamic load can impose a high blade root stress. The presented 3-D comprehensive FSI methodology was able to simulate this phenomenon. Figure 8.4 shows the blade root stresses measured near the blade root. Because of the additional bending load introduced by the air flow along the fan section, the blade root stress was slightly increased. Because the increase of root stress becomes minimal after first quarter of the simulation, the projectile was placed to impact at the time. The result implied that the damage mechanics might be changed by adding the aerodynamic interaction to the comprehensive FOI damage assessment methodology.

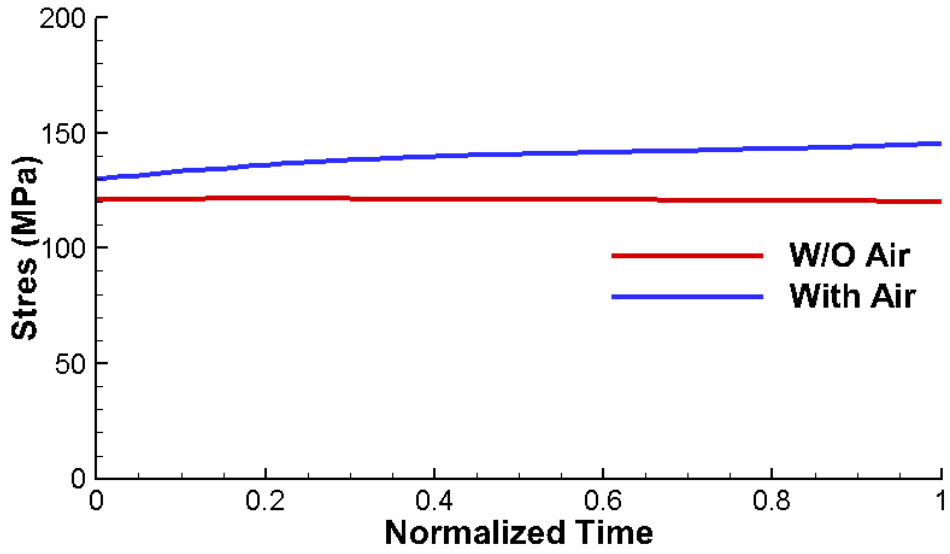

Figure 8.4 CFRP blade root stress comparison between with and without air flow along the system rotating at 226.8 *rad/s*

8.2 Study of Dynamic Response of Turbofan Engine Subjected to FOI with Comprehensive 3-D FSI Methodology

The developed FSI methodology was uniquely employed to the existing FOI simulation conduct a dynamic structural response and damage evolution upon a 2.5 *kg* bird ingestion. The ingestion condition was designed identically to one of the previously conducted investigations (impact at 0.5 *m* leading height and 92 *m/s* ingestion speed) in section 6.2.1. The velocity isosurface contour plot is shown in Fig. 8.5. The velocity contour plot was captured before any failure was initiated on the impacted fan blade. As seen, the velocity distribution across the fan assembly was periodically repeated for the entire fan blades except the impacted fan blades.

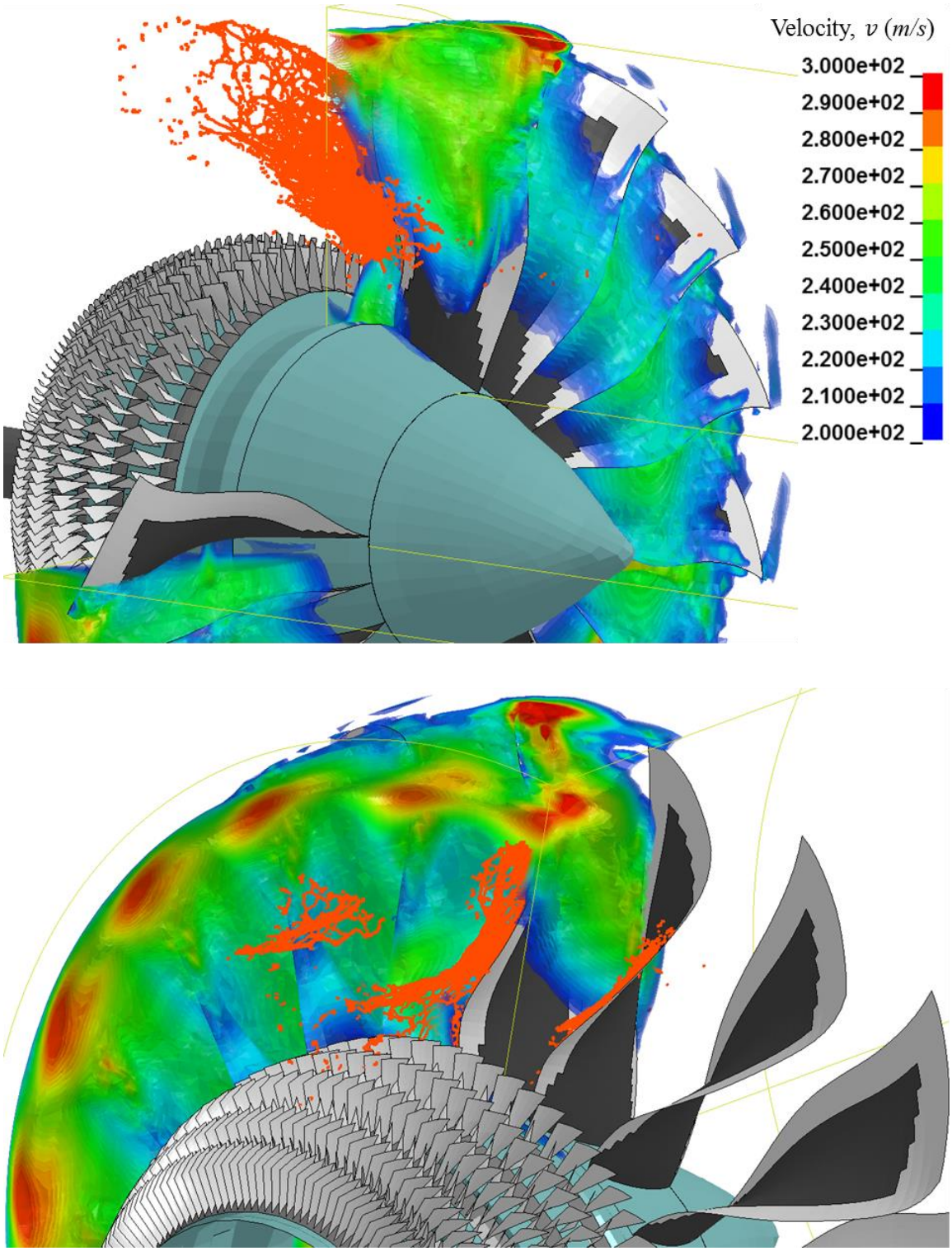

Figure 8.5 Front view (top) and backside isometric view (bottom) of air velocity isosurface along the front fan section after a 2.5 *kg* bird ingestion and impacted at 0.5 *m* leading edge height

The disturbance of fluid was caused by the dynamic response of the target fan blade (fluttering) after the impact. Since the fan blade bends in the rotational direction, the air flow was corresponded

with the motion and was blown toward the rotational direction of the fan assembly rather than the normal flow direction induced by rest of the fan blade. The off-designed behavior was qualitatively predicted in the figure above. The disturbance of air flow due to the damaged fan blade and the corresponding stress distribution along the fan blade are provided in Fig. 8.6.

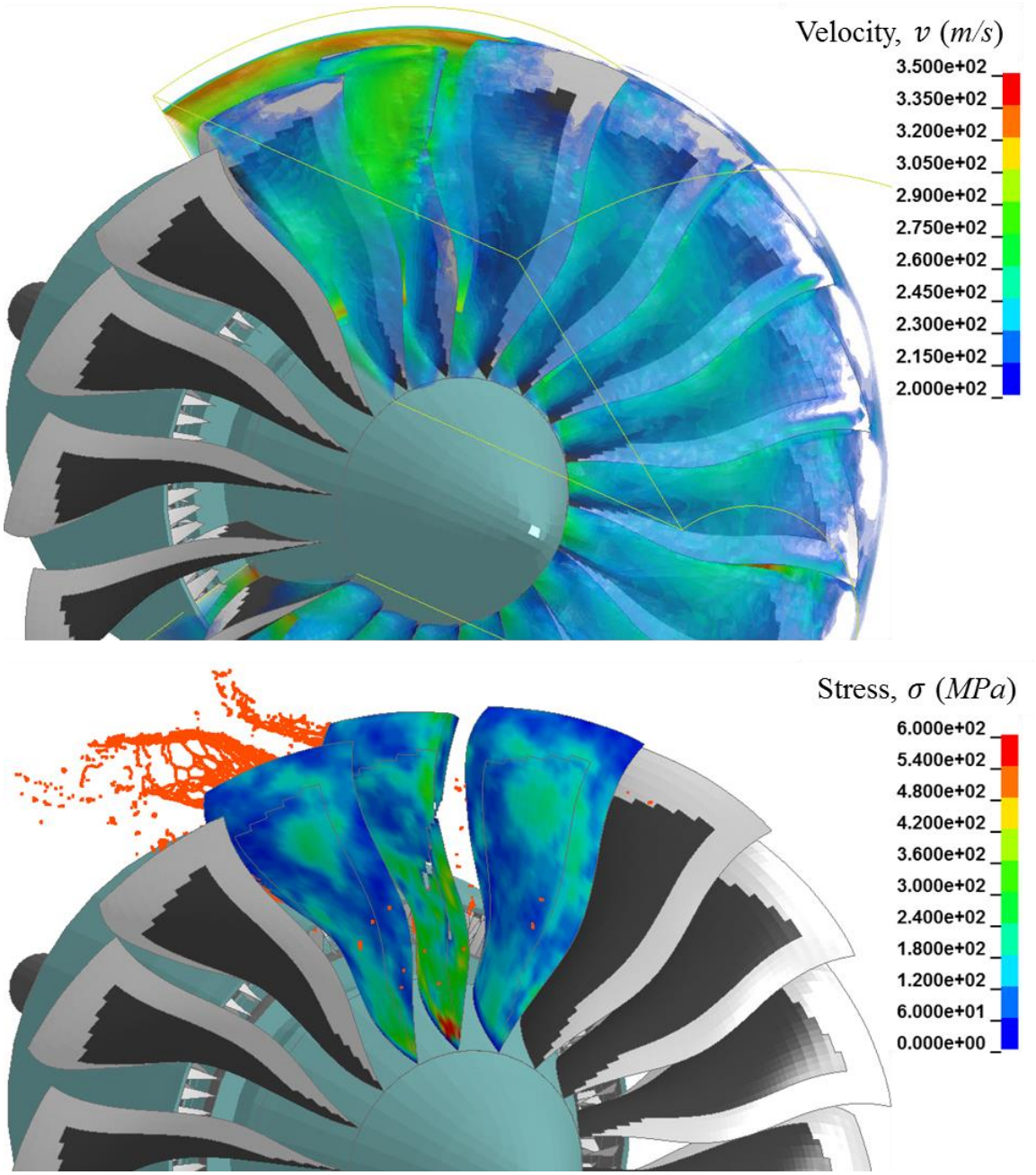

Figure 8.6 Transparently visualized disturbance of air flow along the damaged fan blade (top) and the stress on the target fan blade (bottom)

The 3-D comprehensive FSI methodology was able to successfully capture the aerodynamic interaction in addition to any structural deformation and degradation as shown in Fig. 8.6-(a). The disturbance of air flow corresponded with the fan blade fragmentation which is presented in Fig. 8.6-(b).The implementation of air changed the damage mechanics of a propulsion system subject to a FOI. Because of the interaction with the ingested air, the damaged blade was subjected to a higher bending load, leading to further damage of the fan blade.

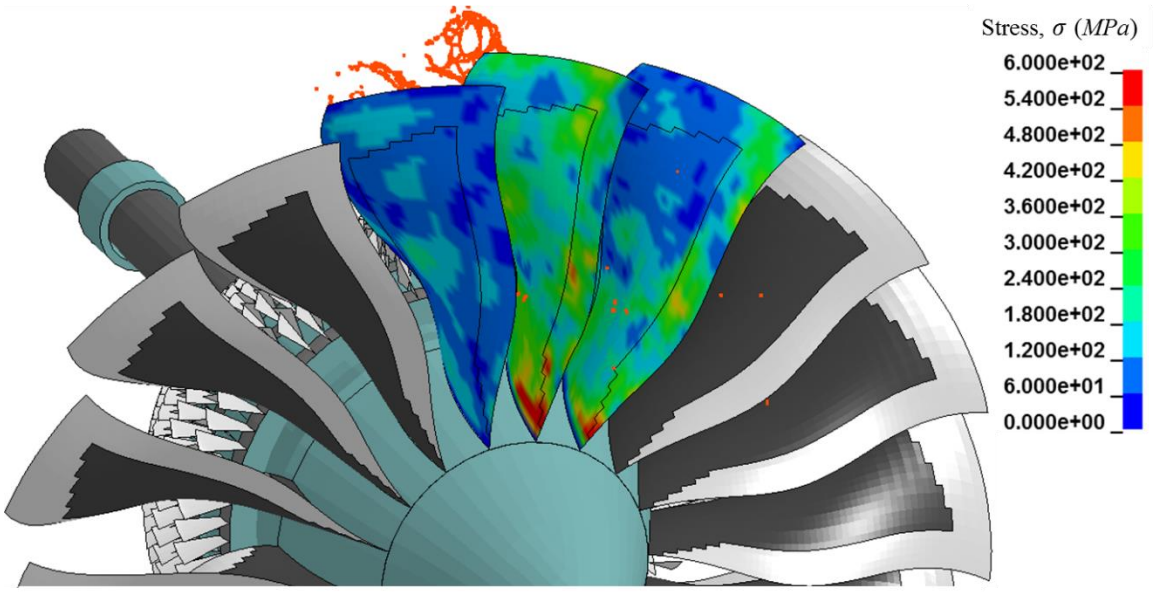

(a) Stress distribution and damage response of impacted fan blade without air flow

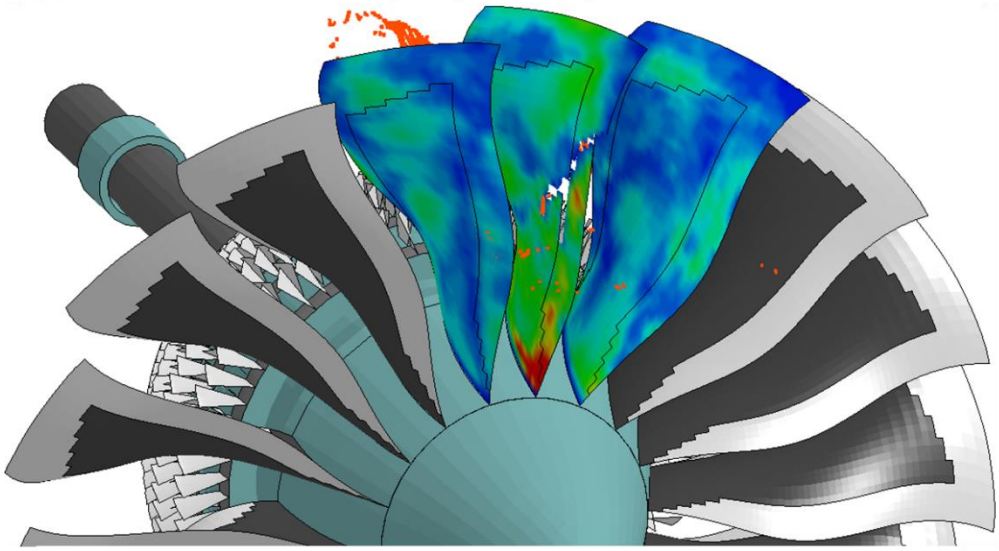

(b) Stress distribution and damage response of impacted fan blade with air flow

Figure 8.7 Comparison of immediate damage response of fan blade hit by a 2.5 *kg* bird between without air flow (a) and with air flow (b) along the front fan assembly (at 0.5 *m* leading edge height)

The two images shown in Fig. 8.7-(a) and (b) are bird ingestion simulation results with and without air flow, respectively for the same instant. The damage response presented in Fig. 8.7-(a) is in between Fig 6.13-(b) and (c) in section 6.2.1. before the leading edge failure started. As shown, the immediate damage response of the entire fan assembly was noticeably changed when the air flow was introduced in the FOI investigation.

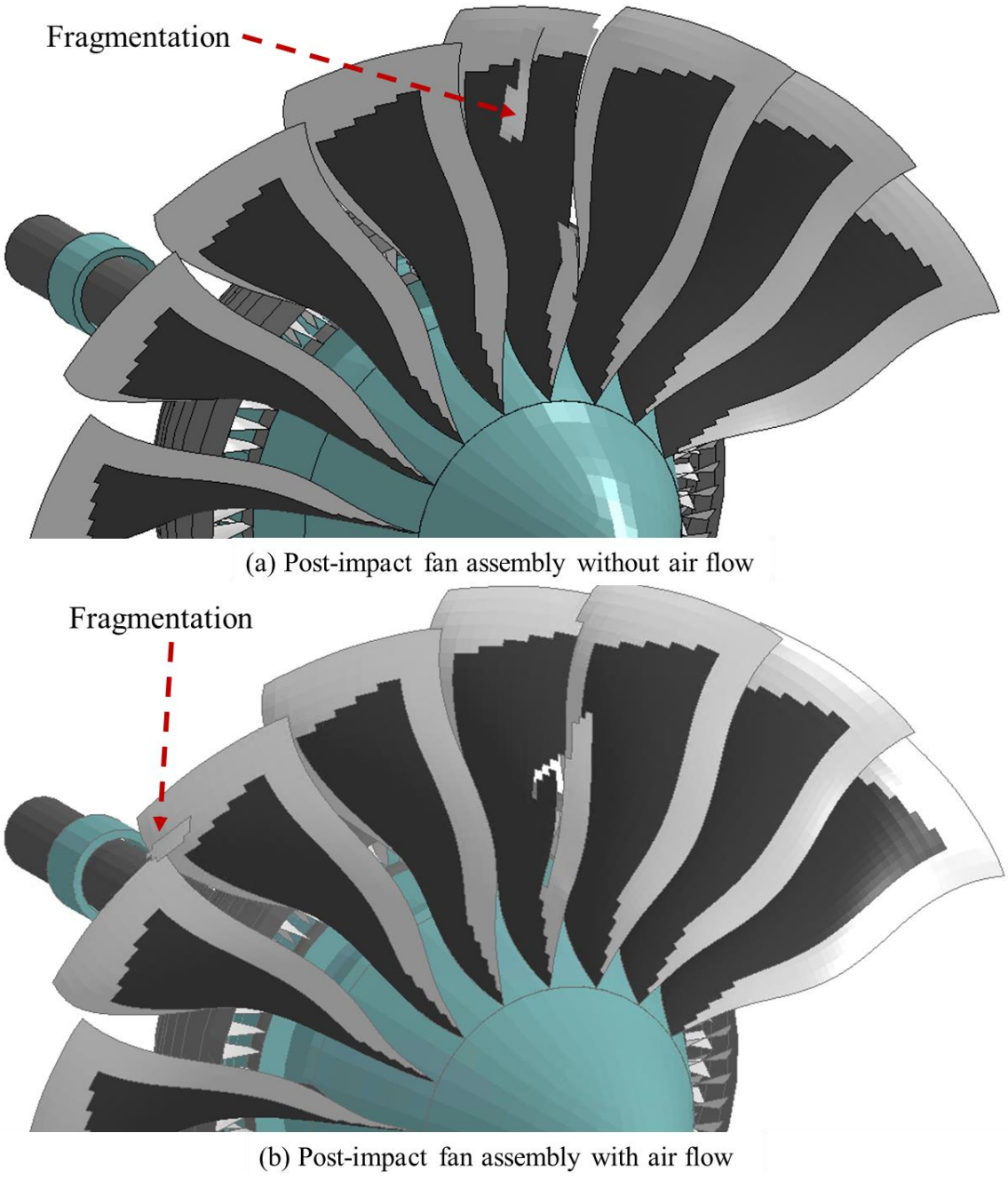

Figure 8.8 Comparison of post-impact damage on fan assembly between without air flow (a) and with air flow (b) (Same time frame as the image shown in Fig. 6.13-(d))

Based on the previous investigation, no immediate structural disintegration was observed as depicted in Fig. 8.7-(a). However, such damage response of the fan assembly was changed soon as the air flow was considered in the computational investigation. Near the impact regime, the fragmentation of fan blade occurred immediately after the initial impact as seen in Fig. 8.7-(b). Because of the more rapid fragmentation in a combination with aerodynamic interaction, the fan blade debris impact location was also shifted.

Figure 8.8 shows the damaged inlet fan assembly after both fan assemblies made a half way revolution. The fragmentation in the simulation without air flow had just started as shown in Fig. 8.8-(a). On the other hand, the fragmentation had already occurred in the airflow simulation and the leading edge fragment was contacting the casing as seen in Fig. 8.8-(b). Because of the FSI, the fan blade debris impact location was noticeably shifted few centimeters backward which was not observed in the previous investigation. Interestingly, the impact velocity of fan blade fragments was reduced approximately 15% to compare with the FOI investigation without air model. The minor deceleration was caused by the debris' drag when it departed from the fan blade.

In addition to the fragmentation of fan blade, an additional damage on fan blade structure was detected when the air flow was considered in FOI investigation. Fig. 8.8-(b) also presents additional damage on fan blade structure. Unlike to the damage presented in Fig. 8.8-(a), the thick composite section was compromised. No further damage evolution was observed, yet the result implied the importance of considering a comprehensive FSI for the FOI investigation.

In an effort to computationally simulate a high-fidelity FOI investigation, a comprehensive 3-D FSI methodology was uniquely implemented to simulate the air flow along the front inlet assembly. Because of the lack of preceding research relating to the presented work, a sequence of analytical calculation was conducted for a semi-validation of the proposed methodology. The computational prediction for the velocity and pressure rise across the inlet fan assembly was close to the analytical calculation. Throughout the investigation, the FSI methodology was able to achieve the interaction between fluid body and deformable structure. The methodology was then combined with the soft body ingestion methodology to conduct the all-inclusive foreign object ingestion with fluid-structure interaction. The investigation successfully simulated the damage initiation, evolution, and fluid-structure interaction simultaneously within a single finite element domain to obtain a realistic structural response upon a FOI.

9 Conclusion

FOI is a relatively common, but critical air incident, occasionally causing severe damage to aircraft. Of the possible impact locations, ingestion into propulsion systems is of high concern, due to the significant threat that it poses to the integrity of the aircraft engines, external aircraft structures, as well as the safety of crew and passengers. Yet, the cost of full-scale experiments to assess the crashworthiness of the commercial jet engines is prohibitively high, requiring extensive efforts to conduct any trials. In order to assess and improve the crashworthiness of propulsion systems when subjected to bird and ice ingestions, a comprehensive computational damage methodology was developed to determine the complex dynamic response and damage progression of propulsion structures.

To begin, an advanced damage modeling methodology was developed to characterize the damage mechanics of a high-bypass propulsion system using a contemporary aerodynamic fan blade design with fiber reinforced polymer material. After the methodology was successfully developed, computationally verified, and partially validated against the existing experiments, it was extended to propose better fan blade and casing designs to improve FOI resistance as well as FBO arrestment. Further, a unique FSI strategy was developed by integrating both fluid and solid continua into a single domain finite element framework to enable the simulation of comprehensive 3-D domain FSI phenomena. Using this strategy, the overall methodology developed was able to capture the interaction between air and structure, which caused additional damage that had not otherwise been discovered in any of the previous FOI investigations.

Throughout the term of this research, it was demonstrated that the developed multidisciplinary and multiphysics computational methodology is a robust approach to create verified, crashworthy propulsion designs that can significantly contribute to improving structural integrity, as well as crew and passenger safety.

9.1 State-of-the-Art Contributions

Because of the complexity of the problem, the methodology was developed in several steps to establish successful damage assessment procedures. Overall, these steps contributed to advancing modeling damage using a highly non-linear FSI strategy.

First, the dynamic behavior of soft body projectiles impacting a target was thoroughly investigated to accurately analyze the impact mechanics. Because of a severe domain separation of the soft body continuum during impact, a meshless Lagrangian element formulation was extensively studied and subsequently applied, assuming that the impact can be classified as a complex FSI phenomenon. Doing so, a high-fidelity FOI damage model was developed for both bird and ice. In particular, the new fluidic ice damage model showed to capture a better trend than the currently existing ice damage model when assessing damage caused by hail impact. Additionally, the coupling of the new ice damage model and the damage assessment methodology helped estimate the trajectory of ice particles after the impact, which can significantly contribute to our understanding of icing issues in relation to propulsion systems. As part of the investigations, the methodology was successfully verified and validated using grid resolution studies, numerical uncertainty analyses, and comparison with existing experimental data for both projectiles.

Next, the structural mechanics were investigated to accurately establish the damage dynamics. Modern high-bypass engines use composite materials which have complicated damage mechanisms compared to conventional homogeneous isotropic aerospace metal alloys. Hence, a thorough study of existing composite damage models was conducted in order to integrate the state-of-the-art damage models and element formulations. 2-D and 3-D composite damage models were explored for both hybrid fan blade and casing structures, respectively. For the casing especially, a mesoscale composite damage model was employed in order to effectively simulate the progressive structural failure and delamination on impact.

After the supporting modules were developed, they were combined into a single domain to enable the coupling of an FOI onto a full-scale high fidelity propulsion model. Although the unique FSI strategy may require a sequence of complete full-scale experiments for a complete validation, it was able to successfully capture the damage initiation and evolution on the impacted system through using a verified and partially validated sub-algorithmic approach. This allowed for many possible damage mechanics to manifest, in addition to better exploiting direct damage on target fan blades, debris ingestion into LPC, and fragment arrest by the casing.

The uniquely developed modeling strategy was then employed to improve the crashworthiness attributes of the design using the high fidelity, fully parametrized virtual propulsion system, numerically compliant with the current regulations. A new casing design was proposed by adding Kevlar layers over the existing structural lay-ups, which successfully arrested any debris ejected from the fan assembly. The proposed Kevlar lay-up minimized the design mass of the casing. Not only a new fan casing design, but new hybrid fan blade structures were proposed to improve the impact resistance of the system. Further investigations as well as full-scale physical experiments

are required to verify the recommended designs. Notwithstanding that, the work demonstrates the potential to contribute to significantly less costly aerospace propulsion designs and certification-by-analysis procedures.

Finally, an overall, highly non-linear, multidisciplinary and multiphysics computational methodology was developed by combining all the unique features discussed above including the use of an advanced element formulation in addition to concurrent application of meshed and meshless structural analysis methods. The novel methodology contributed by enabling, for the first time, the capture of the 3-D interaction between air and propulsion system, while taking additional FOI events into account, and simultaneously analyzing their coupling effects. As a result, the high level methodology was capable of solving and assessing the full aerodynamic field, including air flow disturbances along the impacted, complex, and deforming structures of the fully parametrized, full-scale, high-bypass ratio air breathing engine.

9.2 Future Work

The work detailed in this document could be complemented by extending the efforts in several topics addressed in this section. More accurate impact response and damage mechanics can be achieved by adding the support structures and other non-critical components for the propulsion system, including the mounting mechanism (pylon structures) and possibly the wing. Next, a more representative fiber and matrix stacking sequence will be essential as used by the industry. In this work, the composite fan blade model was developed by referring to the available literature, which might result in different damage estimates compared to as-designed. However, since the developed methodology is fully parametrized, the material definitions can easily be updated. Another recommendation is to use the mesoscale composite model to define the fan blades. In this study, only 2-D composite plies in the form of shell structures were utilized to reduce the simulation run times. Using 3-D composite damage models can also improve the damage response of composite fan blades by capturing both continuum damage evolution and delamination in the event of FOI. The perfected methodology developed as part of this dissertation can directly contribute to the aerospace certification-by-analysis efforts and help establish firm design and optimization numerical procedures.

References

[1] FAA, 2013, “Passenger boarding (enplanement) and all-cargo data for U.S. airports,” **2014**(Jan.31.2014) [Online]. Available: http://www.faa.gov/airports/planning_capacity/passenger_allcargo_stats/passenger/index.cfm?year=2012.

[2] Nicholson, R., and Reed, W. S., 2011, “Strategies for prevention of bird-strike events QTR_03. 11,” Boeing, pp. 16–24 [Online]. Available: http://www.boeing.com/commercial/aeromagazine/articles/2011_q3/pdfs/AERO_2011_Q3.pdf.

[3] Dolbeer, R., and Wright, S., 2008, Wildlife strikes to civil aircraft in the United States 1990–2007, Federal Aviation Administration (FAA) and U.S. Department of Agriculture (USDA), Washington, DC.

[4] NTSB, 1978, Aircraft accident report: Southern Airways Inc., DC-9-31 NI1335U, New Hope, Georgia, April 4, 1977, National Transportation Safety Board, Washington, D.C.

[5] NTSB, 2010, Aircraft accident report: Loss of thrust in both engines after encountering a flock of birds and subsequent ditching on the Hudson River US Airways Flight 1549 Airbus A320-214, N106US, Washington, D.C.

[6] FAA, 1990, Turbine engine rotor blade containment/durability (AC No. 33.94), Washington D.C.

[7] FAA, 2004, Turbojet, turboprop, and turbofan engine induction system icing and ice ingestion (AC No. 20-147), Washington D.C.

[8] FAA, 2009, Federal Aviation Regulations/Aeronautical Information Manual (FAR/AIM) 2015: Bird ingestion certification standards, A.C. No. 33.76, Federal Aviation Administration (FAA), Washington D.C.

[9] Siddens, A. J., and Bayandor, J., 2012, “Detailed post-soft impact progressive damage analysis for a hybrid structure jet engine,” 28th ICAS.

[10] Siddens, A. J., and Bayandor, J., 2013, “Multidisciplinary impact damage prognosis methodology for hybrid structural propulsion systems,” Comput. Struct., **122**, pp. 178–191.

[11] Song, Y., and Bayandor, J., 2015, “Novel implementation of fluid-solid interaction analysis in air breathing propulsion systems,” Volume 1: Symposia, ASME, Seoul, Korea, p. V001T13A001.

[12] Song, Y., and Bayandor, J., 2016, “Analysis of Damage Assessment of Large Hailstone

Ingestion into Advanced High Bypass Propulsion system," 57th AIAA/ASCE/AHS/ASC Structures, Structural Dynamics, and Materials Conference, American Institute of Aeronautics and Astronautics, Reston, Virginia.

[13] Smojver, I., and Ivančević, D., 2010, "Numerical simulation of bird strike damage prediction in airplane flap structure," Compos. Struct., **92**(9), pp. 2016–2026.

[14] Nizampatnam, L. S., 2007, "Models and methods for bird strike load predictions."

[15] Guida, M., Marulo, F., Polito, T., Meo, M., and Riccio, M., 2009, "Design and testing of a fiber-metal-laminate bird-strike-resistant leading edge," J. Aircr., **46**(6), pp. 2121–2129.

[16] Chuan, Z., Xiang-hua, J., Xiang-hai, C., and Tong-cheng, S., 2015, "TC4 Hollow Fan Blade Structural Optimization Based on Bird-strike Analysis," Procedia Eng., **99**, pp. 1385–1394.

[17] Lakshman, N., Raj, R., and Mukkamala, Y., 2014, "Bird strike analysis of jet engine fan blade," 2014 IEEE Aerospace Conference, IEEE, pp. 1–7.

[18] Sinha, S. K., Turner, K. E., and Jain, N., 2011, "Dynamic loading on turbofan blades due to bird-strike," J. Eng. Gas Turbines Power, **133**(12), p. 122504.

[19] Zukas, J. A., 1980, Impact dynamics: theory and experiment- Technical Report No. ARBRL-TR-02271, Aberdeen Proving Ground, MD.

[20] Donea, J., Giuliani, S., and Halleux, J. P., 1982, "An arbitrary lagrangian-eulerian finite element method for transient dynamic fluid-structure interactions," Comput. Methods Appl. Mech. Eng., **33**(1–3), pp. 689–723.

[21] Chen, J.-S., Hu, W., and Hu, H.-Y., 2009, Progress on Meshless Methods, Springer.

[22] Alexander, P., and Naik, R. A., 2011, "Composite fan blade."

[23] Evans, C. R., and Ward, D. D., 2004, "Jet aircraft fan case containment design."

[24] Wojtyczka, C., and Amin, S., 2003, "Fan case design with metal foam between Kevlar."

[25] Quinn, K. W., Busbey, B. C., Szpunar, S. J., Elston, S. B., and Tucker, J. W., 1998, "Composite fan blade trailing edge reinforcement."

[26] GE, 2014, "The GE9X Jet Engine," Gen. Electr. [Online]. Available: http://www.ge.com/stories/aviation-instawalk. [Accessed: 01-Jan-2015].

[27] Wright, T., and Simmons, W. E., 1990, "Blade sweep for low-speed axial fans," J. Turbomach., **112**(1), pp. 151–158.

[28] Mavromihales, M., Mason, J., and Weston, W., 2003, "A case of reverse engineering for the manufacture of wide chord fan blades (WCFB) used in Rolls Royce aero engines," J. Mater. Process. Technol., **134**(3), pp. 279–286.

[29] Denton, J. D., and Xu, L., 2002, "The effects of lean and sweep on transonic fan

performance," ASME Turbo Expo 2002: Power for Land, Sea, and Air, American Society of Mechanical Engineers, pp. 23–32.

[30] Canaday, H., "COMPOSITES VS. METALS," Aiaa/aerosp. Am., (May 2015), pp. 18–23.

[31] Hyer, M. W., 2009, Stress analysis of fiber-reinforced composite materials, DEStech Publications, Inc.

[32] Gower, H. L., Cronin, D. S., and Plumtree, a., 2008, "Ballistic impact response of laminated composite panels," Int. J. Impact Eng., **35**(9), pp. 1000–1008.

[33] Othman, a. R., and Hassan, M. H., 2013, "Effect of different construction designs of aramid fabric on the ballistic performances," Mater. Des., **44**, pp. 407–413.

[34] Gopinath, G., Zheng, J. Q., and Batra, R. C., 2012, "Effect of matrix on ballistic performance of soft body armor," Compos. Struct., **94**(9), pp. 2690–2696.

[35] Hashin, Z., 1980, "Failure Criteria for Unidirectional Fiber Composites," J. Appl. Mech., **47**(2), p. 329.

[36] Chang, F.-K., and Chang, K.-Y., 1987, "A Progressive Damage Model for Laminated Composites Containing Stress Concentrations," J. Compos. Mater., **21**(9), pp. 834–855.

[37] Bayandor, J., Thomson, R. S., Scott, M. L., Nguyen, M. Q., and Elder, D. J., 2003, "Investigation of impact and damage tolerance in advanced aerospace composite structures," Int. J. crashworthiness, **8**(3), pp. 297–306.

[38] Kienast, J., 2009, "Bird strike! The moment 200 starlings were sucked into passenger jet engine on take-off" [Online]. Available: http://www.dailymail.co.uk/news/article-1217035/Bird-strike-The-moment-200-starlings-sucked-passenger-jet-engine-off.html.

[39] 2006, "No Title" [Online]. Available: http://www.jetphotos.net/photo/6583711.

[40] FAA, 2008, Type Certificate Data Sheet (E00078NE).

[41] EASA, 2013, Type certificate data sheet, Tech. Rep., EASA.21J.035.

[42] Hill, P. G., and Peterson, C. R., 1992, Mechanics and Thermodynamics of Propulsion, Addison-Wesley Publishing Co.

[43] Administration, F. A. A. F. A., 2014, Federal Aviation Regulations/Aeronautical Information Manual (FAR/AIM) 33.77: Rain and hail ingestion certification standards, A.C. No. 33.77.

[44] Inman, D. J., and Singh, R. C., 2001, Engineering vibration, Prentice Hall, Upper Saddle River, NJ.

[45] ATSB, 2002, "Examination of a failed Rolls-Royce RB211-524 turbofan engine – Boeing commercial aircraft group, 747-436, G-BNLD, Report No. 20/02 Task, Task File No. BE/200200008, Occurrence File No: BO/200200646," Aust. Transp. Saf. Bur. Canberra

ACT 2601, p. 20.

[46] Carney, K. S., Pereira, J. M., Revilock, D. M., and Matheny, P., 2009, "Jet engine fan blade containment using an alternate geometry," Int. J. Impact Eng., **36**(5), pp. 720–728.

[47] Roberts, G. D., Pereira, J. M., Braley, M. S., Arnold, W. A., Dorer, J. D., and Watson, W. R., Design and testing of braided composite fan case materials and components, Tech. Rep. NASA/TM-2009-215811, Cleveland, Oh.

[48] Wilbeck, J. S., 1978, Impact behavior of low strength projectiles, Tech. Rep. AFML-TR-77-134, Air Force Materials Laboratory (AFML), Wright-Patterson Air Force Base, OH.

[49] Barber, John P. ; Taylor, Henry R. ; Wilbeck, J. S., 1978, Bird impact forces and pressures on rigid and compliant targets, Tech. Rep. AFFDL-TR-77-60, Dayton, OH.

[50] Budgey, R., 2000, "The development of a substitute artificial bird by the International Birdstrike Research Group for use in aircraft component testing, IBSC25/WP-IE3, 17-21 April 2000," Int. Bird Strike Comm., (April), pp. 17–21.

[51] Meguid, S. A., Mao, R. H., and Ng, T. Y., 2008, "FE analysis of geometry effects of an artificial bird striking an aeroengine fan blade," Int. J. Impact Eng., **35**(6), pp. 487–498.

[52] Heimbs, S., 2011, "Computational methods for bird strike simulations: A review," Comput. Struct., **89**(23–24), pp. 2093–2112.

[53] Martin, N. F., 1990, "Nonlinear finite-element analysis to predict fan-blade damage due tosoft-body impact," J. Propuls. Power, **6**(4), pp. 445–450.

[54] Niering, E., 1990, "Simulation of bird strikes on turbine engines," J. Eng. Gas Turbines Power, **112**(4), p. 573.

[55] Petrenko, V. F., and Whitworth, R. W., 1999, Physics of ice, Clarendon Press.

[56] Gold, L. W., 1958, "Some observations on the dependence of strain on stress for ice," Can. J. Phys., **36**(10), pp. 1265–1275.

[57] Arenson, L. U., Colgan, W., and Marshall, H. P., 2015, "Chapter 2 - Physical, Thermal, and Mechanical Properties of Snow, Ice, and Permafrost," Snow and Ice-Related Hazards, Risks and Disasters, J.F.S.H. Whiteman, ed., Academic Press, Boston, pp. 35–75.

[58] Carney, K. S., Benson, D. J., DuBois, P., and Lee, R., 2006, "A phenomenological high strain rate model with failure for ice," Int. J. Solids Struct., **43**(25–26), pp. 7820–7839.

[59] McConnel, J. C., and Kidd, D. a., 1888, "On the plasticity of glacier and other ice," Proc. R. Soc. London, **44**(266–272), pp. 331–367.

[60] Mellor, M., and Cole, D. M., 1982, "Deformation and failure of ice under constant stress or constant strain-rate," Cold Reg. Sci. Technol., **5**(3), pp. 201–219.

[61] Haeberli, W., Hallet, B., Arenson, L., Elconin, R., Humlum, O., Kääb, A., Kaufmann, V.,

Ladanyi, B., Matsuoka, N., Springman, S., and Mühll, D. V., 2006, “Permafrost creep and rock glacier dynamics,” Permafr. Periglac. Process., **17**(3), pp. 189–214.

[62] Kim, H., and Keune, J. N., 2007, “Compressive strength of ice at impact strain rates,” J. Mater. Sci., **42**(8), pp. 2802–2806.

[63] Schulson, E. M., 2001, “Brittle failure of ice,” Eng. Fract. Mech., **68**(17–18), pp. 1839–1887.

[64] Shazly, M., Prakash, V., and Lerch, B. A., 2006, High-strain-rate compression testing of ice, Tech. Mem. NASA/TM—2006-213966, Cleveland, Ohio.

[65] Jones, S. J., 1997, “High Strain-Rate Compression Tests on Ice,” J. Phys. Chem. B, **101**(32), pp. 6099–6101.

[66] Dowling, N. E., 1993, Mechanical Behavior of Materials: Engineering Methods for Deformation, Fracture, and Fatigue 4th ed., Pearson, New York.

[67] Hallquist, J. O., 2015, LS-DYNA keyword manual volume I & II, Livermore, CA.

[68] Banthia, N. P., 1987, Impact resistance of composite fan blades NASA/CR-134707 R74AEG320, Cincinnati, Oh.

[69] Miller, S. G., M., K. H., Sinnott, M. J., Kohlman, L. W., Roberts, G. D., Martin, R. E., Ruggeri, C. R., and Pereira, J. M., 2015, Materials , Manufacturing , and test development of a composite fan blade leading edge subcomponent for improved impact resistance, Tech. Mem., NASA/TM-2015-218340, Cleveland, Ohio.

[70] Pinho, S. T., Robinson, P., and Iannucci, L., 2006, “Fracture toughness of the tensile and compressive fibre failure modes in laminated composites,” Compos. Sci. Technol., **66**(13), pp. 2069–2079.

[71] Tsai, S. W., and Wu, E. M., 1971, “A general theory of strength for anisotropic naterials,” J. Compos. Mater., **5**(1), pp. 58–80.

[72] Pinho, S. T., Iannucci, L., and Robinson, P., 2006, “Physically-based failure models and criteria for laminated fibre-reinforced composites with emphasis on fibre kinking: Part I: Development,” Compos. Part A Appl. Sci. Manuf., **37**(1), pp. 63–73.

[73] Pinho, S. T., Iannucci, L., and Robinson, P., 2006, “Physically based failure models and criteria for laminated fibre-reinforced composites with emphasis on fibre kinking. Part II: FE implementation,” Compos. Part A Appl. Sci. Manuf., **37**(5), pp. 766–777.

[74] Hoof, J. Van, 2000, “Maodelling of impact induced delamination in composite materials,” Carleton University Ottawa.

[75] Matzenmiller, a., Lubliner, J., and Taylor, R. L., 1995, “A constitutive model for anisotropic damage in fiber-composites,” Mech. Mater., **20**(2), pp. 125–152.

[76] Williams, K. V., and Vaziri, R., 2001, "Application of a damage mechanics model for predicting the impact response of composite materials," Comput. Struct., **79**(10), pp. 997–1011.

[77] Hallquist, J. O., 2015, LS-DYNA theory manual, Livermore, CA.

[78] Griffith, a. a., 1921, "The Phenomena of Rupture and Flow in Solids," Philos. Trans. R. Soc. A Math. Phys. Eng. Sci., **221**(582–593), pp. 163–198.

[79] Irwin, G. R., 1948, Fracture dynamics, American Society of Metals Cleveland.

[80] Erdogan, F., 2000, "Fracture mechanics," Int. J. Solids Struct., **37**(1–2), pp. 171–183.

[81] Gama, B. a., and Gillespie, J. W., 2011, "Finite element modeling of impact, damage evolution and penetration of thick-section composites," Int. J. Impact Eng., **38**(4), pp. 181–197.

[82] Tada, H., Paris, P. C., and Irwin, G. R., 2000, The Stress Analysis of Cracks Handbook, Third Edition, ASME, Three Park Avenue New York, NY 10016-5990.

[83] Lemmen, P. P. M., and Meijer, G. J., 2001, "Failure prediction tool theory and user manual," TNO Rep.

[84] Rankine, W. J. M., 1870, "On the Thermodynamic Theory of Waves of Finite Longitudinal Disturbance," Philos. Trans. R. Soc. London, **160**(January), pp. 277–288.

[85] Johnson, J. D., 1996, General features of Hugoniots, Los Alamos Lational Lab (LLNL) Tech. Rep., LA-13137-MS, Los Alamos, New Mexico.

[86] Mie, G., 1903, "Zur kinetischen Theorie der einatomigen Körper," Ann. Phys., **316**(8), pp. 657–697.

[87] Grüneisen, E., 1912, "Theorie des festen Zustandes einatomiger Elemente," Ann. Phys., **344**(12), pp. 257–306.

[88] Steinberg, D., 1996, Equation of state and strength properties of selected materials, Lawrence Livermore National Laboratory Livermore Tech. Rep., UCRL-MA-106439, Livermore, CA.

[89] Thomas J. R. Hughes, 1987, The Finite Element Method: Linear Static and Dynamic Finite Element Analysis: Thomas J. R. Hughes, Prentice Hall, Englewood Cliffs, N.Y.

[90] Hibbitt, H. D., Marcal, P. V., and Rice, J. R., 1970, "A finite element formulation for problems of large strain and large displacement," Int. J. Solids Struct., **6**(8), pp. 1069–1086.

[91] McMeeking, R. M., and Rice, J. R., 1975, "Finite-element formulations for problems of large elastic-plastic deformation," Int. J. Solids Struct., **11**(5), pp. 601–616.

[92] Deka, L. J., Bartus, S. D., and Vaidya, U. K., 2008, "Damage evolution and energy

absorption of E-glass/polypropylene laminates subjected to ballistic impact," J. Mater. Sci., **43**(13), pp. 4399–4410.

[93] Rabie, O., Al-Smadi, Y. M., and Wolff, E., 2013, "Numerical simulations on the performance of passive mitigation under blast wave loading," Special Topics in Structural Dynamics, Vol 6: Conference Proceedings of the Society for Experimental Mechanics Series, Springer, pp. 481–487.

[94] Belytschko, T., Stolarski, H., Liu, W. K., Carpenter, N., and Ong, J. S. J., 1985, "Stress projection for membrane and shear locking in shell finite elements," Comput. Methods Appl. Mech. Eng., **51**(1–3), pp. 221–258.

[95] Cook, R. D., Malkus, D. S., Plesha, M. E., and Witt, R. J., 2007, Concepts and Applications of Finite Element Analysis, John Wiley & Sons.

[96] "LS-Dyna Support: Shell formulations," LSTC Inc DYNAmore GmbH [Online]. Available: http://www.dynasupport.com/howtos/element/shell-formulations. [Accessed: 27-Jan-2016].

[97] Bathe, K.-J., 2006, Finite Element Procedures, Prentice Hall, Upper Saddle River, NJ.

[98] Donea, J., Giuliani, S., and Halleux, J. P., 1982, "An Arbitrary Lagrangian-Eulerian Finite Element Method for Transient Dyanmic Fluid-Structure Interaction," Comput. Methods Appl. Mech. Eng., **33**, pp. 689–723.

[99] Martinet, F., and Chabrand, P., 2000, "Application of ALE finite elements method to a lubricated friction model in sheet metal forming," Int. J. Solids Struct., **37**(29), pp. 4005–4031.

[100] Noh, W. F., 1963, CEL: A time-dependent, two-space-dimensional, coupled Eulerian-Lagrange code, Lawrence Radiation Lab., Univ. of California, Livermore.

[101] Trulio, J. G., 1966, Theory and structure of the AFTON codes, Tech. Rep., AFWL-TR-66-19, Air force weapons laboratory, Nowbury Park, California.

[102] Hughes, T. J. R., Liu, W. K., and Zimmermann, T. K., 1981, "Lagrangian-Eulerian finite element formulation for incompressible viscous flows," Comput. Methods Appl. Mech. Eng., **29**(3), pp. 329–349.

[103] Karimi, A., Navidbakhsh, M., Razaghi, R., and Haghpanahi, M., 2014, "A computational fluid-structure interaction model for plaque vulnerability assessment in atherosclerotic human coronary arteries," J. Appl. Phys., **115**(14), p. 144702.

[104] Dukowicz, J. K., and Kodis, J. W., 1987, "Accurate Conservative Remapping (Rezoning) for Arbitrary Lagrangian-Eulerian Computations," SIAM J. Sci. Stat. Comput., **8**(3), pp. 305–321.

[105] Leer, B. Van, 2006, “Upwind and high-resolution methods for compressible flow: from donor cell to residual-distribution schemes,” Commun. Comput. Phys., **1**(2), pp. 192–206.

[106] Godunov, S. K., 1959, “A difference method for numerical calculation of discontinuous solutions of the equations of hydrodynamics,” Mat. Sb., **89**(3), pp. 271–306.

[107] Van Leer, B., 1977, “Towards the ultimate conservative difference scheme. IV. A new approach to numerical convection,” J. Comput. Phys., **23**(3), pp. 276–299.

[108] Lucy, L. B., 1977, “A numerical approach to the testing of the fission hypothesis,” Astron. J., **82**(12), p. 1013.

[109] Gingold, R. a., and Monaghan, J. J., 1977, “Smoothed particle hydrodynamics: theory and application to non-spherical stars,” Mon. Not. R. Astron. Soc., **181**(3), pp. 375–389.

[110] Li, S., and Ca, B., 2013, “Meshfree and particle methods and their applications,” Appl. Mech. Rev., **55**(1), pp. 1–34.

[111] Gómez-Gesteira, M., and Dalrymple, R. a., 2004, “Using a Three-Dimensional Smoothed Particle Hydrodynamics Method for Wave Impact on a Tall Structure,” J. Waterw. Port, Coastal, Ocean Eng., **130**(2), pp. 63–69.

[112] Liu, G. R., and Liu, M. B., 2000, Smoothed Particle Hydrodynamics. A Meshfree Particle Method, World Scientific, New Jersey.

[113] Monaghan, J. J., 1992, “Smoothed Particle Hydrodynamics,” Annu. Rev. Astron. Astrophys., **30**(1), pp. 543–574.

[114] Fulk, D. a., 1994, “A Numerical Analysis of Smoothed Particle Hydrodynamics,” Air Force Institute of Technology.

[115] Randles, P. W., and Libersky, L. D., 1996, “Smoothed particle hydrodynamics: some recent improvements and applications,” Comput. Methods Appl. Mech. Eng., **139**(1–4), pp. 375–408.

[116] VonNeumann, J., and Richtmyer, R. D., 1950, “A Method for the numerical calculation of hydrodynamic shocks,” J. Appl. Phys., **21**(3), pp. 232–273.

[117] Monaghan, J. J., 1985, “Particle methods for hydrodynamics,” Comput. Phys. Reports, **3**(2), pp. 71–124.

[118] Benz, W., 1990, The Numerical Modelling of Nonlinear Stellar Pulsations, Springer Netherlands, Dordrecht.

[119] Anderson, J. D., and Wendt, J., 1995, Computational Fluid Dynamics, Springer.

[120] Vignjevic, R., 2009, “Review of Development of the Smooth Particle Hydrodynamics,” Predictive Modeling of Dynamic Processes, Springer, pp. 367–396.

[121] Underwood, P., 1983, “Dynamic relaxation: in structural transient analysis,” Comput.

methods transient Anal., pp. 245–265.

[122] Oakley, D. R., and Knight, N. F., 1995, "Adaptive dynamic relaxation algorithm for non-linear hyperelastic structures Part I. Formulation," Comput. Methods Appl. Mech. Eng., **126**(1–2), pp. 67–89.

[123] Papadrakakis, M., 1981, "A method for the automatic evaluation of the dynamic relaxation parameters," Comput. Methods Appl. Mech. Eng., **25**(1), pp. 35–48.

[124] Hughes, T. J. R., Taylor, R. L., Sackman, J. L., Curnier, A., and Kanoknukulchai, W., 1976, "A finite element method for a class of contact-impact problems," Comput. Methods Appl. Mech. Eng., **8**(3), pp. 249–276.

[125] Roy, C. J., 2003, "Grid Convergence Error Analysis for Mixed-Order Numerical Schemes," AIAA J., **41**(4), pp. 595–604.

[126] Roache, P. J., 1994, "Perspective: A method for uniform reporting of grid refinement studies," J. Fluids Eng., **116**(3), p. 405.

[127] Celik, I. B., Ghia, U., Roache, P. J., Freitas, C. J., Coleman, H., and Raad, P. E., 2008, "Procedure for estimation and reporting of uncertainty due to discretization in CFD applications," J. Fluids Eng., **130**(7), p. 78001.

[128] Seidt, J. D., Pereira, J. M., Hammer, J. T., Gilat, A., and Ruggeri, C. R., 2013, Dynamic load measurement of ballistic gelatin impact using an instrumented tube, Report No. NASA/TM—2012-217661, NASA.

[129] Pereira, J. M., Padula, S. a, Revilock, D. M., and Melis, M. E., 2006, Forces generated by high velocity impact of ice on a rigid structure, Tech. Mem., NASA/TM-2006-214263, Cleveland, Ohio.

[130] ASATM, 1999, Standard test methods for properties of continuous filament carbon and graphite fiber tows (ASTM D4018-99), West Conshohocken, PA.

[131] Iremonger, M. J., 1996, "Ballistic impact of fibre composite by fragment-simulating projectiles armours," Compos. Part A Appl. Sci. Manuf., **27**(7), pp. 575–581.

[132] Lee, B. L., Walsh, T. F., Won, S. T., Patts, H. M., Song, J. W., and Mayer, a. H., 2001, "Penetration failure mechanisms of armor-grade fiber composites under impact," J. Compos. Mater., **35**(18), pp. 1605–1633.

[133] Naik, N. K., Shrirao, P., and Reddy, B. C. K., 2006, "Ballistic impact behaviour of woven fabric composites: Formulation," Int. J. Impact Eng., **32**(9), pp. 1521–1552.

[134] CFAN, 2015, "CFAN Products," CFAN [Online]. Available: http://www.c-fan.com/products.htm. [Accessed: 20-Feb-2016].

[135] Hexcel Corporation, 1998, "HexTow® Carbon Fiber" [Online]. Available:

http://www.hexcel.com/Resources/SelectorGuides/HexTow_SelectorGuide.pdf.

[136] Min, J. B., Duffy, K. P., Choi, B. B., Provenza, A. J., and Kray, N., 2012, Piezoelectric vibration damping study for rotating composite fan blades, NASA/TM—2012-217648, Cleveland, Oh.

[137] Coroneos, R. M., and Gorla, R. S. R., 2012, Structural analysis and optimization of a composite fan blade for future aircraft engine, NASA/TM—2012-217632, Cleveland, Oh.

[138] Mao, R. H., Meguid, S. a., and Ng, T. Y., 2008, "Transient three dimensional finite element analysis of a bird striking a fan blade," Int. J. Mech. Mater. Des., **4**(1), pp. 79–96.

[139] Carter, T. J., 2005, "Common failures in gas turbine blades," Eng. Fail. Anal., **12**(2), pp. 237–247.

[140] FAA, 2008, FAA Pilot's handbook of aeronautical knowledge, U.S. Depart of Transportation.

[141] Veres, J. P., and Jorgenson, P. C., 2013, "Modeling Commercial Turbofan Engine Icing Risk with Ice Crystal Ingestion," 5th AIAA Atmospheric and Space Environments Conference, American Institute of Aeronautics and Astronautics, Reston, Virginia, pp. 1–14.

[142] Oliver, M. J., 2013, "a Study on the Physics of Ice Accretion in a Turbofan Engine Environment," Case Western Reserve University.

[143] Veres, J. P., Jorgenson, P. C. E., and Wright, W. B., 2013, Modeling the effects of ice accretion on the low-pressure compressor and the overall turbofan engine system performance, NASA/TM—2013-217034, Cleveland, Oh.

[144] Transportation Safety Board of Canada, 2012, Engine power loss and hard landing Royal Canadian Mounted Police Eurocopter AS 350 B3 (helicopter), C-FMPG Cultus Lake, Report A12P0008, British Co.

[145] Guoqi, Z., Goldsmith, W., and Dharan, C. K. H., 1992, "Penetration of laminated Kevlar by projectiles—I. Experimental investigation," Int. J. Solids Struct., **29**(4), pp. 399–420.

[146] Hosur, M. V., Vaidya, U. K., Ulven, C., and Jeelani, S., 2004, "Performance of stitched/unstitched woven carbon/epoxy composites under high velocity impact loading," Compos. Struct., **64**(3–4), pp. 455–466.

[147] Hearle, J. W. S., and Wong, B. S., 1977, "Flexural fatigue and surface abrasion of Kevlar-29 and other high-modulus fibres," J. Mater. Sci., **12**(12), pp. 2447–2455.

[148] Prichard, J. C., and Hogg, P. J., 1990, "The role of impact damage in post-impact compression testing," Composites, **21**(6), pp. 503–511.

[149] Richardson, M. O. W., and Wisheart, M. J., 1996, "Review of low-velocity impact

properties of composite materials," Compos. Part A Appl. Sci. Manuf., **27**(12), pp. 1123–1131.

[150] Cantwell, W. J., and Morton, J., 1991, "The impact resistance of composite materials - a review," Composites, **22**(5), pp. 347–362.

[151] Dransfield, K., Baillie, C., and Mai, Y. W., 1994, "Improving the delamination resistance of CFRP by stitching-a review," Compos. Sci. Technol., **50**(3), pp. 305–317.

[152] Jegley, D. C., 2007, "Improving strength of postbuckled panels through stitching," Compos. Struct., **80**(2), pp. 298–306.

[153] Souli, M., Olovsson, L., and Do, I., 2000, "ALE and fluid-structure interaction capabilities in LS-DYNA," 7th Int. LS-DYNA Users Conf., pp. 27–36.

[154] Souli, M., Ouahsine, a., and Lewin, L., 2000, "ALE formulation for fluid-structure interaction problems," Comput. Methods Appl. Mech. Eng., **190**(5–7), pp. 659–675.

[155] Alexander, E., Carey, B., DiNardo, M., Gill, H., Gonzalez, J., Harry, M., Isidro, A., Judge, S., Puckett, K., Schoepfer, G., Song, Y., Tilghman, M., Siddens, A., Satterwhite, M., and Bayandor, J., 2012, "Validated Aerospace Soft Impact Modeling Platform," ASME 2012 Fluids Engineering Division Summer Meeting, ASME, Rio Grande, Puerto Rico, p. 789.

[156] Song, Y., Horton, B., Perino, S., Thurber, A., and Bayandor, J., 2015, "A Contribution to full-scale high fidelity aircraft progressive dynamic damage modeling for certification by analysis," Aerospace Sturctura Impact Dynamics International Conference, Seville. Spain, pp. 1–27.

[157] Andersson, O., and Inaba, A., 2005, "Unusual Gruneisen and Bridgman parameters of low-density amorphous ice and their implications on pressure induced amorphization," J. Chem. Phys., **122**(12), p. 124710.

[158] Stewart, S. T., and Ahrens, T. J., 2005, "Shock properties of H2O ice," J. Geophys. Res., **110**(E3), p. E03005.

[159] Gammon, P. H., Kiefte, H., and Clouter, M. J., 1983, "Elastic constants of ice samples by Brillouin spectroscopy," J. Phys. Chem., **87**(21), pp. 4025–4029.

[160] Guoqi, Z., Goldsmith, W., and Dharan, C. K. H., 1992, "Penetration of laminated Kevlar by projectiles—II. Analytical model," Int. J. Solids Struct., **29**(4), pp. 421–436.

[161] Starratt, D. L., 1998, "An instrumented experimental study of the ballistic response of textile materials."

[162] Wu, E., and Chang, L.-C., 1995, "Woven glass/epoxy laminates subject to projectile impact," Int. J. Impact Eng., **16**(4), pp. 607–619.

[163] Degroote, J., Bathe, K.-J., and Vierendeels, J., 2009, "Performance of a new partitioned

procedure versus a monolithic procedure in fluid–structure interaction," Comput. Struct., **87**(11–12), pp. 793–801.

[164] Thurber, A., and Bayandor, J., 2015, "On the Fluidic Response of Structures in Hypervelocity Impacts," J. Fluids Eng., **137**(4), p. 41101.

[165] Song, Y., and Bayandor, J., 2014, "Comprehensive Soft Impact Damage Methodology for Advanced High Bypass Ratio Turbofan Engines," ASME 2014 4th Joint US-European Fluids Engineering Division Summer Meeting, A. 2014 FEDSM, ed., ASME, Chicago, Illinois, USA, p. V01BT13A004.

[166] Chiang, T. P., Sheu, W. H., and Hwang, R. R., 1998, "Effect of Reynolds number on the eddy structure in a lid-driven cavity," Int. J. Numer. Methods Fluids, **26**(December 1995), pp. 557–579.

[167] Koseff, J. R., and Street, R. L., 1984, "The Lid-Driven Cavity Flow: A Synthesis of Qualitative and Quantitative Observations," J. Fluids Eng., **106**(4), p. 390.

[168] Ghia, U., Ghia, K. ., and Shin, C. ., 1982, "High-Re solutions for incompressible flow using the Navier-Stokes equations and a multigrid method," J. Comput. Phys., **48**, pp. 387–411.

[169] Di Mascio, a., Paciorri, R., and Favini, B., 2002, "Truncation Error Analysis in Turbulent Boundary Layers," J. Fluids Eng., **124**(3), p. 657.

[170] Chiang, T. P., Hwang, R. R., and Sheu, W. H., 1997, "On End-Wall Corner Vortices in a Lid-Driven Cavity," J. Fluids Eng., **119**(1), p. 201.

[171] Shankar, P. N., and Deshpande, M. D., 2000, "Fluid mechanics in the driven cavity," Annu. Rev. Fluid Mech., **32**(1), pp. 93–136.

[172] Celik, I. B., Ghia, U., Roache, P. J., Freitas, C. J., Coleman, H., and Raad, P. E., 2008, "Procedure for Estimation and Reporting of Uncertainty Due to Discretization in CFD Applications," J. Fluids Eng., **130**(7), p. 78001.

[173] Kawai, H., Yasumasa, K., and Tanahashi, T., 1989, "Numerical flow analysis in a cubic cavity by the GSMAC finite element method. In the case that Reynolds numbers are 1000 and 3200.," Trans. Japan Soc. Mech. Eng. Ser. B, **55**(515), pp. 1922–1929.

[174] Johnson, G. R., and Cook, W. H., 1985, "Fracture characteristics of three metals subjected to various strains, strain rates, temperatures and pressures," Eng. Fract. Mech., **21**(1), pp. 31–48.

Appendix-A: Parametric Study of Ice Damage Model and EOS

As discussed in section 5.2.2, the fluidic ice damage model for high speed impact was reasonably accurate since the impact behavior of soft body projectile (bird) and ice are considerably similar to each other except the viscosity. To do so, two distinct damage models and two different EOSs were investigated to reduce the complexity of input parameters for the high speed ice impact scenario. A series of sensitivity analyses is provided in this chapter to present the modeling methodology step-by-step as shown in Fig. 2.16. In addition to the combination between the damage models and two EOSs, 4 high speed ice impact scenarios were investigated at three different impact speed to find an adequate damage model and EOS for the FOI progressive damage analysis.

For the first, both solid and fluid ice damage models were assigned to virtual ice projectile with the Tabulated EOS to simulate the effect of damage models. Realistically, the post-damage mechanical strength of ice does not exist. This phenomenon was also applied in both computational damage models. The definition of both numerical ice damage models also governs the virtual ice cannot resist any dilatation and carry any compression loading once the damage initiated. For both damage models, the compressive loading is equally defended by defining the pressure cutoff (PC). In this study, a set of simplified input parameters for solid ice damage model was employed as discussed explored by Carney et al. [58] for the damage prediction. The input parameters are shown in Table A- 1.

Table A- 1 Mechanical properties of dense ice with single crystalline structure at -10°C [58] for solid ice damage model and fluidic ice damage model

Type of damage model	***Solid***	***Fluidic***
Density, ρ (kg/m^3)	897.6	897.6
Dynamic viscosity, μ $(Pa \cdot s)$	*N/A*	0
Young's modulus, E (GPa)	9.31	*N/A*
Initial compressive flow stress, σ_C (MPa)	172.4	*N/A*
Initial tensile flow stress, σ_T (MPa)	17.24	*N/A*
Tangential modulus, E_{tan} (MPa)	6.89	*N/A*
Poisson's ratio, ν	0.33	*N/A*
Pressure cut-off in compression, P_{Cut-C} (MPa)	4.93	4.93
Pressure cut-off in tension, P_{Cut-T} (MPa)	0.433	*N/A*

According to the author, both the tensile flow stress and pressure cutoff in tension are assumed as one tenth of the compressive stress because of the challenge of tensile experiment on ice specimen. The solid damage model requires an additional set of input parameter which is already provided in Table 2-3 to define the strain rate dependency of ice model. As explained, such compressive strength scale factor is also simplified because of the experimental limitation. On the other hand, the input parameter of fluidic ice damage model is much less than the other ice damage model as tabulated in Table A- 1. As mentioned, the relationship between volumetric strain ($\boldsymbol{\varepsilon_v}$) and both the corresponding pressure within the ice continuum and unloading bulk modulus at the instance were measured empirically by Carney et al. [58]. The input parameters of the Tabulated EOS is shown in Table A- 2. Assuming there was no temperature change, the Gruneisen gamma (γ) became zero to remove the internal energy calculation. The Tabulated EOS was then used for damage evolution triggered by the projectile kinetic energy.

Table A- 2 Input parameters for Tabulated EOS [58]

$\boldsymbol{\varepsilon_v}$	**Pressure, *P* (*MPa*)**	**Bulk modulus, *K* (*GPa*)**
0.0	0	8.960
-0.0076920	68.95	8.960
-0.0312500	68.95	2.210
-2.3025999	68.95	6.890

The impact forces-time history of two ice damage model at multiple impact speeds are presented in Fig. A.1. Both result filtered at same frequency as discussed in section 5.2 (25.6 kHz). Although both models had different stress calculation and damage prediction, the quantitative results were considerably similar regardless of the material definition for all impact speeds. The force induced on the target surface during the initial contact was almost identical to each other. The impact time window at same speeds was approximately close to each other as well as the unloading patterns. This implies that the fluidic ice damage model for a high speed impact is a valid substitution to define the ice which requires significantly less unknown input parameters.

This hypothesis becomes a valid approach to simulate a high speed ice impact scenario since the most of the damage on both the projectile and structure does not depend on the mechanical strength of ice projectile. Instead, the damages on both continuum is driven by the shock response upon impact and the momentum of projectile after the shock disintegrate the projectile continuum. By avoiding assumed input parameters, the input uncertainty of ice structure interaction can be reduced and possibly improved to conduct a damage assessment caused by ice ingestion.

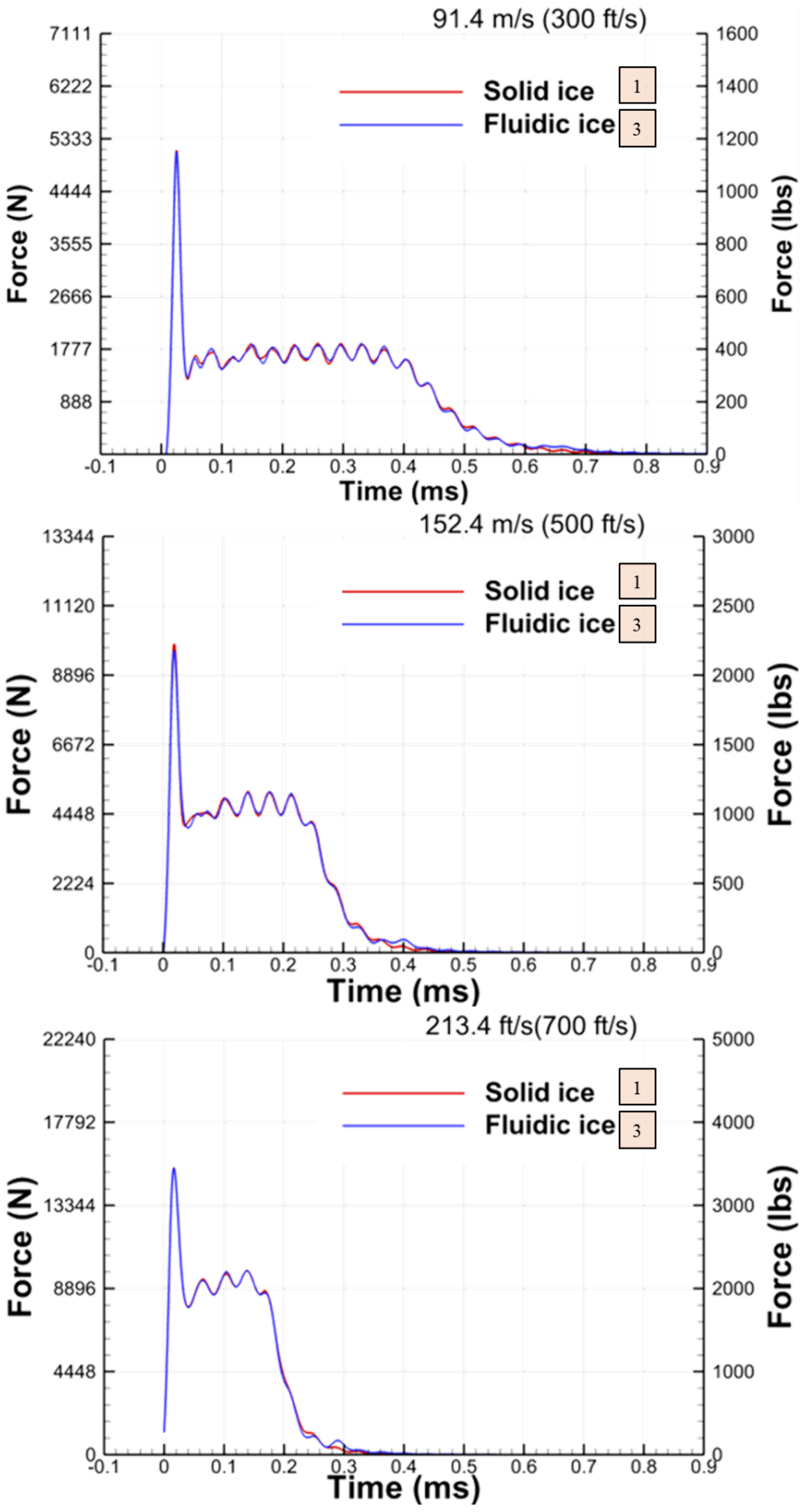

Figure A. 1 Force-time history of high speed ice impact damage model using solid and fluidic damage model with Tabulated EOS

Previously, the difference of shock response for two EOSs was briefly mentioned in section 5.2.3. In order to demonstrate, two different EOSs were employed to explore the impact dynamics while the ice damage model remained as constant (fluidic ice damage model). This was because the energy transformation from an energy state to the other forms is governed by the EOS. In this study, the projectile kinetic energy turned into a high magnitude of the shock response that was strong enough to disintegrate the projectile. As a result, understanding EOS was necessary for a high speed ice impact simulation.

Even though, the ice is extremely difficult to implement any strain gauges or other experimental measurement to collect an information because of its material characteristics. For example, implementing a strain gauge is almost impossible since the gauge cannot be appropriately mounted on the ice surface. As an alternative way to measure the dynamic stress-strain response, Hokinson split bar experiment is commonly selected. However, such a brittle behavior and extremely weak mechanical strength prohibit to measure the high strain rate properties of ice using the Hokinson bar experiment. In addition to the implementation of scientific measurement, controlling the ambient conditions and measuring the volumetric change of ice as a function of compressive loading conditions are extremely difficult. Hence, the Gruneisen EOS was explored to develop as an alternative for high speed ice damage model.

As a proof of concept, the sensitivity analysis for EOSs presented to two distinct shock responses upon impact Since the material behavior and shock dynamics depend on the speed of sound in the projectile continuum, the speed of sound, curve fitting constant, and γ_0 of fully dense ice (*Ih*) at $-10\ ^{\circ}C$ were found [157,158]. The mechanical definition of ice were very similar to the claimed values (longitudinal velocity = 3845m/s) by Gammon et al. [159]. The Gruneisen parameters for ice are tabulated in Table A- 3. The setup of two computational models developed with two EOSs with the fluidic ice damage model, since the effect on changing the ice damage model was negligible. Figure A.2 shows the force-time result of simulation result with the impact speed from 91.4 *m/s* to 213.4 *m/s*.

Table A- 3 Gruneisen EOS parameters for ice

$\boldsymbol{\rho\ (kg/m^3)}$	$\boldsymbol{C\ (m/s)}$	$\boldsymbol{\gamma}$	$\boldsymbol{a}$	$\boldsymbol{S_1}$	$\boldsymbol{S_2}$	$\boldsymbol{S_3}$
900	3610(±61)	-.65	.92(±0.63)	0	0	0

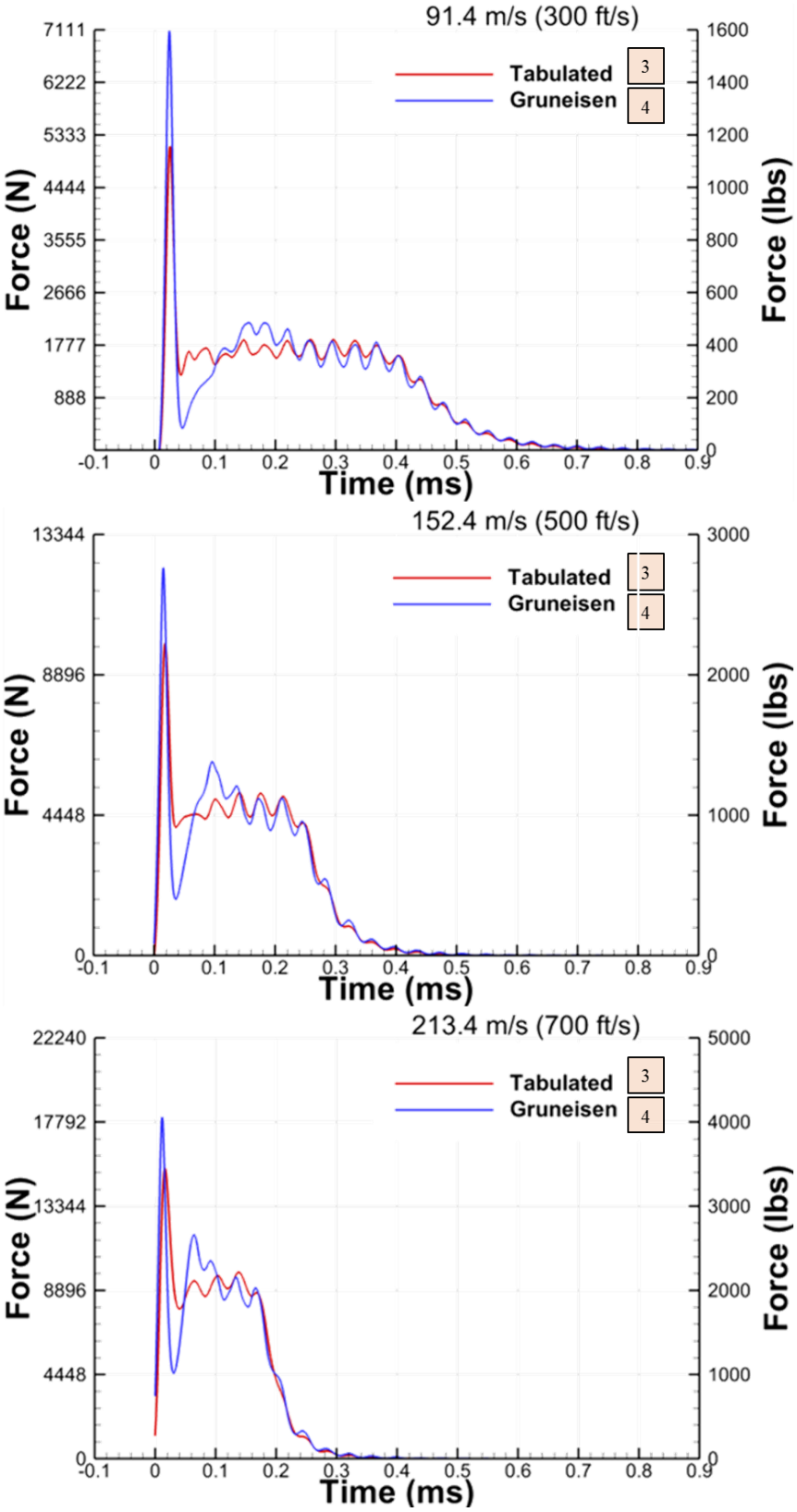

Figure A. 2 Force-time history of high speed ice impact damage model using Tabulated EOS and Gruneisen EOS using fluidic ice damage model

The primary contribution using the EOS is shock response on both continua. In other words, the impact time window does not significantly influence by changing EOS. Figure A.2 proves the hypothesis quantitatively. Except the magnitude of initial contact force, the impact time window of both Tabulated and Gruneisen EOS simulations were almost identical to the each other. After the initial contact, the steady state response was almost identical each other. This was caused by the projectiles' momentum, since they were already disintegrated due to initial shock pressure and turned into a group of particles. One of the distinctive differences between two simulation models is the transition between initial contact force to steady state loading condition. The shock response of Gruneisen model had a sudden massive pressure rise and dissipated through the rest of the continuum. On the other hand, the shock pressure derived by Tabulated EOS was clipped off at 68.5 *MPa* by the insufficient data set as shown in Fig. A.3. Hence, wider shock regime was observed and this caused almost steady state at the interface throughout the entire impact event.

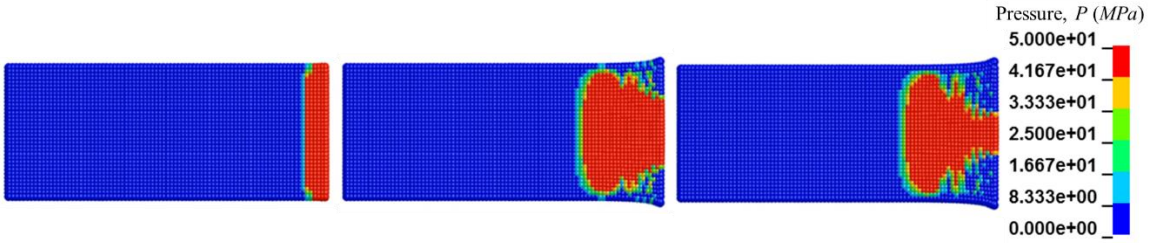

Figure A. 3 Sequence of shockwave propagation through ice projectile using Tabulated EOS during the initial impact

When the impact speed is 91.4 *m/s*, the peak impact force of Tabulated EOS was calculated as 5300 *N*, while the Gruneisen EOS predicted as 7100 *N*. According to the precede ice impact experiment [129], the measured peak normal impact force was 5300 *N*. This implied that the Tabulated EOS was more adequate EOS to calculate the impact force on target surface than the Gruneisen EOS at the current impact speed regime. At 152.4 *m/s* impact speed, the impact force at the target surface for both computational model became similar to the experimental result. Both ice impact damage model defined by the Tabulated EOS and Gruneisen EOS calculated the impact force as 10090 *N* and 12371 *N*, while the impact force on target surface was measured approximately 12100 *N* during the physical experiment. Based on the impact force variation throughout the experiments, both EOSs predicted the results within an acceptable range accuracy. For the impact speed of 213.4 *m/s*, the ice damage model employing Gruneisen EOS predicted the impact force as 18044 *N* and Tabulated EOS 15369 *N*. As the impact velocity reached ballistic regime, the accuracy of high speed ice damage model progressively improved to compare with the physical experiment.

In the section, it was discussed as the shock response of the Tabulated EOS was limited by the experimental investigations. Obviously, the fluidic ice damage model required less inputs and assumptions. Even though, the sensitivity analysis proved that the damage model did not contribute on the result significantly. The force time result was influenced by changing the equation of state. Throughout the sequence of analyses, Gruneisen EOS predicted the better damage prediction for the higher impact speed, while the Tabulated EOS was more adequate for lower impact speed.

Appendix-B: 3-D Composite Damage Model

The purpose of this section is to discuss about the methodology of the 3-D composite damage model which was presented in section 5.3.2, In the section, a brief result about the high speed impact on to 19 plies of Kevlar®, shown in Fig. 3.3, was discussed with a validation against experiment using the back face displacement of composite laminate. Herein, the 3-D composite damage modeling methodology is discussed thoroughly including the investigation for mesh resolution, anisotropic composite damage model selection and additional validation for the high speed impact onto Kevlar® laminate, which is later employed for the soft casing design in the comprehensive analysis.

The numerical damage model is developed by the coupling continuum damage mechanics with interlaminar damage mechanics. By doing so, the progressive failure of each individual ply can be computationally represented as well as the delamination which can occur at the interlaminar regime. The meso-scale composite modeling using continuum damage mechanics has the benefit of being computationally inexpensive to compare with the micro-scale simulation while the qualitative result can show a direct similitude that can be experimentally observed [32,74–76]. Table B- 1 shows a list of fundamental material properties of Kevlar®-29 used for developing 3-D casing model as well as the current study [160]. The properties were used as the material inputs for the computational model along with properties estimated by van Hoof and Gower et al.

Table B- 1 Kevlar 29 parameters based on literature [32,74,160]

Property	Kevlar® 29
$\rho\ (kg/m^3)$	1230
$E_1\ (GPa)$	*18.5*
$E_2\ (GPa)$	18.5
$E_3\ (GPa)$	6.0
$G_{12}\ (GPa)$	0.77
$G_{23}\ (GPa)$	2.71*
$G_{13}\ (GPa)$	2.71*
$\nu_{12}\ (N/A)$	0.25
$\nu_{23}, \nu_{13}\ /A)$	0.33
$\sigma_n\ (MPa)$	34.5
$\sigma_s\ (MPa)$	9.0

* Property proposed by van Hoof

Because of the relatively low projectile impact speed (~150 *m/s*), temperature effects were ignored. In additional to the thermal effect, the energy dissipation through the projectile deformation was neglected throughout the analysis and the projectile became a rigid for further investigation. To justify the rigid assumption, the high speed impact on Kevlar® laminate simulation was conducted with both a rigid projectile and Johnson-Cook damage model. Throughout the analysis, it was concluded that only 0.3% of the initial projectile kinetic energy was dissipated through the projectile deformation while the strain rate sensitive damage model required additional 20% more computational expense. The same conclusion was found in preceding work done by Starrat [161]. The work also claimed that 4% of the initial projectile kinetic energy was used to cause the plastic deformation of projectile upon impact. Therefore, a rigid projectile to develop the methodology for 3-D damage composite model was considered as a valid assumption to develop a soft casing.

B.1 Investigation for Element Formulation

Aforesaid, a proper element formulation selection is important to achieve a high fidelity investigation. Although the reduced element can provide more rapid result, the inappropriate formulation can lead the zero-energy deformation or inaccurate damage prediction due to the degrees of freedom of each individual element. As discussed in section 4, an 8-node constant stress element is robust when analyzing the response of continuum in major cases with minimum computational expense. Hourglass model can mitigate the problems but inappropriate hourglass usage can directly impact on the solution such as overly stiffened the element, which requires a case-by-case tune for each simulation. In order to reduce the computational uncertainty caused by element formation, five different element formulations were investigated: 8-node constant stress, 8-node fully integrated quadratic, 20-node fully integrated, 20-node fully integrated with enhanced strain, and 20-node fully integrated with enhanced strain. Such element formulations were selected by considering both the computational accuracy and cost. For the reduced integration element (8-noded constant stress solid element), the viscous hourglass control was assigned to suppress the zero-energy mode.

To quantify the dependency of element formulation, the delamination energy of each Kevlar® laminate was measured as shown in Fig. B.1. In simulation, the total energy is the summation of kinetic, internal, and delamination energy of both projectile and Kevlar® laminate. Since all five high speed impact simulations using different element formulations were successfully arrested the rigid projectile, the delamination energy was measured as a comparison. The trends of fully

integrated element were similar, while the 8-noded reduced solid element (constant stress) diverged after 0.1 *ms*. Less energy was dissipated through the delamination of Kevlar® laminate when 8-noded reduced integration solid element. Consequently, the majority of initial projectile kinetic energy (~60%) was dissipated through the hourglass energy and this was not an acceptable ratio as discussed. Hence, the 8-node under-integrated solid element was excluded for further investigation. 8-noded fully integrated solid element was rejected because of shear locking issue caused by a poor aspect ratio. The 20-node fully integrated formulation was also eliminated considering the overly stiffen which lead excessive delamination rather than causing a ply damage. Additional problem was associated with an element has a poor aspect ratio. So, another element formulation was also investigated. Both 20-noded enhanced strain element formulations (accurate and efficient) were predicted almost identical to each other while predicting a similar delamination energy to the other element formulations.

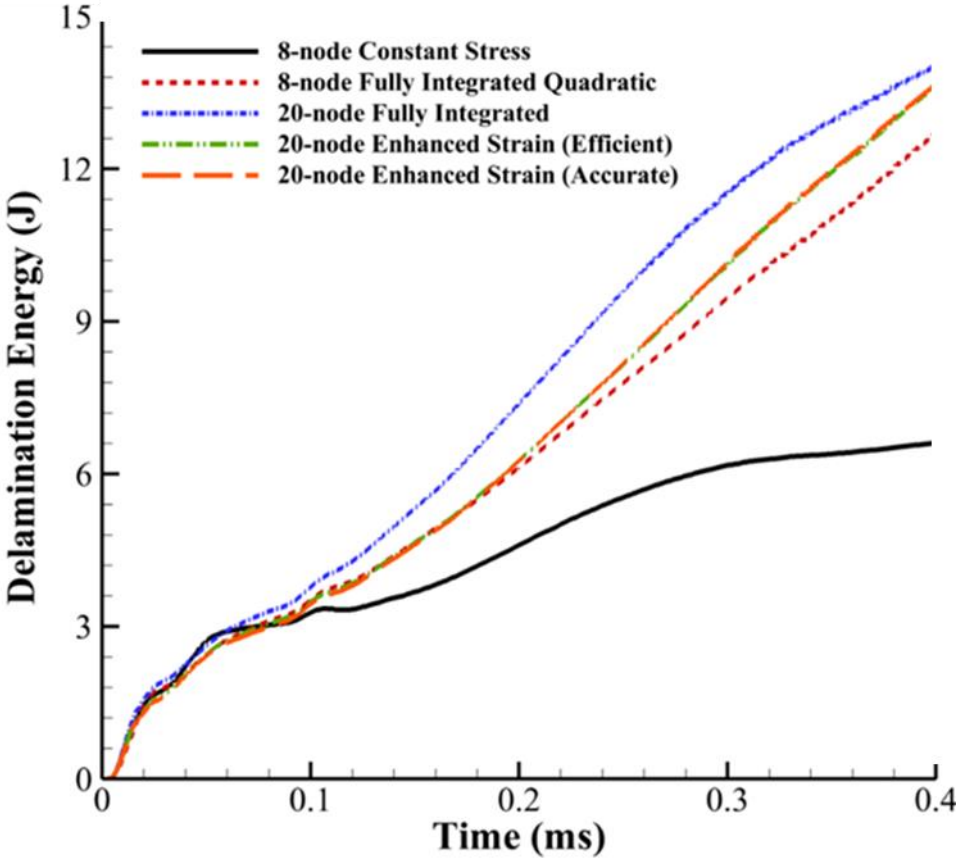

Figure B. 1 Delamination energy plots for each element formulation

By comparing the remaining options to the computation times shown in Table B- 2, the 20-node efficient formulation with enhanced strain is a clear choice due to its relatively low computation time and high accuracy, matching the accurate formulation almost perfectly.

Table B- 2 Normalized computation expense for each element formulation

Element Formulation	*Normalized Computational Cost*
8-noded constant stress	0.67
8-noded fully integrated	*1.78*
20-noded fully integrated	1.00
20-noded enhanced strain (efficient)	1.08
20-noded enhanced strain (accurate)	2.10

B.2 Mesh Study

To quantify the computational uncertainty, six different mesh densities were generated to find the mesh dependency of the 3-D composite damage modeling methodology. These mesh resolutions were generated using a consecutive refinement as a factor of 1.31. This is in accordance with the proposed guidelines by Celik et al. [127]. Figure B.2 shows the percentage of delamination area and computational time with respect to the number of solid elements. The area of delamination was measured at when the speed projectile was reached to zero, because each mesh resolution requires their own time to reach the steady state response of laminate. As shown in the figure, the area of delamination is converged to approximately 7% of the total area of interface included in 19 plies Kevlar® laminate. In accordance with the increase of mesh resolution, the computational expense was also exponentially increased. The plot qualitatively implies the improvement of solution became negligible after a certain mesh resolution (~15K) considering the additional computational expense.

The *GCI* results is tabulated in Table B- 3. The apparent order was calculated as 6.77. The discretization error among coarse to medium mesh resolutions was 3.29%. The error was significantly reduced as the mesh density increased (0.54% between medium to fine mesh).

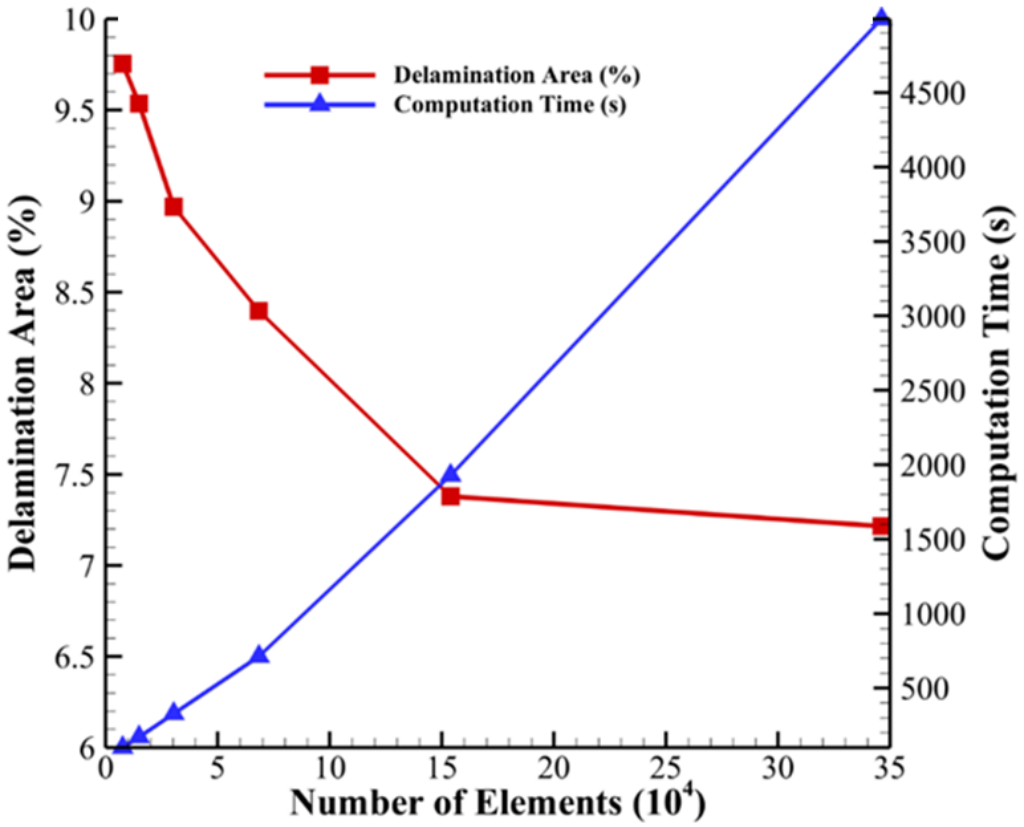

Figure B. 2 Percent delamination area and computation time versus number of elements

Table B- 3 *GCI* result. The subscript (3, 2, and 1) are coarse, mid, and find mesh resolution respectively

N_1, N_2, N_3	**346275, 153900, 68400**
r_{21}, r_{32}	1.31, 1.31
A_1	0.0302
A_2	0.0308
A_3	0.0351
P	6.77
e_a^{21}, e_a^{32}	2.30%, 13.8%
GCI_{21}	0.54%
GCI_{32}	3.29%

The shape of delamination for four mesh densities is shown in Fig. B.3. The group of qualitative results implied that the convergence was achieved at 153,900 elements. Considering other resultant parameters, such as backface displacement, delamination area, and delamination energy, the shape of delamination required higher computational cost. Although the shape of delamination is not quantifiable nor a primary post damage signature, it was concluded that the 153,900 element model was converged. This predicted delamination shape agrees well with that predicted by Naik et al. [133] as well as that experimentally observed by Wu and Chang [162].By considering the diminishing error from medium to fine and increasing computational expense, the medium mesh resolution was the most practical for further investigation using the fully integrated solid elements with enhanced strain formulation.

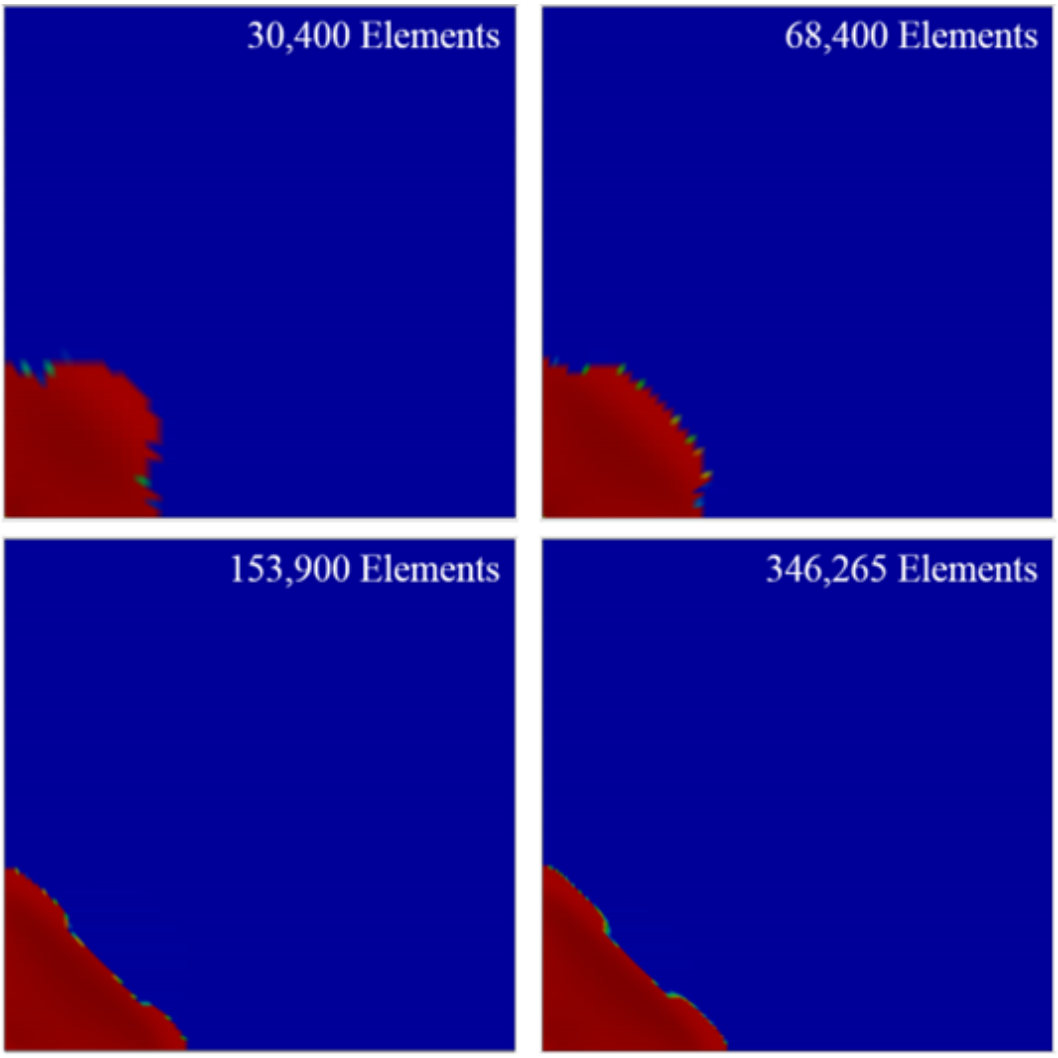

Figure B. 3 Delamination area of the top ply is qualitatively shown for four mesh densities, where red represents full delamination and blue represents zero separation

B.3 Parametric Analysis Using Multiple Damage Models

The backface displacement time response for the 3 composite damage models and experiments were shown in Fig. 5.22-(a). As shown in plot, the deflection rate for proposed 3-D composite damage model was noticeably off from the experimental data. To reduce the discrepancy, a set of parametric study was conducted by changing the elastic modulus, shear modulus, tensile failure strain, shear failure strain, and some other damage parameters. Overall, none of the individual parameters did not influence the result significantly on the deflection rate. Table B- 4 shows the summary of the resultant throughout the computational investigations using different failure criteria. The resultant agreed with the experimental data [32].

Table B- 4 Summary of backface displacement, total delamination area at time of bullet arrest, and number of failed plies for each of the selected material failure models

	Failure Method	Tsai-Wu	Chang-Chang	Orthotropic Damage
Back Face Displacement (mm)	*Stress*	8.04	13.8	*N/A*
	Strain	15.6	14.3	11.5
Overall Delamination Area (m^2)	*Stress*	0.04074	.1191	*N/A*
	Strain	0.0749	0.0689	0.0522
# of Failed Plies	*Stress*	4	16	*N/A*
	Strain	16	15	13

The area of delamination through the thickness direction of composite laminate is shown in Fig. B.4 at the moment of projectile arrest. The shape of delamination of top surface shown in Fig. B.4-(a) exhibits a typical delamination shape proposed by preceding research [133,162]. In Figure B.4-(b), the shape of delaminated area becomes a diamond shape with the delamination area extended along the fiber directions. This extended delamination is due to the spring back of ply layers as tension was released when material failure occurred.

The area of the delamination zone in Fig. B.4-(c) is larger than that of the ply above, and also has a slightly more circular shape. This slight increase in delamination area and inclusion of the curvature of each individual ply, creating greater relative slip area at the interface and thus allowing higher delamination. This effect is even more pronounced in Fig. B.4-(d), which is the lowest interface in the composite and is therefore subjected to the greatest relative slip area at the interface.

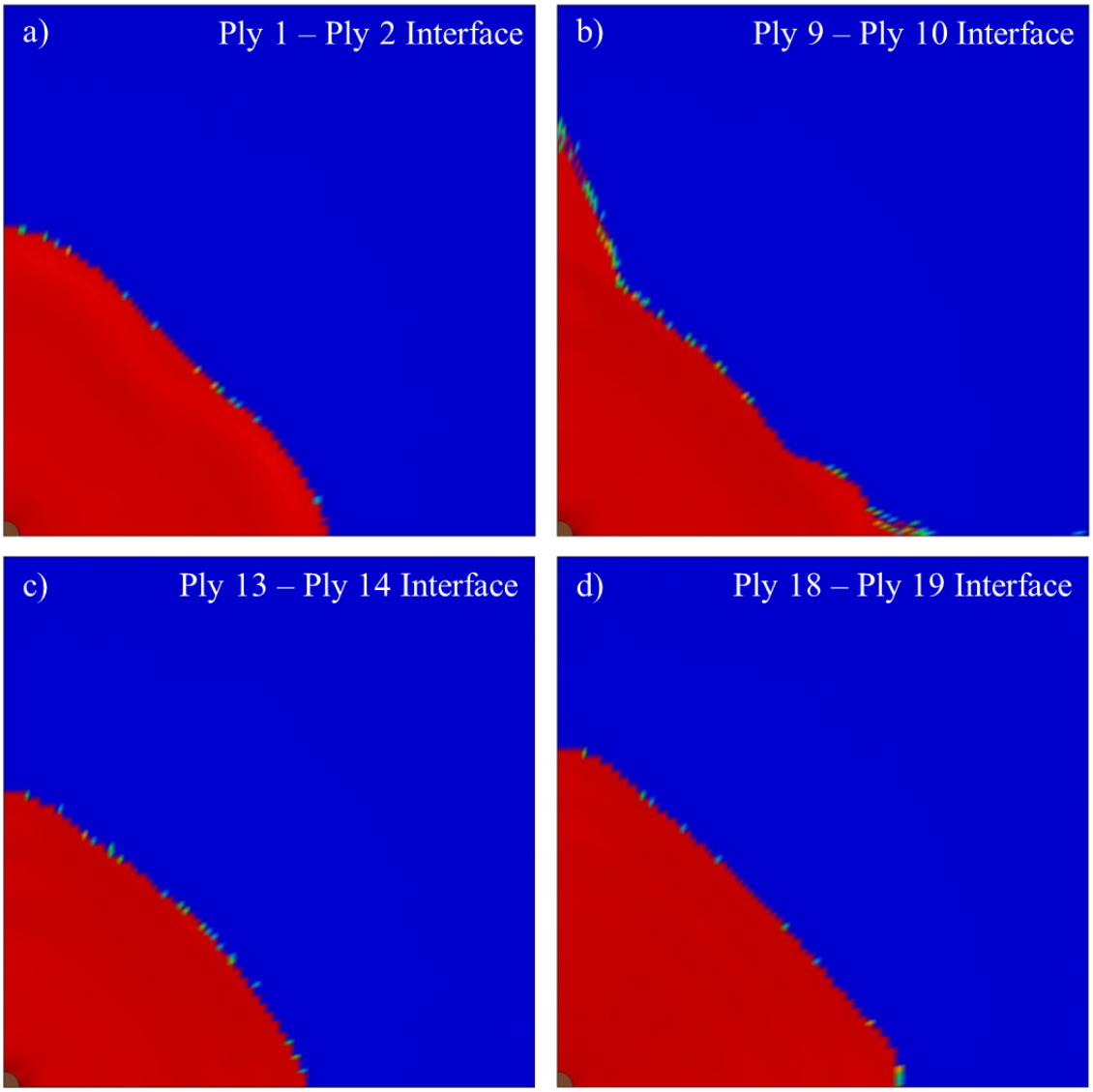

Figure B. 4 Qualitative view of delamination area at different ply interfaces at the time of bullet arrest

Despite of the numerous physical experiments have been performed, accurate finite element representations have rarely been shown nor thoroughly discussed to capture the damage processes upon high speed impact on the composite laminate. Therefore, a mesoscale 3-D composite damage modeling methodology was developed to capture the impact characteristics of Kevlar® 29 under the high speed impact. To simulate the damage initiation and evolution due to the high speed impact, the computational analysis was created based on the combination of continuum mechanics and cohesive zone modeling. For the continuum damage model, multiple composite failure models were employed and extensively compared both qualitatively and quantitatively using multiple

parametric study and compared. The cohesive zone modeling was also investigated to accurately capture the impact physics including interlaminar behavior.

Throughout the parametric study using multiple damage model, it was found that both Tsai-Wu and Chang-Chang damage model overly predicted damage (conservative) to compare with 3-D orthotropic composite damage model. Such disparity might be caused by the plane-stress assumption. This plane-stress assumption could be the reason for the premature penetration observed when realistic material failure properties were used. On the other hand, the 3-D orthotropic composite damage model predicted the accurate results because of through-thickness properties. According to the analyses, the delamination was also shown to have a significant impact on the ballistic performance of the composite. Therefore, the computational model response was validated by comparison with a physical experiment using both backface displacement and area of delamination upon impact as a final metric to determine accuracy.

There are two other impact phenomena, which typically occur on an aramid based composite laminate, was not captured. One is laminate plugging and the other one is fiber wrapping around projectile. Because of the damage was computationally represented as an element deletion, both were not accurately presented. This could cause over-prediction of backface displacement consequently because of the absence of friction based energy dissipation. Despite the lack of detailed material information, the model successfully captured the dynamics of Kevlar® 29 plies upon high speed impact with reasonable accuracy. By coupling those two distinctive computational methodology, a ply level damage and interlaminar damage was captured with relatively lower computational cost than micro-scale level approach which is employed in the comprehensive FOI into a high-bypass air breathing propulsion system.

Appendix-C: Study for Fluid Deformation using ALE for Fluid Field Simulation

The ability to accurately model a fluid-structure interaction (FSI) has become highly important for the design optimization in a wide variety of applications. Analyzing the structural or fluidic response of a system on an individual basis can lead to results that may not reflect experimental observations, requiring the coupling of both to represent the system properly. Alternatively, many works are focusing on coupling two disciplines into a single domain. Such modeling strategies are classified as monolithic methods, where the fluid and structural are solved simultaneously to capture the mutual interaction [163]. The monolithic methodologies tend to be more stable because the interaction is inherent, whereas using two specialized solvers in the partitioned approach can be more efficient.

As monolithic FSI methodologies, both Arbitrary Lagrangian-Eulerian (ALE) and Smooth Particle Hydrodynamics (SPH) are thoroughly investigated. ALE and SPH methods have been successfully shown to accurately model large structural deformations and domain separation [164], making both methods good candidates for monolithic analysis. In recent years, these two methods have become more prevalent in FSI analysis [165,11] due to their ability to calculate relatively accurate solutions.

The lid-driven cavity is a simple problem that is often used as a benchmark study for computational fluid dynamics (CFD) [166] since the developed flow structure is highly complex with significant vortex development despite its simple geometry and setup [167]. Many researches have successfully simulated the problem by using multiple computational methodologies. The quantitative analysis to validate the lid-driven cavity problem was conducted by Ghia et al. [168], since then the work has been revisited as a baseline test case for evaluating for the new computational methodologies.

This section aims to address the fluid modeling capability of two time explicit computational methodologies (ALE and SPH) which are employed for the multidisciplinary analysis in this work. Additionally, the result from both methodologies are validated against an implicit Navier-Stokes solver (Ansys Fluent v.15). Each of these methodologies are used to simulate the development and steady-state profile for a square lid-driven cavity at Re of 100, 500, 1000, and 3200. The result from each computational models is compared to preceding work for the lid-driven cavity problem by extracting the centerline of x and y-velocity profiles from the flow field. A computational

uncertainty of each computational models is quantified to check the mesh dependency as well as required computational expense.

C.1 Computational Model Setup

All analyses were non-dimensionalized using the Re of the cavity flow for comparative purposes, with velocity normalized by U_{lid} and coordinates by cavity height. As shown in Fig. C.1, no-slip BCs were assigned for the left, right and bottom wall of cavity for all computational models except for SPH. The lid drove the fluid inside of the cavity at U_{lid}. A grid resolution study was performed at mesh densities of 64x64, 128x128, 256x256, and 512x512 elements. Then, the converged mesh resolution was used to compare each of the computational models for accuracy at Re of 100, 500, 1000, and 3200.

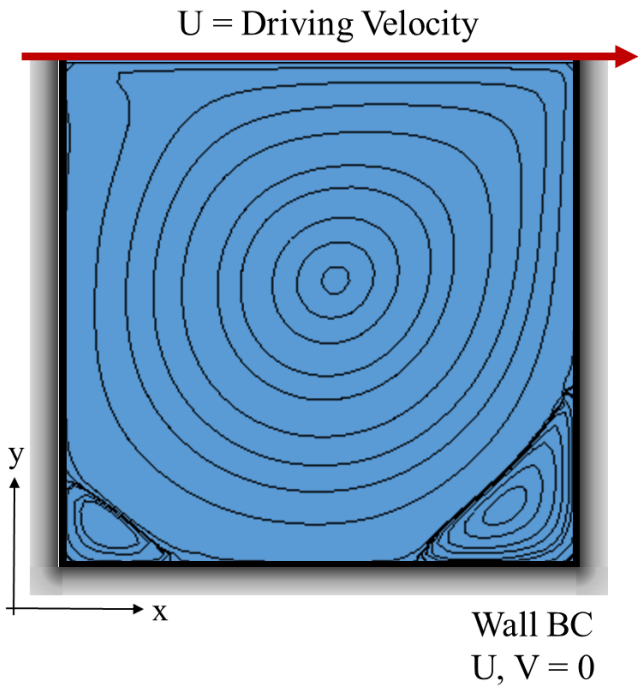

Figure C. 1 Schematic Boundary condition for SPH formulation

Applying BCs to the Eulerian computational models was straightforward because the background mesh was not deforming along with fluid deformation. However, the SPH boundary conditions required special attention because the particles were moving with fluid flow. Figure C.2 shows the schematic, the BC for entire SPH formulation consisted of two parts; (1) fluid particles, and (2) boundary particles, and (3) fluid driving regime. Because of the particle penetration through the boundary layer which has lower mesh density at the boundary, the mesh density of the boundary

was four times that of the fluid. To drive the fluid inside of cavity, an infinitesimal driving regime was created at the top of the domain to induce the velocity along the x-direction.

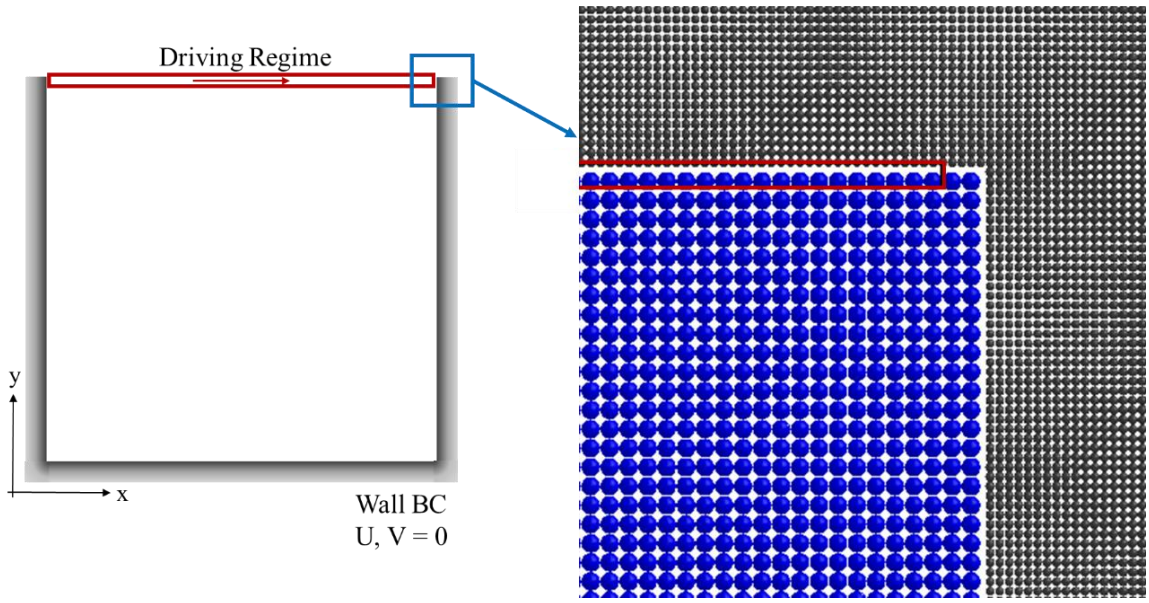

Figure C. 2 Schematic picture for visualization of boundary condition for SPH formulation (Blue = fluid particles, Black = boundary particles)

Additionally, symmetric plane BCs were applied at all boundaries of the cavity to restrain escaping particles that occasionally pass through the particle boundaries. Another unexpected difficulty when using the SPH model was inappropriate time-step evaluation. While mapping the neighboring particles in the beginning, the default initial time-step was excessively high and failed to initiate the simulation. To resolve the stability issue, the initial time-step was required to be manually controlled, in this case it was set to 5E-6s. Even after the simulation was successfully initiated, the proceeding default calculation for time-step resulted in solution divergence, requiring the time-step to be manually set below1E-6s throughout the simulation.

C.2 Verification of Computational Methodologies and Observed Problems

The normalized U and V velocity profiles for each mesh density are plotted along the y and x-direction centerlines respectively in Fig. C.3. Re number of 1000 was selected for the mesh convergence study because it is within laminar flow regime, but the fluid inside can formulate multiple vortical structures inside of the cavity.

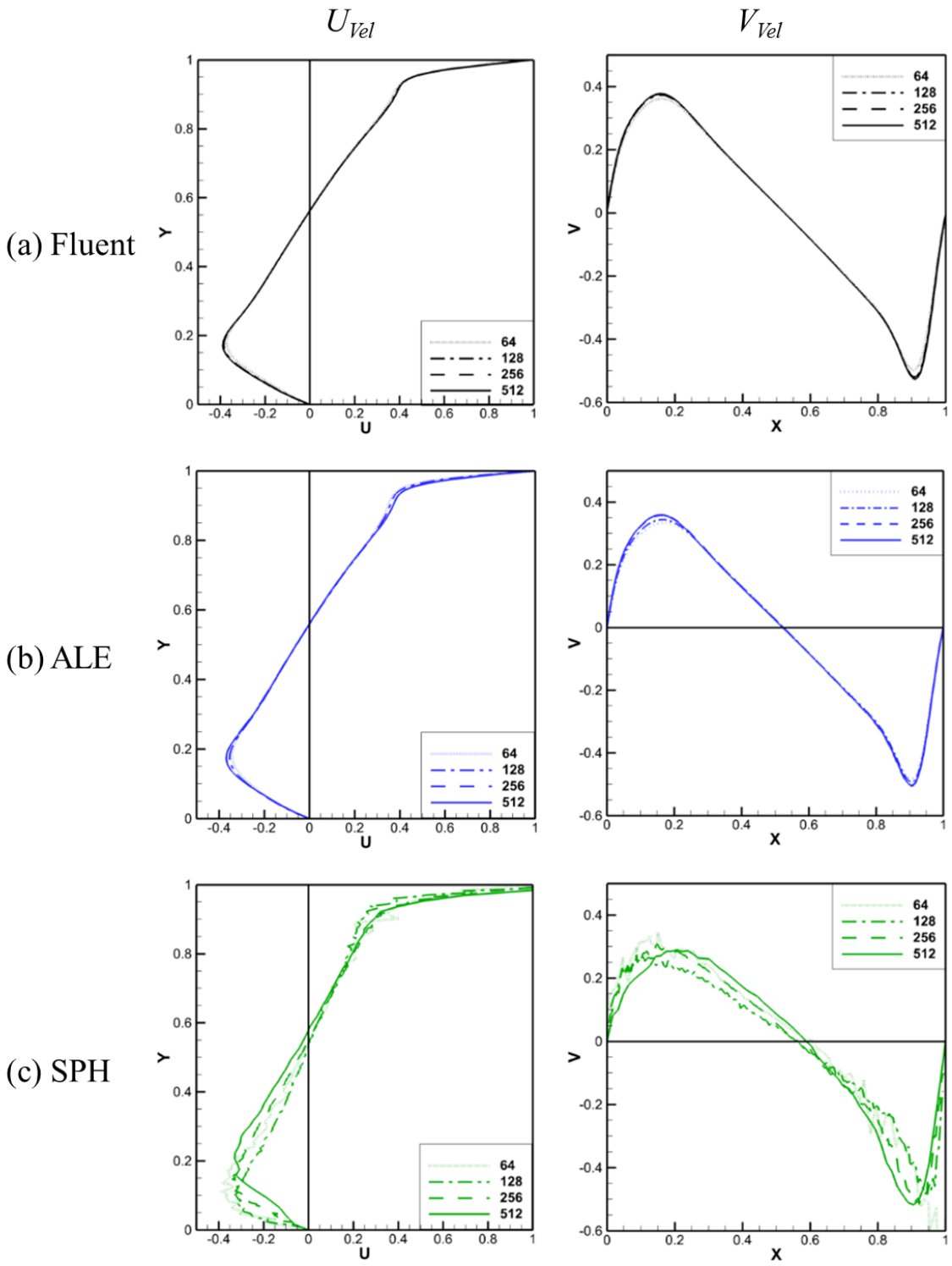

Figure C. 3 U, V velocity profile comparison among multiple computational methodologies (Re=1000)

The velocity profiles calculated by Fluent present the highest level of convergence as shown in Fig. C.3-(a). Even at the lowest grid resolution, 4 profiles are not distinguishable. This was to be expected considering the direct solution of the N-S equations, the use of an implicit method with 10^{-9} convergence tolerance, and the relative simplicity of the problem. Both *U* and *V* velocity profiles calculated using ALE formulation shows a slight discrepancy in velocity magnitude in both the *U* and *V* directions among multiple mesh densities in Fig. C.3-(b). At low mesh density, the fluid deformation was slightly under predicted than both Fluent and ALE solution at high mesh density. When 256 and 512 mesh resolutions were allocated, the velocity profiles became nearly indistinguishable among each other and even from the implicit solution.

The SPH results, on the other hand, do not present any monolithic convergence as a function of mesh density as shown in Fig. C.3-(c). The inflection point for both *U* and *V* velocity profile are influenced by mesh density. The figure implies that the inflection location and velocity magnitude become similar with the other computational methodologies at the highest particle density (512×512). This is because SPH particles were moving along with the fluid deformation, which requires additional average procedure to approximate the particle velocity at the precise location. For the approximation, a particle triangulation was used to approximate the fluid velocity using moving particles. These values were then averaged over ten time steps in an attempt to provide results more representative of the steady state response. The velocity magnitudes were smoothed out noticeably as the mesh density was increased and close to the other computational model.

For the *GCI* study, 64 *U* velocities were measured at the center of cavity (x=0.5). Each data point was then used to quantify the computational uncertainties except for the most top and bottom value, since they fell on the same value due to the applied boundary conditions. Table C- 1 tabulates the computational uncertainties in the medium mesh grid solution for the selected computational models. As expected, the averaged global error ($\overline{\varepsilon_a^{21}}$) of Fluent was lower than other methodologies for both medium and high mesh resolution (2.43% and 3.47% respectively). *GCI* was not significantly improved by increasing mesh density, since the solution was substantially converged to the highest mesh resolution solution. Fluent also achieved the minimum computational uncertainty comparing to the others as shown in Table C- 1. The local order of accuracy of Fluent ranged from 0.13 to 3.99 and the global average order of observed accuracy was reported as 1.91 for the high mesh resolution (128/256/512) case.

Table C- 1 Averaged med-high GCI study for all computational methodologies using *U* velocity along x=0.5 (RE=1000) (Note that GCI and P calculated from med-high pair, 1 and 2, for each mesh group is presented)

Mesh set	*64/128/256*			*128/256/512*	
Fluid Solver	GCI_{21}	P_{21}		GCI_{21}	P_{21}
Fluent	1.23%	1.79		0.29%	1.91
ALE	11.67%	2.21		2.80%	1.97
SPH*	106.4%	1.00		3.66 %	4.34

The averaged global error ($\overline{\varepsilon_a^{21}}$) of ALE solution was slightly higher than that of Fluent solution. The error was calculated as 2.03% and 2.66% for medium and high mesh resolution respectively. *GCI* for lower mesh resolution was considerably high (11.67%), however the result was improved using higher mesh resolution. The apparent order of ALE was varied from 0.031 to 7.25 and its global order of accuracy was 1.97. Considering the 2nd order advection algorithm and remapping algorithm, which was discussed in section 4.3, the apparent order was close to the theoretical discretization order.

The numeric error associated with low-medium mesh of the SPH was considerable (~113%). As a result, additional refinement was applied for the investigation. The *GCI* of 128/256/512 SPH particle resolution was measured to be 3.66% and the averaged error ($\overline{\varepsilon_a^{21}}$) was 30.10% which is still higher than the other methodologies. Such high error was caused by the unsmoothed velocity contour along the cavity center. The unsmoothed velocity contour caused an oscillatory convergence which statically skew the error and *GCI* result near the cavity center where all the velocity profiles are close to each other. However, SPH solution exponentially improved and the fluid deformation became similar to the other computational methodologies at 512×512 particle density. Because of such strong convergence trend toward the higher mesh density, the global order of accuracy was found to be 4.51 which was ranged from 0.40 to 10.22.

For all three computational models, the apparent order was lower than its theoretical order based on the location. This is partially caused by non-monotonic convergence, however it does not state a failure of standard [125,169]. Although the order of observed accuracy was locally lower than the theoretical order, the averaged result reasonably matched the theoretical discretization order. Among the explicit time integral solutions, the computational expense for SPH was by far the highest, followed by. SPH allocated most of their individual computational effort to the element process. Alternatively, ALE allocated a considerable amount of the computational effort to mesh advection and rezoning. For ALE, roughly 36% of computational expense was allocated for element processing, 20% of resources was allocated for mesh advection and other peripheral

calculations at 256×256 mesh density. The ALE mesh advection and remapping increased to 28% of the entire computational expense at 512×512 mesh density while the element processing remained constant. Overall, a higher mesh resolution requires a nonlinear increase in computational cost for element advection and remapping.

Because of the different time integration numerical scheme, the computational expense of Fluent was not presented. In order to compare the computational expense among each methodology, the computational expense was normalized based on the cavity length, minimal computational time of each computational methodology. Among all the computational models, SPH required the highest computational expense (~ $2.5E^6$ *s*) as shown in Fig. C.4. The excessive computational expense was caused by the continuous remapping of neighbor particles and redefining the smoothing length of each individual particle based on the new neighboring particles at each time-step. On the other hand, ALE shows reasonable computational expense to compare with staph formulation. The ALE computational expense was for entire mesh density was an order of magnitude less than that of the SPH.

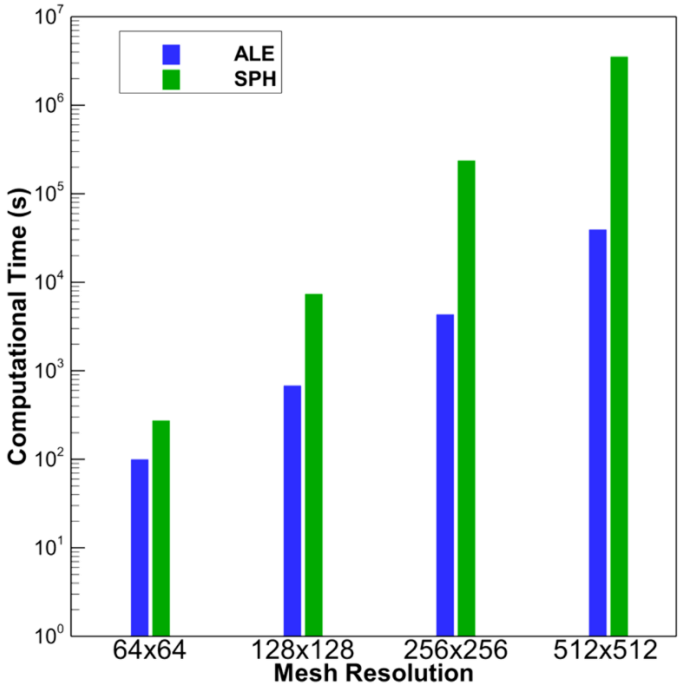

Figure C. 4 Computational expense for ALE and SPH at Re=1000

Finally, the velocity magnitude contour plots of all three computational models are presented in Fig. C.5. Generally, ALE and SPH prediction was qualitatively similar to the Fluent prediction. The primary vortex near the cavity center was clearly shown in all of the computational

methodologies. ALE computational model predicted two vortical structures at the cavity bottom for both sides. In addition to the bottom vortices, the fluid deformation at top of the cavity was also similar to the Fluent result. However, the details of the SPH result were noticeably different from the other computational methodologies. Primarily, the secondary vortices in both bottom left and right corners did not clearly capture as shown in Fig. C.5-(d). In addition to the bottom vortices, the fluid motion at top of the cavity was not similar to the others. This was because of the particle locking behavior. Instead of having vortices, particles at each corner of cavity had random vibrational motion because of the viscous effect from primary vortex. Due to the lack of motion in these areas of particle clustering, the velocity magnitude contours on the bottom and left side were under-predicted.

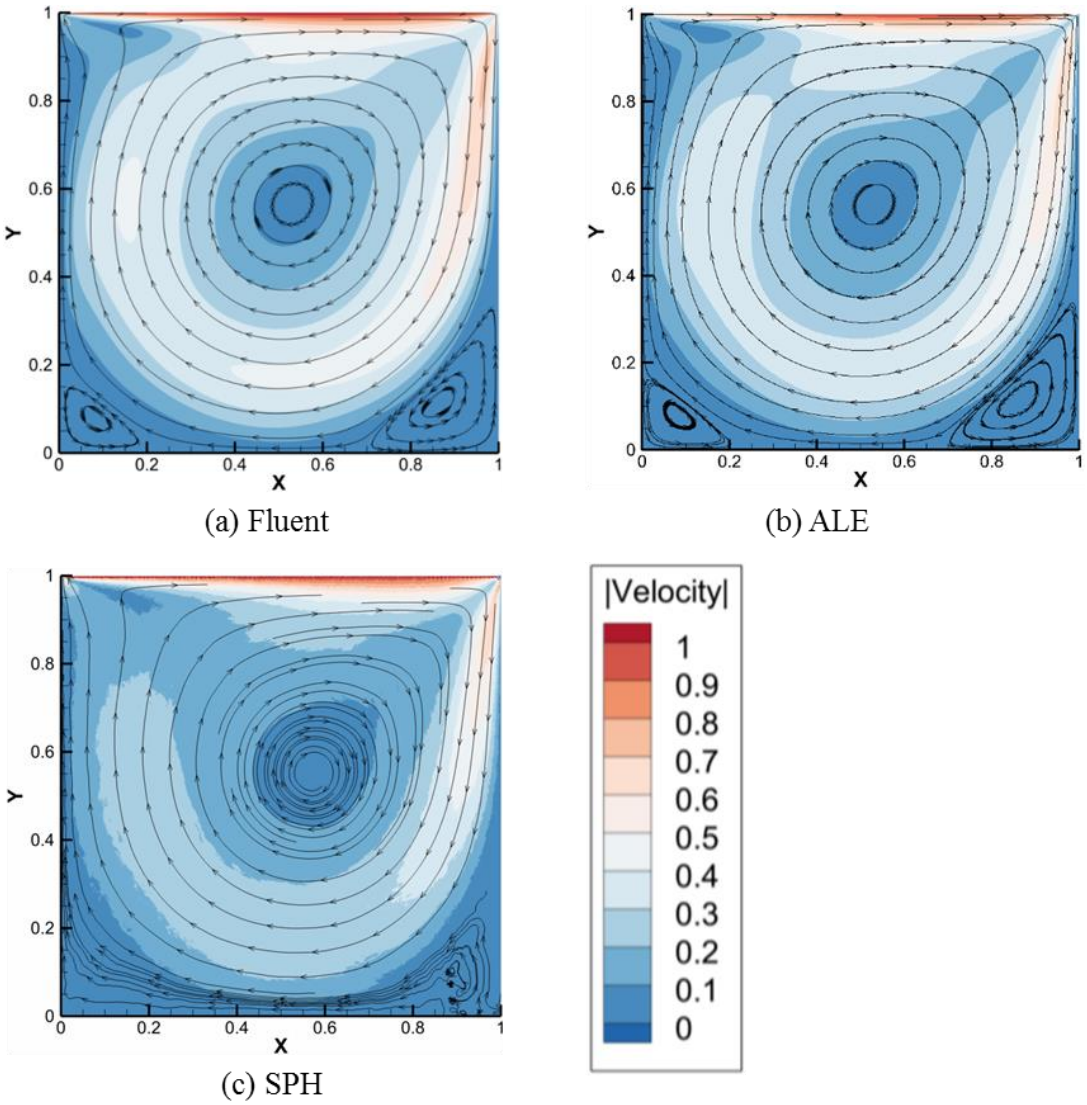

Figure C. 5 Velocity magnitude contour plot with streamline at Re=1000

C.3 Qualitative and Quantitative Comparison between Presented Methodologies and Validation against Physical Experiment

After establishing a mesh-independent result from each computational model, a validation was conducted by comparing between the presented solution methodologies, established computational results, and a physical experiment. In 1982, Ghia et al. [168] computationally analyzed lid-driven cavity flow for a wide range of Re, which had since been established as a benchmark to which many studies compare and verify. Koseff and Street [167] conducted a physical lid-driven cavity flow experiment for Re from 1000 to 10,000.

The presented computational methodologies in this study were compared using the Re 3200 with the grid resolution recommended by the grid resolution study. Overall, the trend of *U* and *V* velocity profiles correlated well with Ghia's result [168] of Re 3200 as shown in Fig. C.6. The profile calculated by FLUENT agreed well Ghia's work. As shown in Fig. C.6-(a), the velocity magnitude for both directions was slightly under-predicted using ALE formulation, though the difference was negligible. Such discrepancy between ALE and FLUENT was diminished even more with increased mesh resolution.

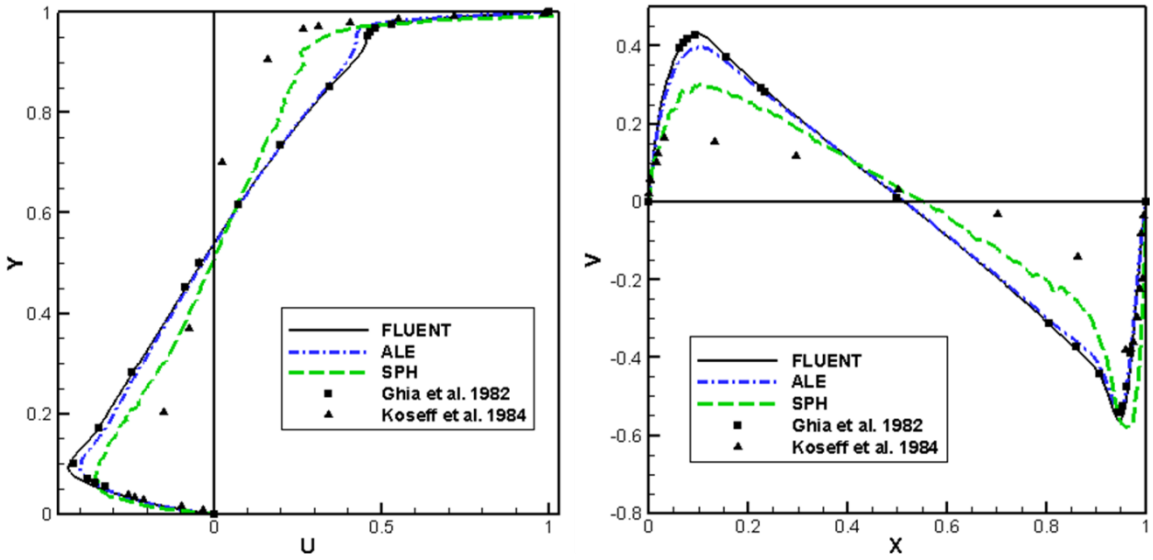

(a) U_{Vel} (b) V_{Vel}

Figure C. 6 *U* and *V* velocity profile comparison among multiple computational methodologies and literatures [167,168] **(Re=3200)**

On the other hand, the velocity magnitude of SPH for both direction was significantly lower than other computational models. As shown in Fig. C.6-(a), the *U* velocity profile was under-

predicted at the negative velocity regime, the location of peak negative fluid velocity was slightly lower than other computational models, and significant under-prediction was observed near the driving regime. Likewise, the *V* velocity was also considerably diverged from the other computational models' result as well as Ghia's result. Figure C.6-(b) shows the *V* velocity on the right side of wall. It was considerably over-predicted did not match well. Also, the *U* and *V* velocity near the cavity center were not similar with the other computational model's prediction.

The simulation results of all the presented computational models were then compared with the experimental work by Koseff and Street [167] and plotted in Fig. C.6. Even though the results agreed well with Ghia et al., the measured velocity magnitudes [167] was noticeably under-predicted in both directions. The primary reason for this disparity was due to the problem caused by the reduced dimension. For the computational work, the domain of fluid was developed as 2-D and the model did not consider any 3-D effect. On the other hand, the physical experiment had the through-thickness viscous interaction with wall. This is also known as end-wall effects. End-wall effects of the cavity in the through-thickness direction causes the primary vorticity to weaken due to the viscous interaction with fixed wall [167,170–173].

The contour plot of velocity magnitude of Re 3200 for all computational analysis is presented in Fig. C.7. For comparison, Fluent was designated as the baseline case since it directly solves the N-S equations as discussed above. Additionally, Ghia's computational result [168] and the cavity experiment [167] at Re 3200 were used in order to conduct a qualitative comparison with the presented computational methodologies. As discussed in Re 1000, Fluent and ALE predicted the secondary vortices at the both side of bottom corners. One of the primary differences between the Re 1000 and 3200 was additional vortex at the top left corner of the cavity. This was also mentioned in Ghia's result [168]. Fluent and ALE were extremely similar against each other, with imperceptible variations in the distribution of contour levels, even including Ghia's result. SPH, on the other hand, diverged in its prediction. Although SPH calculated a primary vortex that was approximate to the other computational models as in Re 1000, the SPH methodology did not clearly represent the recirculation at the bottom two corners nor one at the cavity top. Although higher Re was applied on the cavity, the similar fluid deformation is observed ah shown in Fig. C.7-(c). Uneven particle distributions occurred over the entire domain with particles grouped and stagnated at the corners, exhibiting a vibrational motion as discussed.

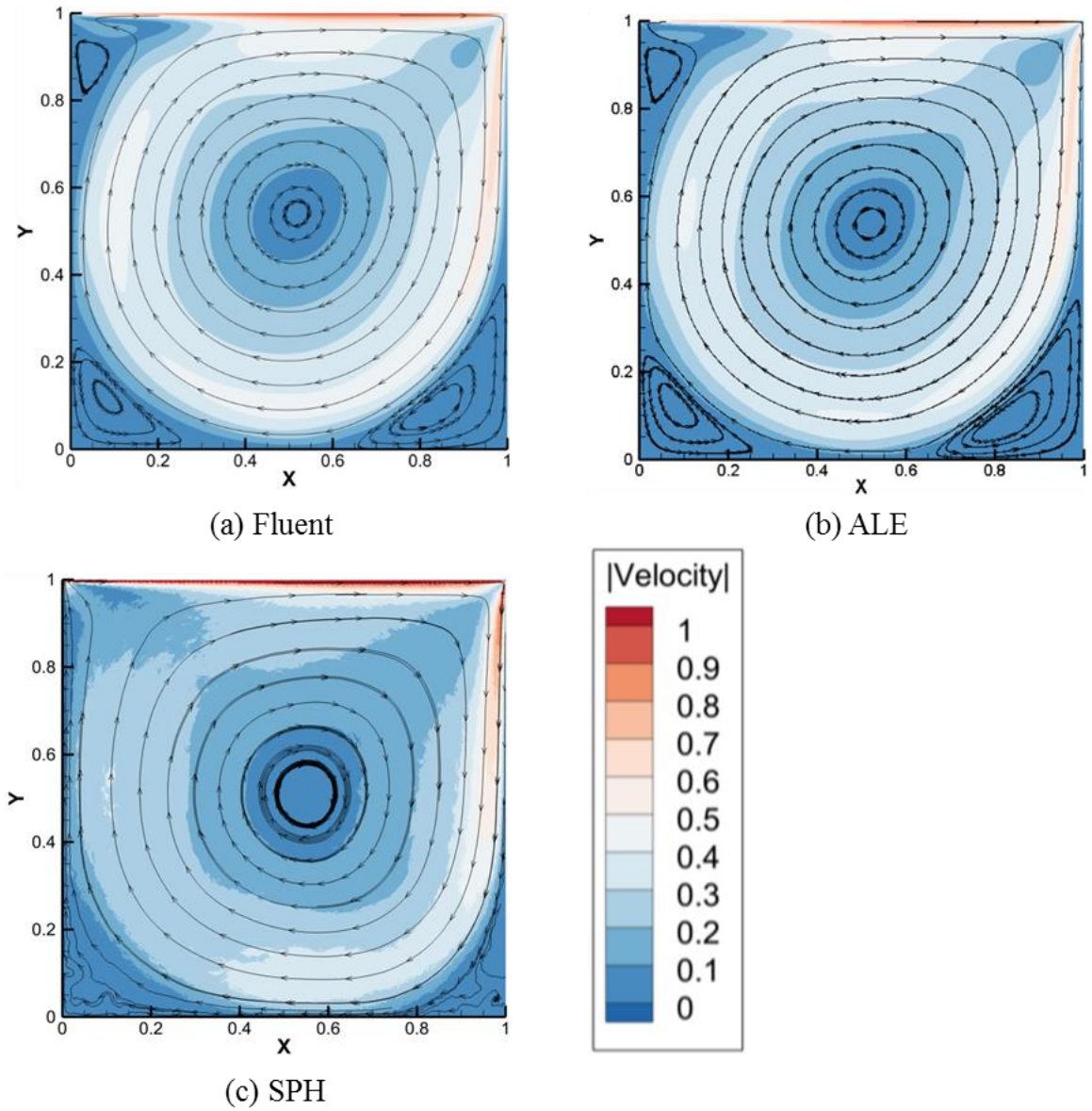

Figure C. 7 Velocity magnitude contour plot with streamline at Re=3200

As a benchmark for ALE and SPH element formulations, a single lid-driven cavity problem was investigated and compared among each. Additionally, the results were compared with Fluent result, preceding researches, and cavity flow experiment. Throughout the *GCI* study, the observed order of accuracy of ALE was reasonable accurate, and the solution presented a strong asymptotic convergence behavior. Being a time explicit fluid calculation methodology with a structured mesh, a penalty-based contact can be established to interface with a structural solver. The computational expense was slightly less than the SPH element formulation. Because of the minor non-linear grid deformation and mesh advection, the apparent order of accuracy of ALE was slightly lower than its theoretical order of accuracy. However, the methodology still proved that it has a potential to

calculate an accurate result. Therefore, it was considered to be an acceptable methodology for comprehensive FSI problem.

On the other hand, the result of SPH was generally the least accurate among the explored computational methodologies, but it was still able to capture the primary vortex in the cavity flow. Throughout the *GCI* study, the SPH presented its own highly mesh dependency. U and V velocity profiles along the center of cavity in both x and y direction matched well with the other methodology results and the literature, yet the fine details of fluidic motion was still missing such as recirculation at the bottom corners. The overall result still proved that the methodology can be a feasible for an FSI problem, assuming a high fidelity fluid result is not required. Possible situations include those with severe mesh deformation or separation caused by fluid, such as hypervelocity impacts, bird or hailstone impact simulations, and explosions.

The lid-driven cavity was revisited to compare the accuracy and computational efficiency using the commercially available time explicit finite element framework. The overall result proved that the presented methodologies were, in general, suitable for fluid analysis from low to transitional flow regime which implies the potential application to fluid-structure interaction.

Appendix-D: Peripheral Information of Comprehensive FOI Simulation

D.1 Johnson-Cook (J-C) Damage Model

In addition to the contact between the fan blade and the foreign object, the contact speed between the casing and the ejected fan blade is also very high when a FBO happens. For such extreme conditions, high strain rate deformations occur and critical shock pressure is induced at the interface in excess of the material strength. Such rapid energy interaction causes a non-linear behavior on the material, which is not considered in the linear elastic-plastic hardening model.

To overcome this shortage, another material failure model is explored. One of the commonly used constitutive material failure models considering the strain rate ($\dot{\varepsilon}$) dependency is Johnson-Cook (J-C) mode. The J-C is derived by purely empirical approach that considers the large deformation, the strain rate hardening, and the thermal softening [174]. The deformation can be calculated by employing the EOS and J-C model. Figure **Error! Reference source not found.** s hows the material response of two typical aerospace materials (Al-6061 and Ti-6Al-4V) with various strain rate ($\dot{\varepsilon}$) using J-C damage model.

Based on the applied strain rate ($\dot{\varepsilon}$), the material response changes noticeably. Generally, the yield strength (σ_o) is gradually increasing as higher speed loading applied on both materials as well as the ultimate tensile strength (σ_u) for both materials. Both materials tend to be more brittle when high speed loading applied. The J-C model is described as Eq. (64) and the damage prediction model is shown in (65):

$$\sigma = \left[\mathrm{A} + \mathrm{B}\left(\varepsilon_{\mathrm{p}}\right)^{n}\right]\left[1 + C * ln\left(\frac{\dot{\varepsilon}}{\varepsilon_0}\right)\right]\left[1 - \left(\frac{T - T_{Roon}}{T_{melt} - T_{Room}}\right)^{m}\right] \tag{64}$$

$$\varepsilon^{\mathrm{f}} = \left[D_1 + D_2 \exp(D_3 * \frac{P}{\bar{\sigma}})\right]\left[1 + D_4 ln\left(\frac{\dot{\varepsilon}}{\varepsilon_0}\right)\right]\left[1 + D_5 * \left(\frac{T - T_{room}}{T_{melt} - T\_Room}\right)\right] \tag{65}$$

where ε_p is the equivalent plastic strain, $\dot{\varepsilon}$ is the plastic strain rate, and ε_0 is the experimental strain rate. The five material constants A, B, n, C, m, and T are evaluated experimentally. A is the yield stress, B and n are the strain hardening constant and exponent, C is the strain rate hardening constant, and m is the temperature softening exponent. Because of the numerical correlation, the contribution

of all three external load (strain, strain rate, and temperature) can be considered and predict material model more precisely by combining the EOS.

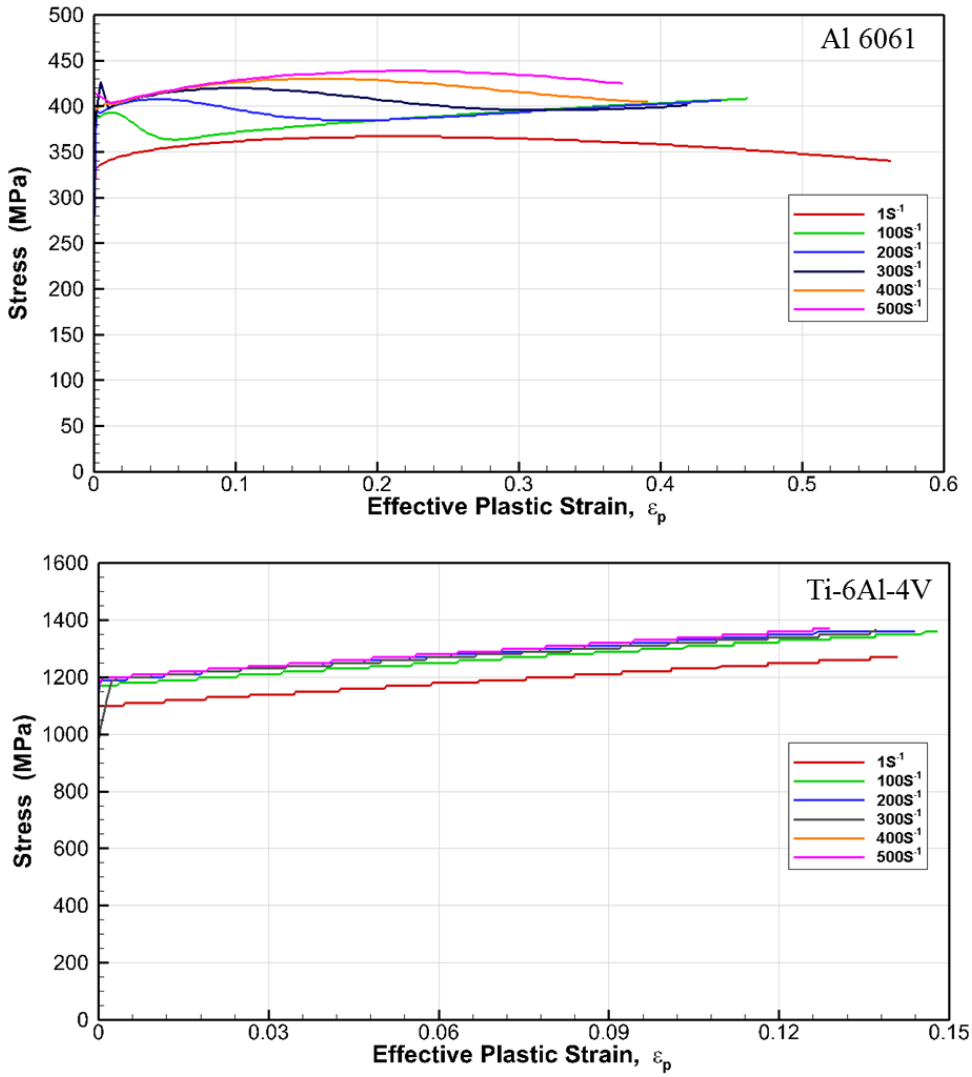

Figure D. 1 Stress-strain response of Al-6061 (top) and Ti-6Al-4V (bottom) at multiple strain rates ($\dot{\varepsilon}$)

$D_{1\text{-}5}$ are the damage parameter, σ_m is the average of the three normal stress, and $\bar{\sigma}$ is the von Mises equivalent stress. D_1, D_2 and D_3 are the damage parameters respecting strain, D_4 is the damage parameter respecting strain rate, and D_5 is the damage parameter respecting temperature contribution. If there is no damage exist all the D parameters equal to zero, and they are gradually increasing once the damage initiated. The numerical representation of the D parameter for the fully damaged continuum is 1.

D.2 Additional Results from Comprehensive FOI Simulations

Energy Distribution. As an example, two energy time plots from the comprehensive FOI simulations were presented in Fig. D.2. The energy was constant throughout the entire simulation for the 0.3 *m* impact simulation. Total energy was conserved as expected.

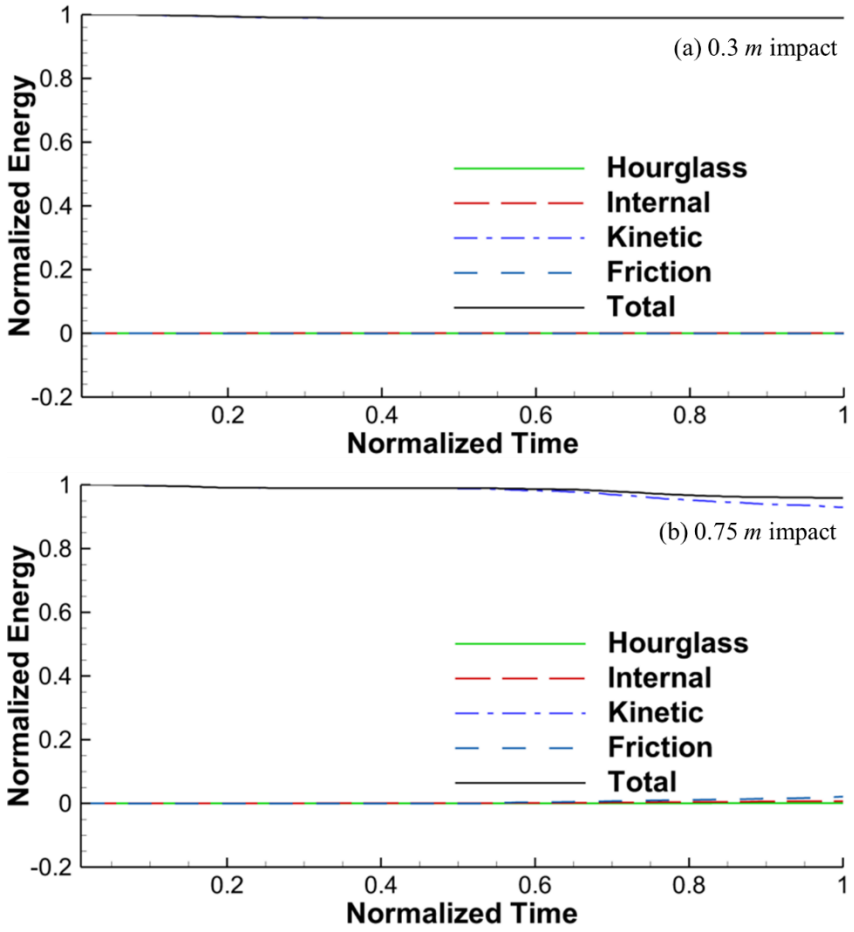

Figure D. 2 Energy-time plot for the aforementioned comprehensive FOI simulations Fig. 6.10 and 6.15 (0.3 and 0.75 *m* respectively)

The figure elucidates the energy distribution throughout the simulation when a bird impact at 0.75 *m* of the fan blade height. The total energy was reduced approximately 4.9% toward the end of the simulation. The energy reduction was resulted in the severe element deletion caused by the FBO and the interaction between fan assembly and casing. The gross hourglass energy was calculated as 9.53 *kJ* throughout the simulation which was caused by using the underintegrated shell elements for the LPC components to save computational cost. The proportion of hourglass energy was less than 1 % which was considered to be reasonable [92,93].

Figure D.3 presents the energy balance result from the simulation presented in Fig. 8.2 in section 8. The internal and kinetic energies evaluated from the rotating system at constant angular velocity. The total energy is the summation of both fluid and structure. Unlike to the previous cases, the energy was being constant then slightly increased as a consequence of the simulation setup.

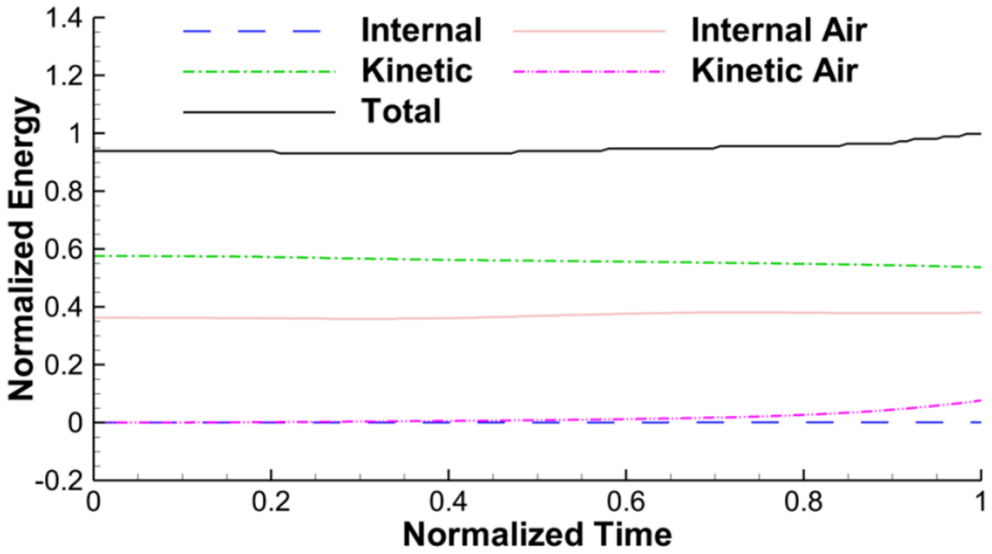

Figure D. 3 Energy-time history for 3-D air flow simulation presented in Fig. 8.2

The rotor assembly including fan blades and LPC blades was set to maintain a constant speed which was driving the fluid progressively faster than the original ingestion speed. Because the interaction between structure and fluid continuously occurred, the energy plot was corresponded with the simulation input. The total energy was approximately constant before the air ingested into LPC, the total energy, then, progressively increased because of the increase of kinetic energy as the fluid start interacting with LPC.

D.3 von-Mises Stress Plot of FOI Simulation using Baseline Model

A sequence of von-Mises stress contour plots of a propulsion system is shown in following images. A 2.5 *kg* bird impacted at 0.5 *m* leading edge height (the same simulation shown in Fig. 6.13 in section 6.2.1).

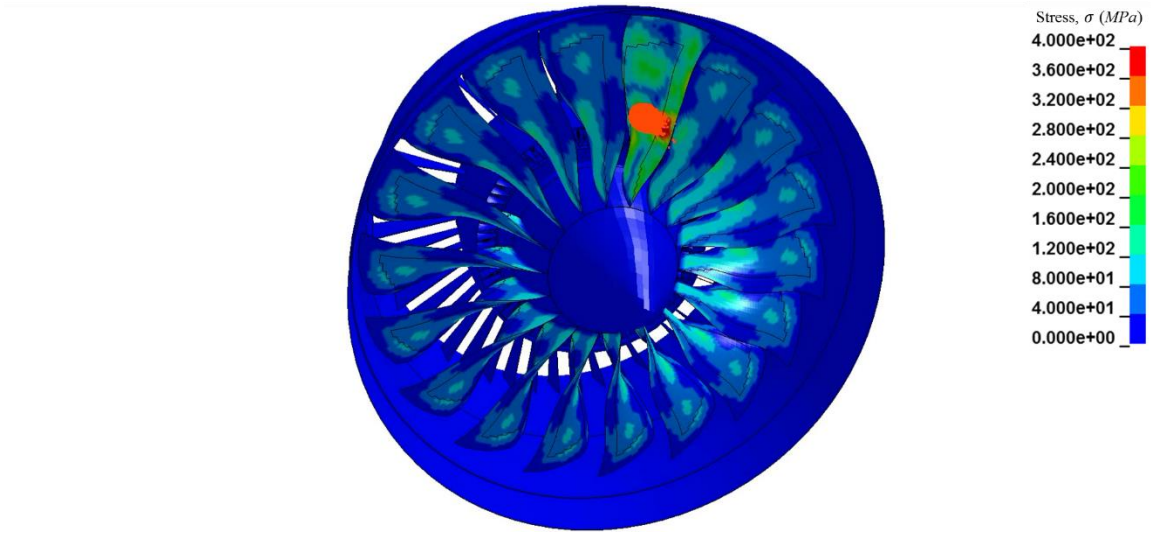
Stress, σ (MPa)
4.000e+02
3.600e+02
3.200e+02
2.800e+02
2.400e+02
2.000e+02
1.600e+02
1.200e+02
8.000e+01
4.000e+01
0.000e+00

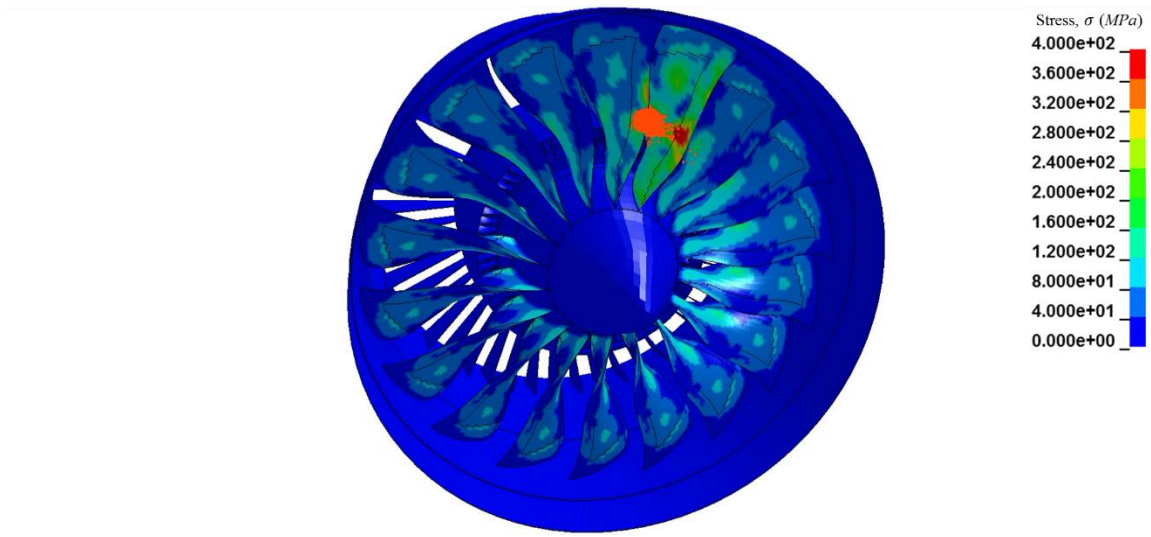
Stress, σ (MPa)
4.000e+02
3.600e+02
3.200e+02
2.800e+02
2.400e+02
2.000e+02
1.600e+02
1.200e+02
8.000e+01
4.000e+01
0.000e+00

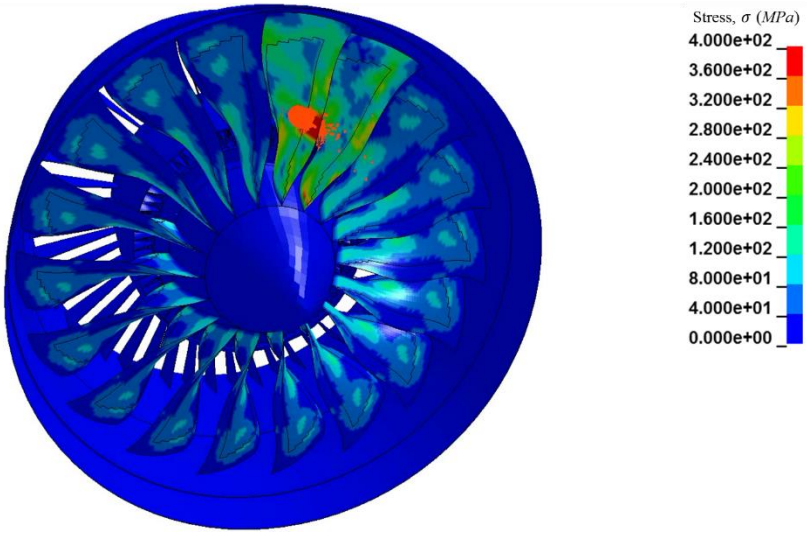
Stress, σ (MPa)
4.000e+02
3.600e+02
3.200e+02
2.800e+02
2.400e+02
2.000e+02
1.600e+02
1.200e+02
8.000e+01
4.000e+01
0.000e+00

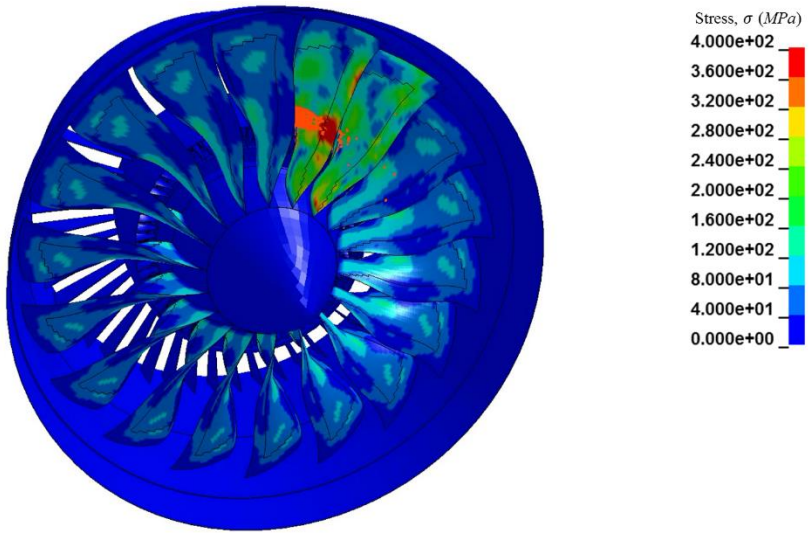
Stress, σ (MPa)
4.000e+02
3.600e+02
3.200e+02
2.800e+02
2.400e+02
2.000e+02
1.600e+02
1.200e+02
8.000e+01
4.000e+01
0.000e+00

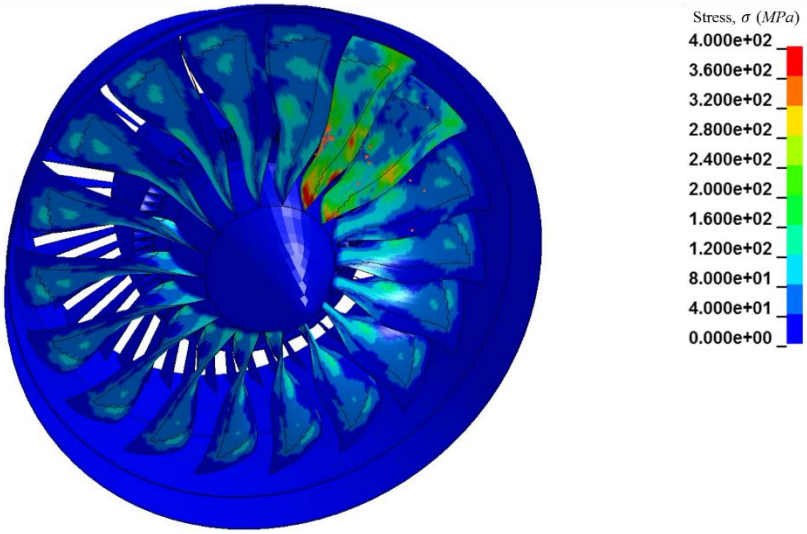
Stress, σ (MPa)
4.000e+02
3.600e+02
3.200e+02
2.800e+02
2.400e+02
2.000e+02
1.600e+02
1.200e+02
8.000e+01
4.000e+01
0.000e+00

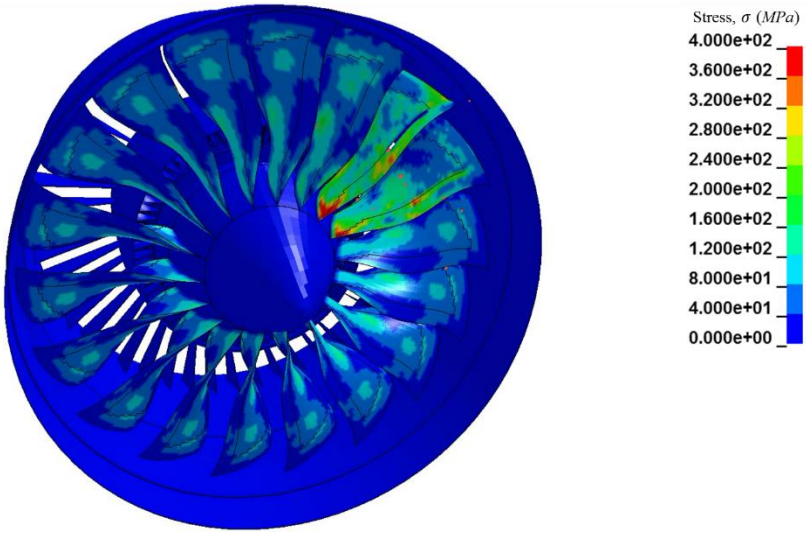
Stress, σ (MPa)
4.000e+02
3.600e+02
3.200e+02
2.800e+02
2.400e+02
2.000e+02
1.600e+02
1.200e+02
8.000e+01
4.000e+01
0.000e+00

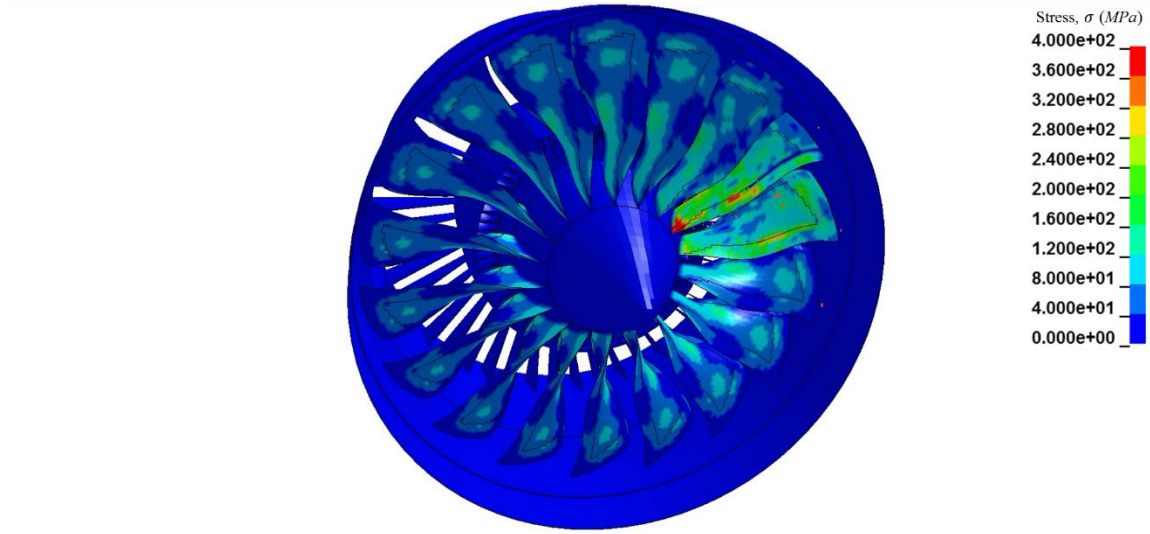
Stress, σ (MPa)
4.000e+02
3.600e+02
3.200e+02
2.800e+02
2.400e+02
2.000e+02
1.600e+02
1.200e+02
8.000e+01
4.000e+01
0.000e+00

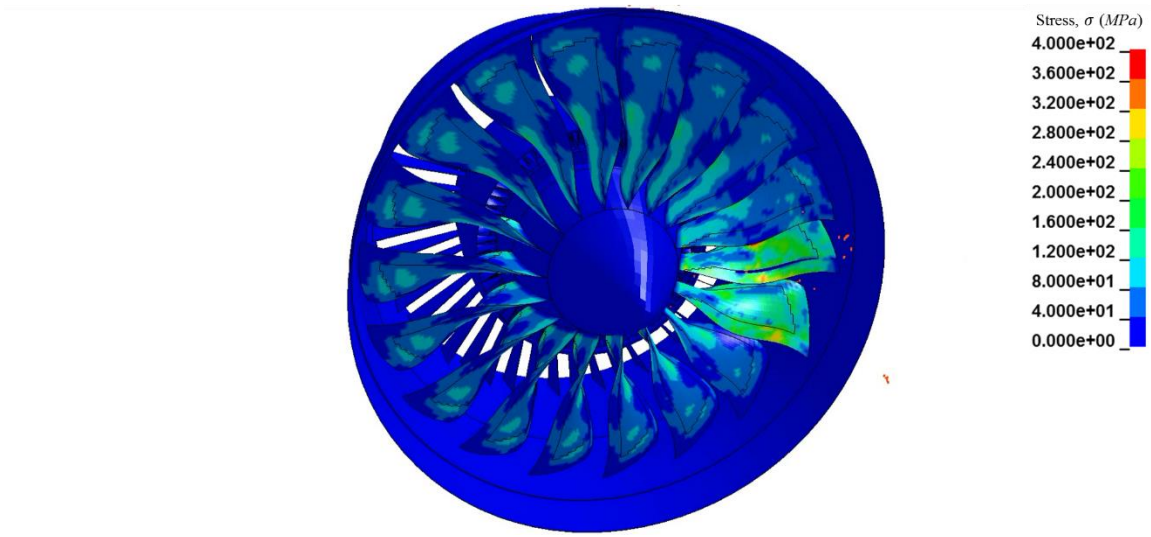
Stress, σ (MPa)
4.000e+02
3.600e+02
3.200e+02
2.800e+02
2.400e+02
2.000e+02
1.600e+02
1.200e+02
8.000e+01
4.000e+01
0.000e+00

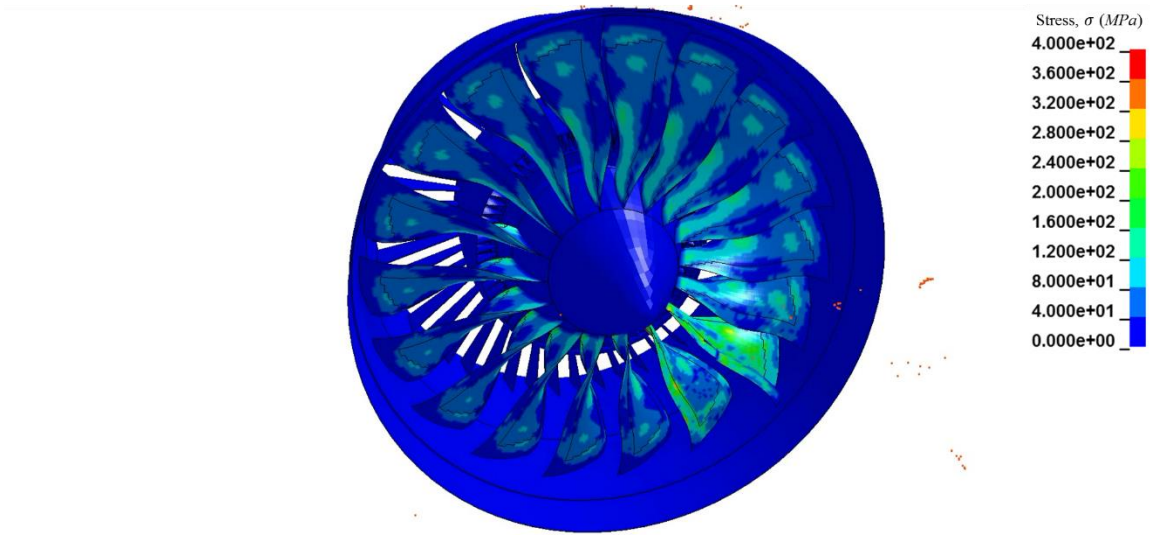
Stress, σ (MPa)
4.000e+02
3.600e+02
3.200e+02
2.800e+02
2.400e+02
2.000e+02
1.600e+02
1.200e+02
8.000e+01
4.000e+01
0.000e+00

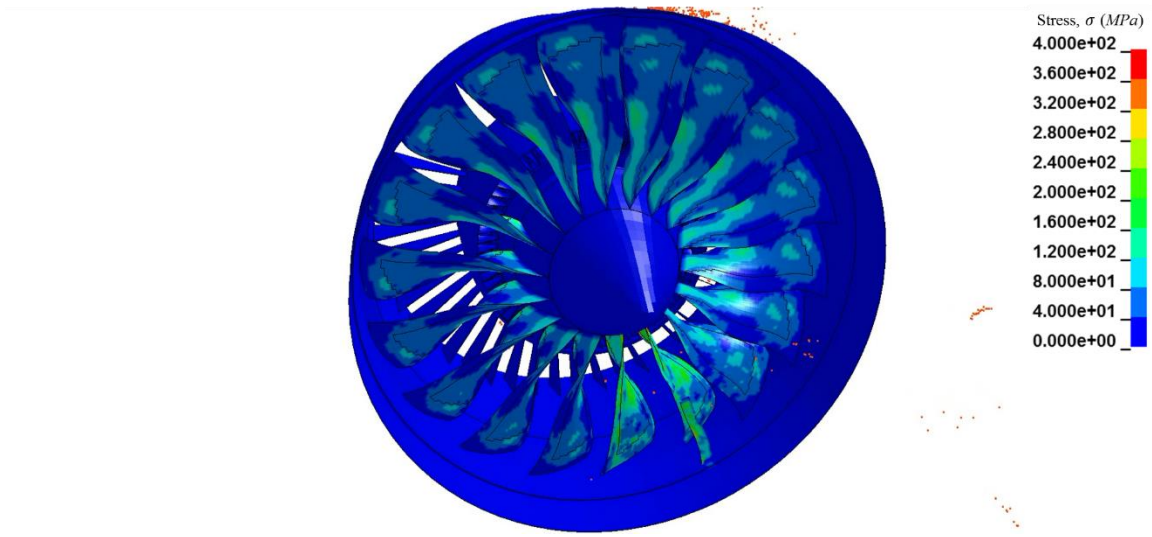
Stress, σ (MPa)
4.000e+02
3.600e+02
3.200e+02
2.800e+02
2.400e+02
2.000e+02
1.600e+02
1.200e+02
8.000e+01
4.000e+01
0.000e+00

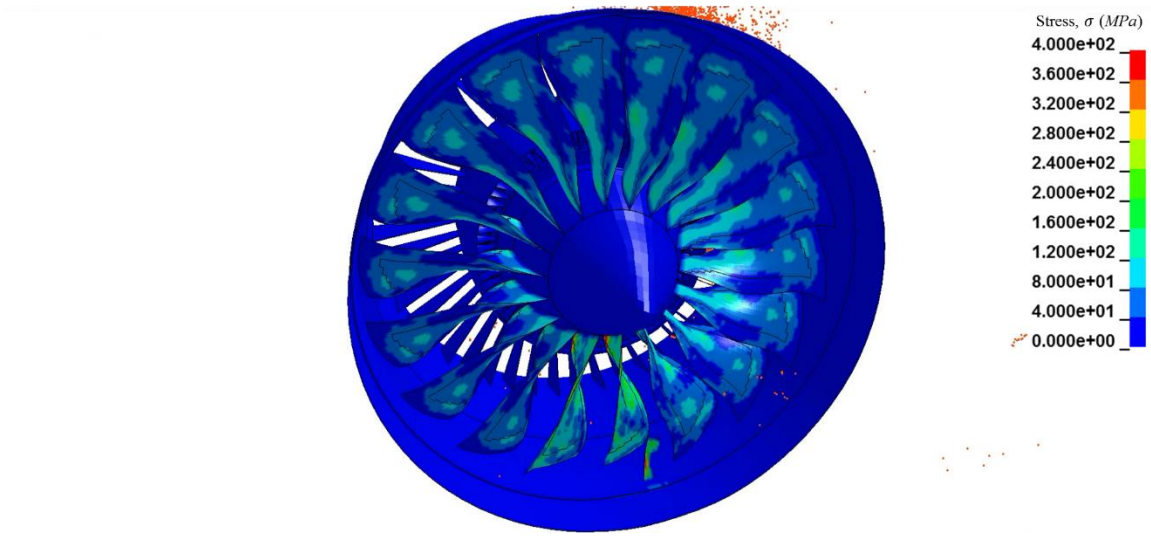
Stress, σ (MPa)
4.000e+02
3.600e+02
3.200e+02
2.800e+02
2.400e+02
2.000e+02
1.600e+02
1.200e+02
8.000e+01
4.000e+01
0.000e+00

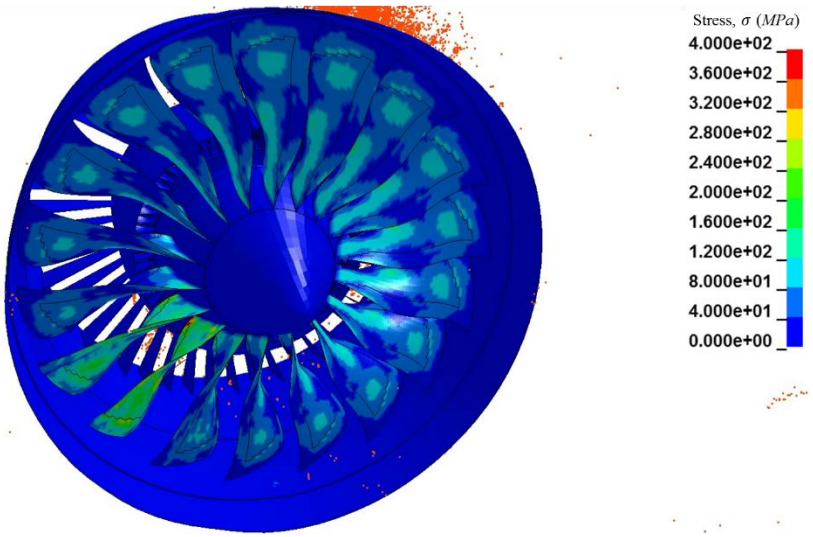
Stress, σ (MPa)
4.000e+02
3.600e+02
3.200e+02
2.800e+02
2.400e+02
2.000e+02
1.600e+02
1.200e+02
8.000e+01
4.000e+01
0.000e+00